TUDelft

Delft University of Technology

Sailing Efficiency and Course Keeping Ability of Wind Assisted Ships

van der Kolk, Nico

Important note
To cite this publication, please use the final published version (if applicable).
Please check the document version above.

Sailing Efficiency and Course Keeping Ability of Wind Assisted Ships

Proefschrift

ter verkrijging van de graad van doctor
aan de Technische Universiteit Delft,
op gezag van de Rector Magnificus prof. ir. K.C.A.M. Luyben,
voorzitter van het College voor Promoties,
in het openbaar te verdedigen op donderdag 25 juni 2020 om 10:00 uur

door

Nicholas Jonas VAN DER KOLK

Master of Science in Marine Technology

geboren te Washington D.C.,
Verenigde Staten.

Dit proefschrift is goedgekeurd door de

promotor: prof. dr. R.H.M. Huijsmans
copromotor: dr. I. Akkerman

Samenstelling promotiecommissie:

Rector Magnificus,	voorzitter
Prof.dr.ir R.H.M. Huijsmans,	Technische Universiteit Delft
Dr.ir. I. Akkerman,	Technische Universiteit Delft

Onafhankelijke leden:

Dr.ir. J.A. Keuning,	Technische Universiteit Delft
Prof.ir. J.J. Hopman,	Technische Universiteit Delft
Dr. I.M Viola,	University of Edinburgh
Dr. J. Wackers,	Centrale Nantes
Prof.dr. P.A.K. Wilson,	University of Southampton
Prof.dr.ir. C. van Rhee,	Technische Universiteit Delft, (reservelid)

for Dr. Eva S. Jonas

But Stubb, he eats the whale by its own light, does he? and that is adding insult to injury, is it? Look at your knife-handle, there, my civilized and enlightened gourmand, dining off that roast beef, what is that handle made of?- what but the bones of the brother of the very ox you are eating? And what do you pick your teeth with, after devouring that fat goose? With a feather of the same fowl. And with what quill did the Secretary of the Society for the Suppression of Cruelty of Ganders formally indite his circulars? It is only within the last month or two that the society passed a resolution to patronize nothing but steel pens.

H. Melville (1851)

Contents

1
Introduction

Figure 1.1.: JAMDA sail installed on coastal freighter in Japan (1980)

Wind propulsion for commercial ships has again garnered interest as a viable propulsion alternative for commercial ships. Of course, the sailing ship fell out of favor as steam and diesel engines matured and offered a reliability that well-served the primacy of time in the modern economy. With the first OPEC crisis in 1973, the global economy and sea shipping sector had to reckon with the profound exposure to risk that a complete dependency on fossil fuels entails. The following decade witnessed a renewed interest in wind propulsion for commercial ships. A notable effort was undertaken in Japan, where 20-odd vessels in the short sea fleet were converted to wind hybrids (Figure 1.1). Recently, the researchers Fujiwara and Ueno have published a series of studies associated with a new (planned) demonstration vessel, the Wind Challenger [84], including testing of a 1/3 scale prototype of a collapsible solid wing sail [38], and a presentation of towing tank results for systematic variation in appendage configurations [74]. However, then as now, the ever-volatile price of oil proved to be an insufficient driver for the wider adoption of wind propulsion. Over the years, interest in wind assistance for commercial ships waned as oil prices normalized. Now, a growing consensus in many societies regarding the need for action to mitigate human impacts on the global climate offers a compelling new driver.

1.1. Drivers for Wind Assist

Around 90 % of world trade is carried by the global shipping industry, accounting for nearly three percent of annual anthropogenic carbon dioxide emissions [99]. [78] report that greenhouse gas emissions of the sea shipping sector are expected to increase by 50-250 % by 2050. The global fleet remains largely powered by Heavy Fuel Oil (HFO), which contains high sulfur content. The shipping industry is responsible for 13 % of total sulfur oxide emissions, and 15 % of nitrogen oxide emissions [99]. Along with other fine particulates, this impact on local air quality is a politically salient issue. The maritime industry is currently under broad-based societal pressure to mitigate its negative impact on the environment and especially on human health.

It is the International Maritime Organization's (IMO) stated ambition to achieve 50 % reduction in carbon dioxide emissions by 2050. The target is offered as a framework for member states intended to bring the shipping industry in line with the Paris Climate Agreement's temperature goal, which seeks to limit global warming to well below two degrees Celsius. More recently, a market-ready zero-emissions ship was promised in 2030. The available de-carbonization pathways that keep global temperature rise below the stated 1.5° target require systemic changes in all sectors of the economy.

The IMO acknowledges that energy efficiency measures are largely underutilized and that market drivers alone are insufficient to bring about the required technical and operational measures [2, 16] and estimates that unrealized potential for efficiency savings in the maritime sector lies between 25 % and 75 % for CO_2 emissions. The shipping industry is relatively unregulated when compared to other sectors of the global economy. The IMO has introduced two regulatory efforts for ships:

Figure 1.2.: E-Ship 1, equipped with four Flettner rotors, has been in commercial operation for nine years.

the Energy Efficiency Design Index (EEDI), imposing increasingly ambitious targets for new-build ships, and the Ship Energy Efficiency Management Plan (SEEMP), intended to improve the operational efficiency of all ships. Other vessel environmental metrics are being considered by the IMO and the European Union, including the Energy Efficiency Operational Index (EEOI). The EEOI mandates incremental improvements for all vessel types. Vessel performance is to be monitored with a system like AIS. Finally, it should be noted that the upcoming 2020 Sulfur Cap has extended present Emission Control Areas (Northern European and North American territorial waters) to a global scope, bringing considerable uncertainty to bunker markets.

Researchers such as [106] have demonstrated that full de-carbonisation of the shipping industry is necessary to stay in line with the Paris agreement. The implementation of short-term emission reduction measures is of vital importance to curb cumulative emissions. At the same time, it has been shown that projected growth for the maritime shipping sector is such that even a full implementation of presently available technology, under existing policy measures, would be insufficient to curb the contribution of the sector to the sum of anthropogenic CO_2 emissions [5]. It is unlikely, for example, that the targets of the European Commission (40 %-50 % reduction by 2050) will be reached, as demonstrated by [2, 32]. It has also been reported that the EEDI is not adequately incentivising the adoption of all innovative measures with the potential for significant savings [96].

Wind-assisted ship propulsion stands apart among available technologies for the energy transition in commercial shipping. A wind-hybrid vessel promises to deliver substantial fuel savings, a result that has been reported by several researchers in recent years [31, 37, 77, 107], and others. This promise of substantial reductions in emissions, for both local pollutants and for greenhouse gases, is achievable in

the near-term. The barrier to broader market uptake of wind-assist concepts is not technological readiness; several viable concepts for wind propulsors are commercially available. Rather, the obstacle is a lack of experience with industrialized sailing and unwillingness to take risks as an 'early adopter'. At the end of 2019, five wind-assist vessels were operating, and at the end of the current year, this figure will grow to 19. Projected wind-assist fleet size is estimated at 3-7k in 2030 (see Figure 1.3).
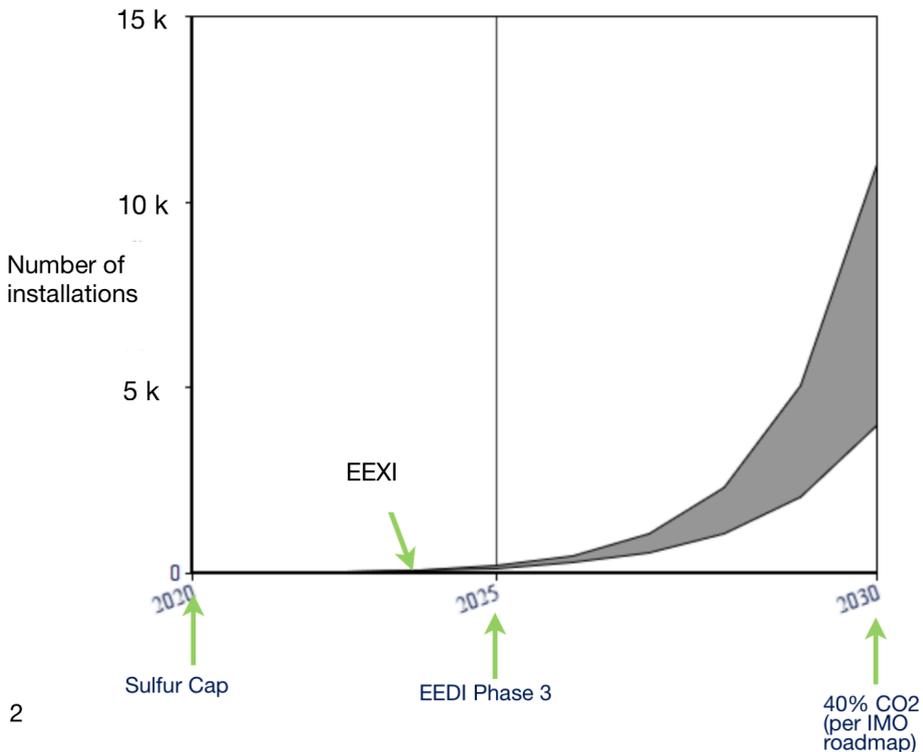
Figure 1.3.: Market projection for energy-efficient ships, showing upcoming regulatory measures.

The further development of this promising technology is hampered by a poor understanding of the interaction effects between wind propulsors and the hydro-mechanics of commercial ships. For the ship owner or operator, this lack of experience with industrial sailing introduces uncertainty in a profoundly risk-averse sector. For the regulator who wishes to promote the uptake of sustainable technologies, the knowledge gap raises the spectre of misdirected policies that fail to advance wind-assisted ship propulsion as a viable component of the energy transition. In fact, wind propulsion is the only intervention in the maritime shipping sector that promises significant reductions in greenhouse gas emissions in the near term. Fur-

thermore, besides the simple arithmetic of fuel savings and limiting exposure to increasingly volatile fuel prices, wind assistance raises the possibility of engaging with an activist consumer class and potentially increasing the perceived value of shipped products.

Relevant research topics encompass a wide range of disciplines, extending beyond physical modeling to include logistics and economics. The further development of this promising technology, and its eventual implementation, will be made possible by these academic, research and industry partners working in concert. Wind-assisted ship propulsion is a dedicated research theme at the Ship Hydromechanics section of Delft University of Technology. Present research under the Sail Assist project is divided between two Ph.D. projects: focusing on the hydrodynamics (the thesis), and the aerodynamics (Giovanni Bordogna) of wind-assisted commercial vessels.

The present thesis work follows two research lines: simulation work, the Delft Wind-Assist series and database; and several experimental campaigns in the large towing tank of the Ship Hydro-mechanics laboratory, SHS-3ME, TU Delft. As part of the Sail Assist research group, and in collaboration with the Polytechnic University of Milan, University of Manchester, and the University College London, the hydromechanic modeling developed in this thesis has been integrated into an techno-economic assessment of wind-assisted ships (Chapter 5).

Source: http://dykstra.nl

Figure 1.4.: The Ecoliner concept, by Dykstra Naval Architects.

1.2. Sailing Preliminaries

To arrive at the achievable fuel savings of the considered wind-assisted ship sailing along a desired route, it is first necessary to study its performance in terms of aerodynamics, hydrodynamics and total fuel efficiency. The performance of a wind-assist concept will depend on the contribution of the wind propulsor alongside the efficiency of the conventional propulsion system. The ratio $T_{\mathrm{Aero}}/\Delta R_{\mathrm{Sailing}}$ is a convenient metric when assessing the performance of a wind-assisted vessel, representing the L/D ratio of the WASP installation. Due to the auxiliary thrust generated by the wind propulsors, the existing engine and propeller operating conditions will change. Not only will the propeller mainly operate in a light-loaded condition, but it will also operate in an oblique flow. Also to be considered is the drag penalty associated with heel and leeway: the *"sailing condition"*. The underwater ship of a conventional freighter is ill-suited for efficient sideforce production, and significant induced resistance is to be expected. Of course, the introduction of a sail-plan will only benefit the vessel if the net thrust gained outweighs any loss in efficiency or increase in resistance.
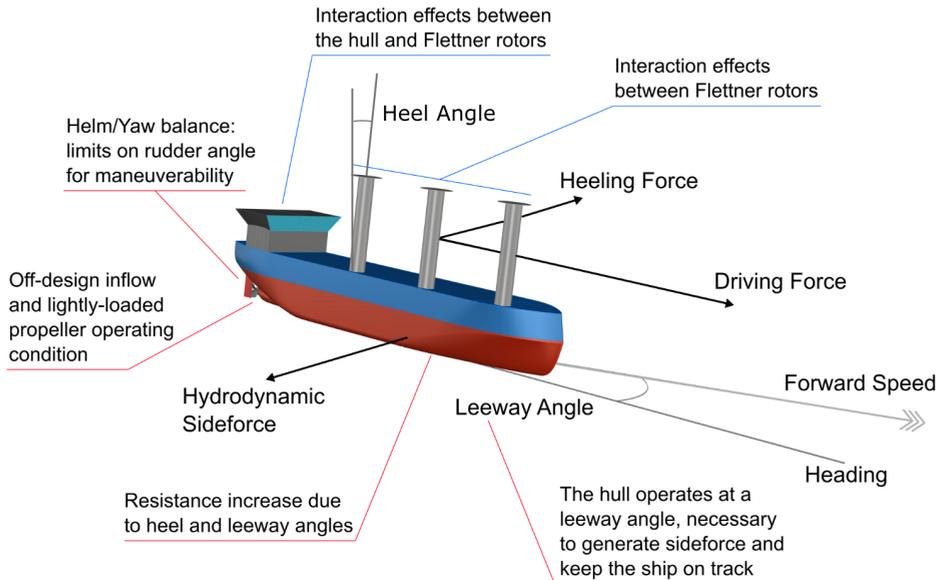
The *Sailing Condition*

Figure 1.5.: Key components of a vessel model.

Fitting a commercial vessel with an auxiliary wind propulsor will introduce a set

of forces and moments besides the desired aerodynamic thrust. These forces need to be balanced by corresponding hydrodynamic reactions. The ship will sail with a leeway angle β about the yaw axis, which is equivalent to the angle of attack for the hull (see Figure 1.5). It is this angle of attack that generates the hydrodynamic sideforce in opposition to the aerodynamic sideforce. Further, the distribution of the hydrodynamic sideforce along the hull will result in a net heeling and yawing moment. Finally, the vertical separation between the aerodynamic and hydrodynamic sideforce components will create a heeling moment. The steady sailing condition requires an equilibrium for all degrees of freedom, and a sailing ship will adopt a constant heel and leeway angle *the sailing condition* to generate the necessary reactionary forces.

Heeling Angle $< \phi >$ An inclination of the vessel about its longitudinal axis. Vessel heel changes the distribution of displaced water volume and leads to a hydrostatic restoring moment.

Leeway Angle $< \beta >$ The angle between the direction of vessel motion and longitudinal axis of the vessel. The leeway angle places the vessel hull in an oblique flow, generating a hydrodynamic sideforce and moment.

In particular, the yaw balance (moment about axis of the leeway angle β) of the ship represents a key modeling and design challenge for wind-assist vessels. A conventional commercial vessel hull, with an undersized rudder as the only appendage, is essentially unfit for sailing. Such a hull will operate with greater leeway angles, and with 'weather helm' as a consequence of this ineffective sideforce generation. The rudder can be used to oppose this destabilizing moment, with an associated resistance penalty. Most of all, the vessel must still be able to maneuver safely. A key task is to find hull form features that can deliver the needed forces effectively and efficiently. This area is new for commercial ships, and designers and/or owners who wish to explore the possibilities offered by wind propulsors must have a reliable and practical method for predicting performance. The influence of the sailing condition on resistance, yaw balance, propeller efficiency, stability, maneuverability and sea-keeping all require careful study.

The use of wind propulsion systems to transform wind energy into forward thrust may be used in two ways:

1. Increase the speed of the ship while maintaining the same engine output the ship would have without wind-assisted propulsion

2. Reduce the use of the main engine while maintaining the same service speed the ship would have without wind-assisted propulsion

The latter solution is generally considered the most interesting from an operational perspective. Other, more complex control rules can include a specified minimum engine power, or arrival time in the context of route optimization.

The total aerodynamic force generated by the installed sail plan will act in some direction that is generally not aligned with the direction of the vessel's forward speed. Beginning with the aerodynamic driving force generated by the wind propulsors, the contribution from each unit is combined into a resultant vector acting (approximately) at the geometric center of the sail plan. A sailing equilibrium calls for a balance of forces and moments. The vertical separation between the aerodynamic center of effort and the waterline gives rise to a heeling moment that must be opposed by a hydrostatic righting moment, giving the vessel a heeling and trimming angle. Any transverse component of the aerodynamic force must be opposed by an hydrodynamic sideforce.

The component of aerodynamic force that is aligned with the vessel motion, or the desired forward thrust, will complement the engine-delivered thrust. If the engine throttle is unchanged, the vessel will increase speed until a new balance between total thrust and ship resistance is reached. The vessel operator may decide to reduce throttle to maintain a constant speed. In this case, the fuel consumption is reduced accordingly. The relationship between reduction in engine-delivered thrust and reduction for fuel consumption is dictated by the efficiencies of the propeller, main engine, and other machinery. The mechanical efficiency of the main propulsor is often optimized for a specific working point corresponding to the design speed of the ship. Furthermore, the propulsive efficiency of the propeller is similarly optimized for a nominal inflow and required thrust. Whether the captain decides to increase speed or reduce throttle, the impact on vessel performance is already subject to an intricate interplay of mechanical and propeller efficiencies.

The ship adopts a heel and leeway angle to support the sail-plan. This combination places the hull—which is otherwise optimized for quite specific and symmetric operating conditions—oblique to the mean flow in the *sailing condition*. The normal wave field produced as part of the wake of this ship will be superimposed on the pressure distribution arising from the sideforce production by the hull, along with the Munk yawing moment [75]. Finally, a vessel heeling angle will bring the vessel "shoulders" closer to the free surface, leading to a further distortion of the wave system. The pressure resistance for a sailing ship will therefore vary with heel and leeway angles, alongside the ordinary Froude number dependency.

The wave system and hydrodynamic sideforce are presented in Figure 1.6. The distribution of sideforce is the manifestation of several hydrodynamic phenomena that are associated with heel ϕ and leeway β. First, there is a strong pressure peak at the bow, a characteristic feature of low-aspect ratio lift. Secondly, a distinct under-pressure along the after stations, the Munk yawing moment, is observed. Also, asymmetry is introduced into the wave system by the pressure field associated with sideforce production. Finally, the vessel heeling angle results in a further distortion of the wave field as the vessel shoulders interact with the free surface.

Although the sailing condition may be analyzed as a quasi-static system where a balance of forces and moments is sufficient, as in Chapter 5, asymmetries in the fluid accelerations (the *virtual mass*) that pass to the wake of the ship hull makes it an intrinsically dynamic system. This energy dissipation, the induced drag associated with sideforce production, is a new component of resistance that must
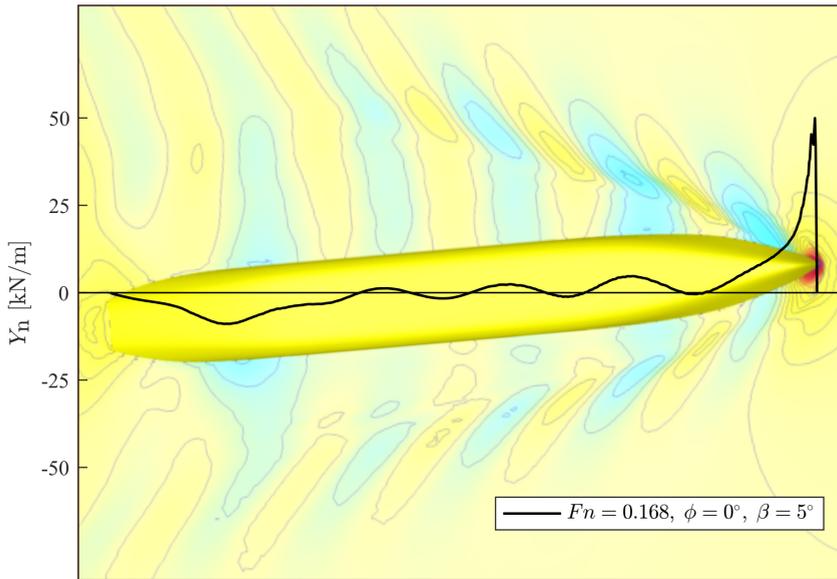
Figure 1.6.: Distribution of hydrodynamic sideforce along hull and vessel wave system for the Ecoliner hull. Simulation result.

be considered in the balance for wind propulsors, engine thrust, and the well-known contributions to the vessel resistance. The commercial ship hull, characterized as a low-aspect ratio lifting surface [11], is inefficient in sideforce production, and this new resistance component may be quite significant.

Finally, the sailing ship in operation with a steady leeway angle will produce an hydrodynamic Munk yawing moment [75]. This destabilizing phenomenon arises when a slender body encounters an oblique flow, where the pressure distribution will tend to reorient the body perpendicular to the flow. The strength of this yawing moment in relation to the sideforce produced is expressed as the hydrodynamic centroid: the centre of lateral resistance (CLR), which is defined as the quotient of the yaw moment and the sideforce [21, 66, 67]. Vessel yaw balance, achieved by aligning the aerodynamic center with the hydrodynamic center (CLR), is a key design constraint; a consequence of the stronger development of the yawing moment (nearly linear with leeway angle) compared against the sideforce, which includes a significant higher-order dependency for leeway angle.

As reviewed, the hydro-mechanics of a sailing commercial vessel will differ from a conventional vessel in four primary aspects: first, the ship resistance will increase due to the heel angle and leeway angle, including an increase in resistance due to sideforce production. Second, oblique propeller inflow and varying operating point will likely reduce the main propulsor efficiency. Also, the pressure distribution associated with the wind propulsors and the sailing condition will alter the vessel wave system. Finally, the maneuverability of a sailing commercial vessel will be impacted by a strong, destabilizing yaw moment. While modeling for each of these

effects is described in this dissertation, **the focus of the scientific effort** lies in studying the efficiency of sideforce production and the course-keeping ability of wind-assisted vessels.

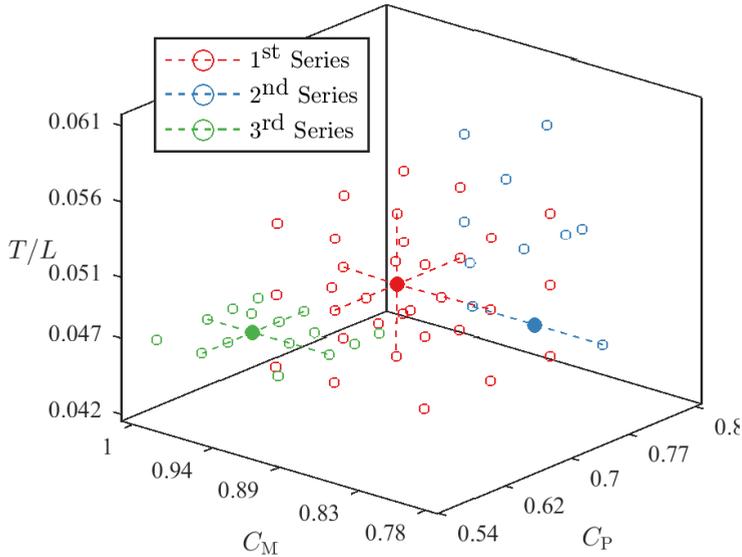## 1.3. Delft Wind-Assist Series

Figure 1.7.: Composition of the Delft Wind-Assist Series

The Delft Wind-Assist series is a set of 60 hull forms developed by researchers at Delft University of Technology. The parent hulls of the series are based on wind-assist concepts by Dykstra Naval Architects, in Amsterdam. The hull forms are defined in a systematic way so that the influence of significant form coefficients for sailing behavior may be isolated and studied. The series is set up to span a design space that is presently meaningful for the application of wind-assist propulsion, including short-sea freighters, low C_P passenger ferries, and full-bodied tankers.

The DWA is composed of three sub-series:

1st Series	General cargo ship: Variations on the Ecoliner (Figure 1.4)
2nd Series	Deadrise series, sailing ships
3rd Series	Low-C_P ships (ferry, cruise, and ro-pax types)

This database of full-scale simulation results is a representation of the sailing response for commercial ships. The sailing characteristics of a vessel that falls within the extents of the series is to be inferred from a meta-model for the response surface. Each sub-series is shown in Figure 1.7. It should be noted that the parent hulls represents vessel on short-sea trade, having displacement between 500 ton and 40,000 ton. Panamax or Cape-sized ships will have a T/L ratio ≈ 0.6, which falls outside the exisiting series.

At last, a final effort was made to use the DWA database to train an artificial neural network (ANN) that was able to replicate the simulation results. The vessel hydro-mechanic response, including body force distributions, the change in resistance, change in dynamic pressure (for sinkage and trim calculations), and propeller inflow wake fraction are within the reach of bulk simulation; e.g. scenario analysis for fleet decarbonization or design optimisation. First results of this collaborative work are in [113]. See Section 6.1.
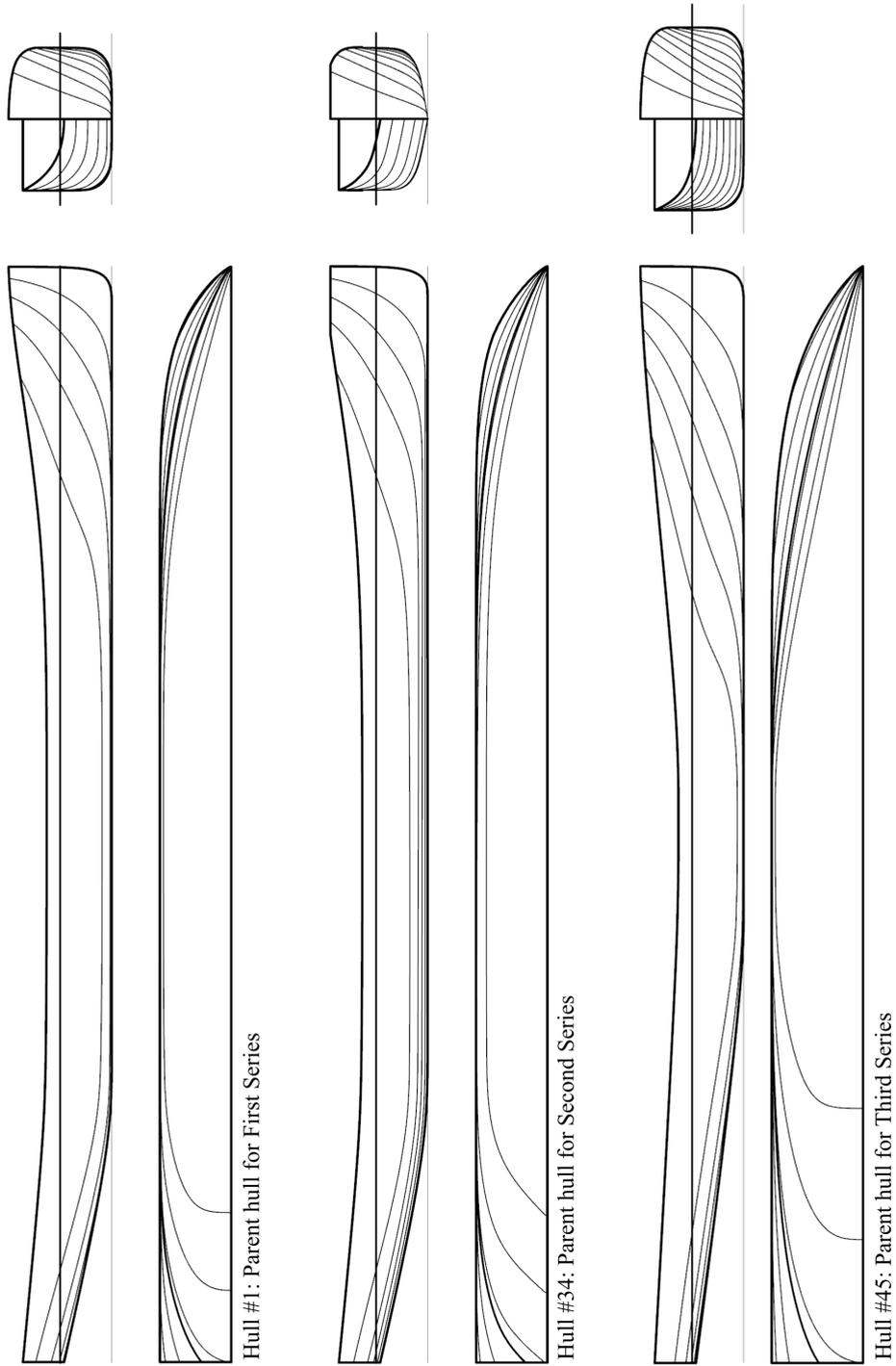
Hull #1: Parent hull for First Series

Hull #34: Parent hull for Second Series

Hull #45: Parent hull for Third Series

Figure 1.8.: Parent hulls of the Delft Wind-Assist systematic series.

1.4. Dissertation Structure

The structure of the dissertation is arranged to begin with a discussion of sailing vessel physics and modeling aspects (Chapter 2). The subsequent two chapters, representing the main work of this thesis, are devoted to the acquisition of vessel performance data in support of this modeling. Where possible, sailing performance for hulls and appendage configuration have been analyzed using a Reynolds-averaged Navier-Stokes computational fluid dynamics (RANS-CFD) simulation tool, described in Chapter 3. Further, empirical data for an extensive set of systematic appendage variations for wind-assist vessels was collected as described in Chapter 4. Finally, Chapter 5 is a techno-economic assessment of wind assist in the present market and regulatory climate.

Chapter 2: Discussion of Vessel Modeling

The second chapter of this dissertation describes modeling approaches for the sideforce production and sailing efficiency of wind-assisted ships. The discussion of modeling for sailing ships is accompanied by select results from the production runs for the hulls of the DWA Series. The discussion of simulation and experimental results follows a synthesis of diverse modeling approaches drawn from the study of sailing yachts and from the ship maneuvering field. This presentation should be regarded as an interim result. The refinement and elaboration of vessel modeling for wind-assisted ships is an ongoing effort, as outlined in Recommendations at the end of this thesis.

Chapter 3: RANS-CFD V&V and Methodology

The third chapter describes the development of a full-scale simulation method as applied to the hulls of the Delft Wind-Assist series. Whereas, in the past, such a database of vessel response for regression analysis would be built using results from towing tank experiments, the maturity of RANS-CFD solvers offers the ready analysis for hull variations. However, it is understood that characteristic flow phenomena for wind-assist vessels will challenge modeling assumptions in the RANS-CFD simulation setup. Fluid flow around the wind-assisted ship operating at a leeway angle will experience separation effects and will become entrained in large vortices, forming the wake of the ship. These modeling challenges point to a conscientious simulation verification and validation study, which is summarized here, with further documentation included in Appendix B. The extension to a full-scale simulation methodology for production runs is described, including a discussion of relevant scaling effects.

Chapter 4: Appendages for Wind-assisted Ships

Wind-assist vessels may be fitted with appendages to enhance their ability to generate hydrodynamic sideforce in an efficient way and in a way that preserves their course-keeping ability. Chapter 4 begins with a discussion of yaw balance and

course-keeping, followed by a presentation of results from experimental campaigns for wind-assist-appended hull geometries. This work grew out of promising results obtained during the experimental validation for the simulation method, wherein the simulation method was unable to reproduce towing tank results for the bilge keel case. This new empirical data set is a contribution not only to the nascent field of sailing commercial ships but also the broader maneuvering literature. RANS-CFD simulation validation for high-aspect ratio appendage types such as rudders and skegs was successful; these results are also presented in this chapter.

Chapter 5: Techno-economic Assessment

Finally, whereas a physical modeling for wind-assist vessels falls under the fields of aerodynamics, hydro-mechanics, and marine engineering—wherein this thesis is devoted to the hydro-mechanics—a complete assessment of the opportunities presented by this technology will include voyage optimization, logistics, and economics. A collaborative effort was initiated by the author to combine vessel modeling at Delft University of Technology with the work of researchers in vessel routing and economics to demonstrate commercial viability. The casual reader would do well to begin with this final chapter (Chapter 5), as it provides a succinct review of the broader problem domain.

2

Modeling for Hydro-mechanic Response

Source: `treshombres.eu/`

A sailing commercial vessel with a cargo of high value consumer products such as wine and chocolate makes trans-Atlantic crossings propelled entirely by the wind.

The cost of shipping is drastically reduced while the perceived value of the shipped product is increased.

In this chapter, the problem domain – the sailing behavior of a commercial ship – is introduced. This discussion of modeling for sailing ships is accompanied with select results from the production runs for the hulls of the DWA Series. Simulation and experimental results accompany a synthesis of diverse modeling approaches drawn from the study of sailing yachts and from the ship maneuvering field. This presentation must be regarded as an interim result. The further development of the Delft Wind-Assist Series (DWA) and refinement and elaboration of vessel modeling for wind-assisted ships is an ongoing effort, as outlined in Recommendations at the end of this thesis.

Introduction

With a wind-assist device, the ship is able to replace some of the engine power with power available from the wind. Modern version of sails such as Flettner rotors can effectively transform this power into forward thrust.
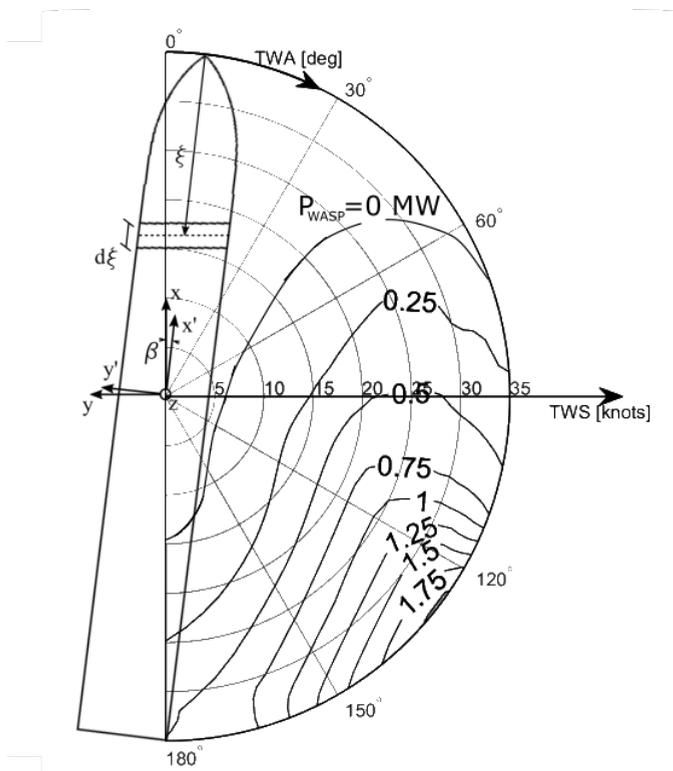

Figure 2.1.: Available wind-assist power, P_{WASP} [MW] for a small coaster (11 knots boat speed). Vessel coordinate system shown.

The available wind-assist power: P_{WASP}, is defined in Equation (5.1) and plotted in Figure 2.1. The polar diagram above is for a small coaster: 5,000 DWT, with 1.3 MW installed power.

P_{WASP} considers the available wind-assist propulsive power against any power needed to operate the wind propulsor. It is defined as:

$$P_{\mathrm{WASP}} = \frac{V_{\mathrm{ref}}}{\eta_{\mathrm{T}}} \left(T_{\mathrm{Aero}} - \Delta R_{\mathrm{Sailing}} \right) - \frac{P_{\mathrm{Rotor}}}{\eta_{\mathrm{Gen}}} \tag{2.1}$$

The aerodynamic thrust, T_{Aero}, is the component of the total sail force that is aligned with the ship motion. In this definition, a total transmission efficiency is included, as P_{WASP} is replacing a corresponding engine brake power, P_{B}. The increase in resistance due to sailing, $\Delta R_{\mathrm{Sailing}}$, which forms the central scientific inquiry of this thesis, is likewise the combination of several resistance components linked to the *Sailing Condition*.

The ship adopts a heel and leeway angle to support the sail-plan. This combination places the hull, which is otherwise optimized for quite specific and symmetric operating conditions, oblique to the mean flow in the *sailing condition*. The normal wave field produced as part of the wake of this ship will be superimposed on the pressure distribution arising from the sideforce production by the hull, along with the Munk yawing moment [75]. Finally, a vessel heeling angle will bring the vessel "shoulders" closer to the free surface, leading to a further distortion of the wave system. The pressure resistance for a sailing ship will therefore vary with heel and leeway angles, alongside the ordinary Froude-number dependency.

Simulation results for vessel resistance for the DWA parent hull are shown in Figure 2.2. Select hulls of the series were subjected to the complete test matrix (63 simulations). Whereas the response surfaces per Fn number are generally smooth, and one can observe an approximately quadratic behavior for resistance increase due to leeway, some deviation is apparent. Especially for Fn =0.21, one can observe a distinct variation at β =5° above the normal quadratic dependency, after which there is apparently an additional linear component.

A second quantity of principal interest for this modeling for wind-assist vessels is the center of effort for the distribution of lateral force, also known as the center of lateral resistance. An example of the sectional loading Y_n is presented in Figure 2.3 for a wind-assist ship in a full-sailing operating condition. Hull #34 is the parent of the Deadrise series, with 10° deadrise. The distribution of the sway force may be represented as force and moment pair C_{Y} and C_{N}. The position of the CLR is determined as the quotient of the yaw moment and the sideforce.

$$CLR = \frac{C_{\mathrm{N}}}{C_{\mathrm{Y}}} \tag{2.2}$$

This topic, an important design constraint for wind-assisted ships, is discussed further in Chapter 4.
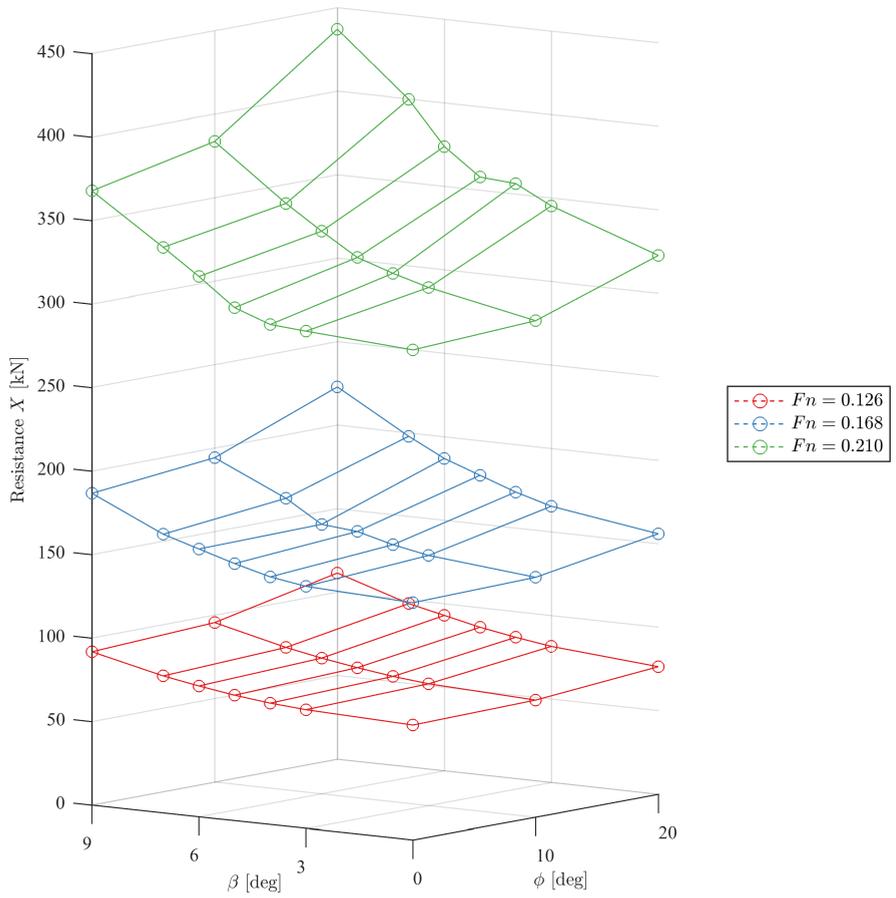
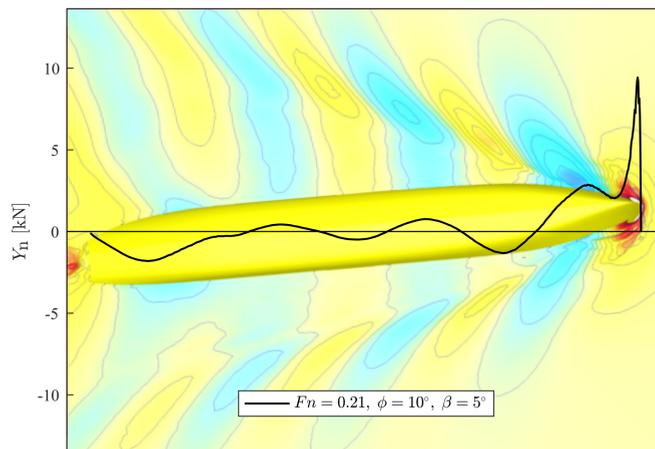Figure 2.2.: Resistance increase for heel ϕ and leeway β for parent Hull #1. Simulation Result.

Figure 2.3.: Distribution of hydrodynamic sideforce, showing wave system (viewpoint is below the ship). Hull #34, leeway angle $\beta = 5°$, heel angle $\phi = 10°$. As the vessel heels, the fore and aft shoulders are brought close to the free surface, causing flow constriction and acceleration. This effect is especially pronounced at large heel angles ($\phi=10°$ is normally adopted as operational limit for manned vessels).

Theoretical Background

Sailing yacht hydrodynamics has been the subject of thorough study by researchers at Delft University of Technology [40, 41, 42, 64, 65]. Although wind-assisted commercial ships and sailing yachts are in some ways dissimilar, there is reason to emulate the methodology of this study, for example, the careful isolation of individual effects, and the application of regression analysis over an extensive database of hull geometries to derive polynomial-based force models for an arbitrary hull form. Finally, a practical approach to the interaction between sideforce and Munk moment has been developed [67, 80]. A key dissimilarity between wind-assist vessels and sailing yachts is that sideforce for a sailing yacht is generated by purpose-designed appendages: the keel and rudder. Still, the lifting-line theory is instructive as a fundamental model for the mechanisms involved in sideforce generation and the relationship between circulation and lift.

For the discussion in this chapter and in Chapter 3, simulation results for the hulls in the DWA are used, presented in Table 2.1. The main particulars for all hulls in the Delft Wind-Assist series, as well as the methodology adopted in defining the series of systematically varied hull forms and the detailed data reduction, are given in Appendix A.

Table 2.1.: Hydrostatics for several hulls of the DWA, presented as percentages of the parent hull value.

	L/B [%]	T/L [%]	C_{P} [%]	C_{B} [%]	R_{b}/T [%]	C_{M} [%]
1 (Parent)	7.67	0.047	0.764	0.719	0.615	0.942
2 (T/L +)	110	110	100	100	91	100
3 (T/L-)	90	90	100	100	111	100
4 (C_{P} +)	100	100	110	110	100	100
5 (C_{P}-)	100	100	90	90	100	100
6 (C_{M} +)	100	100	100	105	50	104
7 (C_{M}-)	100	100	101	93	150	93

Modeling Convention

The sailing performance for wind-assisted ships is synonymous with maneuvering forces for the steady drift condition, i.e. increase in resistance, lateral force (sideforce) production, and yaw moment due to drift (leeway) angle. Whereas the analysis of experimental results will rely also on common decompositions from the study of ship maneuvering, the nomenclature of the study of sailing is adopted in the remainder of this thesis. An important distinction here is that all forces are taken in flow-coordinates and the Taylor expansion written in β, rather than the cross-flow form $< u, v >$ usually adopted for maneuvering (Figure 2.1).

Though the resistance is negative by definition, opposing positive motion along the x axis, the negative sign is omitted under the discussion of results. A right hand rule is adopted with the z axis pointed down. Positive angles of leeway β or rudder angle δ_{Rud} are accompanied by positive forces: the sideforce along Y and the rudder sideforce Y_{Rud}. Similarly, the yaw moment N is positive for positive leeway angles, whereas the heeling restoring moment is negative for positive heeling angle ϕ.

Therefore, a right-handed coordinate system is defined, with z-axis pointed down. All rotations are performed about midship at the calm water line. Forces and moments throughout this thesis are presented in flow-aligned coordinates, $< x, y >$, with the suitable transformation. Heel angles are not considered while decomposing the forces or moments, introducing some inconsistency in the coordinate systems. In the integrated modeling context, the component of aerodynamic force perpendicular to the z'-axis (not shown) is responsible for the heeling moment that is balanced by the hydrostatic righting moment of the ship, whereas the aerodynamic force perpendicular with the z-axis is balanced by the hydrodynamic sideforce. A transformation that considered the angle, ϕ, between these two vectors is incorporated in the solving routine of the vessel model, but not discussed explicitly here in the interest of simplifying the mathematics. Modeling is hereby restricted to the lateral plane, so that the heel angle changes the vessel orientation but not the (vessel bound) coordinate system.
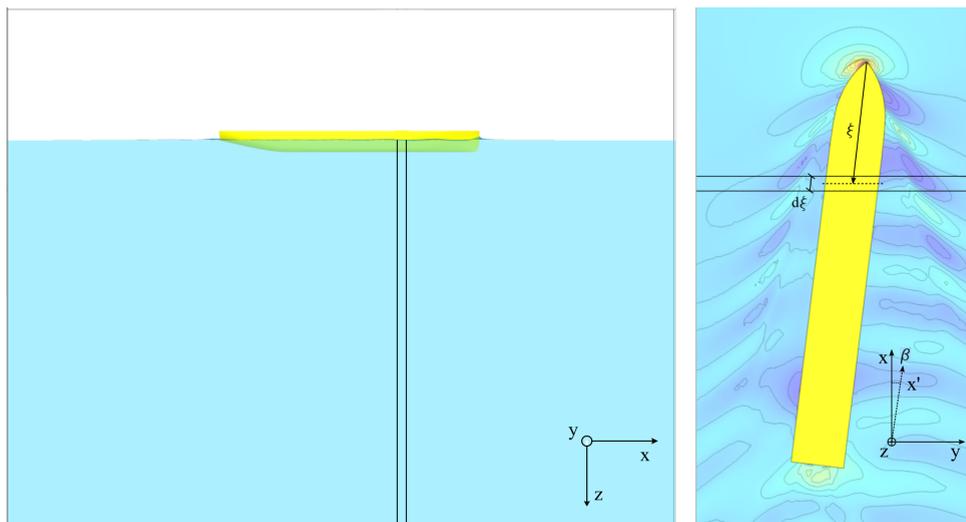
Figure 2.4.: Coordinate system including the local variable ξ, defined w.r.t. midship in the vessel coordinate system $< x', y' >$. Forces are presented in the flow-aligned axis system, $< x, y >$.

Sectional Loading (Sway)

The distribution of hydrodynamic sideforce (sway) along the hull was extracted from simulation results. The field results for fluid pressure and shear stress are integrated on segments of the hull, as in Figure 2.4. In contrast to previous work based on potential flow solutions, the transverse planes are defined in flow-oriented coordinates. The distribution of sideforce along the aft-body is understated compared to results presented by [48]. A dimensional form is adopted for the presentation of these results. The simulations were performed at full scale and no scaling laws are necessary to interpret the results. Furthermore, hulls discussed shared the same principal dimensions; therefore, the non-dimensionalization is a common constant value. Finally, the availability of simulation results at full scale permits an examination of the hydrodynamic reaction without imposing an a priori physical model/scaling assumption.

2.1. Vessel Wave System

The distribution of sideforce is the manifestation of several hydrodynamic phenomena that are associated with the sailing condition. First, there is a strong pressure peak at the bow, a characteristic feature of low aspect ratio lift. Secondly, a distinct under-pressure along the after stations, the Munk yawing moment, is observed. Asymmetry is introduced into the wave system by the pressure field associated with the sailing condition, though the Kelvin wave angle generally remains aligned with the flow direction. Finally, the vessel heeling angle results in a further distortion of the wave field as the vessel shoulders interact with the free surface.

The vessel wave system and the distribution of lateral force are presented for several systematic variations in operating condition on the next pages. In each image, the vessel is oriented so that the flow direction is aligned with the x-axis. The view point is located below the ship, meaning that the underwater ship is visible. The wave system, the wave elevation is indicated with a uniform color-scale and isolines the present results. The limits for wave elevation are fixed for the following figures, resulting in some regions (for higher Fn) where the bow wave elevation exceeds the scale. The distribution of hydrodynamic sideforce is plotted on the y-axis. This result was obtained by integrating fluid pressure and viscous shear stress over hull segments as in Figure 2.4.

Before continuing this discussion, it must be said that while numerical simulations promise a detailed view of the flow behavior around the hull, an uncertainty must be assigned to any quantitative analysis of these flow patterns. To that end, a simulation validation exercise has been carried out for the integrated forces and the wave elevation along the ship (Chapter 3). Although it is not possible (within the context of this Ph.D. project) to validate the distribution of sectional loading or the flow field directly, an appreciation for the loading and shedding patterns can give insight into the flow mechanisms and motivate the structure of the regression formulas. The flow visualizations are instantaneous fields, whereas forces and moments of the validation exercise Chapter 3 and in the Delft Wind-Assist database are time-averaged quantities.
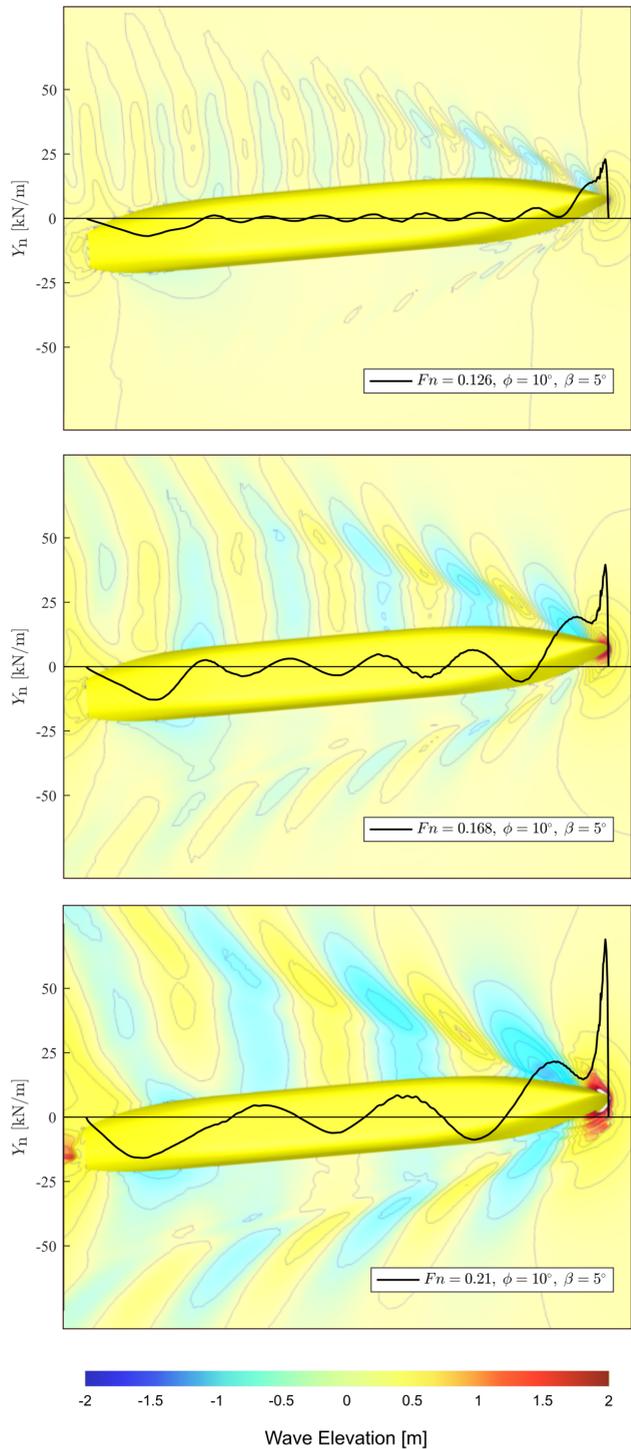
Figure 2.5: Distribution of hydrodynamic sideforce, showing wave system, for increasing Froude Number Fn. A sharp peak at the bow is the most pronounced effect observed. The influence of vessel speed on the wave pattern is apparent. For Fn =0.21, wave elevation near the bow exceeds the color scale. Hull # 1, $\phi = 10°, \beta = 5°$. Simulation result.
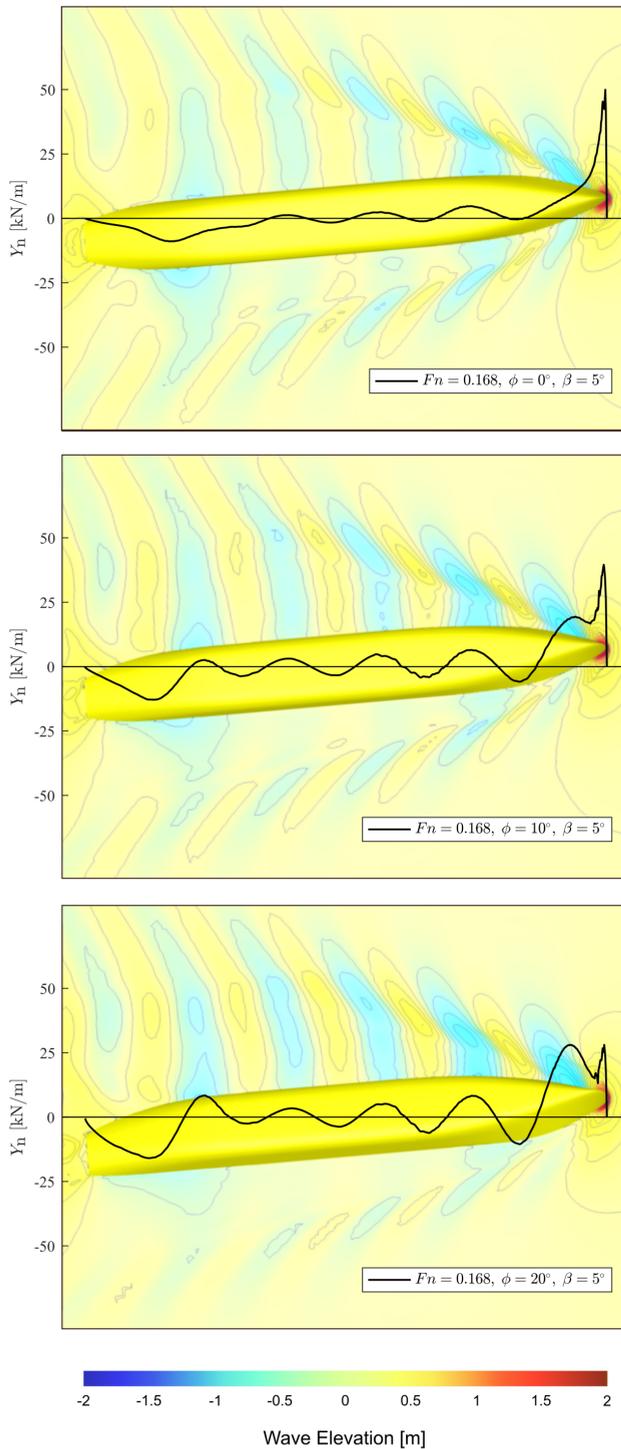
Figure 2.6: Distribution of hydrodynamic sideforce, showing wave system, for increasing heel angle ϕ. As the vessel heels, the fore and aft shoulders are brought close to the free surface, causing flow constriction and acceleration. This effect is evident in the deformation of the free surface along the aft body. The wave toughs at the corresponding stations along the leeward side of the hull are amplified. This effect is especially pronounced at large heel angles: (ϕ=10° is normally adopted as operational limit for manned vessels). Hull # 1, $\beta = 5°, Fn = 0.168$. Simulation result.
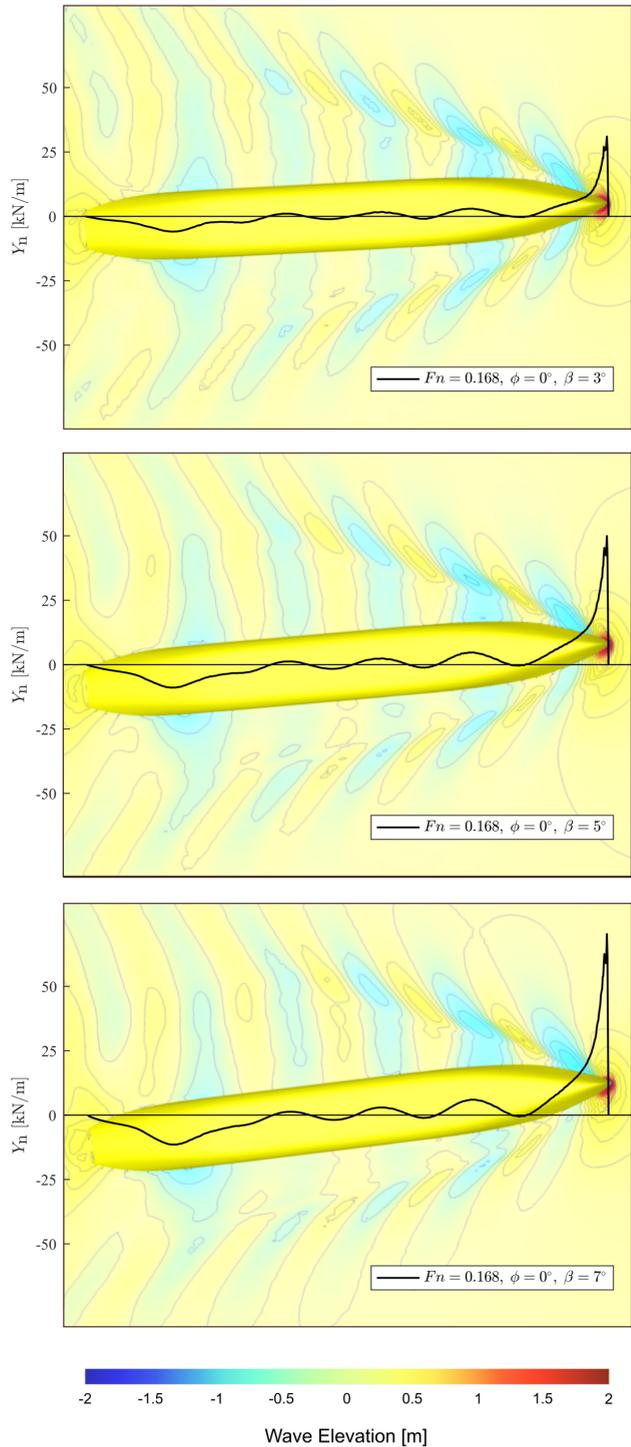
Figure 2.7: Distribution of hydrodynamic sideforce, showing wave system, for increasing leeway angle β. A low-aspect rectangular planform, such as a simplified hull form, develops a concentrated lifting force at the leading edge (Newman, 1977). The pressure peak increases with leeway angle β. This characteristic effect of low-aspect lift (Equation (2.4)) is the primary effect, and is apparently linear with leeway angle. The 'under-pressure' along the aft section is the so-called Munk moment, also a linear effect. Hull # 1, $\phi = 0°, Fn = 0.168$. Simulation result.
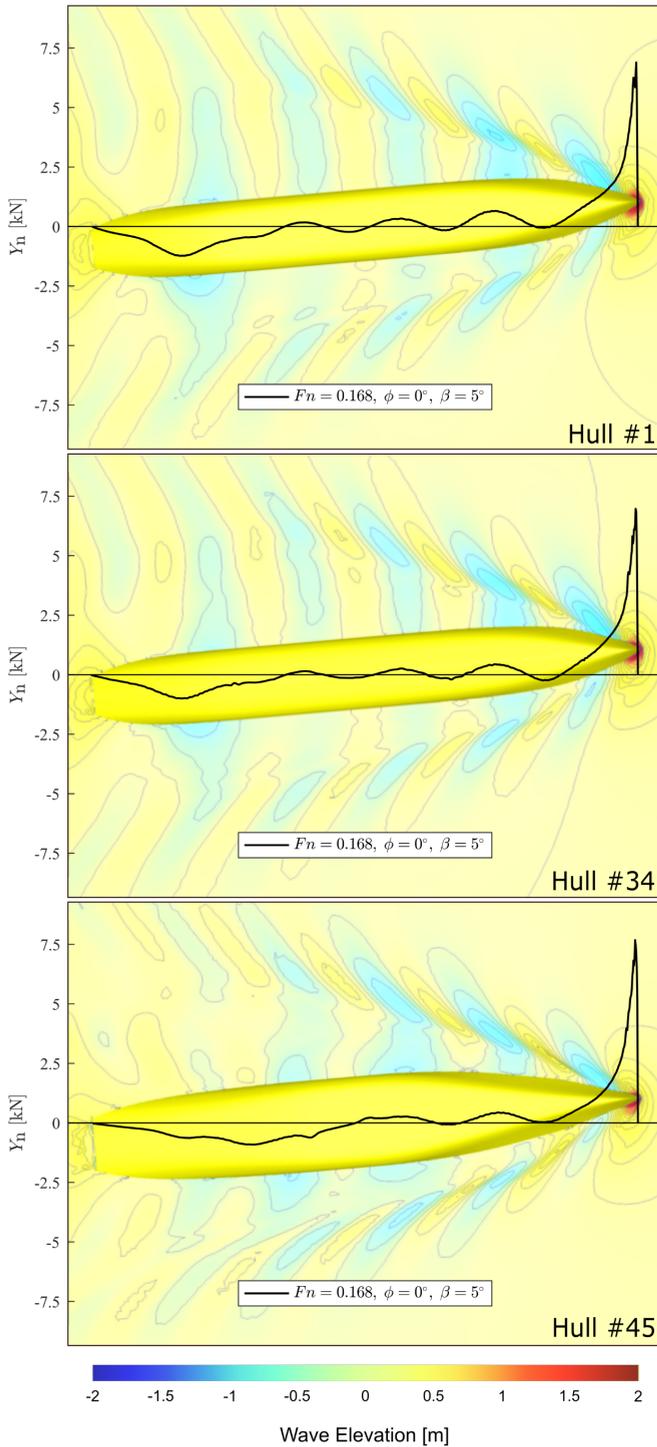
Figure 2.8: Distribution of hydrodynamic sideforce, showing wave system, for parents hulls of the DWA: #1 (top), #34 (middle), and #45 (bottom). Hull #34 is parent of the Deadrise series, having 10° deadrise angle. The Munk moment aft is reduced for this hull. Hull #45 is parent for the low-C_P series, with very short parallel midbody. The finer entrance angle results in a smaller wake, despite the wider breadth. The under-pressure aft extends nearly to midship, following approximately the idealized pressure distribution ([67]). $\phi = 0°, \beta = 5°, Fn = 0.168$. Simulation result.

2.2. Vortex Wake

While tip-effects are incorporated with Prandtl's lifting-line theory, and finite spans are therefore modeled, the assumptions underlying the lifting-line theory are not respected for geometries such as bilge keels or indeed for the hull itself. As the aspect ratio is reduced, it becomes necessary to model the actual distribution of vorticity along the chord length (vessel draft); and for vanishing span-width, the analysis is restricted to a single section. In an approach that began with a wing with infinite chord length, or an aspect-ratio of zero, Bollay describes an: "infinite lattice of airfoils of finite span, [...] a distribution of bound vortices of strength $\gamma(x)$ per unit length along the chord with trailing vortices leaving at some angle" [11]. For the zero-aspect-ratio wing, the bound circulation, down-wash velocity, and lift are all constant across the span. The effective angle of attack does vary according to the influence of upstream 'wings'. Finally, following the lifting-line theory, the lifting force is related to the integral of the chord-wise circulation.
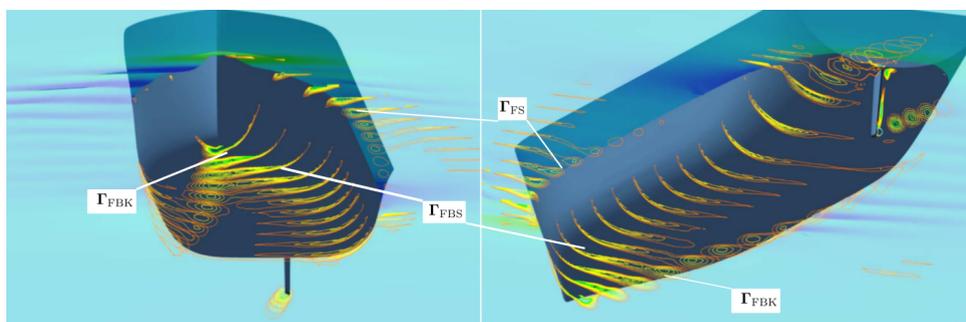
Figure 2.9.: Flow visualization of vortex system showing fore and aft separation locations. Several distinct vortices can be identified, such as the forebody keel vortex, the forebody bilge vortex, and the free surface vortex. Also a distinct tip vortex is visible at the rudder. The rudder produces 30% of sideforce for this operating condition (no modeling for propeller wash). Hull #1, $\phi = 0°$, $\beta = 6°$, $Fn = 0.126$, $\delta_{\mathrm{Rud}} = 3°$. Simulation result.

The hydrodynamics of sailing commercial ship types is characterized by a system of shed vortices that separate from and pass around the hull, forming the wake of the ship (see Figure 2.9). Vessel sailing behavior depends on the strength and separation location for these primary vortices and any secondary/counter rotating components. Many experimental and numerical investigations have explored the changes to the vortex system for varying angles of oblique flow, where again the flow angles considered are generally larger than would be considered operational leeway angles for a wind-assisted ship. From the oil film experiments of [15], to detailed measurements of the vortex wake by [72], to state-of-the-art numerical work such as the detached-eddy simulations by [1, 17, 124], the flow patterns have been well documented. As described by [72], the topology for the wake of a ship sailing with a leeway angle is characterized by several distinct vortices, where the forebody keel vortex (FKV), forebody bilge vortex (FBV) and forebody side vortex (FSV) are relevant here. The strength and separation location of the components

of the vortex wake will vary with the leeway angle. These three vortices can be identified in Figure 2.9, alongside a pronounced tip-vortex for the rudder ($\beta = 6°, \delta_{\text{Rud}} = 3°$). The resulting transverse hydrodynamic loading may be understood as a summation of bound and shed circulation, as under the lifting-line theory for low-aspect wings.

Low-aspect lift is characterized by a "sectional lift angle", whereby locations along the chord are influenced by the down-wash from upstream sections of the lifting profile, and the final down-wash angle is reached well before the trailing edge. For the very low aspect ratios considered in this study, for both the ship hull and the bilge keels, the linear lift coefficient is expected to be independent of the chord, corresponding to the ship length or bilge keel length [46].

2.3. Hydrodynamic Sideforce Generated by Hull

When speaking of sideforce generation by the bare hull, one can make a distinction between circulatory lift generation and cross-flow drag whilst using traditional models. These traditional models are illustrated as follows by [46]:

- A ship with infinite draft will generate a purely circulatory lifting force in the same way as a wing with infinite span.

- A ship with infinite length has no leading or trailing edge and thus no circulation; here the sideforce is generated by momentum transfer as vorticity is shed from the ship.

Conventional lifting surfaces, such as rudders or skegs, are well described by circulatory lift models. The sideforce produced by the hull, or by appendages such as bilge keels, are typical examples of sideforce production by momentum transfer. Of course, the sideforce generated by a real ship will arise due to some combination of these mechanisms. For example, a high-aspect foil with finite span continually passes energy into trailing vortices. Likewise, a low-aspect rectangular planform, such as a bilge keel or a simplified hull form, develops a concentrated lifting force at the leading edge [79].

Neglecting the influence of heel for simplicity, sideforce may be written as the sum of linear and non-linear terms in leeway angle β:

$$Y = Y_\beta \beta + Y_{\beta\beta\beta}\beta^3 \tag{2.3}$$

In this expression, Y_β and $Y_{\beta\beta\beta}$ (and Y_ϕ in particular) are Fn-dependent.

Body forces and moments acting on the ship are written in the most general way—as hydrodynamic derivatives—to express functional dependency for combinations of body orientation and motion. Whereas a dimensional form is retained here, a non-dimensional form, C_Y, is used to scale experimental forces of Chapter 4 and database simulation results for regression analysis. It can be verified that this equation contains odd terms only, as expected for the sway equation. A linear and

non-linear sideforce term is accompanied by a linear heel and Froude number dependency. The estimation of the hydrodynamic derivatives follows from dedicated simulations or an experimental campaign for a particular hull, or from polynomial regression formulae based on a collection of tested hulls as in [53, 59, 65, 109], or for the Delft Wind-Assist Series database (this thesis).

Equation (2.3) is the starting point of the analysis of Hooft [9] and an attempt at synthesizing a sideforce model. Drawing a parallel with the development of the Prandtl lifting-line theory, the first term in equation Equation (2.3) is modeled as a lifting force linear in angle-of-attack β, as in the slender-body models Equation (2.4).

In general, for previous work primarily concerned with the maneuvering of ships, the drift angles considered are larger than what is considered an operational leeway angle for wind-assisted vessels. One notable exception is the experimental and theoretical studies by Beukelman [7, 8, 9], where a ship-like foil with low aspect ratio was towed at angles of attack including four and eight degrees. Wing geometries with square and rounded tips were tested, where the square tips were found to produce more lift and drag. This effect is understood as a result of a contribution by the cross-flow component, arising due to separation effects that will be more pronounced for the sharp wing tip geometry. Similar results are reported in [69]. Finally, lift and moment coefficients calculated by the added mass impulse of [61] were found to agree well with the experimental results for rounded wing-tips, but less-so for the square tip profile. This difference implies that the hydrodynamic reaction is nearly linear for small angles, with a small viscous contribution arising from flow separation [10]. Similar results are reported in [59, 68, 109]. In common engineering practice, maneuvering forces are linearized for small angles.

Linear Sideforce Models

A linear model for hull sideforce is derived from slender body theory (Lighthill, 1986). The model depends on the aspect ratio only.

$$Y = \frac{\pi}{2}T/L\beta q A_{\text{Lat}} \tag{2.4}$$

In which T/L is the geometric aspect ratio of the hull, A_{Lat} is the projected lateral area, LT, and the dynamic pressure q is defined as:

$$q = \frac{1}{2}\rho V^2 \tag{2.5}$$

The slender-body model for vessel sideforce generated by the hull is presented in Equation (2.4). These expressions are attractive in light of their simplicity, and as first approximation are suitable for the small leeway angles considered in this application. One significant shortcoming is the constant center of lateral resistance (CLR), which is an artifact of a linear modeling for sideforce and moment. A further discussion of the CLR is included under Chapter 4.

Simulation results for the sideforce of several hulls from of the DWA series are presented in Figure 2.10, where the sideforce is plotted against leeway angle, β. Variations in the vessel draft, T, are defined by elongating the vessel hull while
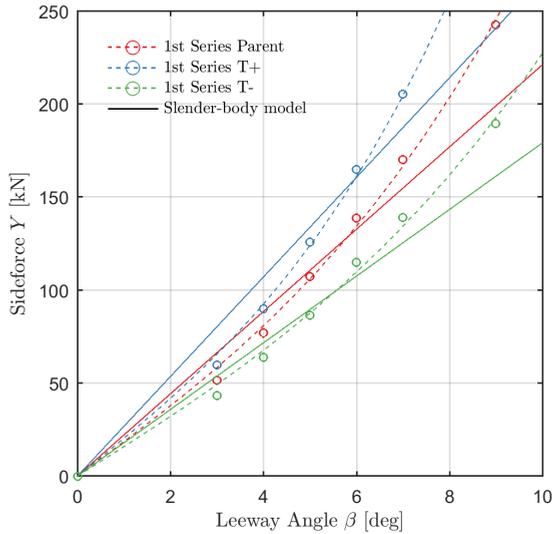
Figure 2.10.: Hull sideforce for varying draft. Simulation result.

keeping the displacement constant (see Appendix A). The linear and non-linear coefficients both increase with vessel draft, or vessel aspect ratio T/L. A non-dimensionalization based on a vessel draft T was applied, for which the results for varying vessel draft collapse as expected, and when comparing results with published experimental data. The fitting for the maneuvering model Equation (2.3) is made using the full range of leeway angles (0°-9°). Though it is apparent that the sideforce value at β=9° (not shown) is influencing the goodness of fit, the simulation validation level was much smaller for sideforce at larger leeway angles. Further discussion of the implications of simulation validation level on fitting of maneuvering coefficients is included in Appendix B.

Alternatively, the hull is considered to be a low-aspect-ratio wing, with a linear sideforce written using the well-known model presented by [61]. The third order term, the cross-flow drag or lateral-edge vortex flow as described by [46], is side-force production by momentum transfer as flow separates from the hull. Hooft and Quadvlieg have related the cross-flow drag component of the sideforce generated by a ship to the strength and separation location for shed vortices originating primarily along the bilges of the ship [47, 48]. Further, they have shown that the separation location will shift along the bilges for varying leeway angle, being concentrated near the bow for small leeway angles.

Hooft considers the hull as a low-aspect-ratio wing, and writes the linear side-force according to the well-known aerodynamic model presented by Jones [61]. In particular, the lifting force is related to the rate-of-change of the fluid momentum, or virtual mass.

$$Y = uv \int_{\xi_f=0}^{\xi_a} \frac{dm_{YY}}{d\xi} d\xi \qquad (2.6)$$

$$\xi = \frac{L_{PP}}{2} - x' \qquad (2.7)$$

In which ξ is the distance behind forward perpendicular, defined in the ship coordinate system $< x', y' >$ as in Equation (2.7). The transverse planes in a vessel-oriented coordinate system, as in Figure 2.11, are not flow-normal, meaning that the inner and outer problem are not correctly delineated (there will be a small, out-of-plane component to the velocity field). This point is an artifact of the setup of most ordinary strip theory programs used to calculate the virtual mass term m_{YY}, where a non-dimensional form is adopted following the derivation of [48, 61, 105], and Appendix A.2.
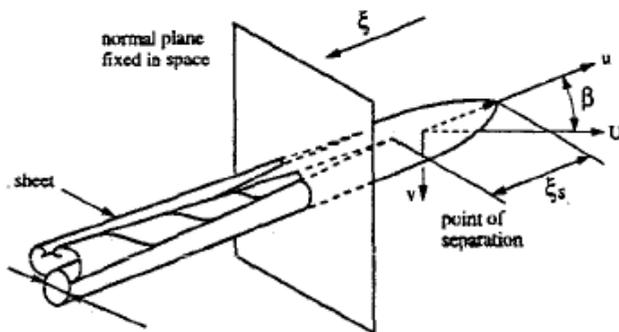
Figure 2.11.: Sketch for analysis of flow around a cylinder at an angle of attack. The vessel-oriented transverse plane is shown, along with the longitudinal vortices. In contrast with the present work, Hooft adopts a maneuvering coordinate system $< x', y' >$, where the velocity U has components $< u, v >$. (image credit Hooft [11])

The virtual mass m_{YY} is otherwise known as the added mass when analyzing ship motions, where it serves to account for the momentum of fluid accelerated with the ship. The sectional added mass coefficients may be readily obtained using potential theory and a strip theory approach. However, when the integral in Equation (2.6) is carried out over the length of the ship, it is found that, as an artifact of the potential flow model, the total lift will be zero. Termed the Paradox of d'Alembert, this condition arises because an ideal fluid will have zero added mass at the bow and stern in the absence of a viscous wake. A three-dimensionality coefficient is introduced to resolve this matter in a practical way. This concept for sectional added mass also underpins the Munk moment method of Keuning and Vermeulen [67], where the integral is taken over half the ship-length and it is assumed that separation along the aft ship has attenuated the under-pressure of the Munk-moment [67].

Non-linear Sideforce Component

Following the analysis of [47], the non-linear term in Equation (2.3) is the remnant after the linear component, as derived from Equation (2.6) above, and is subtracted from experimental results. This term is meant to represent the sideforce produced by momentum transfer as flow separates from the hull, a phenomenon termed cross-flow drag. The modeling is motivated by considering the midship section of the ship extended as an infinite beam, from which it is deduced that the resulting sideforce is due to cross-flow drag only (the second category as delineated by [46]). At small leeway angles, the cross-flow drag will contribute to the sideforce according to the position of separation and the strength of the vortex sheet Figure 2.11. In a sense, the non-linear term is correcting for the simplifications introduced by the potential flow model and the strip theory method outlined above, for which the solution for the inner problem provides values for the sectional added mass without the influence of upstream (or downstream) sections. In fact, shed vortices associated with sideforce production will influence the transverse flow patterns as they pass along the ship.

The segregation of effects according to a linear term that can be readily computed and a higher order remnant has a practical appeal but somewhat obscures the physical process. The linear term as derived from Equation (2.6) requires a three-dimensionality coefficient, accounting for viscous flow separation along the after portion of the ship, to return a non-zero sideforce for the potential solution. Also, the non-linear sideforce component is modeled as a function of the cross-flow drag experienced by a ship with a drift angle of ninety degrees, a condition that is uncharacteristic of the flow under study, where the leeway angle β is typically less than 5°. Further, a definition of a cross-flow drag to account for momentum transfer by longitudinal shed vortices implies a distinction between these mechanisms that is not physical. A momentum transfer is integral to any sideforce production, whether it be circulatory lift or cross-flow drag.

Modeling the sideforce generation for a wind-assist vessel according to the vorticity distribution along length of the hull raises the possibility of elaborating the cross-flow drag models outlined above. Patterns of shedding around a hull with leeway may be characterized by a set of vortex strengths, e.g. the vortex shed at the bow, the vortex shed at the bow wave, the vortex shed at the leading bilge, and so forth. Vortices shed along the length of the hull will interact with the boundary layer of the hull, complicating the task of modeling their path. If this modeling is possible, the induced flow generated by the vortex system at any appendages can be predicted. Finally, the strength of these vortices may be related to (local) hull form parameters. The ability to predict the interaction effects, and the ability to connect the strength of shed vorticity and the sectional loading to (local) hull geometry, are both topics of ongoing work.

2.4. Sailing Efficiency

Finally, sideforce production by the sailing ship, including possible corrective action with the rudder, will introduce an added resistance to the ship arising due to a dissipation of energy in the vortex wake of the ship and disruption of vessel wave system. For equilibrium along the transverse axis, the aerodynamic sideforce is countered by a hydrodynamic reaction, as the fluid must accelerate as it passes around the hull. The generation of sideforce entails a dissipation of kinetic energy and a ship in steady sailing condition will experience a virtual mass effect, as the trailing vortices associated with sideforce production require a steady influx of energy to counter the losses due to dissipation within. This concept is otherwise understood as the starting vortex under lifting-line theory.
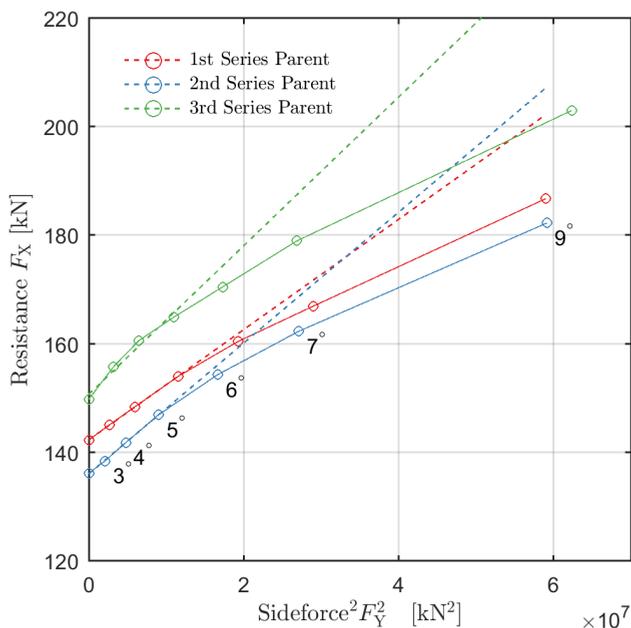
Figure 2.12.: Resistance vs. Sideforce squared for parent hulls of DWA. Linear fitting as under the derivation for the effective draft T_e/T is shown. Simulation Result.

Following theories for low-aspect planforms [46, 61], this induced drag may be significant for commercial ships, meaning that the thrust delivered by a wind propulsor might well be overwhelmed by this increase in resistance. Though the flow mechanisms only vaguely resemble the Prandtl lifting-line and the associated derivation for the induced drag [86], the accounting for energy loss in shed vorticity is especially relevant for the present application. Following the analysis of sailing yachts by [40], the resistance increase due to sideforce production is modeled as an effective draft, T_e [41], which is a metric for the sailing efficiency of the hull.

The expression is derived from the lifting-line theory of wings. In dimensional and non-dimensional form:

$$X = \frac{1}{\pi q T_e^2} Y^2 + R_{\text{Tot}} \tag{2.8a}$$

$$C_X = \frac{1}{\pi AR_{\text{eff}}} C_Y^2 + C_{XO} \tag{2.8b}$$

q in Equation (2.8a) is the dynamic pressure, defined as $q = \frac{1}{2}\rho U^2$. The AR_{eff}, as in Equation (2.8b) is derived from a (linear) curve fit, as in Figure 2.12. Following the form of Equation (2.8), the effective draft is defined as:

$$T_e = \sqrt{\frac{TLAR_{\text{eff}}}{2}} \tag{2.9}$$

A non-dimensional form for the effective draft T_e is made with the vessel draft: T_e/T, providing a convenient metric for the sailing efficiency of the hull. Some difficulty arises on account of the non-linear behavior of the commercial ship hull, which does not conform to the assumptions made under the derivation of Equation (2.8). As can be seen in Figure 2.12, the 3rd Series parent (Hull #45) is markedly less effective in sideforce production. At small leeway angles in particular, strong non-linear behaviour is observed for this hull (see also Figure 2.13a).

The quantity T_e represents the span of a wing profile with equivalent behavior for the induced drag. The modeling for effective draft has pragmatic appeal, but it must be noted that significant liberties are taken when treating a ship hull as a Prandtl wing. For ship geometries, flow characterized as 'tip effects' in Prandtl's theory, where streamlines curl around the end of the foil in response to the pressure gradient, will influence the flow pattern over the entire span (or depth of the hull). Furthermore, a commercial hull form does not present a well-defined trailing edge, which introduces ambiguity for the definition of a circulation, as it is not clear where (or whether) a Kutta condition should be applied. Nevertheless, the flow mechanisms responsible for the development of sideforce: the separation of several well-defined vortices into the wake of the ship, are dissipative processes that introduce a further resistance. This resistance penalty associated with sideforce production is an indication of the sailing efficiency of the ship, and is reported as the effective draft, T_e, representing the efficiency for sideforce production by the hull [64].

The vessel resistance, X, is plotted against the sideforce-squared, Y^2, in Figure 2.13a. The model for effective draft as defined in Equation (2.9) is shown. The induced resistance is apparently not linear for bare hull cases, and the range of leeway angles, β for fitting the (linear) model has been restricted to leeway angles between 0° and 5°, a range that better represents operational leeway angles. As a consequence, the fitted slope is considerably steeper, giving a smaller T_e (a less efficient hull). The second figure shows results for appendages tested during the
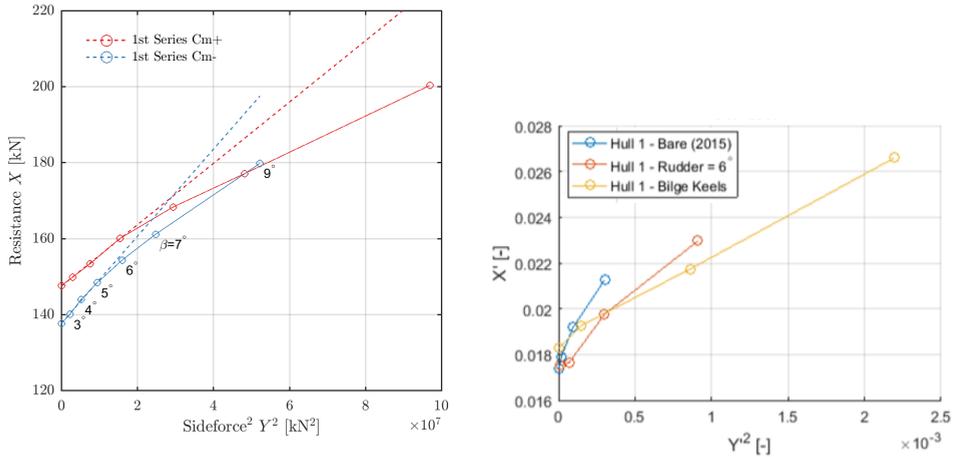
(a) T_e for Hulls #6 and 7, including linear fitting made for T_e for $0° < \beta < 5°$ is shown. Simulation result.

(b) T_e for Hull #1 fitted with rudder and bilge keels. Experimental Result.

Figure 2.13.: Effective draft T_e/T derived from experiments and simulation results.

2016 experiment for simulation validation. Here, the beneficial influence of bilge keels in particular is apparent.

Considerable variation is seen for T_e for the hulls shown in Figure 2.13a, Hull #6 (C_M-) and Hull #7 (C_M+), where the hull with sharper bilges R_b/T is more efficient. As expected, the R_{Tot} value for the C_M- hull is smaller due to a smaller residuary, wave-making resistance. The bilge radius and bilge keel are characteristics of the "wing-tip", and are strongly associated with the second-order sideforce component. The radius of curvature will largely determine the characteristics of the flow passing over the bilge, including the propensity for separation and the strength of any bilge vortex. By presenting a sharp wing-tip at the ship bilge, separation behaviour is induced at smaller leeway angles than otherwise for the curved bilges; therefore, the effective draft, T_e (the reciprocal of the slope), is increased. Response for the bilge keel case in Figure 2.13b is nearly linear with leeway angle, as follows from Prandtl wing theory. Induced resistance is considerably smaller at small angles of attack. This promising results motivated the bilge keel experimental campaign described in Chapter 4.

Conclusion

Modeling approaches for the sideforce production and sailing efficiency of wind-assisted ships have been introduced. This discussion of sailing vessel physics and modeling aspects is intended to introduce the problem domain for readers not familiar with sailing ships. The discussion of modeling for sailing ships was accompanied by select results from the production runs for the hulls of the DWA Series, and follows a synthesis of diverse modeling approaches drawn from the study of sailing

yachts and from the ship maneuvering field. This presentation must be regarded as an interim result. The refinement and elaboration of vessel modeling for wind-assisted ships is an ongoing effort. Present efforts (not included in this thesis) are focused on training a machine learning model using the DWA database. The so-derived model will be 'lite' enough to be implemented within the framework of a performance prediction program and batch simulation efforts (see Section 6.1 at the end of this thesis).

The following two chapters, representing the main work of this thesis, are devoted to the acquisition of vessel performance data in support of this modeling. Where possible, sailing performance for hulls and appendage configuration have been analyzed using a Reynolds-averaged Navier-Stokes computational fluid dynamics (RANS-CFD) simulation tool, described in the next chapter.

3

RANS-CFD Methodology

A bulker transporting crude is retrofitted with wind propulsors.

The owner of this hybrid vessel saves 10 percent on fuel oil annually and receives credit for carbon sequestration as part of European Union sustainable development goals.

This chapter presents a Reynolds-averaged Navier Stokes computational fluid dynamics (RANS-CFD) methodology for computationally affordable assessment of the Delft Wind-Assist Series (Appendix A). This simulation work is performed in the service of a regression-based modeling for the performance of wind-assist vessels. This chapter includes a review of simulation verification and validation, a discussion of modeling choices, and finally an exploration of Reynolds scaling effects observed based on model- and full-scale simulation results. Further documentation of the simulation verification and validation exercise is provided in Appendix B. Production runs are performed with a six-million-cell grid, which gave numerical uncertainties that were commensurate with the uncertainties in the validation data.

Simulation Challenge

Simulations that remain computationally affordable may be unable to model the flow patterns occurring near a sailing commercial ship. Fluid flow around the wind-assisted ship operating at a leeway angle will experience separation effects and will become entrained in large vortices in the wake of the ship. Modeling the occurrence of separation and the evolution of these vortices is the principal simulation challenge, as both phenomena may challenge modeling assumptions made in the simulation setup. A full-scale simulation methodology is considered desirable for the possibility of eliminating the normal towing-tank scaling procedure. Several phenomena, broadly categorized as Reynolds effects, are hereby properly resolved. These effects are understood to play important roles for the sailing performance of commercial ship types, and it is not immediately clear whether the normal procedure for non-dimensionalization and scaling of maneuvering forces is appropriate.

The simulation method for the production runs is designed for the assessment of hull geometry variants of the Delft Wind-Assist Series, an extensive series of wind-assist ship hulls. Considering the volume of work, to be done at full scale, a premium must be placed on economical simulations–precluding near-wall modeling or elaborate turbulence models. Besides the formal validation, several parameter studies for simulation settings were carried out, described also in Appendix B. For the Courant number study, simulation uncertainty was determined using systematic variations for the Courant number to infer a target Courant number for production runs. Also, modeling choices for wall treatment and turbulence modeling were examined by comparing the distributions of comparison error.

The validation statement and the extents of the range for modeling error, made out of necessity at model scale, is not directly transferable to full-scale simulations. A central question here is whether there is a scaling effect for the vessel sailing response, or if the model error is scaling. The Reynolds number was $2\,300\,000$ for the (model-scale) verification and validation exercise, as opposed to the full-scale Reynolds number of $690\,000\,000$. This difference of approximately 2.5 orders-of-magnitude for the Reynolds number corresponds to the transition from intermittent turbulence to fully turbulent flow. Turbulence models may be better suited for high-Reynolds number, fully developed, turbulent wake, suggesting that the validation level should at least not be larger for full-scale simulations. This chapter concludes

with a discussion of scale effects and the validation level. Here, results for the sailing performance of hulls from the Delft Wind-Assist Series are presented for simulations performed at model scale and full scale. The implications of simulation validation levels (model scale) for the data reduction and derived quantities are discussed, including an effort to give physical explanation for the significant systematic differences (see also: Recommendations).

3.1. Full-Scale Simulation Method

The RANS equations are solved with the ISIS-CFD flow solver, developed at Centrale Nantes and commercialized by Numeca International. The ISIS-CFD flow solver is an incompressible unsteady RANS method. The unstructured spatial discretization for the transport equations is based on the finite volume method. Free-surface flows are simulated with a conservation equation for the mass fraction. A detailed description of the solver is provided in [24, 25, 26, 87]. Though the unsteady components of the vessel sailing response are not of interest in the context of this study, the flow condition is essentially unsteady, and an unsteady RANS simulation (URANS) is performed.

It is understood that flow around the hull will include large anisotropic vortices that will play a key role in the sailing performance of the hull. Turbulence is modeled with the Explicit Algebraic Stress Model (EASM), providing a balance between the Boussinesq-modeling and the modeling of Reynolds stresses and giving a more physical approach while remaining viable within the scope of work and for the computational resources available. The evaluation of convective terms in the momentum equation and the turbulent stresses is performed with the ALVSMART scheme, a blended upwind/central scheme based on the local Courant number (Co) [81]. The solution for the free surface is determined following the volume of fluid method, using the BRICS algorithm [81] that is likewise dependent on the local Courant number.

Grid Definition

The grid generation follows the meshing strategy derived from the simulation verification exercise (Section 3.2), in which the mesh refinement was defined to achieve parity among the contributions to the validation level. The following guidelines are adopted for the meshing strategy: refinement diffusion in the downstream direction is favored over the upstream direction. Cell size dx corresponding to $L/500$ is selected following the discussion of results for sideforce uncertainty. A logarithmic wall model boundary condition is applied to the ship hull, though it is understood that the correct prediction of separation strength and location is critical for correctly modeling some components of the transverse force, and that a logarithmic wall model is essentially unfit for this task. However, the increase in cell count for a wall-resolved simulation (no-slip boundary condition) is not realistic for the routine evaluation of hull variants. Domain construction, boundary conditions, and meshing for the free surface are indicated in Figures 3.1 to 3.3. Sizing for the domain

and the Kelvin wedge patch (FS2) is adopted from Numeca best practices [81]. Appropriate adjustments for the boundary layer cells and simulation time step were made for full-scale simulations.

Hull Patch Definition

The ship hull is divided into patches with differing boundary conditions and meshing properties. To manage the total cell count and thereby the computational cost, the mesh is only refined for the underwater portion of the ship. The hull geometry is split into 'Dry' and 'Wet' patches above the undisturbed waterline. An extra bow patch is added to accommodate the bow wave at high Froude numbers (see lower inset of Figure 3.1). Refinement level for 'Wet' patches is set to six, corresponding to cell size$=^{LOA}/_{500}$. The 'Wet' patch is further divided into upstream and wake-side patches, with the refinement diffusion on wake-side patches set to 10. The nominal refinement diffusion employed for the remainder of the mesh is seven. 'Dry' patches are not refined, except through the effect of refinement diffusion for 'Wet' patches. The free-surface is refined to a level nine in the z-direction. The cell count for model-scale simulations was 5.5 million, whereas the cell count for full-scale simulations was 7 million. Details for mesh construction are given in Table 3.1. Mesh definition using refinement levels and refinement diffusion is described in Appendix B.

Boundary Layer Cells

The boundary layer at the ship hull is modeled with a logarithmic-wall-function boundary condition. A near-wall mesh of prismatic cells is introduced such that the innermost cell encompasses the inner layer and buffer layer (regions where viscous shear stress is generated; satisfied for $Y^+ > 15$). Whereas the mesh topology for the Euler mesh is similar to the model-scale mesh for validation, the full-scale boundary layer required further refinement at the hull surface (indicated in Figure 3.2). At full scale, 21 prismatic cells are inserted to satisfy the modeling criterion for Y^+ value at the hull.

A single mesh is used for several operating conditions. The Y^+ at the region of flow acceleration around the forward bilge was considered to be leading when setting the first cell height. The average Y^+ varies between 30 and 60, depending on the Froude number, while the maximum Y^+ varies between 65 and 90. The 'Wet' and 'Dry' patches described above were introduced to manage the increase in total cell count. Cell count for the resultant full-scale mesh is approximately 1.3 million larger than model-scale mesh (20 %), with a correspondingly more computationally expensive simulation.

Simulation Matrix

The nominal test matrix for production runs is 25 simulations, arrayed in a normal drift sweep. Heeled cases are performed with a new mesh. A full sweep (only performed for the parent hulls #1, #34, and #45, and select other cases) was 60 simulations. This represented 25 days of computational effort using the "micro"
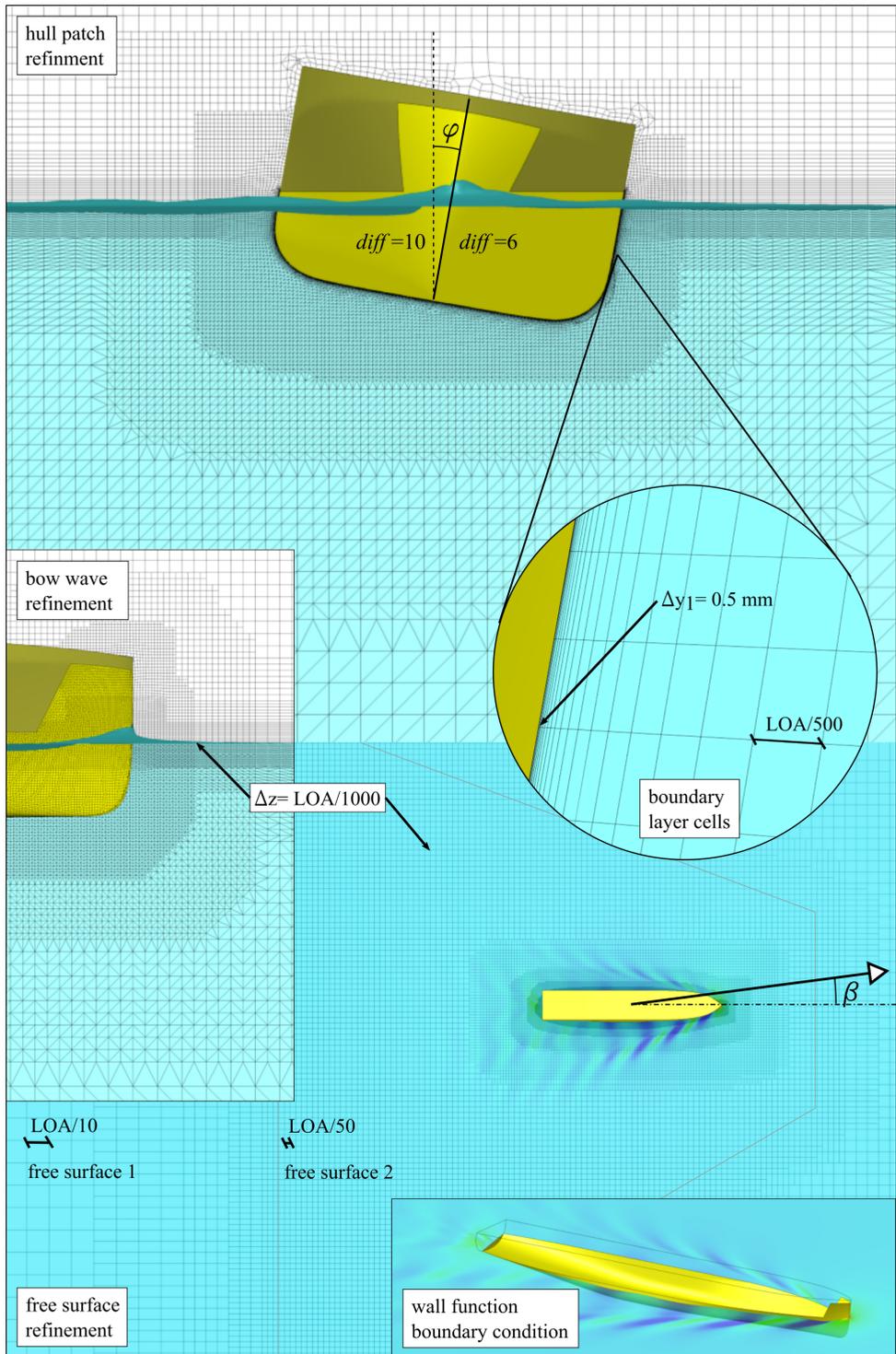
Figure 3.1.: Mesh setup for full-scale simulations

Table 3.1.: Description of full-scale mesh

Euler mesh setup

	X		Y		Z	
	meter	*LOA	meter	*LOA	meter	*LOA
Domain size	690	5	482	3.5	276	2
Initial Cell Size	17.3		17.3		17.3	
Cell size at hull	0.027	1 /500	0.027	1 /500	0.027	1 /50(
Free Surface 1	27.6	1 /5	27.6	1 /5	0.138	1 /1(
Free Surface 2	6.9	1 /20	6.9	1 /20	0.138	1 /1(

Mesh refinement and mesh diffusion

	Refinement level	Refinement diffusion
Hull ('Wet'):		
Wake-side (SB)	6	10
Upstream (PS)	6	7
'Dry'	0	0
Free surface:		
Free surface FS 1	7	7
Kelvin wedge FS 2	7	7

Boundary layer treatment

1st Layer height	0.0005
# of prismatic cells	21
inflation factor	1.3
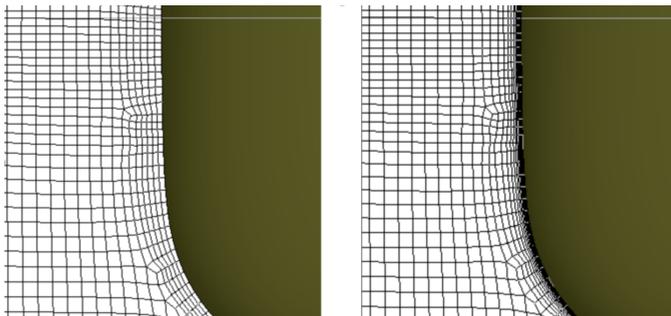
Figure 3.2.: Boundary layer cells model scale (left) / full scale (right).

(a) Computational domain with boundary conditions.

(b) Top view of domain showing vessel/domain motion. Note skewed wedge for wake refinement.
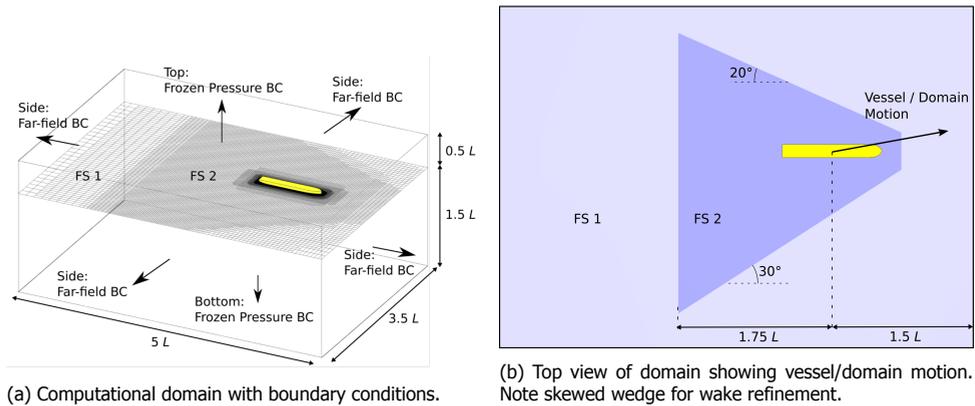
Figure 3.3.: Computational domain

cluster of the Ship Hydro-mechanics Laboratory (4X16 core machine). The simulation effort was therefore migrated to the SARA HPC facility, the Netherlands' supercomputer for scientific research. The total effort, for 60 hulls of the Delft Wind-Assist Series, was 2 500 000 processor hours.

The Drift Sweep procedure [105] was adopted for the efficient analysis of a series of leeway angles and speeds. The drift sweep is a numerical implementation of the planar motion setup used for the experimental determination of maneuvering coefficients. The domain is meshed once, with the ship aligned with the x-axis, and assigned a prescribed motion (including a leeway angle) within a quiescent fluid, as in Figure 3.3. Simulation cases proceed from a converged solution to the next combination of leeway angle and vessel speed using a gradual transition, such that the time required for the convergence of the new solution is reduced compared with re-initializing the computation.

As discussed above, the algorithms for convective terms in the momentum equation and free-surface capturing are both Courant number dependent. A coarse time step corresponding to a Courant number of approximately 100 is adopted during this stage to accelerate the convergence of the flow field. The time step is reduced in the final stage to the target Courant number. Vessel response may be unsteady due to shedding behavior around the hull, but only averaged forces are of interest within the context of this study. Integrated fluid forces on the hull are averaged over one characteristic time interval, equal to L/U, in the flow-oriented coordinate system. The standard deviation for averaged quantities is returned as a measure of the convergence of the simulation to the steady-state solution.

3.2. Verification & Validation

Validation Methodology

Fluid flow around the sailing ship will experience separation effects and will become entrained in large vortices in the wake of the ship. As discussed in the introduction, the efficient modeling of these phenomena is the principal simulation challenge.

Validation Data Set
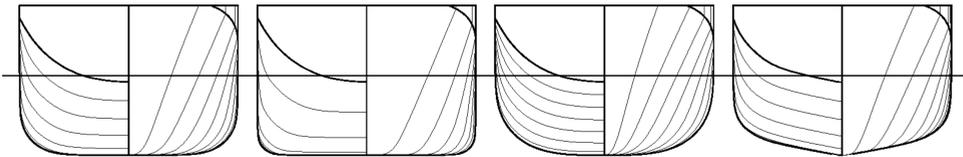
Figure 3.4.: Bare-hull validation cases (from left to right): Hull #1 – Bare (parent), Hull #16 – Bare (C_P +C_M +), Hull #19 – Bare (C_P- C_M-), and Hull #34 – Bare (10° deadrise). Plan view.

The validation data set is composed of four hulls from the Delft Wind-Assist Series (Figures 3.4 and 3.5). Each hull and appended case is tested at three speeds: Froude number Fn= 0.128, 0.168, 0.21, corresponding to 9, 12, and 15 knots at full scale. At model scale, λ=50, the vessel speed is equal to 0.65, 0.87, and 1.09 m/s. Four leeway angles: β =0°, 3°, 6°, 9° were tested, giving a total of 12 operating conditions. The validation data consists of global forces acting on the ship: resistance X, sideforce Y, and yaw moment N. These are evaluated in a flow-aligned coordinate system. The total validation set comprises n=120 points (un-appended cases). The full-scale Reynolds number is approximately 880 000 000. The model-scale Reynolds number is approximately 2 300 000. Details provided in Table 3.2.

The extents of the systematic series and the geometry for validation cases are presented in Table 3.3 and Figure 3.4. Hull #1 and Hull #34 were selected as representative hulls for the series, Hull #1 being the parent hull at the center of the 1st Series, and Hull #34 the parent hull for the Deadrise series (2nd Series). Hull #16, with sharp bilges, is expected to generate pronounced bilge vortices, challenging the capabilities of the fluid modeling in this respect. Hull #19, with a slender form and rounded bilges, will challenge the modeling for flow separation. Together, the validation set is considered to well represent the entire Delft Wind-Assist systematic series. It is assumed that a favorable result for the validation set can be interpreted as a validation statement for the series as a whole.

Explicit Validation Statement

The methodology for validation is taken from the International Towing Tank Con-ference (ITTC) guideline [55, 56, 58] and from the American Society of Mechanical
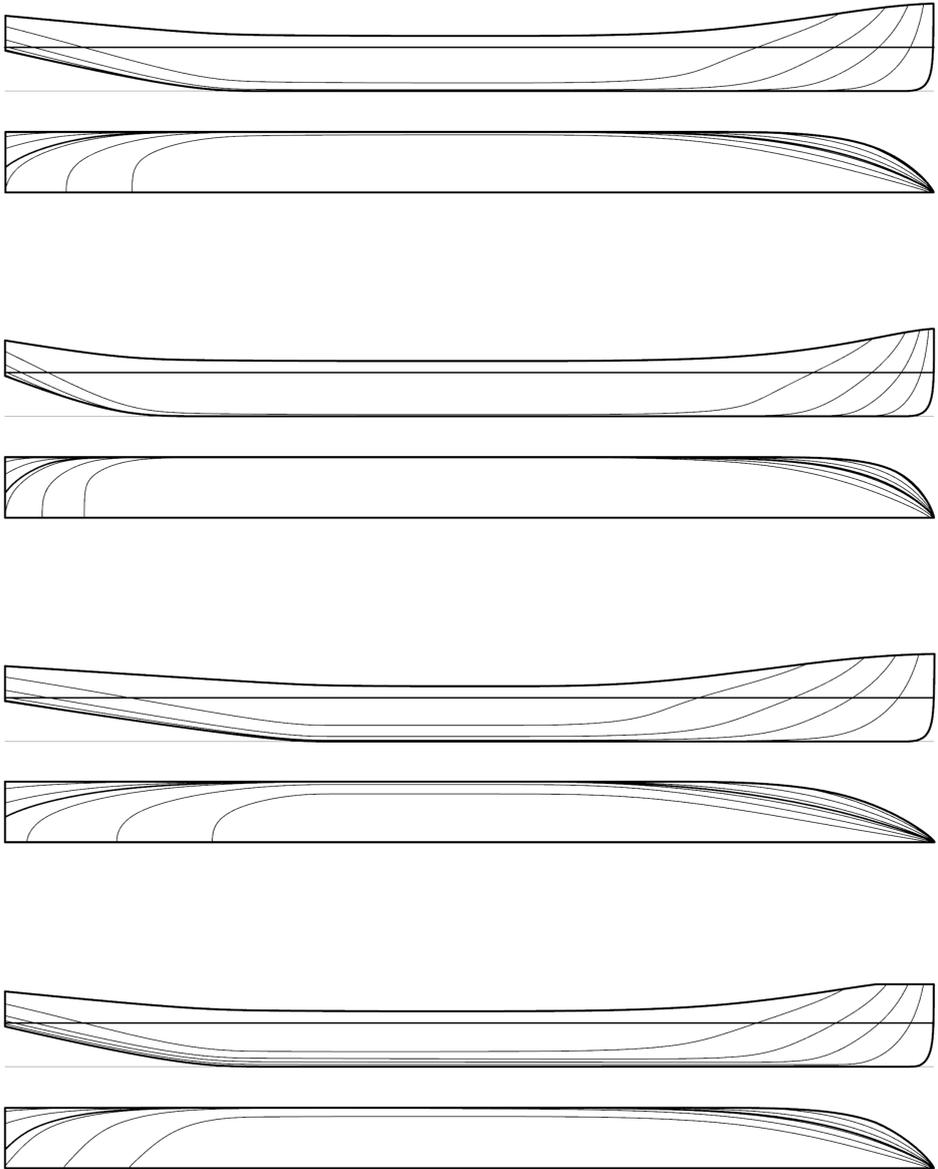
Figure 3.5.: Bare hull validation cases (from top to bottom): Hull #1 – Bare (parent), Hull #16 – Bare (C_P +C_M +), Hull #19 – Bare (C_P- C_M-), and Hull #34 – Bare (10° deadrise). Profile/Top view.

Table 3.2.: Main particulars for the Ecoliner Parent hull.

	Full Scale	Model Scale $\alpha = 50$
LOA [m]	138	2.76
Beam [m]	18	0.36
Draft [m]	6.5	0.13
Displacement [kg]	$11\,896 \times 10^3$	92.8
C_B	0.719	0.719
C_P	0.764	0.764
C_M	0.942	0.942
LCB [%]	50.13	50.13
Wetted Surface m^2	3.293	1.312

Table 3.3.: Bare-Hull Validation Data Set.

	C_P [-]	C_M [-]	T/L [-]	Deadrise [°]
Hull #1 – Bare (parent)	0.764	0.942	0.047	0
Hull #16 – Bare ($C_P + C_M +$)	0.840	0.984	0.047	0
Hull #19 – Bare (C_P- C_M-)	0.689	0.874	0.047	0
Hull #34 – Bare (10° Deadrise)	0.764	0.838	0.047	10
DWA Series Minimum	0.549	0.787	0.042	0
DWA Series Maximum	0.840	0.988	0.061	14

Engineers (ASME) standard [4].

The following validation statement is adopted from [58]:

- $|E| < u_{\mathrm{Val}}$: The comparison error falls within the uncertainty band defined by validation standard uncertainty. The modeling error is within the 'noise level' of the validation exercise. The simulation is validated with a validation level equal to u_{Val}.

A validation statement is made according to the relationship between the comparison error, defined as the difference between simulation and experimental values: $E = Sim - Exp$, and the validation standard uncertainty, u_{Val}, which is a combination of the uncertainties associated with the simulation and experimental data.

One objective of this validation exercise is to bound the modeling errors with a bandwidth defined by the validation standard uncertainty:

$$\delta_{\mathrm{Model}} \in [E - u_{\mathrm{Val}}, E + u_{\mathrm{Val}}] \tag{3.1}$$

An example of a model error, and a central complication for the validation data, is the possible effect of the turbulence stimulators on separation location and on the strength of any separated vortices (as determinants for the sideforce in particular). From boundary layer theory, the increase in mixing near the wall in the wake of turbulence strips (in the stimulation of a fully-developed boundary layer) should delay separation due to curvature for the fore-body bilge vortex, or even due to an adverse pressure gradient for the bow vortex. For the model-scale simulations, the boundary layer (which is turbulent by virtue of the wall modeling) development will nevertheless be retarded when compared to the tank tests (where the strips are employed to recreate the full-scale boundary layer characteristics near the bow). In this case, one might argue that the simulation better resembles a real ship. However, the validation exercise measures the degree to which the simulation is able to reproduce experiments and the fault is therefore a modeling error for the simulation.

Similarly, vessel sinkage and trim, which was allowed during the 2015 experiments [103] and constrained for the 2016 experiments (Appendix B), is constrained for all simulations. Although the 2016 experiment is less realistic, one component of the simulation modeling error has been removed. The focus here is to test the capabilities of RANS-CFD for separating flow structures, and the validation cases might better be thought of as ship-like forms.

The simulation validation is performed in the strict sense (model scale to model scale), attempting to reproduce the experimental results. The discrepancies in modeling for the tank experiment and those for the simulation are elucidated and bounded by the validation effort. The modeling error may be inferred from the results of the validation exercise without making assumptions about the probability distribution of the components of u_{Val} if the magnitude of the comparison error is (much) larger than the validation level:

$$|E| \gg u_{\mathrm{Val}} \tag{3.2}$$

in which case $\delta_{\text{Model}} \approx E$. Otherwise, as will generally be the case here, the modeling error is obscured by the 'noise level' of the validation exercise, or u_{Val} ([4]). Any correction for systematic modeling errors requires an unambiguous categorization of the numerical and modeling errors and a low validation level.
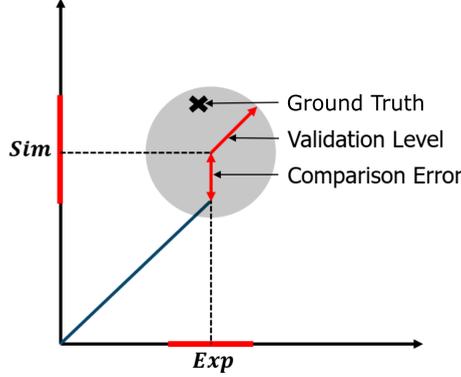
Figure 3.6.: Schematic of relationship between Ground Truth, validation level, and comparison error.

The relationship between simulation and experimental values, associated uncertainties, validation level, and the Ground Truth is indicated schematically in Figure 3.6. The RSS combination of simulation and experimental uncertainties gives the circle with radius equal to u_{Val}, or the precision level of the exercise. Determining u_{Val} is thus a central task in the validation exercise. Following the derivation from the ASME standard, the error for a simulation result is separated into a component arising due to the modeling assumptions and approximations (δ_{Model}), and a component arising from the numerical solution of the equations, (δ_{Num}). Input uncertainties are excluded in this exercise. The numerical error is expressed as an uncertainty, U_{Num} [30, 90]. Assuming U_{Num} and U_{Exp} are uncorrelated, and neglecting U_{Input}, the following definition is adopted:

$$u_{\text{Val}} = \sqrt{U_{\text{Num}}^2 + U_{\text{Exp}}^2} \qquad (3.3)$$

The validation level, u_{Val}, is of interest as a measure of the uncertainty of simulation data. If the validation statement is affirmative, the simulation is able to predict the Ground Truth with precision commensurate with the validation level. This estimate of the uncertainty for simulation data is retained for further work in regression analysis.

Multi-variate Validation Statement

A validation statement is made for simulation of the hulls of the Delft Wind-Assist Series by applying a multivariate validation metric as proposed in [44] to the validation data set. It is assumed that the validation exercise and the statistics for

the comparison error of the validation cases will be representative of the entire wind-assist series. The multivariate metric compares the radius of a hyper-ellipse defined by the set of validation points with a reference radius for a corresponding normal distribution. The radius r and r_{ref} are defined [44]:

$$r = \sqrt{E^T \mathbf{V}_{\text{Val}}^{-1} E} \tag{3.4}$$

$$r_{ref} = \sqrt{n + \sqrt{2n}} \tag{3.5}$$

E is the vector of n comparison errors, and $\mathbf{V}_{\text{Val}}$ is the co-variance matrix, a diagonal matrix with the squared validation uncertainty for each validation point along the diagonal. If the ratio r/r_{ref} is larger than one, then the comparison errors are generally larger than the validation level. For r/r_{ref} less than one, the errors are less than expected for the corresponding normal distribution with n degrees of freedom. Following the same argumentation as for the single-point validation statement above, the simulation is regarded as validated for r/r_{ref} less than one, with a validation level according to the values for u_{Val}.

Distribution of Comparison Error

The distribution of comparison errors is presented in Figure 3.16 for cases where the leeway angle $\beta \neq 0°$. Resistance runs at $\beta = 0°$, a routine application of RANS-CFD, were excluded to create data sets with the same number of entries ($n = 36$) for resistance, sideforce, and yaw moment. The comparison error E is made relative using a constant equal to one half of the range of the measurands:

$$E_{\text{Ens}} = (100) * \frac{Sim - Exp}{\left(\frac{1}{2}(max(Exp) - min(Exp))\right)} \tag{3.6}$$

This definition for an ensemble comparison error was adopted to facilitate the presentation of the entire validation set as a distribution of relative errors. It is a compromise that attempts to accommodate the range in order-of-magnitude for the sideforce and yaw moment by scaling the comparison error approximately in proportion with the validation uncertainty. If each error is expressed as a percent of the experimental value, errors that do not scale with the measurand would be overstated for smaller values of sideforce and yaw moment. Under the present definition of an ensemble comparison error, E_{Ens}, the normalization by a constant value for all errors will understate the relative error for small values of sideforce and yaw moment and overstate the relative errors for large values. For small values of sideforce, the validation level is larger in percentage terms, motivation the suppression of these errors. The opposing tendency exists for larger measurands.

Experimental Uncertainty

Experiments were designed to obtain validation data with minimal uncertainty. The validation data was collected during two experimental campaigns, in 2015 and 2016

(Figure 3.7). The setup for the experiment was altered for the 2016 campaign. The fully constrained setup, with the six-component measurement frame, rather than the sailing yacht setup, gave better control over the position of the model, and provides extra flexibility when designing the arrangement of sensors, again with the aim to minimize experimental uncertainty. The 2016 experiments are described in the remainder of this section. The yacht setup of the Delft Ship Hydro-mechanics Laboratory is documented in [65, 103].

The experimental uncertainty is determined according to the ITTC guideline for planar motion tests ([54]). This presentation is only brief. A review of experimental uncertainty of the 2016 validation campaign and the 2018 bilge keel campaign (Chapter 4) is given in Appendix B. The bias error for model alignment was the primary reason for switching to the hexapod setup. The result was excellent: where the alignment was previously the leading contribution to the experimental uncertainty (2015 test with the yacht setup), now the precision error is the leading contribution, whereas the alignment is one of the smallest.

(a) Sailing yacht experimental setup for 2015 campaign.
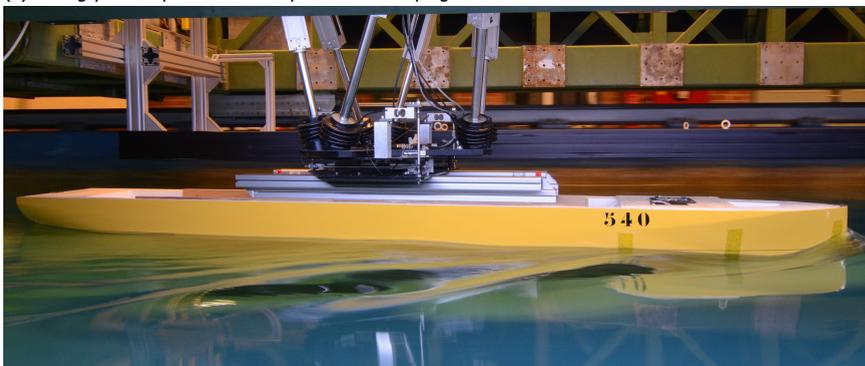
(b) Hexapod / 6dof frame setup for 2016 campaign

Figure 3.7.: Experimental setup for 2015 and 2016 validation campaigns.

The bias error for forces measured with the six-component frame was estimated by repeating the calibration process for the fully assembled frame. The six-component

Table 3.4.: Details for calculation of experimental uncertainty for Hull #34 − Bare at Fn=0.168 and leeway angles $\beta = 9°$, for X. The uncertainty u' is given as a percentage of the measured value. The precision error is the dominant term.

Θ	$\frac{\partial X}{\partial \Theta}$	δ_Θ	u_Θ [N]	u'_Θ [%]
F_X	0.014	0.0243 N	0.047	1.8
β	0.012	0.17°	0.010	0.4
T	0.29	0.0015 m	0.059	2.3
P			0.120	4.6

measurement frame contributes to the stiffness of the measurement system. A variety of forces and moments were applied to the frame, giving a correction to the calibration for X, Y, and N of 0.5 %, 1.2 %, and −1 %, respectively. The remaining disparity, including a significant hysteresis effect, was used as the sensitivity coefficient for force measurement (B_X). The hysteresis phenomena observed for strain gauges is exacerbated for the mechanically-complex measurement frame. Anticipating that the vibrations of a moving carriage would encourage a settling of the frame, a set of measurements was made with a typical carriage speed. In fact, the hysteresis effect was significantly reduced. The estimate for B_X, is therefore likely a conservative value. See Appendix B for details.

All measured forces were rather small so the definition of relative errors is difficult. The alignment of the model for each case was measured with ten repeat runs, with five positive leeway angles and five negative leeway angles, which allowed for a test for the symmetry of the system and also gave an indication for the precision of the setup. These runs were arranged so that the position of the model was changed before each run, i.e., the model was not simply towed repeatedly for a single condition. The distribution of repeat measurements for positive and negative runs is demarked with +/- 2σ, given in percentage of the measured force. This represents (approximately) the 95 % confidence interval. The yaw moment precision error (which does not scale with the measurand) diminishes in relative significance. Alignment uncertainty is approximately 2-6%. See Figure 3.8 and Table 3.4.

Numerical Uncertainty

This section provides a summary of the verification exercise. The results of this study are used to inform the meshing strategy for simulation and to select the requisite grid spacing and time step for a desired numerical uncertainty, so as to achieve parity amongst the contributions to the validation level u_{Val}. The interested reader can find further material in Appendix B.

Several governing bodies publish standards for CFD simulation verification, including the International Towing Tank Committee (ITTC) and the American Society of Mechanical Engineers (ASME). The Grid Convergence Index (GCI) of Roache [90] is commonly accepted, thanks in part to his strong advocacy for standardization of journal policies regarding uncertainty reporting for computational fluid dynamics.
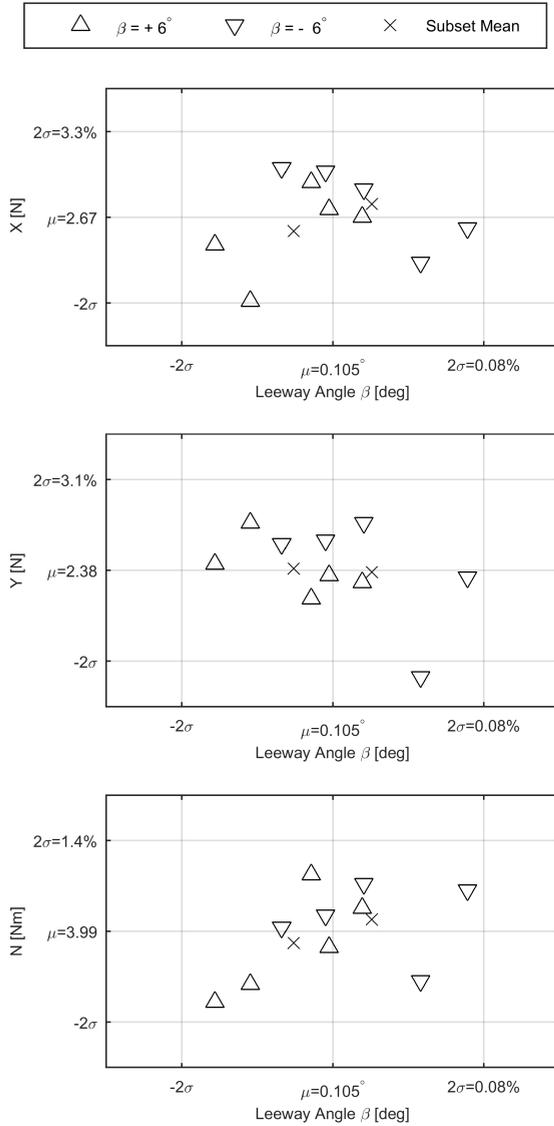
Figure 3.8: Repeat measurements for Hull #1 – Rudder (2016): the rudder angle was set to positive and negative angles (five runs with 6° leeway, 6° rudder, and five runs with −6° leeway, −6° rudder).

His influence is seen throughout subsequent work on this topic. The ITTC recommendations include the correction factor method of Stern and Wilson [101], the GCI of Roache, and an approach for oscillatory convergence. Several methods are investigated in [112]: the GCI of Roache [90], its elaboration by Eça and Hoekstra [30], the Correction Factor of Stern [101], and the Approximate Error Spline of Celik [20]. The method of Eça and Hoekstra was most robust for its ability to cope with nonconforming observed order of convergence and otherwise anomalous convergence behaviour, and this method is followed when possible for the remainder of this study.

The method presented in [30] is based on the following equation:

$$U_{Eca} = \begin{cases} F_S \delta_i + \sigma_{fit} + |\phi_i - \phi_{fit}| & \sigma_{fit} < \Delta \\ 3\sigma_{fit}/\Delta_\phi (F_S \delta_i + \sigma_{fit} + |\phi_i - \phi_{fit}|) & \sigma_{fit} \geq \Delta \end{cases} \tag{3.7}$$

As can be seen, the numerical uncertainty is highly sensitive to the factor of safety F_S, which is based on the data range parameter, Δ_ϕ and the standard deviation of the fit σ_{fit}. Supporting material in Appendix B.

Otherwise, the Correction factor of Stern and Wilson is adopted. The correction factor may be interpreted as an elaborated safety factor. C, F_S is determined by comparing the observed rate of convergence with the theoretical order for the simulation, and as a measure of the proximity of the grids used to the asymptotic range:

$$C = \frac{r^p - 1}{r^{p_{Est}} - 1} \tag{3.8}$$

If the observed order, p, is equal to the estimated order then C is unity. For solutions outside the asymptotic range ($C \neq 1$), the sign and magnitude of C is used to determine the uncertainty according to:

$$U_C = \begin{cases} [9.6(1 - C)^2 + 1.1]|\delta_{RE}| & |1 - C| < 0.125 \\ [2|1 - C| + 1]|\delta_{RE}| & |1 - C| \geq 0.125 \end{cases} \tag{3.9}$$

The final form of Equation (3.13) has developed from communications between Stern et al. [101, 102] and Roach [90], the product of which being that these approaches exhibit comparable behavior. For example, for the limit as $C \to 1$, $U = 1.1|\delta_{RE}|$. This approach gives a smooth behaviour for the F_S, in contrast with the method of Roach or Eça.

Grid Set Definition

Simulation verification as described above and in Appendix B requires a set of grids that are geometrically similar and cover a range of grid sizes within the asymptotic range. Geometric similitude is achieved in the simplest sense by progressive subdivision of mesh cells. For three-dimensional problems, the resulting grids may grow to exceed computing limits, so that a compromise is necessary according to
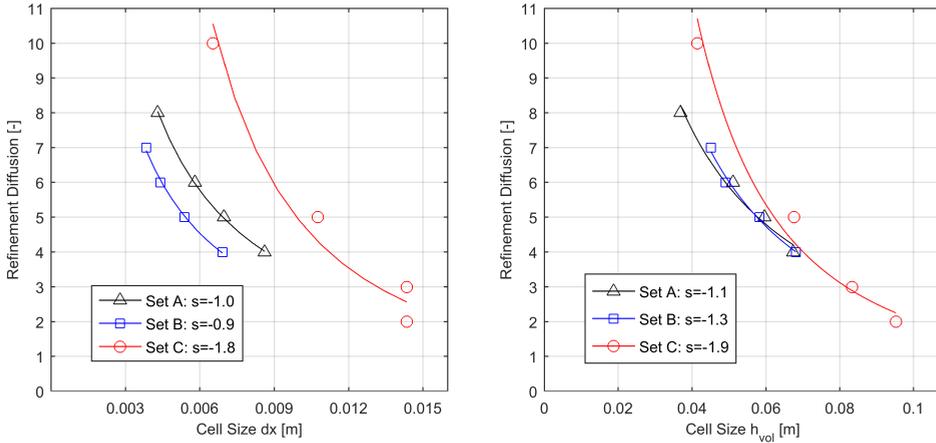
Figure 3.9.: Definition of grid sets A, B, and C. The exponent in the curve fit for each set is provided in the legend as s.

the available computational power. To whit, one subdivision of the grid (in three dimensions) is in principle an eight-fold increase in cell count.

An unstructured mesh for three-dimensional, complex geometries requires a definition for grid size. This dimension must be a length that is descriptive of the grid, and should decrease monotonically for a set of grids, preferably with constant refinement ratio r. Roache suggests the following:

$$h_{\mathrm{Vol}} = \sqrt[3]{\frac{Vol}{N_{\mathrm{cell}}}} \tag{3.10}$$

in which vol is the volume of the computational domain and N_{cell} the number of cells. This definition for cell height is a global quantity: it does not reflect the distribution of cells throughout the domain according to the refinement diffusion, which is of particular importance for capturing flow structures around the hull. Alternate definitions for this characteristic cell size have been proposed, for example an analysis based on the cell count at the ship surface. As a consequence of these ambiguities in the volumetric cell height metric h_{Vol} defined in Equation (3.10), the observed order of convergence may not agree with the theoretical order of convergence. In other words, a second-order discretization that is expected to converge with $(dx)^2$ may not behave accordingly with $(h_{\mathrm{Vol}})^2$.

The construction of sets of geometrically similar unstructured grids using the Numeca meshing tool, Hexpress, is achieved by varying initial cell subdivision, which defines the cell size, and refinement diffusion, which defines the thickness of each refinement level, such that refinement diffusion doubles with each grid subdivision $(dx/2)$. This inverse proportionality condition is satisfied if the exponent fit $s = -1$ as in Figure 3.9.

Three grid sets were defined for this verification exercise, including one subset without boundary layer cells. Grid sets were defined to test the influence of cell distribution within the domain, the influence of refinement diffusion ratio, and the effect of grid similarity on the discretization uncertainty. Each set is composed of four grids, spanning approximately one complete subdivision of the coarse grid. Table 3.5 contains details for mesh construction.

Grid set A - Higher refinement diffusion

Grid set B - Smaller cell size at hull

Grid set C - Twice diffusion rate ($s = -2$)

Grid set Cnobl - No boundary layers inserted ($s = -2$)

The domain refinements in the near- and far-field are varied for grid sets A and B. The balance favors refinement in the far-field for grid set A and refinement at the ship for grid set B, meaning that for similar cell counts, the cell size at the ship hull is larger for set A than for set B. Grid set C was defined with particular interest for the influence of refinement diffusion on the uncertainty for lateral force. Compared with sets A and B, the refinement diffusion is increased at twice the rate, while the cells at the hull were elongated to an aspect ratio of four to manage the size of the computational grids. The dx reported for grids C is the average of the cell dimensions at the hull. Finally, a subset of grid set C was defined that does not contain boundary layer cells. For grid set Cnobl, not shown in Figure 3.9, the fitting for diffusion rate vs. cell size h_{Vol} returns s_h=-2.06.

A further complication is the inclusion of boundary layer cells at the hull, which will vary in number according to size of the Eulerian mesh, dx, and physical modeling requirement for the cell height adjacent to the hull. The maximum Y^+ along the leading bilge was considered to be the driving consideration, as separation is expected at that location. Simulations are carried out at model scale, with a relatively low Reynolds number of 2 300 000, and the requirements of the log-law wall model were quickly satisfied with increasing grid refinement. By relaxing the requirements for the log-law model, it was possible to define a grid subset without boundary layer cells. For grid C2nobl, the compromise between cell height metrics $[dx, h_{\mathrm{Vol}}]$ and refinement diffusion is apparent in the initial cell height, which is smaller than desired for Y^+.

Discussion of Verification Result

The simulation verification exercise is performed for the forces integrated over the ship hull: resistance X, sideforce Y, and yaw moment N. In the following, the calculation of the simulation discretization uncertainty U_{D} will be discussed for each component.

Table 3.5.: Details of mesh construction.

Grid ID	N 10 000 000	h_{Vol} m	h/h_1	BL Cells	Y^+ Mean	Y^+ Max	Courant Max	Courant FS
A4	2.0	0.067	1.83	5	56.5	84	3.9	2.6
A3	3.0	0.060	1.61	4	47.9	75	7.4	4.2
A2	4.7	0.051	1.38	3	47.9	73	6.0	2.8
A1	12	0.037	1.00	3	52.5	80	6.7	3.3
B4	2.0	0.072	1.51	4	54.4	78	7.5	5.0
B3	3.2	0.061	1.29	3	55.1	79	6.1	4.3
B2	5.3	0.052	1.09	3	53.8	80	5.3	4.2
B1	6.8	0.048	1.00	3	49.0	87	5.7	3.8
C4	0.88	0.095	2.30	5	51	122	4.0	1.8
C3	1.4	0.083	2.01	5	53	128	3.8	2.1
C2	2.6	0.068	1.63	3	53.1	114	4.7	1.9
C1nobl	8.8	0.041	1.00	0	40.8	89	2.9	1.5
C4nobl	0.73	0.089	2.15		60.4	93	5.5	3.4
C3nobl	1.1	0.077	1.86		52.2	86	5.9	2.8
C2nobl	2.0	0.062	1.50		42.5	81	5.4	1.8
C1nobl	8.8	0.041	1.00		40.8	89	2.9	1.5

Figure 3.10.: Resistance convergence for grid discretization (left: $\beta = 6°$, right: $\beta = 9°$). U_D indicated with error bars.

Table 3.6.: Calculation details for grid uncertainty estimate for resistance and sideforce.

Grid Set	R	p_{Obs}	Fit	σ_{fit}/Δ_ϕ	F_{S}	ϕ_0	$U_{h_{\mathrm{Vol}}\approx 0.07}$ [%]
Resistance							
Grid Set	R	p_{Obs}	Fit	σ_{fit}/Δ_ϕ	F_{S}	ϕ_0	$U_{h_{\mathrm{Vol}}\approx 0.07}$ [%]
A ($\beta = 0°$)	-0.53	17.7	δ_2	1.44	3	2.36	12
C ($\beta = 0°$)	0.44	7.43	δ_2	0.88	3	2.33	8.1
A ($\beta = 6°$)	1.56	9.29	δ_2	0.92	3	2.56	9.3
B ($\beta = 6°$)	-0.30	1.30	δ_{RE}	1.10	3	2.54	18
C ($\beta = 9°$)	1.85	6.78	δ_2	0.79	3	2.82	11
Sideforce							
Grid Set							
A ($\beta = 6°$)	1.81	2.72	δ_{12}	0.19	3	1.27	32
B ($\beta = 6°$)	1.0	1.66	δ_{RE}	0.29	1.25	1.15	21
C ($\beta = 9°$)	1.13	2.55	δ_{12}	0.06	3	2.22	14
Cnobl ($\beta = 9°$)	0.88	2.38	δ_{12}	0.01	3	2.20	6.0

Resistance

The results for discretization uncertainty for $\beta = 0°$ appear to be congruent (Figure 3.10). Calculation details for Equation (3.7) are provided in Table 3.6. The observed order of convergence is greater than the upper bound prescribed by Eça and Hoekstra, so that a safety factor of three is applied for both cases. A similar, high observed order of convergence for resistance has been reported by Eça and Hoekstra [29]. The method switches to the second-order fit. The Richardson extrapolated values for these grid sets show excellent agreement for all leeway angles tested. For leeway angle $\beta = 6°$, the meshing approach taken for grid set A is apparently superior, returning approximately half the uncertainty as grid set B, even as the δ_{RE} fitting is used in the uncertainty procedure for grid set B. On the other hand, the convergence ratio R is less than one for grid set B, indicating oscillatory convergence, leading to $\sigma_{fit}/\Delta_\phi > 1$ and a safety factor of 3.

Sideforce (sway)

The uncertainty estimation for sideforce is compelling. The value of p_{Obs} and the ratio σ_{fit}/Δ_ϕ indicates that confidence is placed on these. Grid set B, where resolution of the ship is favored, has an observed order of convergence that is in accordance with the interval specified by Eça and Hoekstra. An 11.8 % difference between the ϕ_0 value for grid set A and B is observed. The discrepancy may be a product of the differing fits δ_{12} and δ_{RE}. This discrepancy underscores the substantial grid
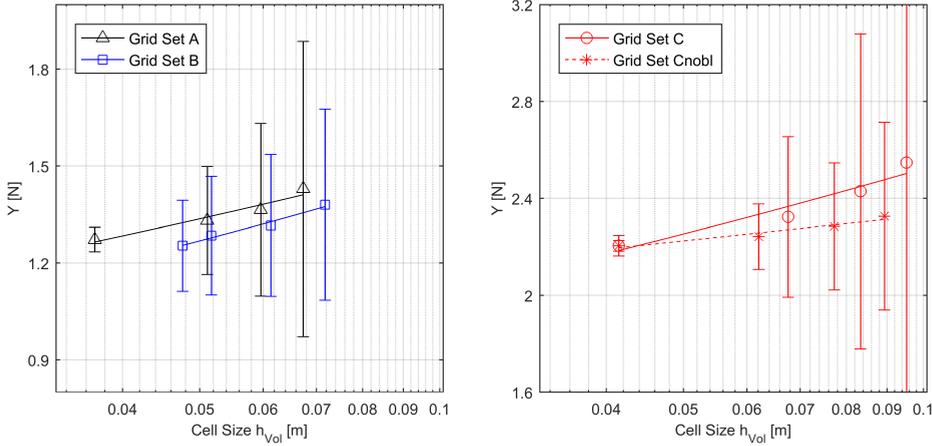
Figure 3.11.: Sideforce convergence for grid discretization (left: $\beta = 6°$, right: $\beta = 9°$). U_D indicated with error bars.

uncertainty for sideforce. Still, the largest grids A1 and C1nobl have an uncertainty of approximately 3 %.

Grid set Cnobl, constructed without boundary layer cells, return the smallest uncertainties (see Figure 3.11). Calculation details (Table 3.6) indicate that the quality of the fit and the degree of confidence in the uncertainty assessment are superior to that of grid set C. Grid set C and Cnobl are otherwise identical. In fact the grid quality for Cnobl is detrimentally impacted by the absence of boundary layer cells as seen in Figure 3.15. The boundary layer cells of grid set C have disrupted geometric similitude, and while the physical modeling (inconsistent Y^+ spacing) and numerical properties (non-orthogonal cells near to the wall) have both been compromised, grid set Cnobl returns superior calculation metrics and lower uncertainties. This differece is interpreted as the influence of geometric similitude on the uncertainty assessment methods, suggesting that the uncertainties returned following the methodologies in this paper may be overstated.

Yaw moment

Simulation uncertainty for yaw (almost entirely a potential effect - the Munk moment), was very small. These details are omitted here, but can be found in Appendix B.

Simulation Convergence / Iterative Error

The iterative uncertainty for solutions of unsteady flow equations, including numerical convergence and any unsteady flow effects is assessed by reviewing the normalized L_2 residuals for the flow equations and the standard deviation for the integrated body forces used as verification quantities. Simulation convergence for

67

the simulation residuals for the U_1 velocity component and the pressure P are reported as:

$$L_2 = \sqrt{\frac{\sum_{i=1}^{N_P} (|\Delta\phi_i|)^2}{N_P}} \tag{3.11}$$

Where $\Delta\phi_i$ is the normalized residual, a measure of the change in the flow quantity ϕ between time steps.

For the verification exercise, the integrated forces on the ship are the quantities of interest. They are averaged over a sample interval equal to two characteristic time intervals $2L/U$, as in Figure 3.12. The standard deviation for these quantities is reported as a metric for simulation convergence to the steady solution that is of interest. The contribution of statistical errors associated with averaging of unsteady phenomena is neglected. The simulation residuals are reduced to at least 0.000 01 for all cases. The contribution of iterative errors to the numerical uncertainty, as in Equation (B.1), is assumed to be negligible (see Table 3.7).
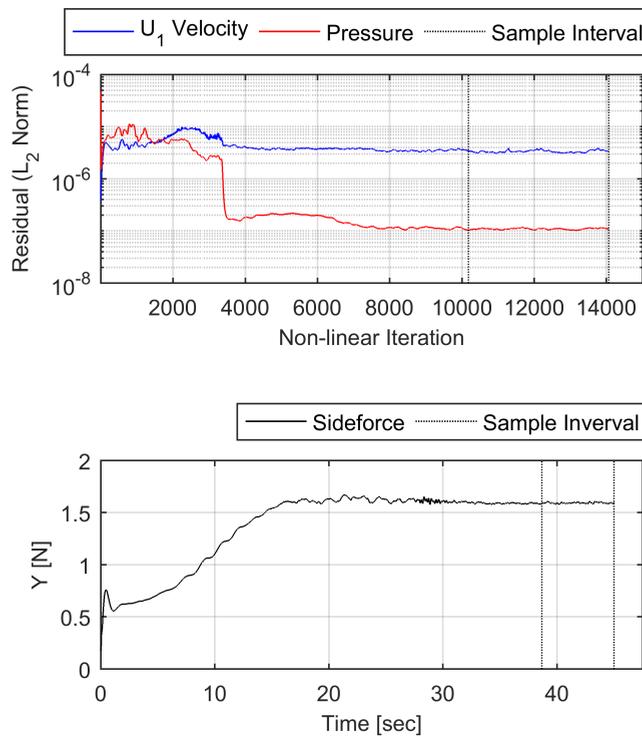
Figure 3.12.: Simulation convergence for a verification case. The sample interval equal to two characteristic time intervals is indicated.

Table 3.7.: Simulation residuals and convergence behaviour.

Grid ID	U_1 Residual L_2	P Residual L_2	σ_X [%]	σ_Y [%]	σ_N [%]
A4	3.38×10^{-6}	1.69×10^{-7}	0.09	0.51	0.88
A3	2.44×10^{-6}	1.06×10^{-7}	0.15	0.33	0.48
A2	3.34×10^{-6}	1.10×10^{-7}	0.15	0.49	0.69
A1	2.93×10^{-6}	8.75×10^{-8}	0.32	1.24	1.58
B4	3.51×10^{-6}	1.01×10^{-7}	0.05	0.27	0.37
B3	5.24×10^{-6}	1.20×10^{-7}	0.07	0.62	0.56
B2	3.25×10^{-6}	1.28×10^{-7}	0.16	0.93	1.14
B1	2.79×10^{-6}	1.41×10^{-7}	0.23	1.16	1.27
C4	1.68×10^{-6}	9.51×10^{-10}	0.11	0.44	0.65
C3	4.21×10^{-6}	3.40×10^{-8}	0.05	0.40	0.98
C2	1.34×10^{-6}	1.40×10^{-8}	0.08	0.28	0.40
C1nobl	9.62×10^{-8}	1.81×10^{-9}	0.29	1.38	2.23
C4nobl	1.58×10^{-6}	4.08×10^{-7}	0.12	0.31	0.32
C3nobl	8.26×10^{-7}	2.24×10^{-10}	0.07	0.44	0.44
C2nobl	6.49×10^{-8}	1.54×10^{-10}	0.10	0.35	0.52
C1nobl	9.62×10^{-8}	1.81×10^{-9}	0.29	1.38	2.23

Parameter Studies

Besides the formal validation presented above, several parameter studies for simulation settings carried out, described also in Appendix B. For the Courant number study, simulation uncertainty was determined using systematic variations for the Courant number to infer a target Courant number for production runs. Also, modeling choices for wall treatment and turbulence modeling were examined by comparing the distributions of comparison error.

Courant Number Study

The Courant number is a measure of the relation between spatial and temporal discretization. It represents the passage of a fluid parcel along grid cells for each time interval (Equation (3.12)). It is normally tied to a stability criteria (the *CFL condition*) under explicit formulations. For blended/upwind convective schemes such as the ALVSMART [81], the Courant number may be much larger than 1, meaning that a fluid parcel can pass several grid cells per time step dt without introducing stability issues for the solver. Still, a Courant-independent solution is desired.

$$Co = U \frac{dt}{dx} \tag{3.12}$$

In the aforementioned procedure for determining the numerical uncertainty, the time step is scaled together with the grid cell size, maintaining a constant Courant number and a consistency for the numerical method for the grid set. The discretization uncertainty obtained with the procedure includes the effect of space and time discretization. However, it is desirable to inform the choice of time step for validation runs and production runs, as the blending/switching of discretization schemes and the interface compression algorithm are functions of the local Courant number. The influence of the choice of time step is investigated with a series of simulations for varying time step. Courant values between 0.25 and 50 were achieved, based on cell refinement at the hull, away from the free surface.

Table 3.8.: Details of Courant number study.

Courant (target)	Courant (realized)		
	Grid A2	Grid B1	Grid B3
0.25	0.24		
0.5	0.49		0.36
1	0.98	1.17	1.09
4	2.97	4.64	4.30
16		18.41	16.99
50		54.06	

The target Courant number for validation and production runs is selected based on systematic variations in the Courant number performed on three grids, A2, B1, and B3. Mesh A2 and B1 share the same Euler mesh, ΔX, sharing the same theoretical behavior for Courant number. Simulations for variations in Courant number were performed at 6° leeway. Details for the Courant number study are presented in Table 3.8, with results for resistance and sideforce shown also in Figure 3.13. The temporal uncertainty corresponding to a target Courant number of four is reported. This is the same target Courant number used for the discretization uncertainty calculations presented above.

(a) Resistance

(b) Sideforce
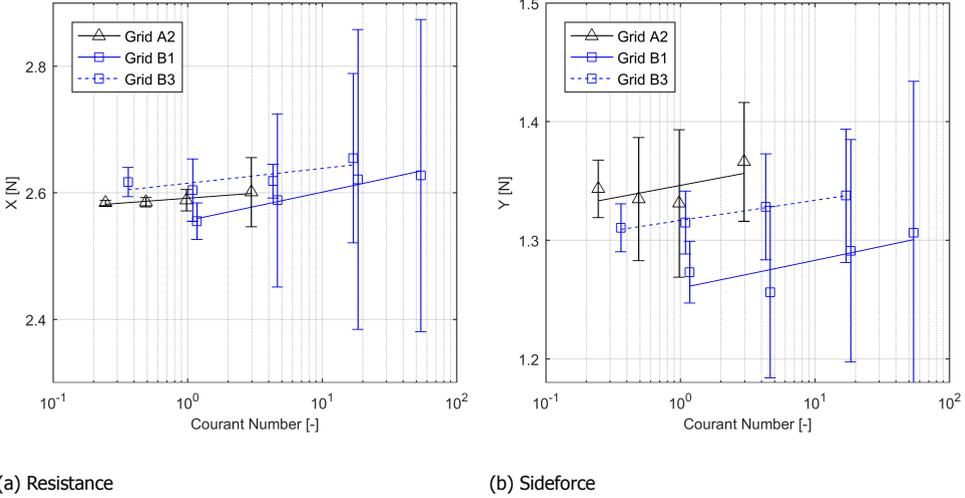
Figure 3.13.: Simulation convergence for Courant number variation. ($\beta = 6°$) U_{T} indicated with error bars.

If an RSS combination for the simulation error is assumed as in Equation (3.13), as adopted from [101]:

$$U_{\mathrm{D}}^2 = U_{\mathrm{G}}^2 + U_{\mathrm{T}}^2 \tag{3.13}$$

then the results calculated for U_{D} and U_{T} at $Co=4$ may be used to infer conclusions about the composition of the numerical uncertainty (iterative errors have been neglected throughout this study). The influence of the range of data in relation to the

Table 3.9.: Calculation details for Courant number parameter study for resistance.

Grid	R	p_{Obs}	Fit	σ_{fit}/Δ_ϕ	F_{S}	ϕ_0	$U_{\mathrm{Co}\approx4}$ [%]
A2	0.30	1.15	δ_{RE}	0.05	1.25	2.58	2.1
B1	1.0	0.53	δ_{RE}	0.67	1.25	2.52	9.0
B3	−0.89	2.33	δ_2	0.64	3	2.61	1.0

extents of the asymptotic range has been discussed. The increased safety factor for anomalous convergence behavior reflects the poor confidence placed on the uncertainty estimation. Results for Courant variations on grid A2 are regarded as the most meaningful.

Calculation details for grids A2, B1, and B3 indicate that confidence is placed in the time uncertainty estimates (see Table 3.9). The Richardson extrapolations for zero time step and zero grid spacing show close agreements. The ϕ_0 value for grid A2 and B1 differ by 2.3 %. Finally, the ϕ_0 values for zero time step and zero grid spacing for grid sets A and B differ by less than 1 % each. A marked increase in the uncertainty estimate is observed for the set of large Courant numbers, performed with grid set B1. The contribution of time-discretization uncertainty is only significant for the resistance, for which U_D =4.4 %, U_G =3.9 %, and U_T =2.1 %. A target Courant number is determined by linear interpolation of the averaged values for U_T such that the contributions of the spatial and temporal uncertainties to the discretization uncertainty are equal. This condition is satisfied for Courant number equal to 8.

Table 3.10.: Statistics for distribution of comparison errors.

E_{Ens}	$\mu_{\mathrm{Ens}}[\%]$	$\sigma_{\mathrm{Ens}}\,[\%]$	$CI95_{\mathrm{Ens}}\,[\%]$
Validation Set			
Resistance X	−0.6	5.0	10.8
Sideforce Y	−2.0	7.5	17.4
Yaw Moment N	0.9	4.2	9.3
Wall Treatments (Y)			
$EASM$ (Val. Mesh)	−2.0	7.5	17.4
Wall-resolved $EASM$ (A3)	2.6	5.3	13.3
Log-law $EASM$ (A3)	−4.7	9.0	23.0
Log-law $k-\omega$ (C2)	−11.3	12.6	32.7

Turbulence model and wall treatment

The comparison error (sideforce - Y) for two wall treatments are plotted as histograms in Figure 3.14. The wall-resolved mesh is based on mesh A3, shown also in Figure 3.15 below. The statistics of the distributions, and for variations in turbulence model are included in Table 3.10. The negative outliers in Figure 3.14 (left) correspond to Hull #16, with sharp bilges, where pronounced separation of bilge vortices is expected. Simulation for sideforce using log-law boundary condition is consistently under-predicted for this hull. The results for the k-ω SST turbulence model affirm the selection of the EASM turbulence model, as the modeling of anisotropic turbulence has centered the distribution and reduced the number of
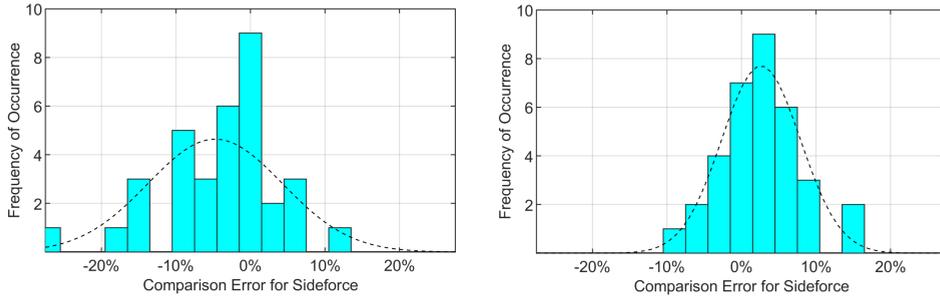
Figure 3.14.: E_{Ens} (sideforce) for logarithmic wall model (left) and wall-resolved boundary condition (right) (n=36).

outliers. Whereas the results for a wall-resolved simulation show further improvement, this approach is not considered to be feasible in light of the scope of full-scale production runs.

The absence of boundary layer cells for grid set Cnobl influences the solution near the wall as seen in Figure 3.15, where a detail of the hull is shown as the keel line turns from the parallel mid-body towards the upward-sloping buttock lines of the pram stern. A cross-section of the computational domain is shown in the x-z plane including cell borders and color contours for the eddy viscosity ratio. Three solutions are shown: grid A3, with four boundary layer cells (top), grid C2nobl (middle), and a wall-resolved mesh (bottom), where a no-slip boundary condition is imposed at the hull. For this mesh, thirty boundary layer cells are inserted to achieve a Y^+ less than one. The thickness of the region of eddy viscosity production is similar for all meshes, and lies within the thickness of the boundary-layer cell region for grid A3 (top). The reduction in eddy viscosity ratio along the upward sloping keel, observed for the wall-resolved simulation, is less evident for grid A3. Finally, the absence of boundary layer cells for grid Cnobl clearly influences the flow inside the boundary layer, where mesh irregularities were introduced in the snap-to-geometry step during mesh construction. Interestingly, the quality of the data for Richardson extrapolation, as measured by p_{Obs} and the ratio σ_{fit}/Δ_ϕ indicate that greater confidence is placed in the uncertainty estimates based on grid set Cnobl (see Appendix B). As discussed, the methods for uncertainty assessment are predicated on geometric similitude, which is better preserved for the grid set without boundary layer cells

Meshing strategy for validation and full-scale runs

The mesh resolution and time step is defined such that the contribution of the numerical uncertainty is commensurate with the other uncertainties in the validation exercise. At the same time, the mesh definition must be computationally affordable considering the volume of simulations planned.

Estimates for numerical uncertainty for validation simulations are given in Ta-
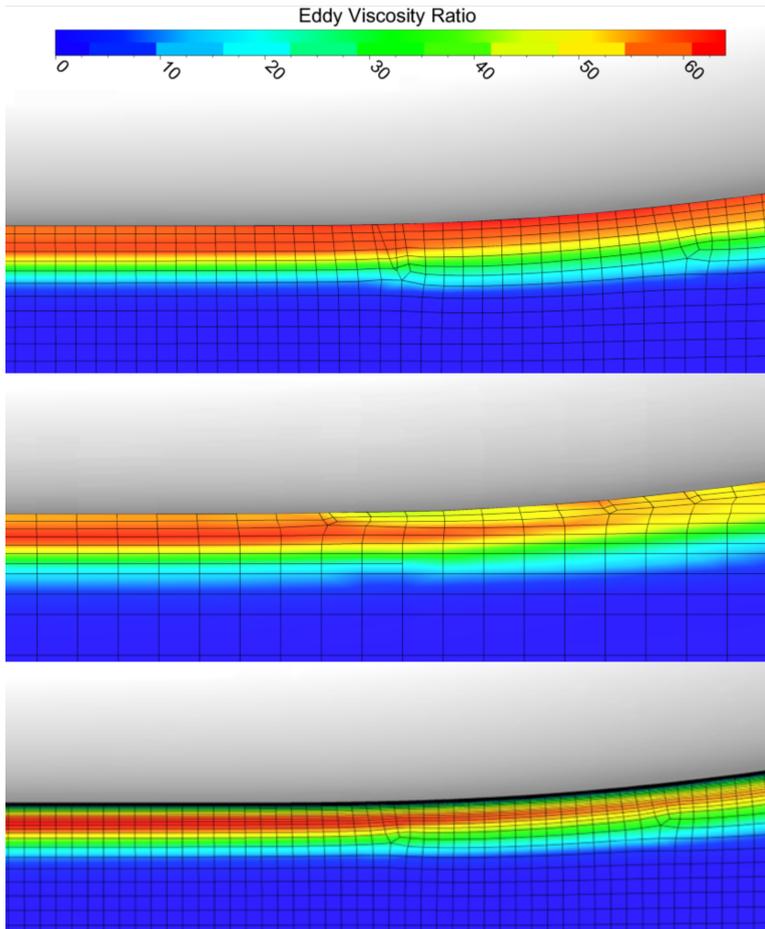
Figure 3.15.: Boundary layer development for grids A3, C2nobl, and a wall-resolved solution (top to bottom). Color contours indicate eddy viscosity ratio.

Table 3.11.: Numerical uncertainty for simulation validation.

	U_{Num}: X [N]	U_{Num}: Y [N]	U_{Num}: N [N m]
$\beta = 0°$	0.14		
$\beta = 6°$	0.11	0.13	0.34
$\beta = 9°$	0.23	0.14	0.35

ble 3.11, with a cell size dx=0.0054 and a refinement diffusion equal to 10 in the downstream direction. The corresponding grid size is h_{Vol} =0.05, for 6 000 000 cell count. The numerical uncertainties were approximated by linear interpolation using h_{Vol} and available results on grids sets A and C. The time step is selected to achieve a target Courant number of 8.

The meshing strategy can be best understood by recalling the grid set definition in terms of the cell size dx and the refinement diffusion (see Figure 3.9).

First, the large uncertainty values reported for grid set B are interesting as the cell size dx for grids B1-B3 is smaller than the cell size dx for Grid A2. On the other hand, the two largest grids, A1 and C1nobl, where quite small uncertainties are computed for all force components, have the largest refinement diffusion (Figure 3.11). This is interpreted as a consequence of proper resolution of the wake of shed vorticity associated with sideforce production. For the grid definition for validation simulations, the refinement diffusion parameter should be prioritized over cell size dx. The general trend for the poor performance of grid set B does not hold for the uncertainty for sideforce U_{Num}: Y. For grids A2-A4 and B2-B4, where the refinement diffusion varies uniformly, one can observe the influence of the cell size dx on the sideforce uncertainty, which increases quickly for grid set A after grid A2 (cell size $dx = 0.006$ ($\approx L/500$).

As described in the introduction, the purpose here is to support the validation exercise and thereby the study of wind-assisted commercial ships. Therefore, the best possible mesh is made according to the meshing guidelines based on the analysis for the four grid sets. The uncertainty for this mesh is estimated based on the above exercise, not assessed directly. The further allocation of computer resources would have been indiscriminate, but were another grid set/Courant number analyzed, then the meshing guidelines would be updated accordingly, again with the aim to improve the final mesh definition for production runs.

The distribution of comparison errors for the validation data set is shown in Figure 3.16. The errors for each component appear to be normally distributed. The statistics of the distribution are presented in Table 3.10, including a 95 % confidence interval (based on Student-t tables) of the ensemble comparison error. It is understood as an *estimate* for the range of the comparison errors for the Delft Wind-Assist Series. For the sideforce in particular, a −2 % mean offset indicates there is a systematic under-prediction by the simulation. The negative outliers in Figure 3.16 correspond to Hull #16, with sharp bilges, where pronounced separation of bilge vortices is expected. Simulation for sideforce is consistently under-predicted for this hull.

Validation for Production Runs

The validation statement is made for the bare hull r/r_{ref} in the Wind-Assist Series, followed by the visualization of the bow wave profile for Hull 34 − Bare. The ratio r/r_{ref} is adopted as a multiple-point validation metric. There are three validation points (resistance X, sideforce Y, and yaw moment N) for each hull at each operating condition, or 120 validation points in total. Results for r/r_{ref} are also presented
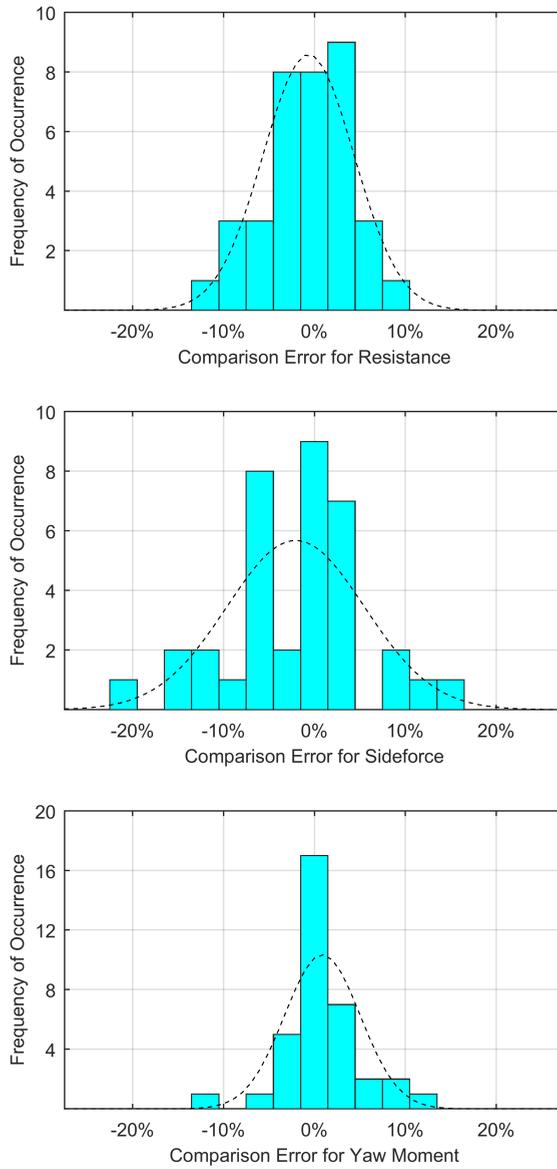
Figure 3.16.: E_{Ens} for validation data set, using $EASM$ turbulence model. $\beta \neq 0°$ ($n = 36$).

per force component. Select figures are included here. See Appendix B for a detailed description of this exercise.

Several assumptions are required for the numerical uncertainty, which is only available for the parent hull (Hull #1), at $Fn=0.168$ and for leeway angles $\beta= 0°$, 6°, 9°. The computational effort required to determine the numerical uncertainty for additional r/r_{ref} and operating conditions was prohibitive. The numerical uncertainty for the sideforce in particular may be the dominant contribution to the validation level.

Subset 1 - Direct estimate for numerical uncertainty available: $Fn=0.168$; $\beta= 0°$, 6°, 9°. $n=7$.

Subset 2 - All hulls at the same operating conditions as subset 1. $n=28$.

Subset 3 - Complete validation set. $n=120$.

Results for r/r_{ref} are presented for several subsets of the validation data set, defined according to the assumptions made for the numerical uncertainty. Subset 1 is defined by cases where the numerical uncertainty is directly available, for $Fn=0.168$ and for leeway angles $\beta= 0°$, 6°, 9° ($n=7$). Subset 2 consists of all hulls of the bare-hull validation set at the same operating condition as Subset 1, where it is assumed that the numerical uncertainty is unchanged for varying hull geometry ($n=28$). Finally, r/r_{ref} is given for the complete validation set ($n = 120$). Here it is assumed that the numerical uncertainty at $Fn=0.168$ and leeway angle $\beta=3°$ is equal to the uncertainty at $Fn=0.168$ and $\beta=6°$. The numerical uncertainty at other speeds in the validation data is assumed to scale with the magnitude of the measured quantity.

Table 3.12.: Validation level u_{Val} for Hull #1 – Bare.

Fn	Leeway	Resistance X		Sideforce Y		Yaw Moment N	
		[N]	[%]	[N]	[%]	[N m]	[%]
0.128	0°	0.103	7.8				
	3°	0.094	6.8	0.089	28.8	0.189	13.8
	6°	0.096	6.6	0.099	13.7	0.238	8.5
	9°	0.150	9.4	0.117	9.0	0.282	7.0
0.168	0°	0.180	7.7				
	3°	0.161	6.6	0.148	25.2	0.372	14.0
	6°	0.166	6.4	0.157	11.9	0.423	8.3
	9°	0.268	9.3	0.189	8.0	0.495	6.7
0.21	0°	0.310	7.6				
	3°	0.276	6.5	0.229	23.5	0.587	13.4
	6°	0.281	6.3	0.249	11.8	0.665	8.2
	9°	0.452	9.3	0.305	7.9	0.791	6.6

Explicit Validation Case

All components of the validation standard uncertainty are available for Hull #1 − Bare at Fn=0.168 and for leeway angles $\beta = 0°, 6°, 9°$. The mesh contains 6 million cells, requiring four hours to perform one simulation with the available computing resources.

A very good agreement between the simulation result and the experimental value is reported in Table 3.13. The comparison error is less than the validation uncertainty for all cases, and the simulation is validated at the respective validation levels. The experimental and numerical uncertainties are of similar magnitudes.

The ratio r/r_{ref} must be considered against the validation uncertainty, which form the entries of the co-variance matrix $\mathbf{V}_{\mathrm{Val}}$. The validation uncertainty for Hull #1 − Bare is presented in Table 3.12 (in absolute and relative terms). The validation uncertainties for other r/r_{ref} will vary as the experimental uncertainty can be computed for all cases, but the values for Hull #1 − Bare are representative. The magnitude of the sideforce at low speeds and for small angles is such that the validation uncertainty, when expressed in relative terms, may exceed 25 %.

Simulation validation for the complete Wind-Assist Series are presented in Table 3.14. The multiple set-point validation metric r/r_{ref} is less than one for all subsets and all entries, meaning that the comparison errors are generally less than the associated uncertainties. Following the validation approach outlined above, the simulation method for the Delft Wind-Assist Series is validated at the validation levels summarized in Table 3.12. r/r_{ref} ≪1 for all entries for the first subset indicates that the comparison error for these cases is much less than the associated validation uncertainties. The simulation results for Hull #1, at these operating conditions, are in very close agreement with the validation data.

Bow Wave Profile
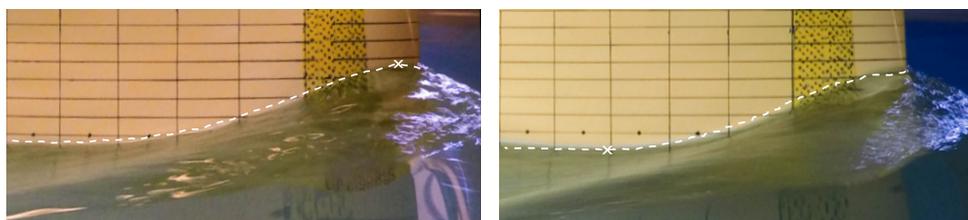
(a) Pressure side   (b) Suction side

Figure 3.17.: Bow wave profile corresponding to the median error (Fn=0.168 and $\beta = 6°$). The images have been overlaid with the wave elevation obtained by simulation, including the peak/trough values used for comparison (marked with x).

The bow wave elevation was measured with cameras and using grid markings on the model. A formal validation statement is not possible as the uncertainty associated with the simulation waterline was not determined. A good quantitative agreement is reported for the maximum bow wave height and location (pressure

Table 3.13.: Validation for Hull #1 – Bare.

	U_{Exp} [-]	U_{Num} [-]	u_{Val} [-]	%	E [-]	%
$Fn = 0.168, \beta = 0°$						
X [N]	0.080	0.140	0.180	7.6	0.026	1.67
$Fn = 0.168, \beta = 6°$						
X [N]	0.117	0.107	0.166	6.4	0.034	1.42
Y [N]	0.0888	0.133	0.157	11.9	−0.005	−0.37
N [N m]	0.251	0.336	0.422	8.3	−0.074	−1.46
$Fn = 0.168, \beta = 9°$						
X [N]	0.124	0.227	0.268	9.3	0.028	1.08
Y [N]	0.126	0.137	0.189	8.0	−0.080	−3.39
N [N m]	0.350	0.347	0.495	6.7	0.117	1.59

Table 3.14.: Details of the validation for the Delft Wind-Assist Series.

r/r_{ref}	All	X	Y	N
Subset 1	0.17	0.17	0.14	0.13
Subset 2	0.60	0.39	0.73	0.58
Subset 3	0.59	0.30	0.84	0.45

side), and the minimum wave height and location (suction side). The distance between the simulation and experimental value is reported as a comparison error $\delta_E = \sqrt{\delta_X + \delta_Y}$. The median error values occurred for Fn=0.168 and $\beta = 6°$. For this case, the comparison error for the bow wave crest (pressure side) is $\delta_E = 4.6$ mm. The comparison error for the bow wave trough (suction side) is $\delta_E = 5.0$ mm. The results for this case are shown in Figure 3.17.

3.3. Reynolds Scaling Effects and Simulation Validation

Several Reynolds effects are relevant to the hydro-mechanics of a sailing ship. For example, the inception of separation phenomena is delayed with increasingly turbulent flow, as the larger fluid momentum in the boundary layer is better able to negotiate adverse pressure gradients and surface curvature. Flow separation over the curved surface of the vessel bilges, contributing to the non-linear sideforce—a typical example of phenomena that is Reynolds-number dependent—is understood to be relevant for the vessel course stability and sailing efficiency. Also to be considered is the increase for the range of length scales present in a full-scale vortex, and the corresponding increase in the rate of energy diffusion. Finally, any separated vortex will pass along the vessel hull where it will encounter and interact with the vessel boundary layer.

Simulations performed at full scale resolve the discrepancy in scaling for the rather-to-thick model-scale boundary layer, something that would be impossible otherwise. A full-scale simulation method also resolves a key modeling error, introduced by the scaling of model scale, towing tank results, in which turbulence stimulators added to achieve correct behavior for the frictional resistance. The hereby excited boundary layer may interact with the separation behavior along the forebody.

Calm-Water Resistance

Reliable calm-water resistance prediction with RANS-CFD tools at full-scale has been an industry standard for some time. The numerical estimation of the wall friction coefficient using logarithmic law-based turbulence modeling is calibrated (to some extent) using high-quality model test data, so a good agreement here should not be surprising. Many ship-builders use a 'correlation coefficient' to match extrapolated model scale values to sea trail data when making powering predictions. Simulation results for resistance are in good agreement with experimental data. The systematic fault observed for Mull #34 is a geometric error in the model construction.

Values for R_T obtained from simulations at model scale and full scale should be related according to the well-known Froude scaling law for model tests. Froude similarity preserves similarity for the gravity waves generated by the ship, and the corresponding resistance. The concessions made for the Reynolds number corrected by adopting a suitable, full-scale friction coefficient. Determination of the
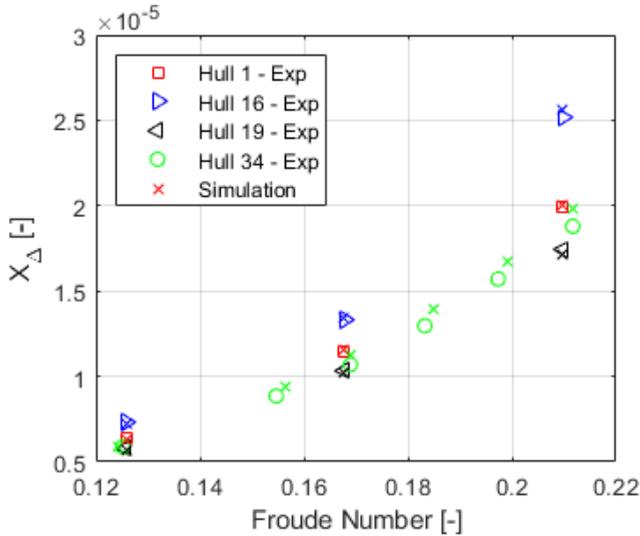
Figure 3.18.: Experimental and simulation results for calm water resistance.

form factor, $(1 + k)$, by experiment is quite problematic due to the possibility of flow re-laminarization along the hull. Simulations performed without the free surface would be a sensible further refinement of this study.

Table 3.15.: Form factor, $(1 + k)$, obtained from simulation and during experimental campaigns

| Hull | Simulation | | Experiment |
	Full-Scale	Model-Scale	Model-Scale
Parent	1.123	1.119	1.031
Hull #6 C_M +	1.132	1.100	
Hull #7 C_M-	1.115	1.083	
2nd Series parent	1.090	1.087	1.092
Mean	1.115	1.0970	1.062

Extrapolated values from model-scale simulations are on average 4 % larger than full-scale results (Figure 3.19). The form factor, $(1+k)$, is estimated from low speed runs at $Fn = 0.13, 0.17$. The form factor obtained from simulation is presented along with available experimental results in Table 3.15. The form factor obtained from full-scale simulation is approximately 33 % larger than the value obtained at model scale. This is in accordance with results presented in [28]. On the other hand, the form factor determined from experiment is about half as large as the value obtained from model-scale simulation. If the average $(1 + k)$ from experimental runs is adopted $((1 + k) = 1.047)$, the average discrepancy is 2 %.
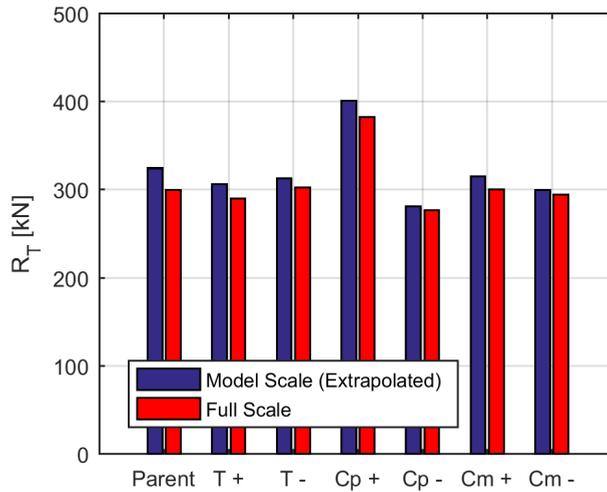
Figure 3.19.: Simulation results for resistance, showing extrapolated model-scale values and full-scale values. Simulation result.

Sailing Efficiency

As introduced under Chapter 2, the principal quantities of interest for the hydro-mechanics of wind-assisted vessels are the increase in resistance due to sideforce production, X_i, and center of lateral resistance (CLR), which is related to the maneuverability of the vessel under sail (see Figure 3.20). For the purposes of this discussion, the vessel effective draft and the behavior for the center of lateral resistance are presented in dimensionless form.

The 95% confidence intervals for maneuvering coefficients, the CLR, and the effective draft is rather large. For example, the number of available data points for fitting a third-order polynomial is limiting for the higher-order terms in the maneuvering equations. In light of the relative magnitude of the uncertainties associated with fitting the models, only linear terms will be considered here. Any trends observed for the non-linear component are insufficiently pronounced in light of the number of data points used for the third-order fit.

For modeling of wind-assist vessels, the resistance increase due to sideforce, X_i, is the relevant quantity. In subsequent analysis for the derivation of a regression model for wind assist vessels, the efficiency of a hull is also expressed as an effective draft T_e. This quantity is related to the slope of a linear fit through data for several leeway angles.

$$X_i = X - X_{\beta=0°} \tag{3.14}$$

This derived quantity is determined from simulation and experimental values and presented in Figure 3.21. This quantity is approximately one order-of-magnitude
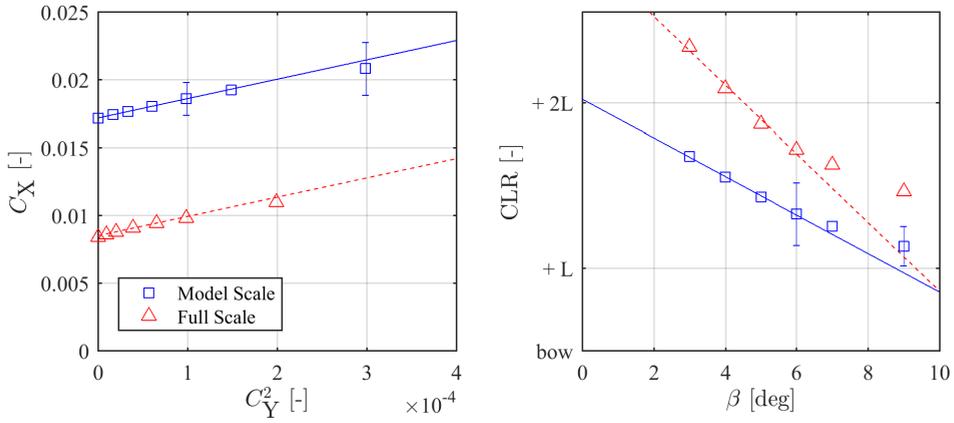
Figure 3.20.: Simulation results at full scale and model scale for effective draft and center of lateral resistance. Fitted models and simulation validation levels are shown
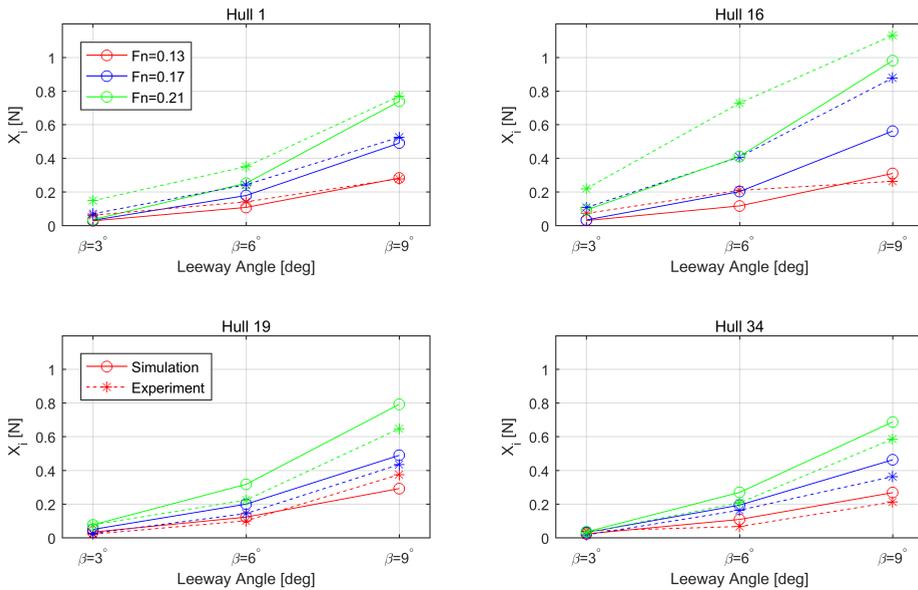
Figure 3.21.: Simulation and experimental results from the bare-hull validation set for resistance due to leeway.

83

smaller than the data used for this validation exercise. The validation uncertainty for resistance, when expressed as a percentage of X_i, lies between 25 % and 200 % (without considering the combination/correlation of errors for the values $X_{\beta=0°}$, X). Still, a good agreement for the trends in this data is observed, considering the order-of-magnitude of the data and the uncertainties present.

The comparison between simulation and experimental results is poorest for Hull #16, the fuller hull with small bilge radius. Stronger separation behavior at the bilge and a larger, more energetic wake of vortices is expected for this hull, and the simulation is apparently unable to capture the behavior completely. The effective draft T_e/T is shown for Hulls #6, #1, and #7 in Figure 3.20, which are the hulls with varying bilge radius. In fact the response for Hull #6 (C_M +) is somewhat improved. It is difficult to say more in light of the uncertainties present.

The data at 9° leeway (for maximum X_i) where the validation level for resistance is approximately 25 % of X_i, can be sufficient to determine the effective draft of the vessel. Though the magnitude of X_i is quite small compared to the uncertainties present for resistance, the linear modeling for the effective draft T_e permits an analysis that relies on the larger values only, for which the validation level is no longer prohibitive. If higher-order modeling is desired than the number of data points and the uncertainties in fitting will obscure any effect that may be captured.
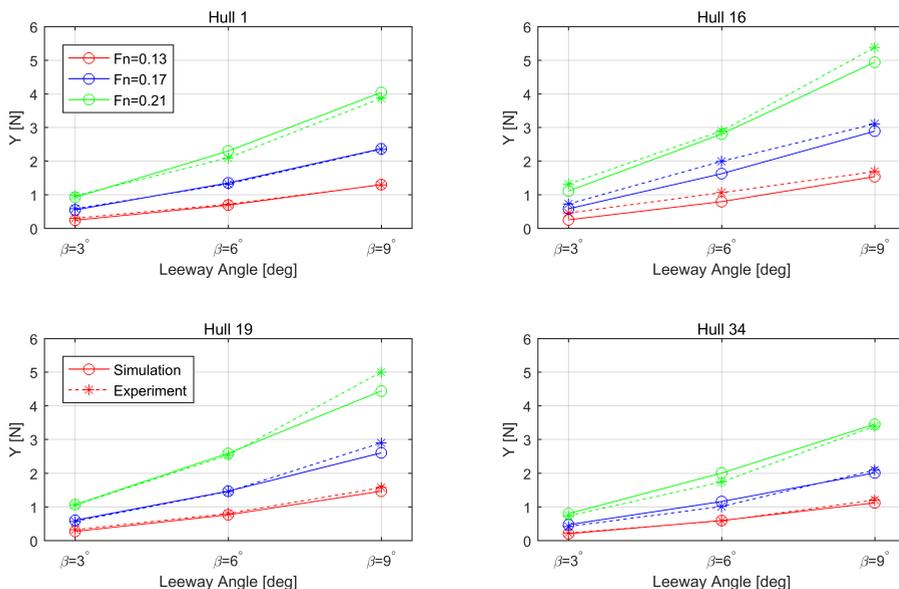
Figure 3.22.: Simulation and experimental results from the bare-hull validation set for sideforce.

Validation results for sideforce and yaw moment presented in Figures 3.22 and 3.23 show close agreement, with the exception of the sideforce for Hull #16. Here, a consistent under-prediction is observed for the hull where strong separation behavior is expected. As discussed above, it is likely that logarithmic wall modeling is
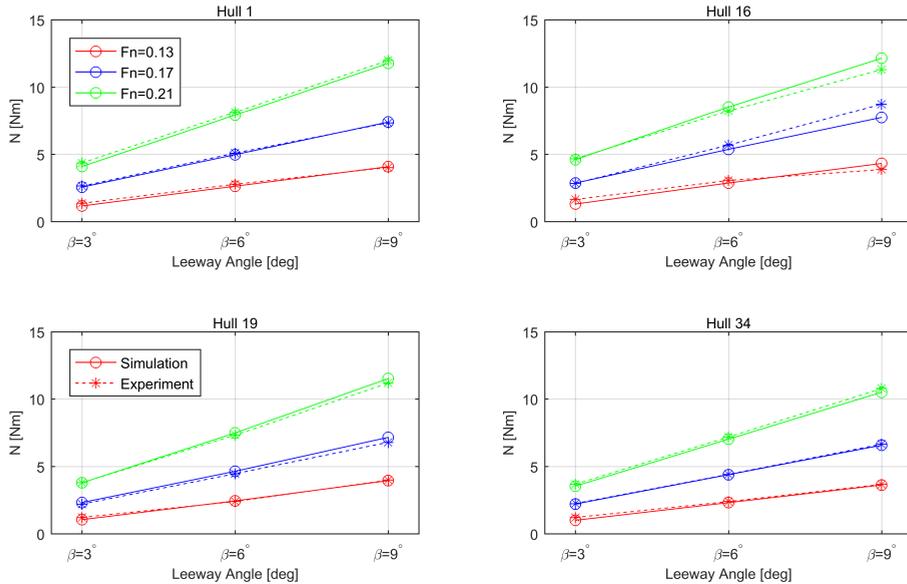
Figure 3.23.: Simulation and experimental results from the bare-hull validation set for yaw moment.

inadequate for the separation behavior associated with cross-flow drag, a sideforce component that should be quite strong for this hull. For reference, $r/r_{\text{ref}} = 1.26$ for sideforce Y for Hull #16. This appears to be a systematic error for all operating cases, raising the possibility of implementing a correction for the simulation value. For context, the comparison error is on average 33 % larger than the validation level for this hull. In contrast with the sideforce, the comparison error for yaw moment for Hull #16 is much smaller, yielding an $r/r_{\text{ref}} = 0.68$. A wall-resolved boundary layer modeling may be a more appropriate simulation approach, but the computational cost is deemed prohibitive in light of the volume of simulations anticipated.

Maneuvering Forces

Maneuvering coefficients for full-scale and model-scale simulation (Figure 3.25) are computed as described in Chapter 2, for which the hydrodynamic derivatives are non-dimensional (the notation Y'_β and N'_β has been omitted). β is in radians.

A normal non-dimensionalization for maneuvering forces is adopted, where the dynamic pressure q and the lateral area is used, as also applied to experimental results and for the DWA database (Chapter 4 and Appendices A and B).

For all hulls, the linear sideforce coefficient is markedly reduced, whereas the yaw moment is slightly increased. For both tendencies, this may be explained by considering that higher-Reynolds flows will be better able to negotiate adverse pressure gradients. However, considering the simulation validation levels included in Figure 3.24, only the disparity observed for the sideforce coefficient is meaningful.
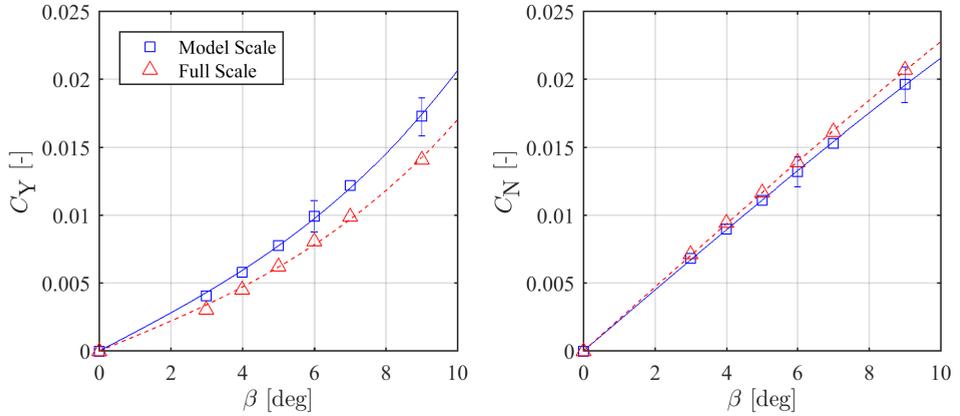
Figure 3.24.: Sideforce and yaw moment for full-scale and model-scale simulations of Hull #1, showing validation level for model-scale value. ($Fn = 0.168, \phi = 0°$).
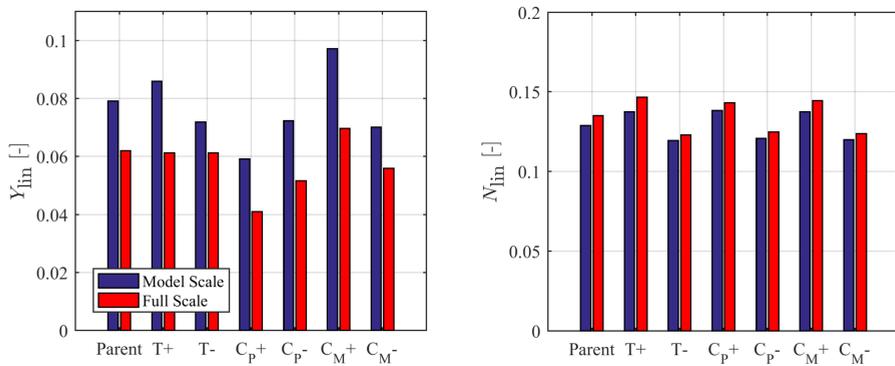
Figure 3.25.: Extrapolated model-scale simulations, presented alongside full-scale simulation values.

This in spite of the very good validation result for the yaw moment.

Vessel course keeping ability

The second quantity of principal interest for this modeling for wind-assist vessels is the center of effort for the distribution of lateral force, also known as the center of lateral resistance. The position of the CLR is determined as the quotient of the yaw moment and the sideforce (dimensionless form).

$$CLR = {}^{1}/_{L} \frac{N}{Y} \tag{3.15}$$

C_M+ Parent C_M-
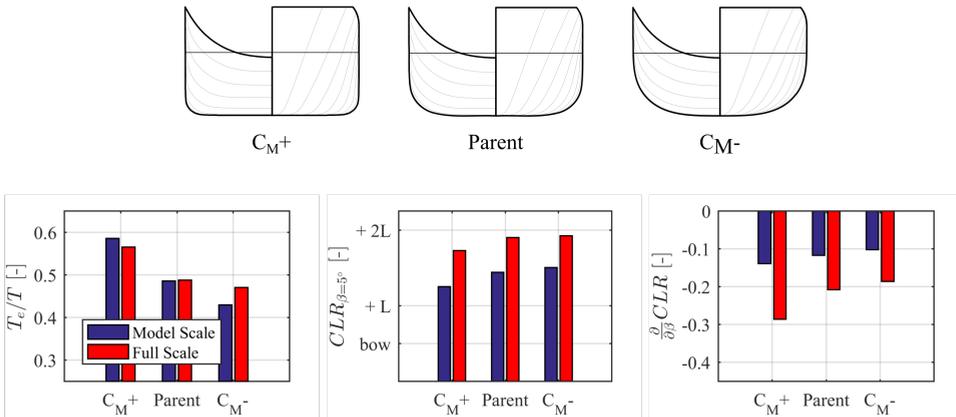
Figure 3.26.: Sailing performance based on model-scale and full-scale simulations for variations in hull bilge radius

The CLR, where a standard uncertainty propagation rule is applied, has a high sensitivity coefficient for the sideforce, Y, in the denominator. This returns uncertainties in the range of 25% for the CLR. Still, a pronounced, systematic effect is observed for both CLR and $\partial CLR/\partial\beta$ in Figure 3.26. Delayed separation at full-scale Reynolds numbers will serve to both suppress the sideforce and enhance the yawing moment, a combination that is rather detrimental for vessel course stability. This effect should be studied at full scale. A satisfactory result was obtained for the simulation validation of this quantity. For appended-hull cases in particular (discussed further in the next chapter), the CLR was very well predicted. The impact of these appendage types on the course-keeping for wind-assist vessels may be investigated with the RANS-CFD tool.

Conclusions

The implications of the validation result for resistance, sideforce, and yaw moment on these derived quantities has been outlined. The linear modeling for the T_e,

representing the efficiency of the hull, means that data at 9° leeway, for maximum X_i, can be sufficient to determine the effective draft of the vessel, though higher order effects may also be relevant. Following the discussion of Chapter 2, the linear modeling may be restricted (as in Figure 3.20) to a range of small angles that is representative of ordinary vessel operating conditions ($\beta < 6°$), or a more elaborate modeling may be used.

Simulation for wind-assist vessels is possible with RANS-CFD. Fluid flow around these ships is characterized by the occurrence of separation and by a wake of large vortices, both phenomena that likely challenge modeling assumptions made for the boundary layer and while averaging the Navier-Stokes equations. Modeling separation behavior and the evolution of vortices in the wake of a wind-assist ship while maintaining a computationally-affordable simulation methodology is the principal simulation challenge. In general, the validation level in this exercise was such that modeling errors cannot be distinguished from the uncertainties present in the exercise. One exception is a consistent offset in the comparison error for sideforce for Hull #16 (Figure 3.22), possibly caused by a failure of the logarithmic wall modeling to capture separation behavior for the sharp bilges of this hull. A correction for this systematic under-prediction may be appropriate. For context, the comparison error is on average 33 % larger than the validation level for this hull. The log-law modeling for the boundary layer is also not sufficient to capture separation behavior at the bilge keel. The shortcoming of the log-law boundary layer modeling was expected, but the added computational cost of wall-resolved boundary layer modeling was deemed prohibitive in light of the volume of simulations anticipated.

4

Appendages for Sailing Ships

A ferry operator in Scandinavia leverages public subsidies to install wind propulsors on several ferries.

An environmentally conscientious public is engaged and ferry traffic increases while operating costs are reduced.

In this chapter, sailing performance of ships fitted with diverse appendages is discussed. The main matter is a presentation of experimental results for bilge keels and center-line barkeels. The present study is an extension of the experimental work of [74].

Introduction

Wind assist, an environmentally-friendly auxiliary propulsion system for commercial ships, is identified by [73, 100, 106, 107, 122], among others, as a key intervention for the energy transition in the maritime shipping space. Wind-assisted ship propulsion promises substantial reduction in greenhouse gas emission in the near term. The technical and commercial viability of sailing for modern commercial vessels has been the subject of study since the OPEC oil crisis of 1973 (see for example [94]). At that time, progress towards real-world implementation in Japan was most advanced, culminating in a full-scale demonstration ship and 17 installed systems in the Japanese short-sea shipping fleet [125]. More recently, the researchers Fujiwara and Ueno have published a series of studies associated with a new (planned) demonstration vessel, the Wind Challenger [84], including testing of a 1/3 scale prototype of a collapsible solid wing sail [38], and a presentation of towing tank results for systematic variation in appendage configurations [74]. The present study, concerned with the sailing performance of bilge keels, is an extension of the experimental work of [74].

4.1. Course Stability for Sailing Ships

The ship hull creates hydrodynamic sideforce in reaction to the transverse component of the force created by the wind propulsor by adopting a leeway angle: an angle of attack for the hull. The sailing ship in operation with a steady leeway angle will also produce a strong hydrodynamic Munk moment about the yaw axis [75]. This destabilizing phenomenon arises when a slender body encounters an oblique flow, where the pressure distribution will tend to reorient the body perpendicular to the flow.

The theoretical pressure distribution associated with the Munk moment is presented in Figure 4.1, including an indication of the actual distribution for a viscous flow. Here, some portion of the under-pressure along the aft ship is attenuated by separation effects.

The center of lateral resistance (CLR) expresses the strength of the yawing moment in relation to the sideforce produced, as the centroid of the lateral load. It is measured with respect to the midship:

$$CLR = \frac{N}{Y} \tag{4.1}$$

The importance of vessel yaw balance; with CLR and $\partial CLR/\partial \beta$ as determinants for vessel course-keeping and directional stability, and key design constraints for sailing
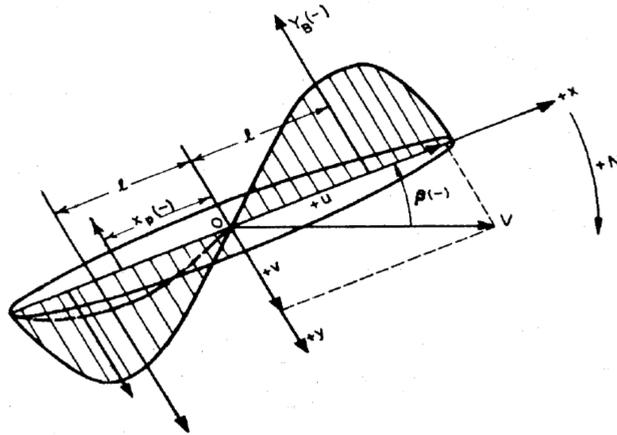
Figure 4.1.: Pressure distribution associated with Munk moment [67].

vessel hydrodynamics; has been discussed by [21, 66, 80] in their investigations of sailing yachts.

Behavior for the CLR is shown in Figure 4.2 for several appendage configurations: the bare hull (un-appended), the nominal appended hull design with rudder set for zero degrees, a short bilge keel in the most forward position, and a long bilge keel occupying the full length of the parallel midbody. The CLR is given for leeway angles β of three, six, and nine degrees.

First, observe the CLR for the un-appended hull, which lies more than half a ships-length ahead of the bow (shown only for nine degrees leeway), a consequence of the stronger development of the yawing moment—linear with leeway angle—compared against the sideforce, which includes a significant higher-order dependency for leeway angle. The CLR moves aft as the leeway angle increases, an effect that is driven by an increase in flow separation along the bilges. This effect is manifest as a rising contribution for the higher-order sideforce term in the sway equation, and an attenuation of the "Munk" moment for the yaw equation by flow separation along the vessel aft-body. Yaw balance, achieved by aligning the aerodynamic center of the wind propulsors with the hydrodynamic center (CLR) of the hull [21], is impossible.

For the rudder case, for zero degrees rudder angle, the CLR remains well ahead of the ship bow, a result also reported by [39, 97]. Any corrective action by the rudder will introduce a further resistance, the induced resistance of the rudder. The slender body modeling may be applied to the ships rudder. Under the modeling usually applied when deriving mathematical models for maneuvering simulations, interaction effects, such as end-plate, and free surface effects (which might become relevant for larger heel angles) are modeled with empirical coefficients.

The rudder for a conventional cargo vessel is dimensioned to work in the wash of the propeller, where it experiences a flow that is accelerated by the working of the
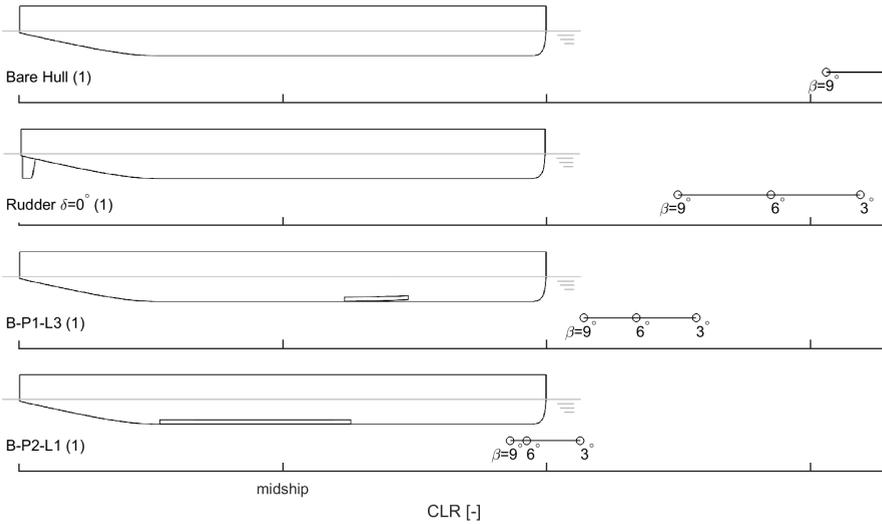
Figure 4.2.: Vessel CLR for several appended hulls. Experimental result.

propeller. When wind propulsors are able to contribute thrust and the main propulsor thrust is thereby reduced, the flow velocity over the rudder is correspondingly reduced. These two effects will compound: the destabilizing moment responsible for weather helm generally increases with aerodynamic thrust, and while the rudder can be used to oppose this destabilizing moment, it will become less effective as the main propeller thrust is reduced.

The third and fourth cases shown in Figure 4.2 are bilge keel geometries from the set of appendages variations tested in the present research. Both variations exhibit superior performance compared to the rudder case: the CLR is shifted aft to the close proximity of the bow. Also, the variation of CLR with leeway angle is reduced (the grouping of CLR values becomes more compact).

A minimal value for the variation for the CLR with leeway angle is written as minimization for the variation in CLR for leeway β, and heel ϕ:

$$min(\nabla_{\beta\phi}CLR) \tag{4.2}$$

The rudder angle δ_{Rud} may also be considered, as under the study of maneuvering of ships. If the linear maneuvering models that follow from slender body theory are substituted, the CLR will be constant for all leeway angles, at L/2 ahead of the ship bow. The variation for the CLR with leeway angle, $\partial CLR/\partial\beta$, is detrimental for vessel course keeping, where a minimal value is desired (a compact grouping for the CLR as in Figure 4.2. These attributes characterize a balanced and course-stable sailing ship.

4.2. Theoretical Background

The sailing performance for wind-assisted ships is synonymous with maneuvering forces for the steady drift condition, i.e. increase in resistance, lateral force (side-force) production, and yaw moment due to drift (leeway, β) angle. Whereas the analysis of experimental results will rely also on common decompositions from the study of ship maneuvering, the nomenclature of the study of sailing is adopted in the remainder of this paper.

In general, for previous work primarily concerned with the maneuvering of ships, the drift angles considered are larger than what is considered an operational leeway angle for wind-assisted vessels. One notable exception is the experimental and theoretical studies by [7, 8, 9], where a ship-like foil with low aspect ratio was towed at angles of attack including four and eight degrees. Wing geometries with square and rounded tips were tested, where the square tips were found to produce more lift and drag, which is understood as a result of a contribution by the cross-flow component arising due to separation effects that will be more pronounced for the sharp wing tip geometry. Similar results are reported in [69]. Finally, lift and moment coefficients calculated by the added mass impulse of [61] were found to agree well with the experimental results for rounded wing-tips, but less-so for the square tip profile. This finding implies that the hydrodynamic reaction is nearly linear for small angles, with a small viscous contribution arising from flow separation [10]. Similar results are reported in [59, 68, 109]. In common engineering practice, maneuvering forces are linearized for small angles.

The bilge keel is a common appendage type that is normally applied to regulate roll motion, in particular for slow-moving ships. The cross-sectional geometry for typical commercial ships results in a roll degree-of-freedom that is particularly susceptible to underdamped resonant behavior. The promotion of flow separation is the working principle of the bilge keel, whereby the viscous damping term in the roll equation is increased. The addition of bilge keels serves to excite the eddy-making process, which is only present for bare hulls at large roll angles. This viscous damping contribution has been the subject of many investigations, beginning with that of Froude in 1865 [36]. Important contributions in more recent times include the work of [49], who demonstrated that the eddy-making damping is nearly independent of Froude number, and [14, 33], who applied a vortex tracking method to the problem. For the conventional application, the bilge keel is subject to an oscillating flow induced by the roll motion of the ship. This unsteady process is normally investigated in U-shaped water tunnels, as in [33, 93], among others, or with an oscillating cylinder as in [114].

The present study for bilge keel and centerline keels in steady (oblique) flow corresponds to a special case of the unsteady process considered by previous researchers. Faltinsen reports results for the influence of bilge radius and bilge keel height that are reproduced in the present work. Faltinsen also addresses the scaling challenge inherent in any experimental investigation of bilge keels, where the working mechanism is Reynolds-number dependent. This issue is addressed further under experimental design in Section 2.1.

The hydrodynamics of sailing commercial ship-types is characterized by a system of shed vortices that separate from and pass around the hull, forming the wake of the ship. Vessel sailing behavior depends on the strength and separation location for these primary vortices and any secondary/counter rotating components. Many experimental and numerical investigations have explored the changes to the vortex system for varying angles of oblique flow, where again the flow angles considered are generally larger than would be considered operational leeway angles for a wind-assisted ship. From the oil film experiments of [14], to detailed measurements of the vortex wake by [72], to state-of-the-art numerical work such as the detached-eddy Reynolds-averaged Navier-Stokes simulations by [1, 17, 124], the flow patterns have been well documented. As described by [72], the topology for the wake of a ship sailing with a leeway angle is characterized by several vortices, of which the forebody keel vortex (FKV), forebody bilge vortex (FBV), and forebody side vortex (FSV) are relevant here (indicated in Figure 4.3).
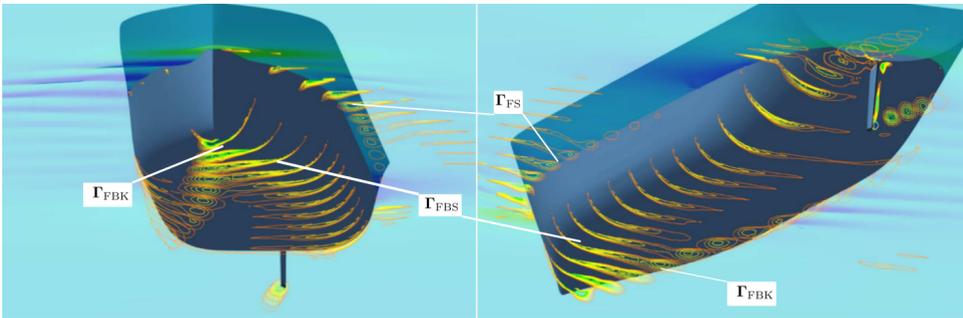
Figure 4.3.: Flow visualization of vortex system showing fore and aft separation locations. The forebody keel vortex [FBK], the forebody bilge vortex [FBS], and the free surface vortex [FS] are indicated. Also a distinct tip vortex is visible at the rudder. The rudder produces 30% of sideforce for this operating condition (no modeling for propeller wash). Hull #1, $\phi = 0°$, $\beta = 6°$, $Fn = 0.126$, δ_{Rud} =3°. Simulation result.

As discussed above, the strength and separation location of the components of the vortex wake will vary with the leeway angle. For sailing ships, placement of bilge keels or centerline keels raises the possibility of specifying the separation location for components of the vortex wake, thereby manipulating the topology of the vortex system. Desirable effects, when attempting to influence the vortex wake in order to improve the sailing performance of the ship, are the promotion of the higher-order sideforce component and the attenuation of the Munk yawing moment.

Finally, sideforce production by the sailing ship, including possible corrective action with the rudder, will introduce an added resistance to the ship arising due to a dissipation of energy in the vortex wake of the ship. Following theories for low-aspect planforms [45, 61], this induced drag may be significant for commercial ships, meaning that the thrust delivered by a wind propulsor might well be overwhelmed by this increase in resistance. Though the flow mechanisms only vaguely resemble the Prandtl lifting-line and the associated derivation for the induced drag [86], accounting for energy loss in shed vorticity is especially relevant

for the present application.

Following the analysis of sailing yachts by [40], the resistance increase due to sideforce production is modelled as an effective draft, T_e [41], which is a metric for the sailing efficiency of the hull. The quantity T_e is related to the effective aspect ratio, representing the span of a wing profile with equivalent behavior for the induced drag. The modelling for effective draft has pragmatic appeal, but it must be noted that significant liberties are taken when treating a ship hull as a Prandtl wing. For ship geometries, flow characterized as 'tip effects' in Prandtl's theory, where streamlines curl around the end of the foil in response to the pressure gradient, will influence the flow pattern over the entire span (or depth of the hull). Furthermore, a commercial hull form does not present a well-defined trailing edge, which introduces ambiguity for the definition of a circulation as it is not clear where (or whether) a Kutta condition should be applied. Nevertheless, the flow mechanisms responsible for the development of sideforce - the separation of several well-defined vortices into the wake of the ship - are dissipative processes that introduce a further resistance. This resistance penalty associated with sideforce production is an indication of the sailing efficiency of the ship, and is reported as the effective draft.

Present Experiments

This publication presents experimental results for the sailing performance of low-aspect ratio appendages: bilge keels and centerline keels. The experimental data is made publicly available to support further academic work and the eventual commercial uptake of wind-assist technology for commercial shipping. A discussion of main effects observed is included in the present publication. A detailed description of the model and appendage construction can be found in Section 4.3, along with a description and motivation of the experimental design. The model and appendage geometry is included at the end of this manuscript. Data reduction formulas are detailed in Appendix A.2, including an uncertainty assessment for measured and derived quantities. Experimental results are presented and discussed in Section 4.4. Due to the large volume of data collected, the discussion is restricted to key effects. All quantities derived in this analysis are included in the data set, available in an online archive [115].

4.3. Methodology

Experimental Design

The objective for the experimental campaign is to collect data to facilitate a modelling for the influence of bilge keels on the sailing performance of a wind-assisted ship. Bilge keel height and position are identified as the primary independent variables for the experimental design. Following the discussion of low-aspect lifting surfaces provided in Section 4.2, it is expected that the position of the bilge keel leading edge will dominate the hydrodynamic response. The appendage variants

are arranged into sub-sets with constant aspect ratio to test to what extent this class of appendages acts as a conventional lifting surface. The behavior for such an appendage, well-described by circulatory lift models, is expected to correlate with the appendage aspect ratio, defined as $AR = 2h/l$. The appendages variations were located along the parallel midbody insofar as possible. Bilge keel position with respect to bare-hull separation phenomena is also of interest. The appendage position P1, located at the forward shoulder for Hull #1, and P5, located at the aft shoulder, are expected to interact directly with bare-hull separation phenomena.
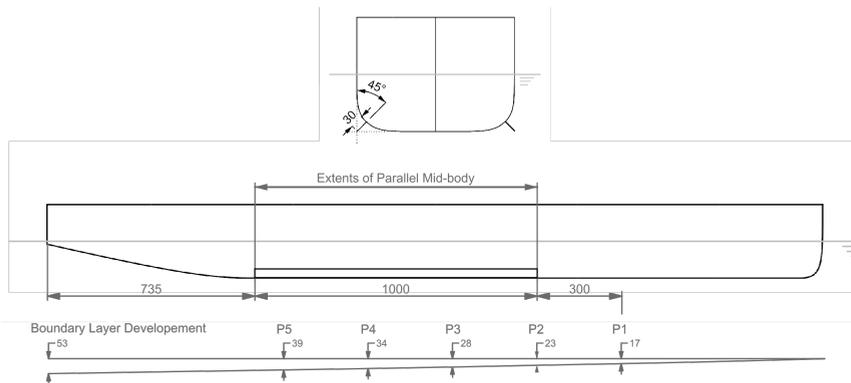
Figure 4.4.: Bilge keel geometry B-P2-L3-H3 (1). The estimated model-scale boundary layer development is given in mm

The instigation of flow separation in the boundary layer is the working principle, and a principal challenge in experimental design is the efficacy of the bilge keel appendage in a model-scale boundary layer. The bilge-keel behavior within the rather-to-thick model scale boundary layer, and the subsequent interaction between the vortex system and the boundary layer, pose elemental difficulties in the interpretation of these results for the full-scale application. A simple geometric scaling for the bilge keel would not be appropriate, as the resulting model-scale bilge keel height would remain quite close to the inner region of the boundary layer, extending less than one third through the total boundary layer thickness (determined using δ_{99}, according to the $1/5$ power law for a turbulent boundary layer thickness). The nominal bilge keel height used in the experiment is chosen such that the bilge keel extends unambiguously through the entire thickness of the boundary layer (shown also in Figure 4.4). A set of bilge keels with systematically varied bilge keel height was tested to control for this scaling effect, where it is understood that the flow mechanism of interest is Reynolds-number dependent.

The bilge keel and centerline keel variations are defined to test for the behavior for varying centerline keel appendage length and appendage position, and to study the difference with performance with identical bilge keels and centerline keels. Appendage variations are tested on three hull models: Hull #1 (parent hull for the Delft Wind-Assist Series) Hull #16, which is derived from Hull #1 by increasing the
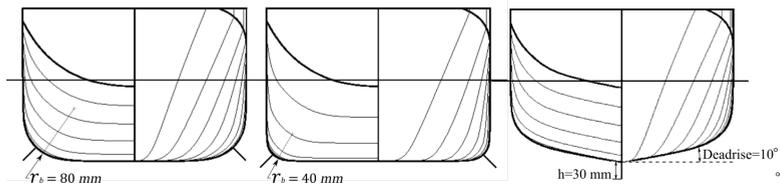
Figure 4.5.: Bilge keel B-P2-L1-H3 on Hull #1 (left) and Hull #16 (center), and C-P2-L1-H3 on Hull #34 (right).

prismatic and midship coefficients, and Hull #34, which is derived from the Ecoliner parent (Hull #1) by adding 10° deadrise angle while keeping the same prismatic coefficient and draft. Hull #16 has an elongated parallel midbody (1300 mm compared with 1000 mm for Hull #1) and a reduced bilge radius (by 50%). The centreline keel variants are tested on Hull #34, for which the R_{b}/T is somewhat increased compared with Hull #1. The following nomenclature is adopted for the appendage variants: each bilge keel variant is labeled with four numbers, specifying the longitudinal position, keel length and keel height, and finally, the hull number. For example, the bilge keel case in Figure 4.4 is B-P2-L3-H3 (1) (Bilge keel, Position 2, Length 3, Height 3, Hull #1). The bilge keel occupies the full extent of the parallel mid-body. Special cases are designated with a single number as BS1, BS2. All appendages variations and main particulars for the hulls are provided in Figures 4.19 and 4.20 and Tables 4.2 and A.7 at the end of this manuscript.
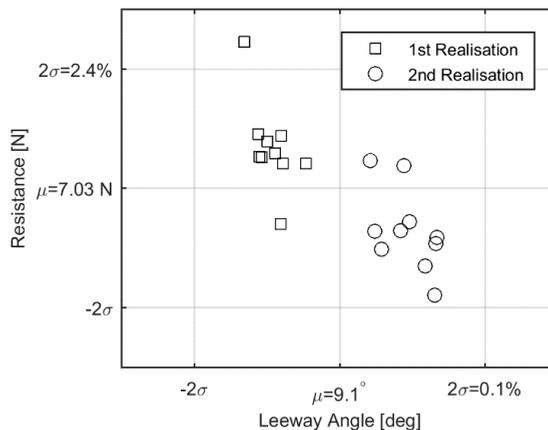
Figure 4.6.: Complete set of 20 repeat measurements for resistance for B-P3-L1-H3 (16)

The experimental campaign was conducted in the large towing tank at the Delft Ship Hydromechanics Laboratory at Delft University of Technology. The experimental setup was designed to facilitate quick and precise arrangement for each appendage variation. This choice was motivated by the small magnitude for the

quantities of interest, a high sensitivity to model alignment and geometric errors, and an experimental design that called for multiple variations for the appendage geometry. The hexapod and six-degree-of-freedom measurement frame are used in the same configuration as during the validation experimental campaign [115], and grids are tested for fixed trim and sinkage. Each hull model was fitted with an alignment frame designed to enable repeatable, precise mounting of the model to the six-degree-of-freedom measurement frame. The position of the model is recorded using a Certus ™optical tracking system. All signals are filtered with a low-pass filter set to 100 Hz before sampling to prevent aliasing. The signal is sampled at a frequency of 1000 Hz and written to disc. An average is made over a 40-second measurement, which is made after the carriage acceleration is complete and 10 seconds have passed to allow for the flow to reach a steady condition. The nominal rest period between runs was 20 minutes. All bilge keel variants were towed at a Fn number of 0.21. The nominal testing matrix for each bilge keel variant was defined as a combination of an equal number of positive and negative leeway angles, and the test program was arranged so that positive and negative leeway angles and any repeat runs were interspersed regularly. The first run of each day, and the first run after a weekend, was marked in the measurement log.

The bilge keel geometry and bilge keel position for each variant were realized with care. The assembly of appendage B-P3-L1-H3 (16) is shown in Figure 4.7. The reproducibility of the appendage geometries was tested by rebuilding and retesting bilge keel B-P3-L1-H3 (16) at the end of the experimental campaign. A set of repeat measurements was made for both realizations, as shown in Figure 4.6 for the resistance. Though a distinction between the realizations of the geometry is evident, the grouping of the results is quite close. The 95% confidence interval for the complete set of 20 repeat measurements is 2.5 %. A further discussion of the assessment of the geometric bias and other uncertainty components is given in Appendix B.

Bilge keel B-P3-L1-H3 (16)

(a)

1mm slit cut into bilge of model

(b)

Bilge keel assembly

(c)
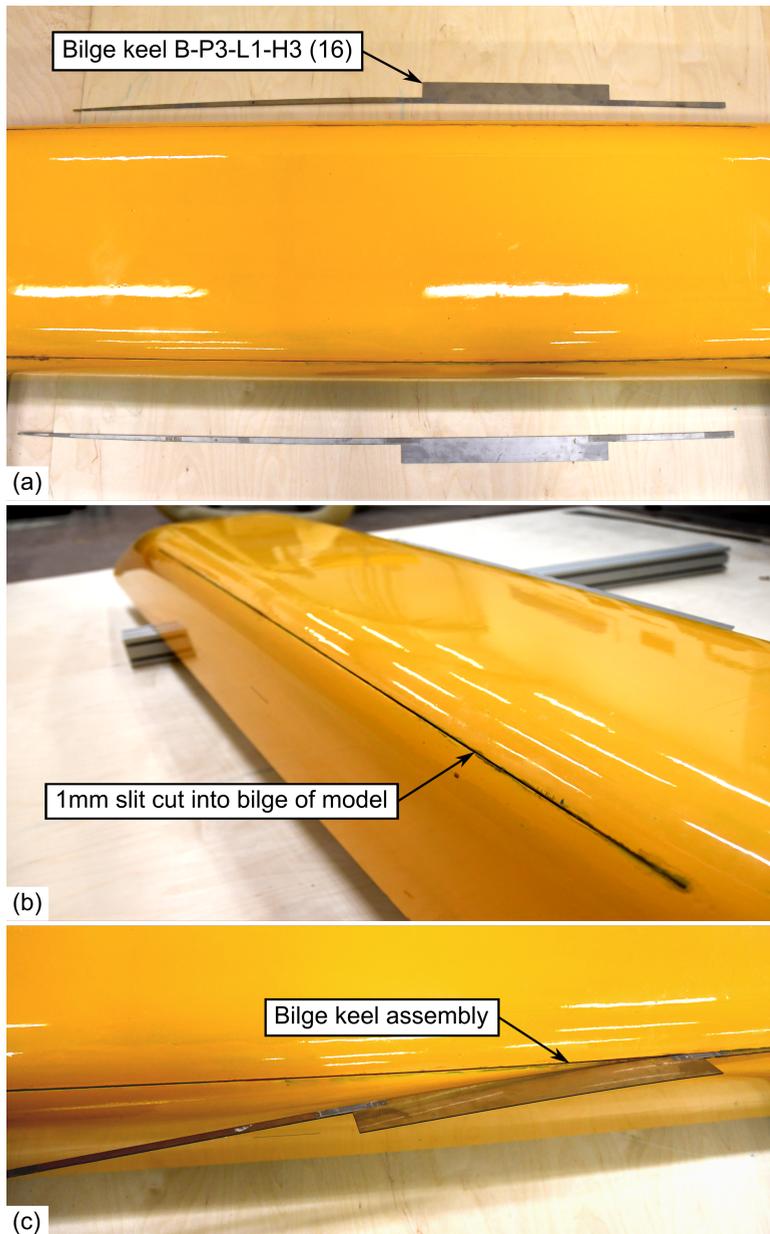
Figure 4.7.: Assembly of bilge keel B-P3-L1-H3 (16)

4.4. Discussion of Sailing Performance

In the following discussion of the effective draft and CLR for systematic variations for bilge keel height (span), keel position, and keel length, the presentation of results includes absolute and relative values. The combination of uncertainties in measured quantities, and the added uncertainty associated with fitting, results in large uncertainties. For relative quantities in particular, this must temper any conclusions made about trends in the data. Only linear coefficients for sideforce and yaw moment are considered in relative terms (Equation (4.3)). As a general statement, the substantial uncertainties as indicated in figures must temper any conclusions made.
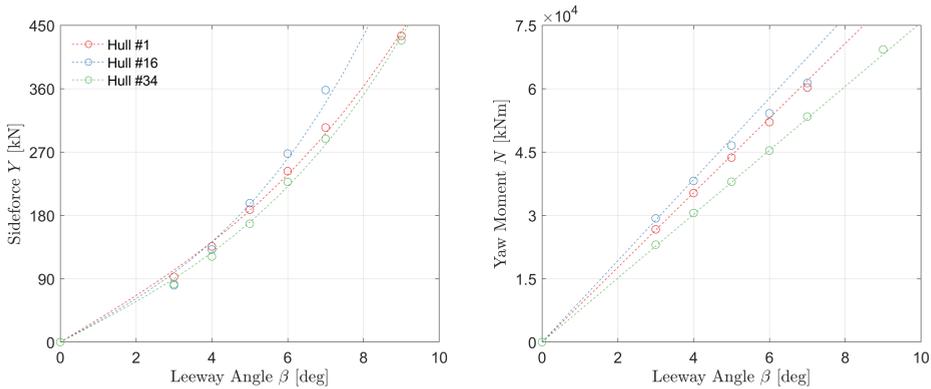
Figure 4.8.: Bare-hull sailing performance for Hulls #1, #16, and #34. (left: sideforce, right: yaw moment) Fn =0.21, ϕ=0°. Simulation result.

Table 4.1.: Sailing performance for un-appended hulls

	T_e/T [-]	Y_β [-]	$Y_{\beta\beta\beta}$ [-]	N_β [-]	$N_{\beta\beta\beta}$ [-]
Hull #1 – Bare	0.59	0.09	1.37	0.13	−0.25
Hull #16 – Bare	0.62	0.11	1.67	0.14	−0.68
Hull #34 – Bare	0.82	0.088	2.61	0.12	0.03

$$\Delta Y_\beta = Y_\beta - Y_\beta|_{\text{Bare}} \tag{4.3a}$$
$$\Delta N_\beta = N_\beta - N_\beta|_{\text{Bare}} \tag{4.3b}$$

Bilge keel variants were tested on two hulls – Hull #1 and Hull #16 – where Hull #16 is a much fuller ship and has a 50% smaller bilge radius. Bare-hull sailing performance for Hull #16, with lengthened parallel midbody and smaller bilge

radius, is improved compared with Hull #1 for all metrics of sailing performance (see Table 4.1). In particular, the non-linear component of both sideforce and yaw moment are increased (negatively in the case of the moment). Hull #34 shows improved performance for the yaw coefficients in particular, as well as the effective draft. The uncertainties for this hull were somewhat larger due to a manufacturing error (see Section 4.3). The bare hull value is indicated in the figures throughout the subsequent discussion of results.

As expected, the introduction of bilge keels increases the resistance at zero degrees leeway compared with the bare-hull value (Figure 4.9a). For bilge keels of varying height, the increase is in proportion with the increased surface area. In the results for the resistance, an asymmetry for the positive and negative leeway angles is evident. It was not possible to discern an alignment fault based on the resistance measurements alone.
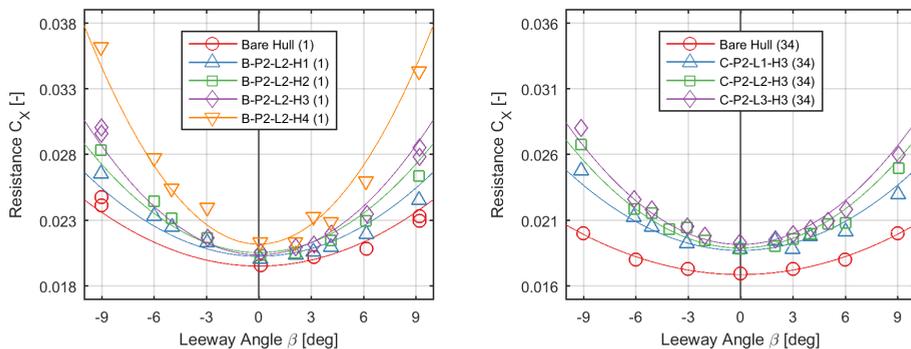
(a) Measured resistance data and fitted maneuvering model for variations in bilge keel height (Hull #1).

(b) Measured resistance data and fitted maneuvering model for variations in centerline keel length (Hull #34).

Figure 4.9.: Vessel resistance for systematic variations in centerline keel length (left) and bilge keel height (right).

The bias indicated by the asymmetry for resistance values at leeway, observed in Figure 4.9, is much larger than the alignment bias (see Figure 4.6). This effect is persistent in the remainder of the data set for Hull #34 (Figure 4.9b), and less so for hulls #1 (Figure 4.9a and #16, suggesting that the fault has two sources. On one hand, there is apparently a misalignment in the measurement frame. Also, Hull #34 was constructed with a geometric fault (the milling machine coordinate system was skewed by approximately 3 mm over 2.7 m model length). The resistance, and the induced resistance (resistance arising due to sideforce production in particular), presented the greatest measurement challenge for the experimental system.

Four sets of appendages are plotted in Figure 4.10, where the x-axis has been scaled with the bilge radius. The set for pure variations in appendage height is displayed as filled black circles. In Figure 4.10 for the effective draft, a linear fit is added to underscore the nearly perfect correlation between appendage height and effective draft. Two sets for constant bilge keel aspect ratio are displayed as red triangles. Finally, the appendage geometry B-P2-L2-H3, which was tested on both

hulls, is plotted as open black circles. Figure 4.11 contains results for variation in appendage position, tested on Hull #1 and Hull #16.
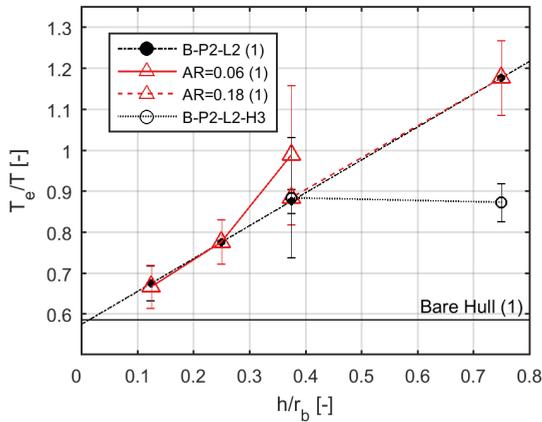
Figure 4.10.: Effective draft for variations in bilge keel height, aspect ratio, and h/R_{b}.

Two appendage sub-sets with constant aspect ratio are defined to test whether this class of appendages behaves as a normal lifting surface, for which the effective draft is expected to correlate with the appendage aspect ratio. Instead, the effective draft is nearly perfectly correlated with the results for variation in appendage height, a point that is underscored with a linear fit to the set B-P2-L2 (1) in Figure 4.10. The data reduction adopted for this presentation of results does not consider the varying planform area of the appendage. For this set, a scaling by the appendage planform area is equivalent to scaling by appendage height, meaning that this result is a constant response for effective draft. A similar scaling applied to the results for constant aspect ratio was attempted, but further analysis is needed.

A final set was defined for a variation in the ratio keel height to bilge radius, h/R_{b}. The bilge keel B-P2-L2-H3 was tested on both Hull #1 and Hull #16, for which the bilge radius decreases by a factor of two (see Figure 4.5). For both the quantities presented, and for the other maneuvering coefficients, the sailing performance is apparently independent of this ratio. It should be noted that the Hull #16 bare hull value for $Y_{\beta\beta\beta}$ is 1.67, and T_e/T =0.62 (see Table 4.1).

The effective draft is presented in Figure 4.11, including the bare-hull value for reference. For both bilge keels and centerline keels, the trend is well-evident: the coefficient appears to vary in proportion with the appendage length, a constant response when scaled by the appendage planform area. Whereas the sailing efficiency for a hull fitted with bilge keels increases by at least 50% over the bare hull value, and this value appears to increase for the longest bilge keel (L3), the centerline keel does not appear to improve the sailing efficiency of the hull. It must be noted that the uncertainty for the effective draft for results of Hull #34 was such that these results were omitted from the journal publication. The effective draft as a function of bilge keel position does not appear to vary, especially in light of
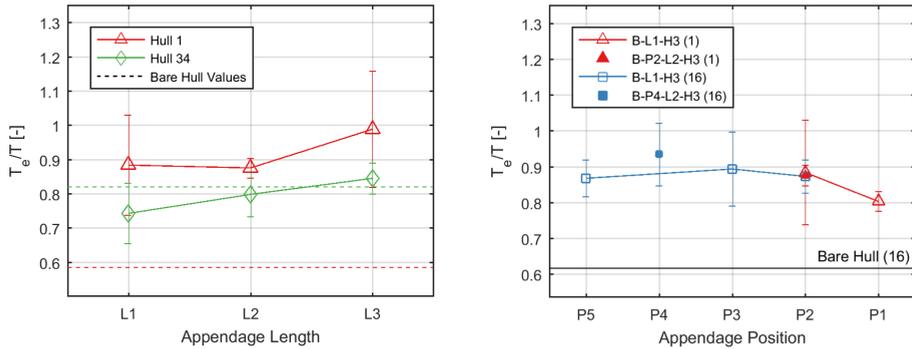
Figure 4.11.: Behavior for systematic variations in keel length (left) and position (right).

the uncertainties present. The results for Hull #1 suggest that the forward keel positions are detrimental for the sailing efficiency.
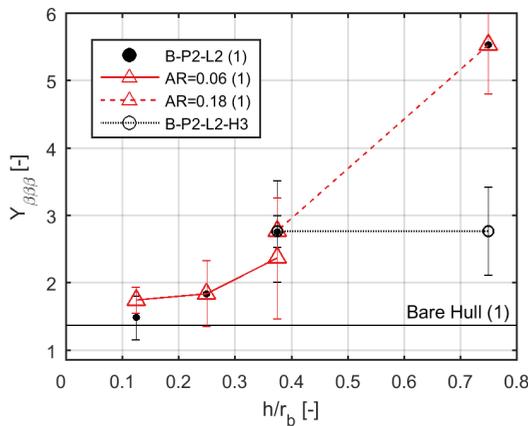
Figure 4.12.: Non-linear sideforce coefficient variations in bilge keel height

   As outlined under experimental design, the first objective for the set of varying appendage heights is to ascertain that the bilge keel behaves as expected within the model-scale boundary layer. It is understood that the bilge keel should act to promote flow separation along the leading bilge, contributing to the non-linear sideforce term. In Figure 4.12 for the non-linear sideforce coefficient, the response in the neighborhood of the nominal bilge keel height for the experiment (H3)— corresponding to h/r_b=0.375—is nearly linear with keel height, a result also reported by [33], whereas the behaviour at small values of h/r_b appears to approach the bare hull value asymptotically. Bilge keel H1 (h/r_b=0.11) is a geometric scaling for a representative full-scale bilge keel (h=0.5 m at full scale). This bilge keel height does not excite the expected response for the non-linear sideforce term.
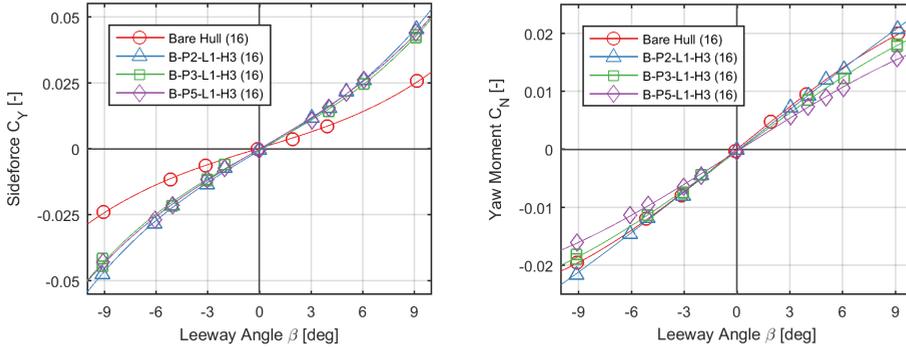
Figure 4.13.: Measured sideforce data and fitted maneuvering model for variations in bilge keel position.

The measured data for sideforce and yaw moment are presented in Figure 4.13, including fitted maneuvering models. The yawing moment is most influenced by variations in appendage position, whereas the sideforce is nearly insensitive. It is interesting to note the response for appendage P2-L1-H3 (the most forward position shown) in yaw, for which the non-linear behavior is reduced compared with the bare hull.
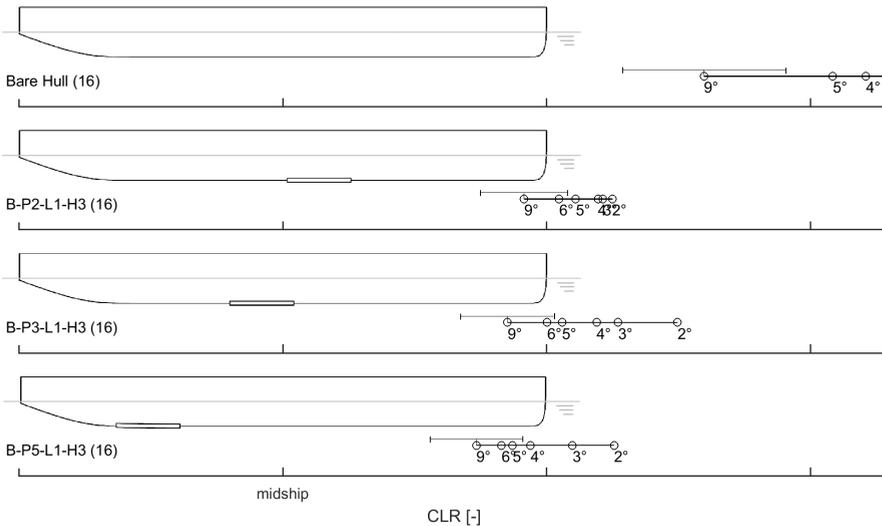
Figure 4.14.: The center of lateral resistance for variations in appendage position. The associated uncertainty for nine degrees leeway is indicated for reference

The corresponding vessel CLR is given in Figure 4.14 for the same bilge keel variations. Approximately similar behavior is observed for keels located at P3 and P5, where the CLR values for the bilge keel P5-L1-H3 are shifted aftward. The result

for the CLR of the bilge keel at P2 is exceptional in that the grouping for varying leeway angles is much more compact than the other cases. A small variation for CLR with leeway angle indicates that the distribution of lateral force along the hull is steady as the leeway angle changes. Following the work of [47], the separation location for the bilge vortex associated with the non-linear sideforce term will shift along the leading bilge according to the leeway angle. Variation in CLR with leeway angle is in part due to this effect. A second phenomenon at play is the attenuation of the Munk yawing moment by separation effects along the aft body. Both effects are associated with the separation of bilge vortices, and are confined to larger leeway angles for the bare hull case.

(a) Linear yaw moment N_β

(b) Non-linear yaw moment $N_{\beta\beta\beta}$
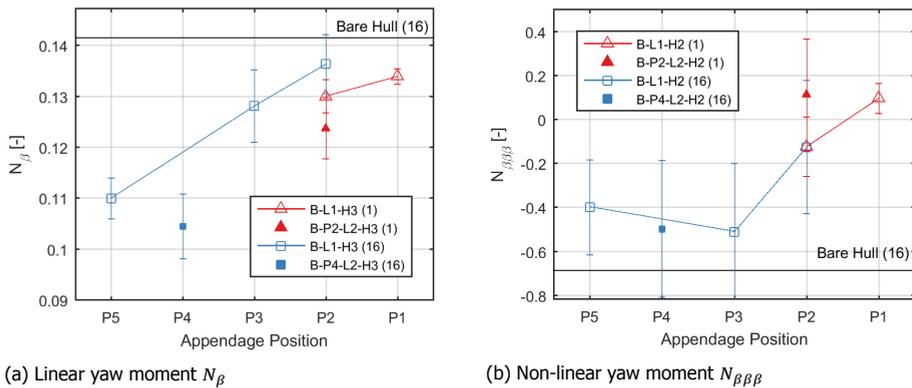
Figure 4.15.: Yaw coefficients for variations in bilge keel position

The linear and non-linear maneuvering coefficient for the yaw moment is plotted in Figures 4.15a and 4.15b, together with the bare hull value for Hull #16 as reference. Besides the results for the appendage set presented above, data for appendages tested on Hull #1 are included, as well as two cases for appendage length L2 with solid markers. The trend observed in the raw data is clearly evident here: as the bilge keel is moved aft, the linear yaw moment is reduced. The results for the non-linear coefficient are subject to the same qualifications as for the non-linear sideforce above, besides which, the non-linearity for the yaw moment is a rather small effect. Nevertheless, the response is markedly different for forward keel positions P1 and P2 (for reference, the Hull #1 bare hull value for $N_{\beta\beta\beta}$ is -0.25).

The vessel CLR for the deadwood cases is presented in Figure 4.16. The increase in aft lateral area clearly shifts the CLR aft, a result that is well understood from previous work by Skogman [97] and others. For the deadwood cases of Figure 4.16, the CLR was very well predicted by simulation. The impact of these appendage types on the course-keeping for wind-assisted vessels may be investigated with a RANS-CFD tool [118].
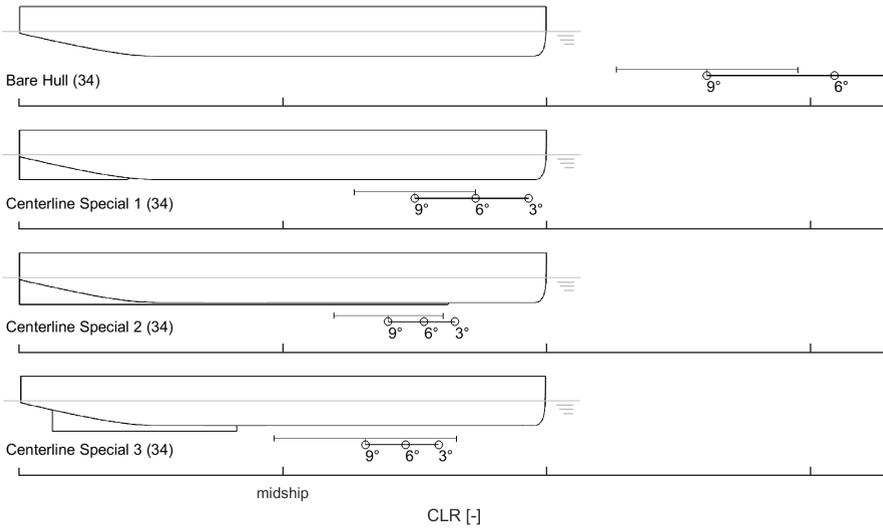
Figure 4.16.: The center of lateral resistance for deadwood variants (CS1-CS3). The associated uncertainty for nine degrees leeway is indicated for reference.
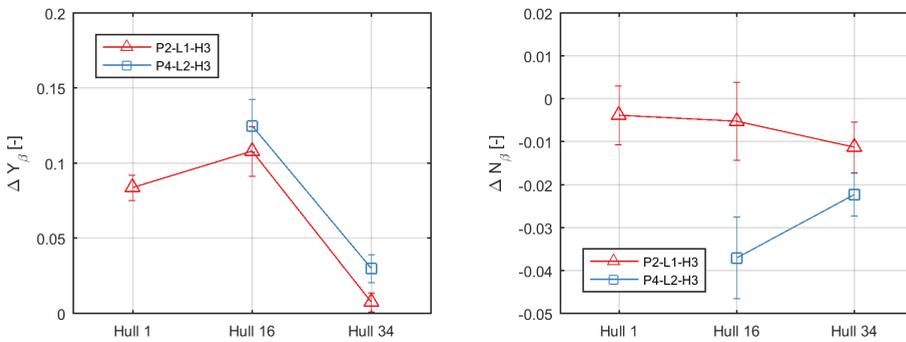
Figure 4.17.: Relative response for linear sideforce and yaw moment coefficient for identical bilge keel and centerline keel variants.

Conclusion

The working principle for bilge keels is the promotion of flow separation. For sailing ships, placement of bilge keels raises the possibility of specifying the separation location and of inducing flow separation at leeway angles for which separation would not yet occur for the un-appended hull. Results for small keel heights affirm the dimensioning adopted for the test, where a simple geometric scaling would not be appropriate. The behaviour observed in the neighborhood of the nominal height, set such that the keel extends unambiguously through the entire height of the model-scale boundary layer, conforms to results reported by [33]. There is a linear relationship between bilge keel height and the coefficients for sideforce and sailing efficiency (indicating a constant behaviour if the appendage planform area is considered). In contrast with the bilge heel height, bilge keel position influences both the linear and non-linear coefficients for the yawing moment, rather than the sideforce strength. One exceptional result to highlight is the keel at position P2 (approximately midship), for which the variation in CLR with leeway angle is markedly reduced. The yaw response is nearly linear for appendages at positions P1 and P2 (linear behaviour for both sideforce and yaw would return a CLR with no variation for leeway angle). Response for bilge keel length is restricted to sideforce, whereas yaw moment is unaffected. As for the bilge keel height, the linear response for the linear coefficient implies a constant response if the appendage planform area is taken into account.

Bilge keels and centerline keels are categorized as boundary-layer appendages, where the working principle is the promotion of flow separation in the vessel boundary layer. The appendage typology is shown to mitigate the strong Munk yawing moment that is characteristic for wind-assisted commercial vessels, and to promote the non-linear sideforce component. Also, the sailing efficiency (resistance increase due to sideforce) of a hull fitted with bilge keels or centerline keels, presenting a sharp tip profile to the lateral flow, can be improved dramatically. An optimal arrangement of bilge keels will result in a pattern of separation that is beneficial to the course-keeping of the vessel and its sailing efficiency. Experimental results from towing tank experiments for the sailing performance of bilge keels, centerline keels, and other special typologies have been presented. The bilge keel, already commonplace in the naval architecture of ships, finds new purpose as an effective appendage for wind-assisted commercial ships.

Acknowledgements

Table 4.2.: Main particulars for the Ecoliner Parent hull.

	Full Scale	Model Scale $\alpha = 50$
LOA [m]	138	2.76
Beam [m]	18	0.36
Draft [m]	6.5	0.13
Displacement	11 896 t	92.8 kg
C_B	0.719	0.719
C_P	0.764	0.764
C_M	0.942	0.942
LCB [%]	50.13	50.13
Whetted Surface m^2	3.293	1.312

Hull #1: Parent hull for First Series

Hull #16: Full-bodied with sharp bilges

Hull #34: Parent hull for Second Series
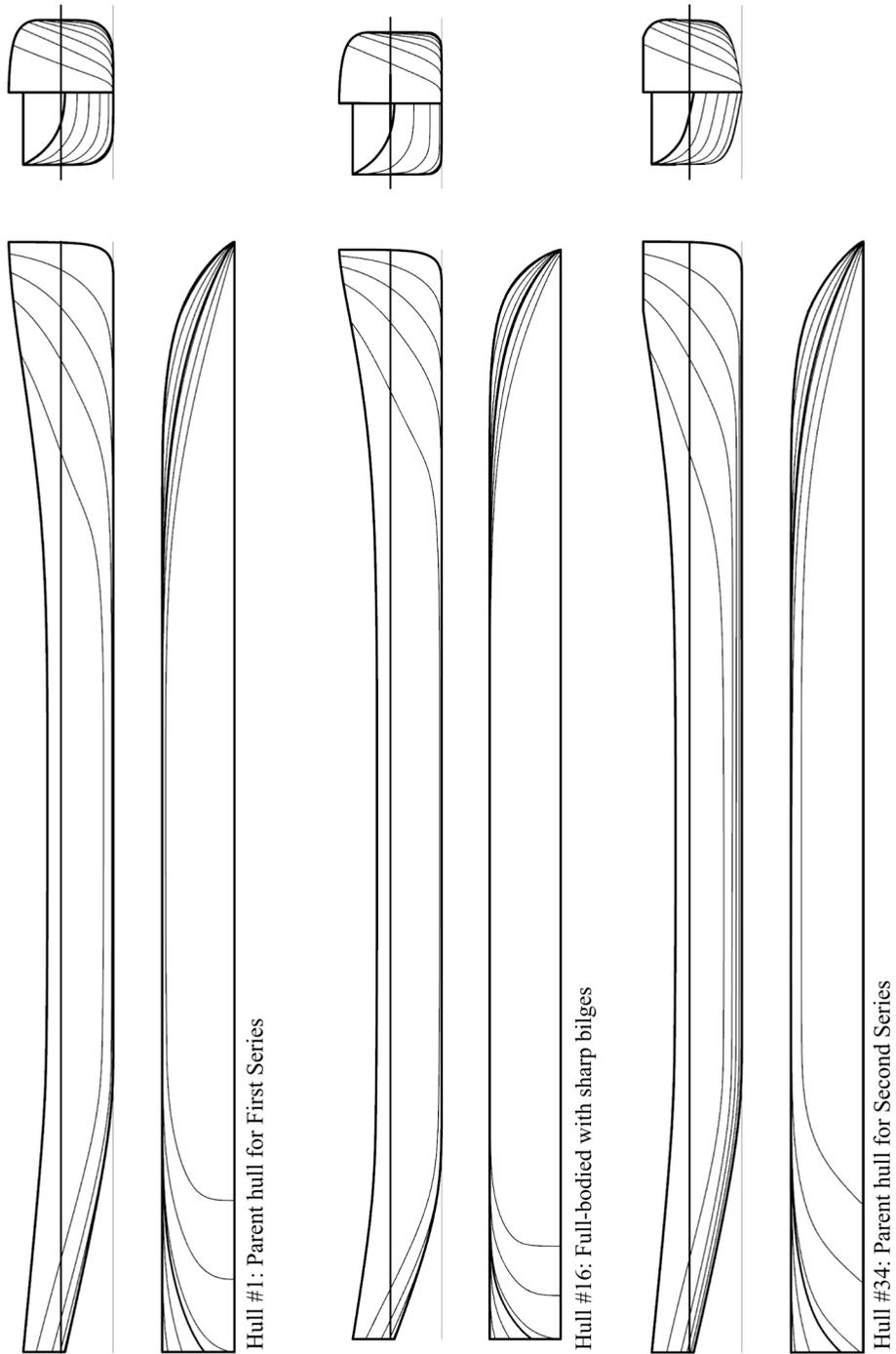
Figure 4.18.: Linesplan for Hulls #1, #16, and #34.

Hull 1

Extents of Parallel Mid-body

735   1000   300

P5   P4   P3   P2   P1

B - P2 - L1 - H3 (1)

B - P2 - L2 - H3 (1)

B - P2 - L3 - H3 (1)

B - P1 - L1 - H3 (1)

B - P2 - L2 - H4 (1)

B - P2 - L2 - H2 (1)

B - P2 - L2 - H1 (1)

B - P2 - L1 - H1 (1)

Bilge Special 1 (1)

Bilge Special 2 (1)

Hull 16

Extents of Parallel Mid-body

585   1300   150

P5   P4   P3   P2   P1

B - P2 - L1 - H3 (16)

B - P3 - L1 - H3 (16)

B - P5 - L1 - H3 (16)

B - P4 - L2 - H3 (16)
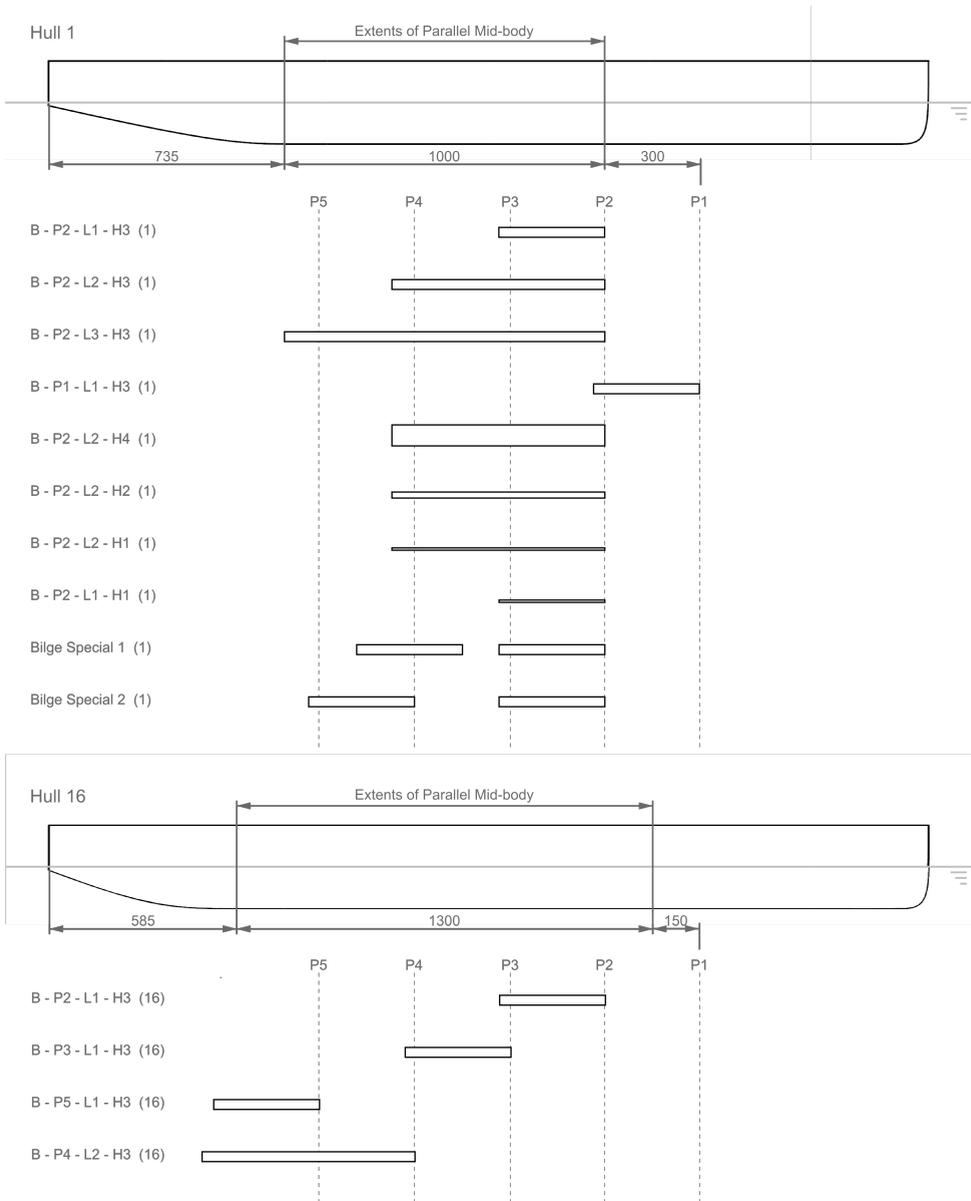
Figure 4.19.: Bilge keel variants

Table 4.3.: Complete array of testing matrix

Keel Set	Identifier	Position [mm]	Length [mm]	Height [mm]	Hull
f(length) - Bilge Keel	B-P2-L1-H3 (1)	1735	333	30	1
	B-P2-L2-H3 (1)	1735	667	30	1
	B-P2-L3-H3 (1)	1735	1000	30	1
f(length) - Centerline Keel	C-P2-L1-H3 (34)	1735	333	30	34
	C-P2-L2-H3 (34)	1735	667	30	34
	C-P2-L3-H3 (34)	1735	1000	30	34
f(position)	B-P1-L1-H3 (1)	2035	333	30	1
	B-P2-L1-H3 (1)	1735	333	30	1
	B-P2-L1-H3 (16)	1735	333	30	16
	C-P2-L1-H3 (34)	1735	333	30	34
	B-P3-L1-H3 (16)	1435	333	30	16
	B-P5-L1-H3 (16)	835	333	30	16
	B-P2-L2-H3 (1)	1735	667	30	1
	B-P4-L2-H3 (16)	1135	667	30	16
	C-P4-L2-H3 (34)	1135	667	30	34
f(height)	B-P2-L2-H1 (1)	1735	667	10	1
	B-P2-L2-H2 (1)	1735	667	20	1
	B-P2-L2-H3 (1)	1735	667	30	1
	B-P2-L2-H4 (1)	1735	667	60	1
f(AR=0.06)	B-P2-L1-H1 (1)	1735	333	10	1
	B-P2-L2-H2 (1)	1735	667	20	1
	B-P2-L3-H3 (1)	1735	1000	30	1
f(AR=0.18)	B-P2-L1-H3 (1)	1735	333	30	1
	B-P2-L2-H4 (1)	1735	667	60	1
$f(^h/_{h_b})$	B-P2-L1-H3 (1)	1735	333	30	1
	B-P2-L1-H3 (16)	1735	333	30	16
f(CL keel)	C-P2-L1-H3 (34)	1735	333	30	34
	B-P2-L1-H3 (1)	1735	333	30	1
	B-P2-L1-H3 (16)	1735	333	30	16
	C-P4-L2-H3 (34)	1135	667	30	34
	B-P4-L2-H3 (16)	1135	667	30	16
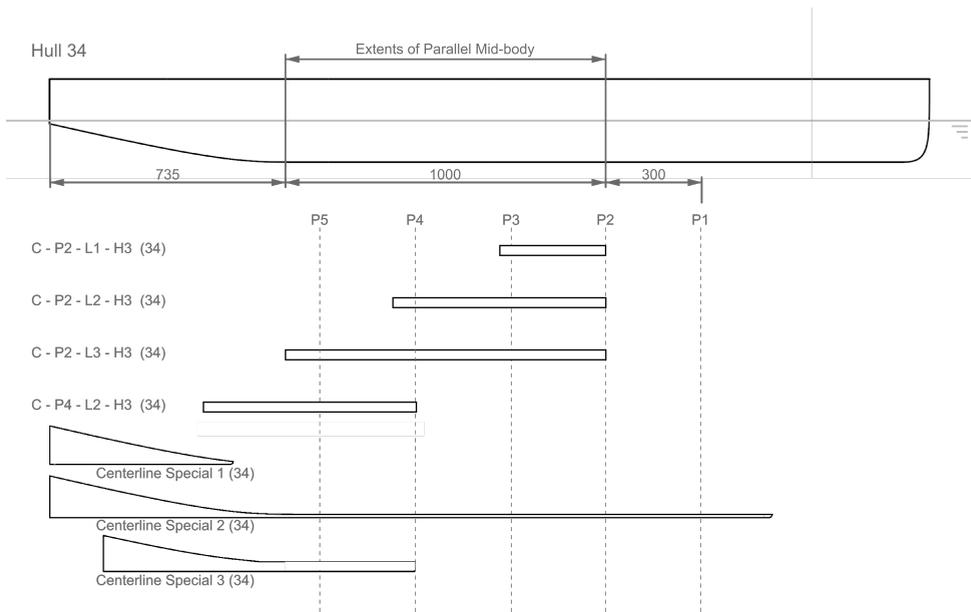
Figure 4.20.: Centreline-keel appendages
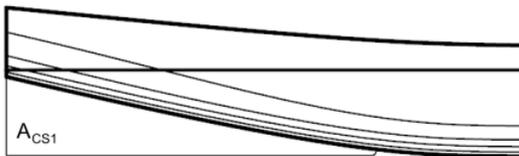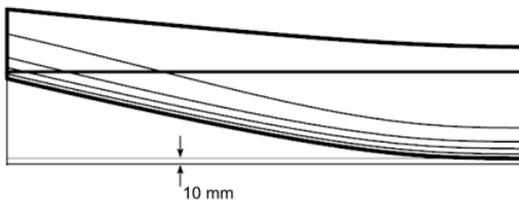
Figure 4.21.: Deadwood variations tested on Hull #34, parent hull of the 2nd Series of the DWA series.

5

Wind-Assist for Commercial Ships

Nico van der Kolk
Giovanni Bordogna
James Mason
Jean-Marc Bonello
Arthur Vrijdag

MIDSHIP SECTION

PROFILE
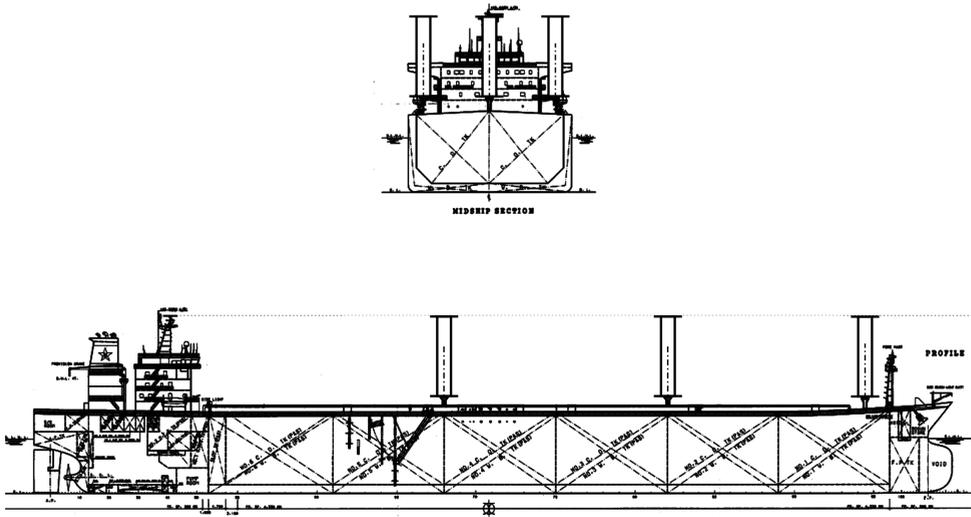
A wind-hybrid Panamax ship with five Flettner rotors works in the global trade for ethically sourced dry bulk.

Compliance under environmental regulations is accompanied by a halving of operational expenses; while the perceived value of the shipped product is increased.

Introduction

The global shipping industry carries approximately 90% of world trade by weight, accounting for nearly 3% of anthropogenic carbon dioxide emissions [99]. If left to business as usual, [78] report that greenhouse gas (GHG) emissions in the industry are expected to increase by 50-250% by 2050 compared with emissions in 2012. Alongside this, the shipping industry is responsible for around 13% and 15% of the global SOx and NOx emissions respectively due to human activities, significantly impacting human health [99]. In this paper, we present an assessment of a vessel equipped with Flettner rotor technology within present-day market and regulatory conditions. We demonstrate that this "steel sail" technology can reduce the carbon intensity of the maritime sector by 30% for regions with beneficial wind conditions. Interaction effects between disciplines are highlighted. A discussion of key engineering, design, and economic constraints for these ships is included. The methodology for each contribution is outlined in an accompanying methodX article.

As with all sectors, the maritime industry is under pressure to mitigate its impact and deliver change in line with the limits laid out in the [110] by implementing ever-stricter emissions regulations. In 2018, the International Maritime Organization (IMO) adopted an initial strategy for GHG reduction, aiming to reduce the total yearly GHG emissions by at least 50% of 2008 levels by 2050 [51]. However, [106] demonstrate that full de-carbonization of international shipping is necessary by near the middle of the century to stay in line with the limits in the Paris Agreement, highlighting the vital importance of short-term emission reduction measures if the industry is to meet this goal. Under an ever-stricter regulatory regime, the present fleet of commercial ships faces environmental obsolescence. In particular, a generation of vessels built prior to 2013 will soon face environmental obsolescence as operational monitoring for environmental performance is imposed for the whole fleet.

One short- to mid-term mitigation option is wind-assisted ship propulsion (WASP) [43]. WASP is a reintroduction of the sail to commercial shipping. Several concepts, including Flettner rotors (Figure 6.1), wing sails, and towing kites, are commercially available and multiple studies show that substantial emission reductions are attainable [6, 12, 23, 31, 37, 77, 107, 119]. The technology is also one of a limited number of near-term mitigation measures that offer reductions in both carbon dioxide and other pollutants, such as SOx and NOx [13], and is included under the Environmental Efficiency Design Index (EEDI), an IMO regulation that mandates progressive carbon reductions for new-build vessels. Direct fuel savings offer a compelling operational driver, mitigating risk from the high price-volatility in global crude markets (as experienced since January 2016). Furthermore, the upcoming introduction of the 2020 Sulfur Cap and the broader move towards alternative fuels such as hydrogen, ammonia and bio-fuels will likely constitute a significant increase in operational costs [71]. A broader discussion of regulatory, market-based, and operational drivers for the uptake of WASP is included in [119].
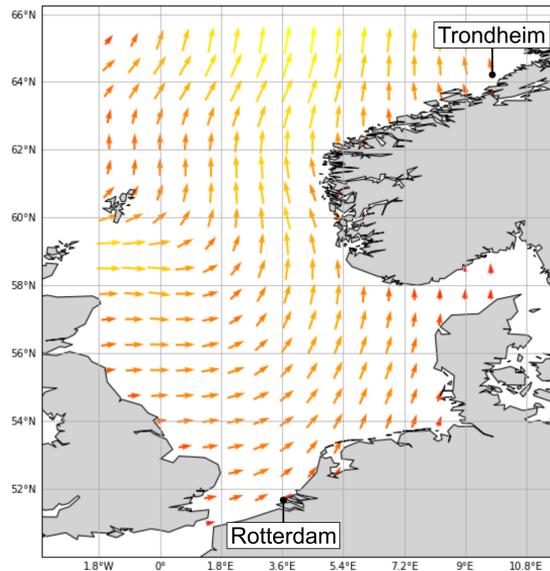
While the mitigation potential of WASP is clear, and several viable concepts for wind propulsors are commercially available, there is a general lack of experience with industrialized sailing and unwillingness to take risks as an 'early adopter'. A wide range of fuel savings is reported in literature and by WASP technology providers, and there is general uncertainty regarding the implications of a WASP system for commercial operations. Modeling efforts for fuel savings by wind-assisted vessels (as in [6, 23, 107] for example) often rely on the power contribution of wind propulsion to arrive at a corresponding fuel reduction, an approach that does not consider the implications of the 'sailing condition' on vessel resistance, or operational constraints such as heel stability and vessel maneuvering. Similarly, optimal operation of wind propulsors within these constraints is not considered. Another key barrier to the uptake of WASP is the sensitivity of fuel savings to varying weather conditions between different shipping routes and on the same route over time [34, 88]. Finally, there only limited attempts have been made to investigate the economic impact of WASP. For example, the integration of WASP with route optimization to increase fuel savings [6, 126] must be considered against economic implications of any increase in voyage time.

For the ship owner or operator, this lack of experience with industrial sailing introduces uncertainty in a profoundly risk-averse sector. For the regulator who wishes to promote the uptake of sustainable technologies, the knowledge gap raises the spectre of misdirected policies that fail to advance wind-assisted ship propulsion as a viable component of the energy transition. In fact, wind propulsion is one of the only market-ready interventions in the maritime shipping sector that promises significant reductions in greenhouse gas emissions in the near term. Furthermore, besides the simple arithmetic of fuel savings and limiting exposure to increasingly

volatile fuel prices and the prospect of environmental obsolescence, wind-assistance raises the possibility of engaging with an activist consumer class and potentially increasing the perceived value of shipped products.

This paper presents a techno-economic assessment of a WASP installation for a large commercial ship sailing on a North Sea route between Rotterdam (The Netherlands) and Trondheim (Norway). The WASP device considered is the Flettner rotor, which creates an aerodynamic driving force using the Magnus effect [35]. In exchange for limited absorbed engine power, Flettner rotors generate a significant amount of thrust with a reduced "sail" area.

Table 5.1.: Vessel main particulars and details of Flettner rotor installation.

Vessel main particulars	
LOA	149.7 m
Beam	24.6 m
Draft	9.5 m
Displacement	25 700 t
Deadweight	19 500 t
GM	0.683 m
Flettner rotor design / costs	
Rotor height (span)	30 m
Diameter	5 m
Weight (3 rotors)	177 t
Buying cost (3 rotors)	$2.7 M
Installation cost (3 rotors)	$780 k
Maintenance cost (2% CAPEX annually)	$70 k
Lifetime	25 yrs

The ship considered in the present case study is the DAMEN 19500 DWT bitumen/asphalt tanker, the BTa 19500 (Table 5.1). Cargo handling requirements for this vessel type conform to deck access limits that accompany a substantial WASP installation. The vessel deadweight tonnage is representative for regional operation. Technical data for the vessel was provided by DAMEN shipyards. The approach for the case study is based on a comparison between the fuel consumption of a vessel equipped with wind propulsors and a reference ship. The vessels are identical, apart from the addition of wind propulsors for the WASP design, and an identical approach is applied in the subsequent analyses for vessel modeling and weather routing. A net-present value (NPV) assessment is presented based on the fuel savings delivered by the WASP installation. The discussion includes a sensitivity analysis for fuel price and environmental market based measures (MBM) such as port incentives and carbon pricing (CP).

5.1. Vessel Model

The Delft WASP vessel model is a performance prediction tool that functions much like a sailing yacht velocity prediction program [21, 63]. The underlying principle is a force balance in four degrees of freedom: surge, sway, roll, and yaw, and an optimization routine for Flettner rotor operation (analogous to sail trim setting). The modeling is reviewed here for each component: aerodynamics, hydro-mechanics, engine model, weather routing, and the economic/environmental assessment with emphasis on interaction effects.

Wind propulsion systems may be used in many ways to transform wind energy into forward thrust. Maintaining the nominal service speed is considered the most acceptable for vessel operators in present-day supply chains, whereby wind thrust is used to replace main engine thrust and the fuel consumption is correspondingly reduced. Flettner rotor settings are selected to achieve minimum required propeller thrust at the given vessel speed. Alternative vessel operating modes can be defined, such as pure sailing or a specified minimum vessel speed.
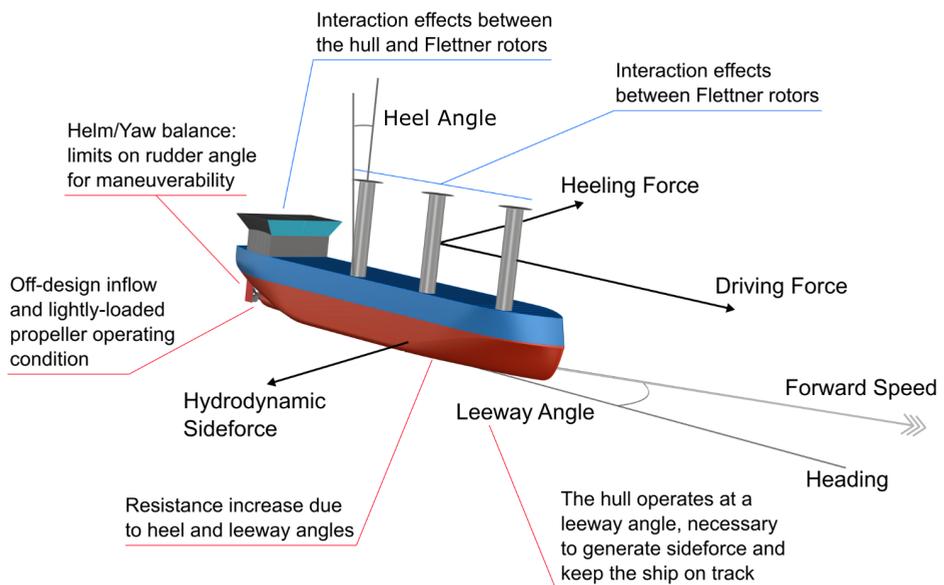
Figure 5.1.: Key components of the vessel model

A balance of forces and moments for the remaining degrees of freedom (sway, roll, and yaw) is a necessary condition for WASP vessels because the desired wind-generated driving force is generally accompanied by a transverse aerodynamic force, known as the heeling force in sailing yacht nomenclature (see Figure 5.1). The heeling force and associated moment must be balanced by corresponding

hydro-mechanic reactions. The vessel will adopt a steady heeling angle and leeway angle (known as drift in the maneuvering field), or the "sailing condition", with an associated increase in resistance. As a hybrid vessel, the benefits of aerodynamic thrust generated by the wind propulsor must be considered against any increase in resistance. As a final note, the heel angle, leeway angle, and associated rudder angle are subject to operational constraints, an important design issue.

The performance of the ship is represented by several metrics, for example, the available wind-assist power, P_{WASP}, is plotted in Figure 5.2. P_{WASP} considers the wind-assist propulsive power against any power needed to operate the wind propulsor. It is the WASP contribution to the total propulsive requirement, defined as:

$$P_{\text{WASP}} = \frac{V_{\text{ref}}}{\eta_{\text{T}}}(T_{\text{Aero}} - \Delta R_{\text{Sailing}}) - \frac{P_{\text{Rotor}}}{\eta_{\text{Gen}}} \qquad (5.1)$$
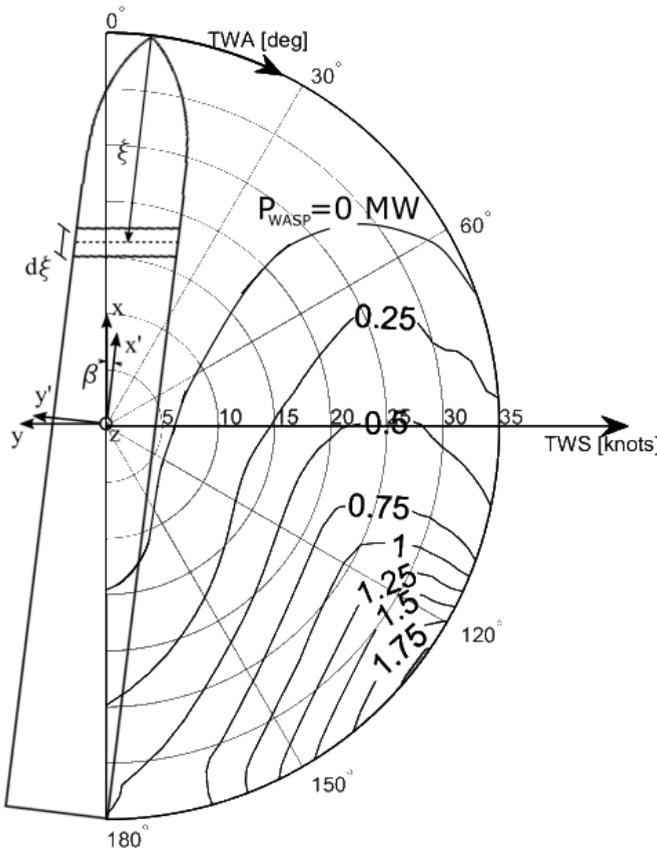
Figure 5.2.: Available wind-assist power, P_{WASP}. Installed main engine power = 1.3 MW Vessel coordinate system shown.

The expression appears also in the EEDI formula, without the term $\Delta R_{\text{Sailing}}$. Ef-

ficiency values for the main propulsion system (η_{T}), and the generator (η_{Gen}) are prescribed by the IMO.

A design can be evaluated and improved based on these polar diagrams, or this information can be passed to a weather routing program or used to define the control systems of the wind propulsor. Finally, vessel performance with wind assist operation can be optimized, and studied for environmental impact and economic investment evaluations.

Thrust Benefit as Wind-assist Design Metric

The thrust benefit (TB) is a convenient performance metric for wind-hybrid vessels. Beginning with the total propulsive power requirement of the ship, ($R_{\mathrm{Tot}}V_{\mathrm{ref}}$):

$$R_{\mathrm{Tot}}V_{\mathrm{ref}} = P_{\mathrm{B}}/\eta_{\mathrm{T}} + R_{\mathrm{WASP}} \tag{5.2a}$$

Substituting from Equation (5.1), the left-hand side is the new propulsive requirement for the ship, including any added resistance due to sailing, whereas P_{Rotor} appears on the right-hand side:

$$(R_{\mathrm{Tot}} + \Delta R_{\mathrm{Sailing}})V_{\mathrm{ref}} = \frac{P_{\mathrm{B}}}{\eta_{\mathrm{T}}} + T_{\mathrm{Aero}}V_{\mathrm{ref}} - \frac{P_{\mathrm{Rotor}}}{\eta_{\mathrm{Gen}}} \tag{5.2b}$$

Further rearranging the expression and removing P_{Rotor}:

$$(R_{\mathrm{Tot}} + \Delta R_{\mathrm{Sailing}}) = \frac{P_{\mathrm{B}}}{\eta_{\mathrm{T}}V_{\mathrm{ref}}} + T_{\mathrm{Aero}} \tag{5.2c}$$

The TB considers only the WASP contribution to thrust, not any power needed to operate the Flettner rotors.

$$1 = \frac{P_{\mathrm{B}}}{\eta_{\mathrm{T}}V_{\mathrm{ref}}(R_{\mathrm{Tot}} + \Delta R_{\mathrm{Sailing}})} + \boxed{\frac{T_{\mathrm{Aero}}}{(R_{\mathrm{Tot}} + \Delta R_{\mathrm{Sailing}})}} \tag{5.2d}$$

Finally dividing through by the total resistance, ($R_{\mathrm{Tot}} + \Delta R_{\mathrm{Sailing}}$), the TB is defined as the ratio of WASP thrust and total resistance.

$$TB := \frac{T_{\mathrm{Aero}}}{R_{\mathrm{Tot}} + \Delta R_{\mathrm{Sailing}}} \tag{5.3}$$

The TB, often expressed as a percentage, represents the balance between wind propulsion and the main engine propulsion (first term in Equation (5.2d)), and is therefore a first approximation for the expected fuel savings. This form of TB is self-referencing, whereas other definitions [37] compare a wind-assist ship with a reference case without wind propulsors. This level of analysis does not consider changes in the main engine propulsive efficiency.

Sailing performance metrics such as TB are typically presented in a polar plot as in Figure 5.3, in which the vessel performance is given for a range of true wind speed (TWS) and for all wind angles (TWA). The angle is defined in the ship reference
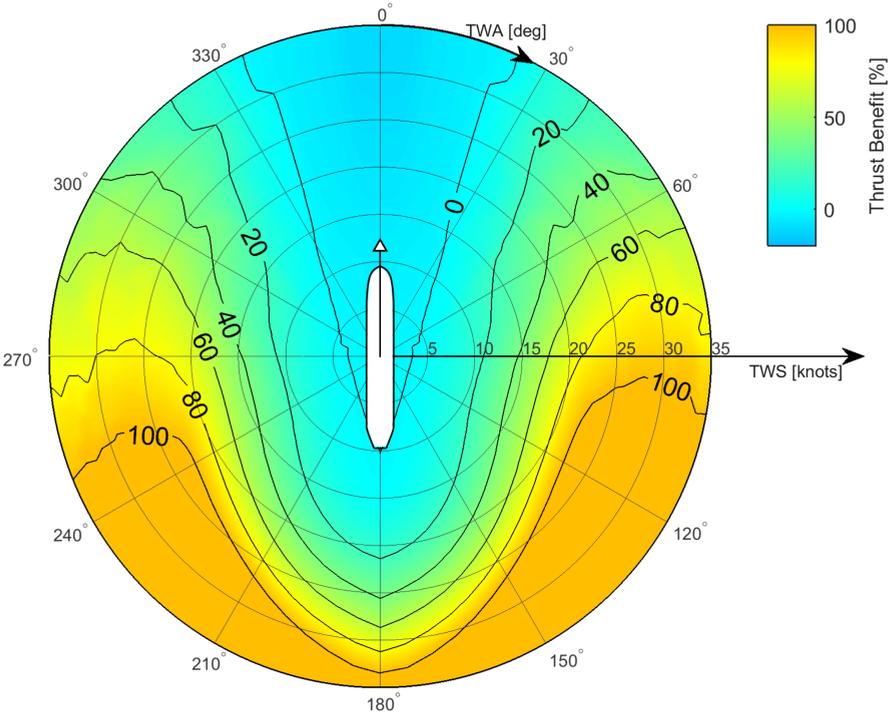
Figure 5.3.: Polar diagram showing thrust benefit for a design candidate. 12.4 knots boat speed.

frame, relative to the ship heading (indicated for this polar with a vessel): the ship is sailing directly into the wind at $TWA = 0°$ (resulting in negative TB due to the added air drag of the Flettner rotors), and with the wind astern for TWA =180°. Asymmetry observed in the polar is a product of the off-center arrangement of Flettner rotors (arranged 'In-line', as in Figure 5.1), which gives the vessel better course-stability for starboard courses ($0°<TWA<180°$). The WASP installation is de-powered (similar to reefing for a sailing yacht) on upwind courses ($TWA <90°$ and $TWA >270°$) for TWS greater than 20 knots. An effect of one of the operational constraints (heel angle in this case), this threshold for de-powering can inform the sizing and placement of the wind propulsors. Besides providing insight into the effectiveness of a WASP configuration for a given vessel, the thrust benefit lends itself well to a route-specific analysis.
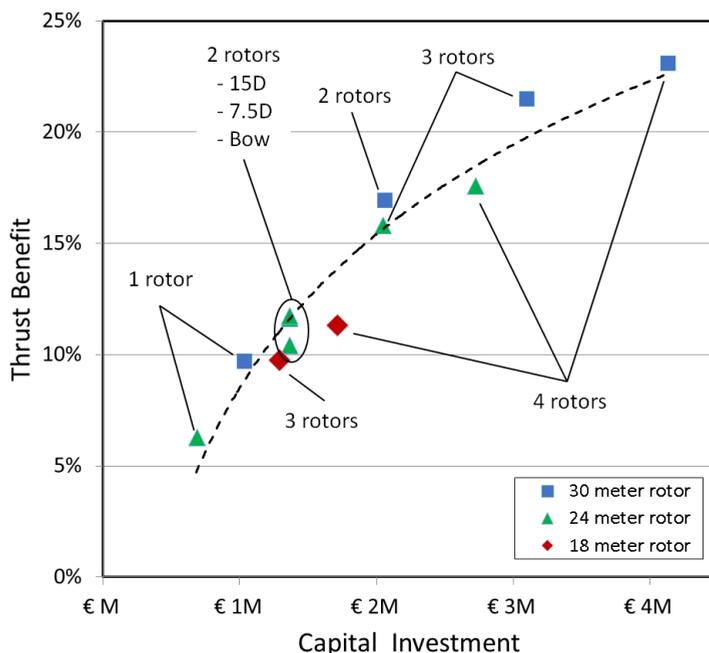
Figure 5.4.: Thrust benefit result for several wind-assist design candidates on North Sea route

Several design candidates are assessed on expected performance over the route between Rotterdam and Trondheim based on contribution of a WASP installation to the vessel EEDI score (see Section 5.3). The rotor dimensions correspond to the rotor types offered by NORSEPOWER. who provided technical data for the wind propulsors. The array of design candidates is shown in Figure 5.5.

30m rotor

2-rotor variants

15D

24m rotor

7.5D

Bow

18m rotor

Single Rotor   Double Rotor   3 rotors in-line   2x2 rotors
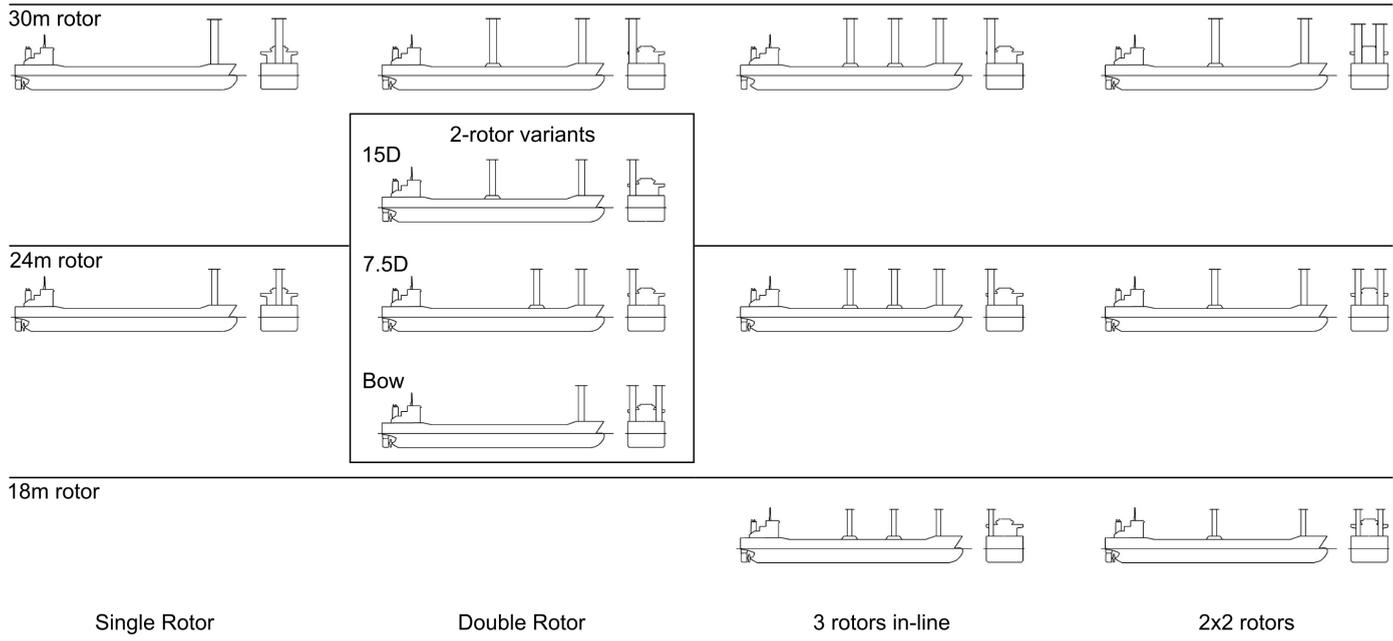
Figure 5.5.: Array of WASP installations considered for the DAMEN BTa 19500 vessel.

Results for the thrust benefit along the North Sea route are presented in Figure 5.4. Wind data for the route between Rotterdam and Trondheim, expressed as percentiles in a wind scatter matrix, are used to create a weighted sum of the entries in the polar diagram (Figure 5.3), giving the expected performance of the design candidate sailing along the route. There is apparently a point of diminishing returns after which further investment in WASP propulsion gives marginal improvement in vessel performance. This behavior is caused by aerodynamic interaction effects between rotors and by rotor de-powering due to operational constraints for heeling angle and the maneuverability of the ship. For example, installing two 30 meter Flettner rotors yields a 7.3% improvement for thrust benefit over the single 30 meter rotor and adding a third rotor results in a further 4.5% improvement, whereas a fourth rotor yields only 1.6%. Also, it appears that installing fewer, larger rotors is more effective than installing a larger number of smaller devices. Finally, the effect of different arrangement for the rotors on the ship deck is discernible in the results for variations in the positioning of two 24-meter Flettner rotors. For an identical investment, the two-rotor bow configuration is 1.4% less effective, again due to aerodynamic interaction effects. Aerodynamic interaction is apparently no longer significant for rotors with at least 7.5-diameter spacing, whereas it is detrimental for the two-rotor bow and 2x2 rotor configurations.

Aerodynamics

From an aerodynamic perspective, it is also interesting to compare the velocity ratios of the various Flettner rotors installed on the ship to understand the effects of the aerodynamic interaction on the results. The velocity ratio, k, is defined as the ratio between the Flettner rotor tangential velocity and the incoming wind speed.

$$k = \frac{U_{\text{tan}}}{V_{\text{wind}}} \tag{5.4}$$

As with the angle of attack for a sail, k is the parameter that determines the amount of lift and drag generated by the Flettner rotor. The way the Flettner rotors are operated, the velocity ratio k, will depending on the wind speed and wind direction, and has a direct influence on the amount of fuel savings achievable by the ship.
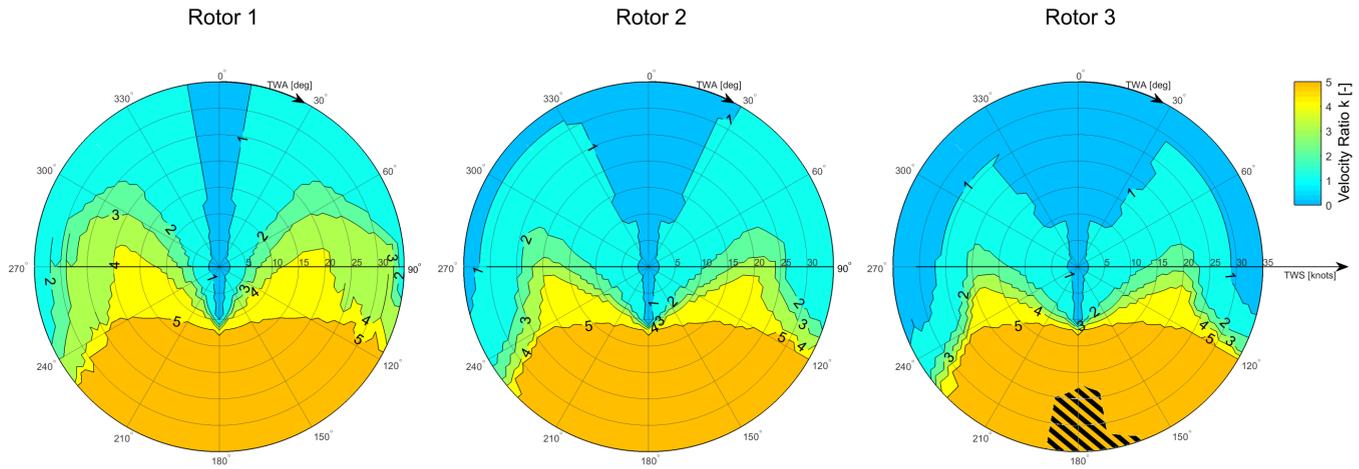
Figure 5.6.: Optimum velocity ratios for Flettner rotors 1-3. The hatched portion of the polar of Rotor 3 indicates a negative velocity ratio (-5).

Figure Figure 5.6 shows the results of the velocity ratios of the three installed Flettner rotors in order to achieve the best overall performance of the ship, i.e. the highest fuel savings. The results of the velocity ratios indicate that the three Flettner rotors work similarly, although some important differences can be noted. The polar diagrams are not symmetric due to the installation of the wind propulsors on the starboard side of the ship. This asymmetry means that the Flettner rotors operate differently whether the ship is sailing on a port or starboard tack. All three rotors adopt a low velocity ratio when the ship is sailing upwind, and a larger velocity ratio when the wind comes from astern. This difference is because when sailing at small TWA it is more beneficial to have a high lift/drag ratio, and this occurs at low velocity ratios ($k \approx 1$). Conversely, at large TWA, the forward thrust is generated both by the lift and the drag force. High values of lift and drag occur at large velocity ratios. It should be noted that a plateau for both the lift and the drag force is found at $k = 5$, meaning that a further increase of the velocity ratio would only produce a detrimental rise of the Flettner rotor power consumption.

Another important aspect to notice is that when de-powering is needed in order to maintain an optimal ship overall performance, Rotor 3 is the first to be spun at a lower velocity ratio or is switched off altogether because, by doing so, the aero-dynamic center of effort is shifted forward towards the bow, which helps to reduce the weather helm to comply with the limitations for rudder angle, as well as the associated increase in induced hydrodynamic resistance. Finally, the hatched por-tion of the polar of Rotor 3 corresponds to an operating condition where a negative velocity ratio, i.e. the rotor is rotating in the opposite direction compared to the other two rotors and generating lift in the opposite direction, which is beneficial for vessel helm balance.

Hydro-mechanics

This survey of vessel hydro-mechanic response will focus on the vessel heeling angle and rudder angle, the two operational constraints imposed on the vessel. As discussed, the vessel will adopt a combination of heel and leeway angles to generate the needed hydro-mechanic reaction: a restoring moment to support the heeling force of sail plan, and a sideforce to oppose the lateral aerodynamic force and keep the vessel on track. A destabilizing 'Munk' yawing moment accompanies the vessel leeway angle, requiring corrective action by the rudder.

The polar diagrams for heel angle and rudder angle are provided for starboard side only in Figure 5.7. Vessel response for heel and rudder angles should be reviewed alongside the Flettner rotor velocity ratios (Figure 5.6), and the engine fuel consumption Figure 5.10. The operational limit of 10° for both angles is reached for TWS of approximately 20 knots, though for different ranges of TWA. The two main modes of sailing, upwind and downwind courses, are distinguished by the isolines for zero degrees in both polar diagrams, corresponding to an apparent wind angle (AWA) of 90°. The change from positive heel and rudder angles to negative heel and rudder angles is a counter-intuitive result that may be understood by considering the orientation of the aerodynamic lift and drag vectors for the Flettner rotors. For
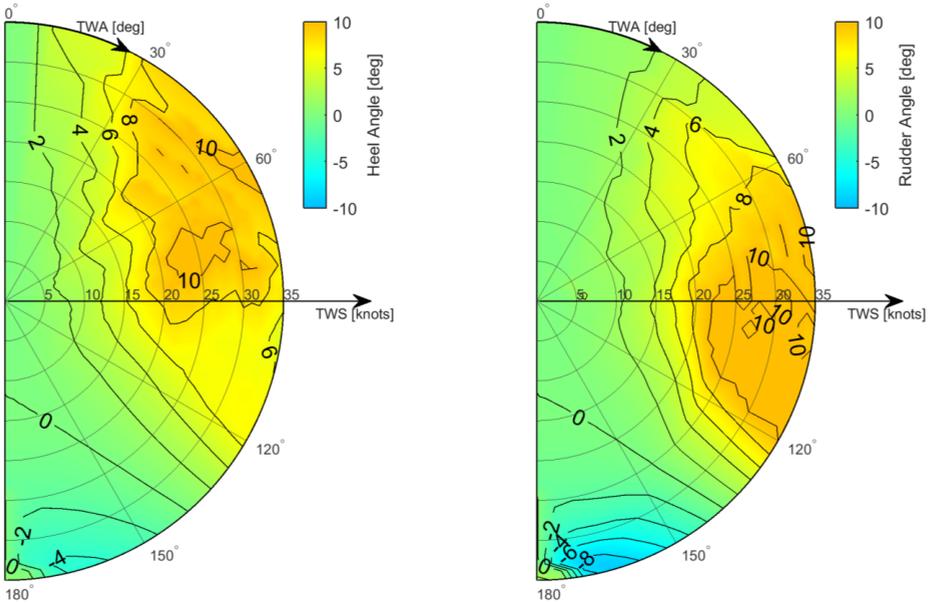
Figure 5.7.: Vessel heel angle (left) and rudder angle (right) for the starboard side only. An 10° operating limit is imposed for both angles. 12.4 knots boat speed.

AWA greater than 90°, the aerodynamic lift vector will result in a heeling moment towards the wind direction, resulting in a negative heeling angle.

The maneuverability of a ship with WASP will experience a compounding effect, whereby the reduced propeller thrust for large values of TB results in a reduced propeller wash over the rudder. Operating conditions with large TB correspond to large aerodynamic forces, including the heeling force, and generally coincide with cases where a steering correction is needed. For example, in the sector for TWS greater than 20 knots and TWA between 90°-120°, where the engine-delivered thrust is approximately zero, the rudder angle limit requires a sharp de-powering of Rotors 2 and 3 (Figure 5.6). These effects limit the operating points of the WASP vessel, especially for TWA between between 90°-120°, where a large portion of the vessel driving force is provided by the WASP installation.

Marine Engineering
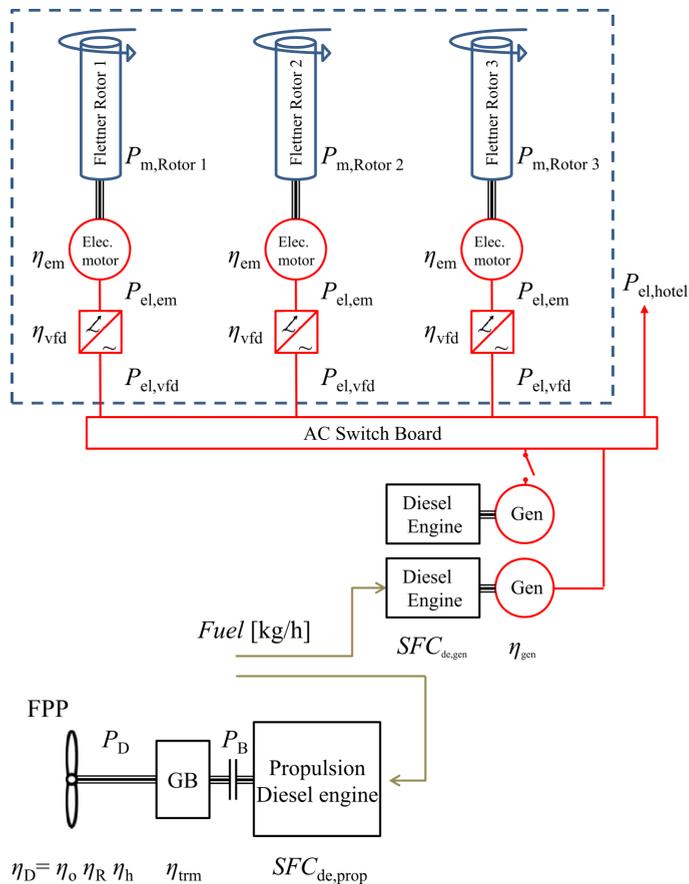
Figure 5.8.: Schematic of the main propulsor and ship electric grid

The required engine speed, brake power, and total fuel consumption for each combination of true wind speed and direction was determined for a ship with and without WASP, with a fixed ship speed of 12.4 kts.
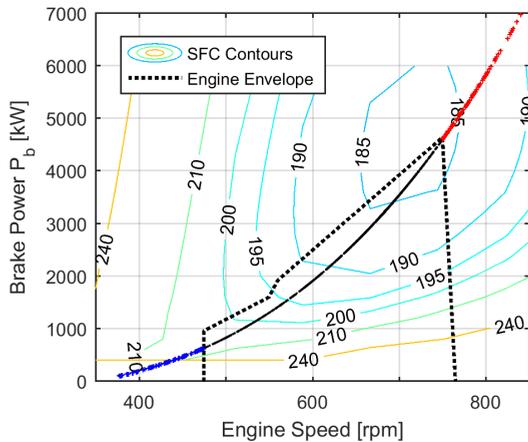
Figure 5.9.: Main engine speed envelope and SFC curves. Flags are indicated with red and blue markers.

They are presented in a combined manner along with the engine envelope in Figure 5.9, showing a very wide spread, ranging from below minimum engine speed to above maximum engine speed. The operating points within the engine envelopes show that the engine SFC for WASP concepts is highly dependent on the wind condition.

The colored markers in Figures 5.9 and 5.10 indicate operating points that are not possible because they are located outside the engine operating envelope. The red markers in the "wind from ahead" situation indicate that the engine cannot deliver the power/speed required to sail at the fixed ship speed, as the resistance has been increased due to the strong headwinds and corresponding wave condition. These operating conditions correspond to a ship speed reduction due to strong headwinds/seas, which is currently not captured in the vessel model or routing model. However, for these cases, the reference ship and the WASP concept will be similarly hindered (i.e. the fuel savings will be zero).

The blue markers in the "wind from astern/beam wind" condition indicate that the required engine speed is less than the minimum engine speed. In reality, the engine would run around minimum engine speed and the ship speed increase slightly, or the engine would be switched off and the ship would sail more slowly. The blanked region in the "wind from astern/ beam wind" condition indicates that the sails by themselves deliver sufficient thrust to achieve the vessel speed without engaging the engine. For this condition, the WASP concept will accelerate to a higher vessel speed where a new balance is found between resistance and aerodynamic thrust. However, this is not incorporated in the present modeling.

In combination with the rotor-related fuel consumption, this results in a total
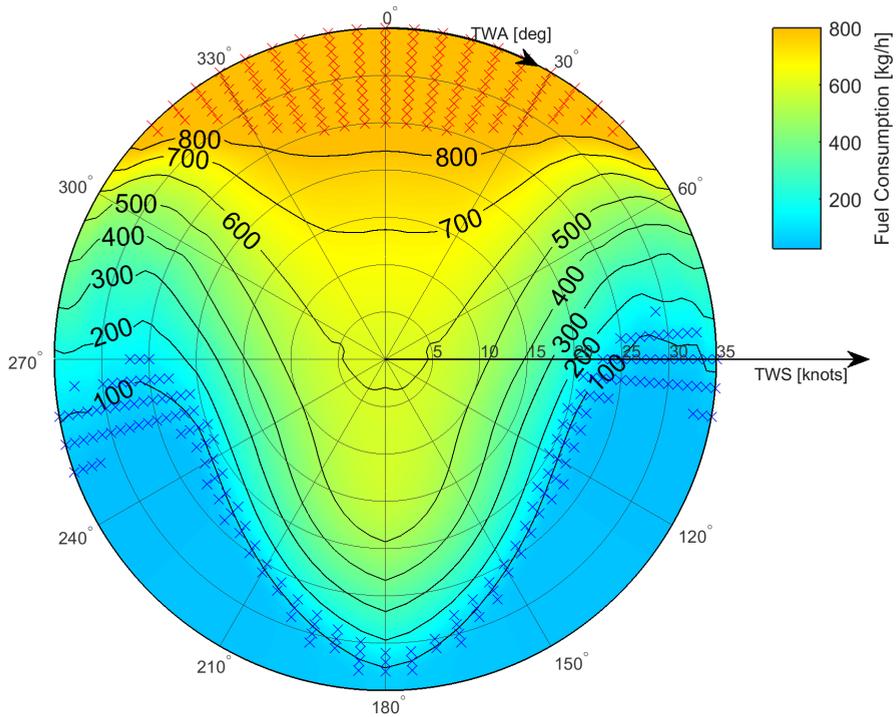
Figure 5.10.: Fuel consumption polar for WASP case. Red crosses indicate operating points outside the engine envelope.

fuel consumption for each combination of TWA and TWS. For the majority of wind conditions, the WASP vessel requires less fuel at this fixed ship speed. To investigate the effect on the total voyage-related savings, the data from Figure 5.10 are passed on to the voyage simulation module.

5.2. Weather Routing

Route optimization is analogous to satellite navigation in cars, and involves implementing an algorithm to calculate the optimal path of a ship traveling between two ports minimizing, for instance, journey time, distance traveled or fuel consumption. When used to reduce the fuel consumption of a WASP vessel, route optimization uses meteorological data to allow the vessel to deviate from the conventional shortest-path route to seek advantageous wind conditions. Routing maximizes the efficacy of the wind propulsors in minimizing the vessel's fuel use and emissions.

Figure 5.11.: An example of the North Sea route between Trondheim and Rotterdam. The map shows both the shortest distance route (red) and fuel-optimized route (green) for the date 01-01-2016 at 00:00:00.

The fuel savings from three rotors are calculated by comparing the three-rotor case against the reference case on the shortest distance route. The results show yearly-averaged fuel savings of between 17.3% and 29.3%. The average and median value is presented in Table 5.2. For these non-normal distributions, the median

Table 5.2.: Fuel savings for the three-rotor case on both northbound and southbound voyages in 2015 and 2016, including the voyage time increase from route optimization.

		Fuel Savings [%]		Voyage Time Increase [%]	
		Average	Median	Average	Median
2015	Shortest distance	23.7	18.4		
	Northbound	29.3	24.8		
	Southbound	18.0	14.9		
	Fuel-optimized	32.2	26.9	13.9	9.5
	Northbound	36.5	32.7	13.0	9.0
	Southbound	27.9	24.1	14.8	10.2
2016	Shortest distance	19.7	15.3		
	Northbound	22.1	17.4		
	Southbound	17.3	14.5		
	Fuel-optimized	26.9	22.2	12.0	6.6
	Northbound	27.9	22.0	10.1	5.0
	Southbound	25.8	22.4	13.9	8.2
All	Shortest Distance	21.7	16.8		
	Fuel-optimized	29.5	24.7	13.0	7.8

value better represents the fuel savings that a ship would expect to achieve when traveling on this route for one journey. The results demonstrate greater fuel savings on the northbound journey due to the presence of a dominant south-westerly wind. There is a clear variation in fuel savings when comparing the simulations for 2015 and 2016, especially for the northbound journey, once again highlighting the significance of simulating fuel savings across multiple years. The savings from this study are lower than previous estimates in the North Sea by [107], though Traut assess both different vessel and rotor sizes, and make simplifications for interaction effects in their vessel modeling.

The impact of route optimization is calculated by comparing the fuel-optimized route for the three rotor case with the shortest distance route for the reference case. The results show yearly-averaged fuel savings of between 25.8% and 36.5% when combined with WASP. Fuel-optimized routing for the northbound journey increases absolute yearly-averaged fuel savings by approximately 6%, while the southbound journey shows the largest increase in absolute fuel savings (10% in 2015 and 8.5% in 2016). This increase concurs with previous studies [6, 126]. The fuel savings from route optimization in this study are limited by the implementation of a constant vessel speed.
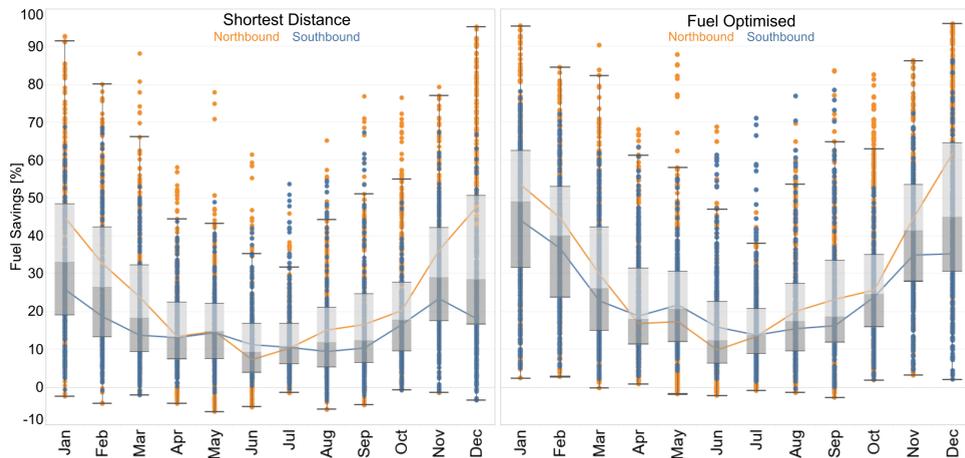
Figure 5.12.: Box and whisker plots showing the distribution of fuel savings for the shortest distance (left) and fuel-optimized (right) routes for a combination of 2015 and 2016. The median value for northbound (orange) and southbound (blue) voyages are also shown as continuous lines.

Figure 5.12 shows a box and whisker chart displaying the distribution of results for the shortest distance and fuel-optimized routes. The fuel savings display significant fluctuations depending on month, as also seen in previous studies [100]. The spread of fuel savings for each individual month is also large. This variability is widely accepted as one of the key barriers to the uptake of wind propulsion [88]. The months where the fuel savings are greater on the shortest distance route demonstrate the largest absolute impact from route optimization, with average fuel savings of over 50% in both January and December.

A consequence of using fuel-optimized routing, where the ship strays away from the shortest-distance path in search of advantageous weather conditions, is a potential increase in the total voyage time of each journey. This increase depends on each journey's weather conditions and does not follow a set pattern. The routing model can impose a set limit on this; however, [92] demonstrate that strict limits on this increase significantly constrains the additional fuel saving impact of route optimization. Therefore, this study imposes no limit. The average and median increases for voyage time are included in Table 5.2.

5.3. Economic and Environmental Assessment

The installation of wind propulsors can significantly improve the vessel EEDI score (Figure 5.13). Besides helping with present-day EEDI compliance, they offer resilience under a changing, increasingly stringent regulatory scheme. For example, whereas the reference design for the BTa 19500 provided by DAMEN shipyards was optimized for Phase 2 compliance, designs with larger WASP installations (three and four 30-meter Flettner rotors) are Phase 3 compliant. In contrast with results for TB, one can observe that the ship EEDI score shows steady improvement as the number and size of rotors is increased (excepting the 2x2 rotor case, discussed above). The global wind-scatter matrix specified for the EEDI calculation is a significantly lighter wind condition than will be encountered along the North Sea route. WASP designs will therefore have less need to de-power to respect operational constraints. Also, under the present EEDI formulation, the contribution of the WASP propulsive power (first term in Equation (5.5)) is determined using the aerodynamic thrust only, without considering increases in resistance due to sailing.

Wind-assist Contribution to EEDI Rating

WASP technology is included in Energy-Efficiency Design Index (EEDI), the IMO regulation mandating carbon-reduction for new-build vessels, under the category "Innovative energy efficiency technologies" [50]. Furthermore, a vessel's EEDI score is tied to diverse Green Port Fees designed to incentivize uptake of carbon-reduction in commercial shipping [83]. For example, the port of Rotterdam offers a 30% rebate on harbor fees for green ships [85].

Under the EEDI, the available effective power of the Flettner rotor wind propulsion system is determined as in Equation (5.1). This discussion of the EEDI is limited to the calculation of the available effective power, $f_{\text{eff}}P_{\text{eff}}$:

$$
f_{\text{eff}} \cdot P_{\text{eff}} = \frac{0.5144 V_{\text{ref}}}{\eta_{\text{T}}} \sum_{i=1}^{m} F(V_{\text{ref}})_{i,j} \cdot W_{i,j} - \\
\sum_{i=1}^{m} P_{\text{Rotor}}(V_{\text{ref}})_{i,j} \cdot W_{i,j}
$$

(5.5)

For the calculation of the first term (the delivered propulsive power), the total efficiency of the main propulsor, η_T, is set to 0.7 if no other value is available. $F_{i,j}$ is the driving force provided by the wind propulsor, T_{Aero}, calculated at each combination of TWS and TWA. Finally, a weighted average is made using the IMO-specified global wind-scatter diagram, $W_{i,j}$, which is based on a survey of world-wide shipping routes [5]. The second term is the required power to operate the Flettner rotors. This term is also multiplied by the global wind scatter matrix.
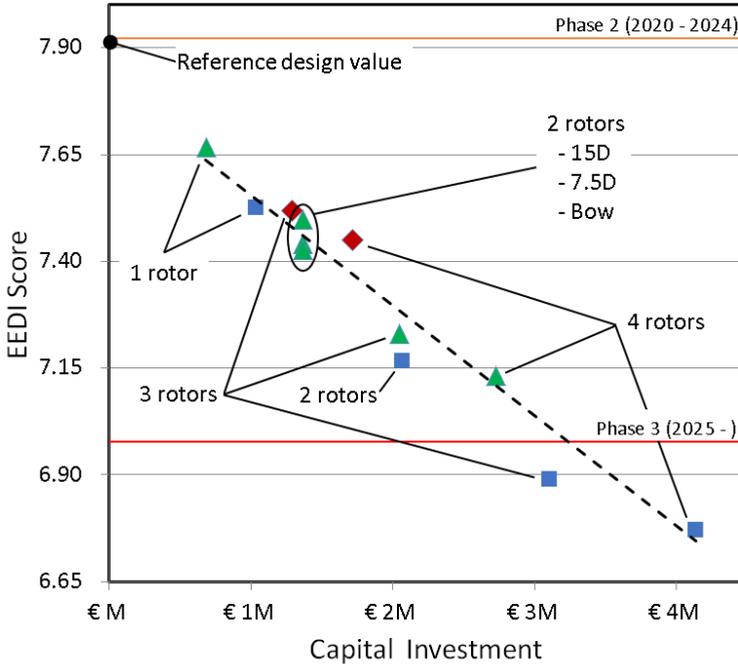
Figure 5.13.: EEDI score for wind-assist design candidates. The reference design and target EEDI values for Phase 2 and Phase 3 are indicated

Based on the considerations for investment effectiveness and regulatory compliance outlined above, the design with three 30-meter Flettner rotors arranged in-line is selected for further analysis. The details of the selected system are given in Table 5.1. The arrangement of Flettner rotors is asymmetric; along the starboard side of the vessel deck. This configuration was adopted to allow the structural foundation of the Flettner rotors to be tied into the main frames of the vessel. In addition, this configuration allows for full deck area access when the vessel is berthed port-side-to. Operability constraints for vessel loading and unloading are not considered in further detail for this study.

Economic Assessment

In order to assess the economic viability of the WASP technology from a commercial perspective, the Net Present Value (NPV) based on the Capital Expenditure (CAPEX) (I_O) and discounted cash flow projection (C_t) from the WASP installation is used to determine an expected payback period. This calculation assumes current economic conditions, and does not presuppose any significant change imposed on, for example, the price of carbon.

$$\text{NPV} = -I_O + \sum_{t=1}^{n} \frac{C_t}{(1-r)^t} \tag{5.6}$$

The cash flows associated with the installation are a function of fuel savings, and any additional costs incurred during the operational lifetime of the rotors are calculated. The assumptions adopted in the economic assessment are summarized in Table 5.3. At the baseline case cost of bunker, a range of payback between

Table 5.3.: Assumptions for economic and environmental analysis.

Variable	Symbol	Value	Unit	Description
CAPEX	I_O	3.5 M	$	Cost of Installation
Maintenance	M_t	2	%	% of CAPEX
Utilisation	ν	0.66		240 days at sea per year
Discount rate	r	5	%	Rate for discounted cash flow
Bunker price	B_P	550	$/t	BW0.1S at Rotterdam
Specific carbon content		3.08	$gCO_2/$ gLSHFO	CO_2 content for LSHFO

12 and 14 years is projected with the assumptions presented in Table 5.3 and based on the seasonal and statistical performance variation. Figure 5.14 presents the sensitivity of the payback period with reference to bunker price for a $200 range around the baseline and the range of expected payback period based on the variation in weather conditions experienced along the route throughout different periods of the year. The fuel savings from route optimization significantly reduce the expected payback period to between 8.8 and 10.7 years. Given the fact that this study considers constant velocity operation, route optimization significantly increases the voyage time, thus reducing the amount of transport work carried out over a specified time period, which decreases the amount of revenue that could be earned. The gains from weather routing can be augmented with the introduction of speed optimization which may allow for a compromise between fuel savings and utilization.

Apart from the direct benefits from the fuel savings, several port- and flag-state-driven schemes offer incentives to vessels that implement fuel savings technologies such as discounts on port fees based on the allocation of independent standards or indices. With the increased availability of data through AIS, fleet databases and EU
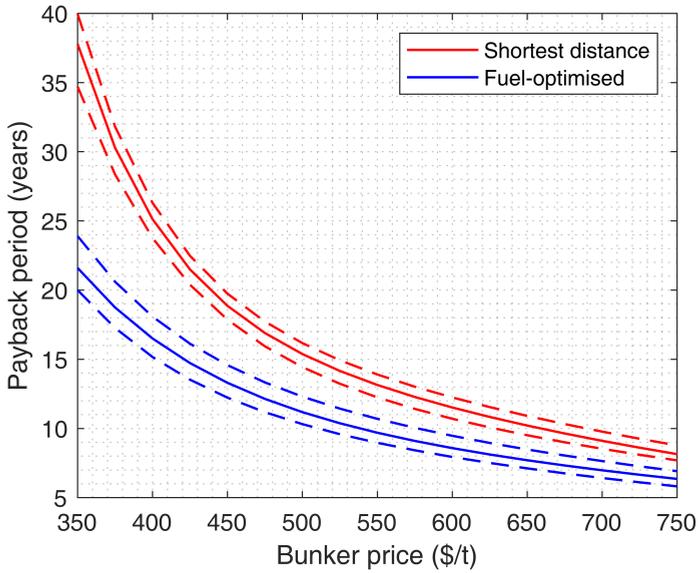
Figure 5.14.: Payback period on Rotterdam-Trondheim route with bunker price sensitivity.

Table 5.4.: Payback periods for different scenarios.

Payback Period [years]			
	Mean	Maximum	Minimum
Shortest distance	13.1	14.0	11.9
CP $100/t	4.8	5.5	4.2
CP $300/t	3.6	4.2	3.2
CP $500/t	2.9	3.4	2.4
ESI min	9.7	10.5	8.9
ESI max	8.2	9.0	7.6
Fuel-optimized	9.7	10.7	8.8
CP $100/t	3.7	4.2	3.3
CP $300/t	2.8	3.2	2.5
CP $500/t	2.3	2.6	2.0
ESI min	7.7	8.3	7.0
ESI max	6.7	7.4	6.3

MRV data, independent metrics will allow for comparisons with vessels in the same peer group [95]. In this case study, the Port of Rotterdam and Trondheim have discount schemes for port dues based on the Environmental Sustainability Index (ESI) that could lead to monthly savings of between $7,900 and $13,000 based on the assigned rating [85, 108]. While this incentive-based mechanism is increasing in popularity, it faces a split incentive market barrier with time-chartered vessels where the owner of the vessel does not benefit from the port dues discounts and thus investment is less attractive unless the vessel is spot chartered or operated by the owner [62, 88].
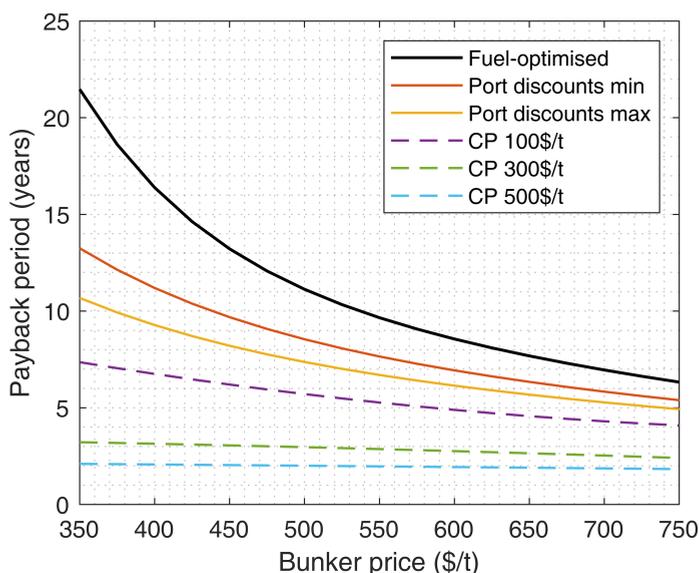
Figure 5.15.: Payback period on Rotterdam-Trondheim route with port due discount and CP sensitivity.

Another mechanism that is frequently proposed for curbing GHG emissions is the use of carbon pricing (CP) (assuming a carbon factor of 3.08 gCO_2/gLSHFO as per [99]. In their quantitative analysis, IMarEST concluded that a carbon price in the range of 100 - 500$/t may be required to align shipping with the IMO 2050 emissions ambition [52]. The large range is attributed to the assumptions related to renewable electricity price projections for various scenarios. The application of both these strategies is presented in Figure 5.15, where both can be seen to make a significant difference, making a stronger case for investing in WASP given the additional resilience to possible future environmental policy. At a policy level, the IMO is also looking at a carbon intensity-based metric as part of its short-term policies compiled through the DCS, thus investment in WASP could provide a measure of resilience to avoid vessels becoming stranded assets due to environmental obsolescence [19]. Another approach to CP considered is the model used by the UK Department for Transport in the recently published strategy aimed at de-carbonization of the sector,

which proposes staggered incremental CP starting in 2025 [98]. However, when even the most stringent assumed scenario was considered (zero GHG by 2050) for a hypothetical investment in 2020, the payback period well precedes the introduction of CP.

Finally, the study calculates the reduction in carbon emissions associated with the fuel savings by using the specific carbon content of the fuel. The increase in voyage time due to route optimization has a subsequent impact on these carbon savings. Assuming that a constant volume of cargo must be transported on the route, the number of ships traveling on this route must increase, which is accounted for in this analysis. If the fleet is operating at full capacity, the fleet size may have to increase to transport the same volume of cargo, producing additional CO_2 from shipbuilding. However, if the fleet is underutilized, for example in periods of economic recession where supply exceeds demand [70], increasing a ship's voyage time from implementing route optimization will allow the ship the save fuel, with no increase in fleet size necessary. However, [18] show emissions from shipbuilding to be comparatively small. Alongside this measure, the carbon intensity of the vessel transport work is calculated for each case over a full year. Carbon intensity is a measure of the transport efficiency of a vessel, and is expressed for an individual voyage as the Energy Efficiency Operational Indicator (EEOI):

$$EEOI = \frac{CO_2 \text{emissions [g]}}{\text{performed transport work [ton.nM]}} \tag{5.7}$$

Where the performed transport work is the mass of cargo multiplied by the distance over which the cargo is transported.

The CO_2 savings for the shortest distance and fuel-optimized case are 21.7 and 29.5 respectively (Table 5.5), corresponding to 2,450 and 3,330 tonnes of CO_2 saved per year. Table 5.5 also shows the EEOI for all cases. As the EEOI is an operational measure of the transport efficiency of an individual vessel, this value reduces for both the WASP and the fuel-optimized case. However, the fuel-optimized WASP obtains an additional benefit from traveling a longer distance, as the EEOI definition uses the actual distance traveled, which produces an inflated EEOI, as route optimization will increase the distance traveled but ultimately involves the same port-

Table 5.5.: Results from environmental assessment. Reference ship EEOI = 8.1E-3.

		WASP	Fuel-optimized WASP
CO_2 Savings	[t]		
Per Journey		29.5	40.1
Per Year		2450	3330
CO_2 Savings	[%]	21.7	29.5
EEOI	[gCO_2/tM]	6.34×10^{-3}	5.06×10^{-3}
Adjusted EEOI	[gCO_2/tM]	6.34×10^{-3}	5.71×10^{-3}

to-port distance. This factor does not affect other operational efficiency measures, as the vessel will usually follow the shortest-distance path. This study accounts for this factor by introducing an adjusted EEOI, which uses the port-to-port distance (shortest distance) in the EEOI calculation. Using these adjusted EEOI values, the percentage reduction in the EEOI is calculated as 21.7% and 29.5% for the WASP and fuel-optimized cases respectively (Table 5.5). This result matches the CO_2 savings for both the WASP case and fuel-optimized case, therefore correctly accounting for the increase in distance traveled. This adjusted EEOI should be regarded as a better measure of the operational efficiency of a route-optimized vessel.

Discussion and Conclusions

The performance of a WASP concept ship, a 19,500 DWT asphalt tanker with three Flettner rotors, has been assessed for operation on a North Sea route. The analysis was performed using a comprehensive vessel model, a fuel-optimized routing algorithm, and an economic assessment for payback period and net present value. The average fuel savings for the WASP concept vessel over two years of operation is 29.5, corresponding to CO_2 savings of 3,330 tonnes annually and a payback period of 9.7 years under present fuel prices, excluding a CO_2 price and other environmental incentives.

The vessel modeling presented is the combination of three main modules representing the work of the TU Delft Wind Assist research group: in aerodynamics, hydro-mechanics and marine engineering. The description of the vessel modeling has been necessarily brief due to the scope of work presented. A number of design and engineering effects are highlighted here:

- Optimal settings for the Flettner rotor velocity ratios can mitigate detrimental aerodynamic interaction effects between rotors.

- It was possible to de-power the Fletter rotors when the transverse stability or course-keeping ability of the ship were compromised.

- The need for rudder correction due to the destabilizing 'Munk' yawing moment generally increases with aerodynamic thrust, but the rudder will become less effective as the main propeller thrust is correspondingly reduced.

- The engine selection for WASP cases must be made with care considering the variation of the engine operating point within (or without) the engine envelope.

The Flettner rotor installation used for the present study was selected following a design space exploration in which candidate designs were assessed using a route-specific thrust benefit (TB) and vessel EEDI score. A point of diminishing returns was identified after which further investment in WASP propulsors offered marginal improvement for expected fuel savings along the route. This result was linked to operational constraints placed on vessel heel and leeway angles and on aerodynamic interaction effects occurring for close Flettner rotor spacing. The vessel EEDI

score, calculated with significantly lighter wind conditions than encountered along the North Sea route, was less affected by these operational constraints.

Yearly-averaged fuel savings from WASP on a route between Trondheim and Rotterdam are estimated and WASP is shown to produce significant savings on a shortest-distance route. Route optimization is also shown to deliver significant additional fuel savings when combined with WASP and annual fuel and CO_2 savings could typically be between 26% and 37% in the North Sea, depending on weather conditions. Route optimization requires additional ships to maintain the same service, due to the increase in voyage time incurred. The next iteration of this collaborative work will incorporate variable vessel speed in the vessel modeling and routing optimization, which has the potential to significantly increase both fuel and CO_2 savings and enable a closer examination of WASP vessel operation within commercial constraints.

Both regulatory- and market-based drivers will be key factors when considering the economics of Flettner rotors. Traditionally, WASP technologies have been difficult to finance due to the conservative attitudes of financial institutions that will favor more mature technologies perceived as carrying less risk [104]. The model presented in this work offers a robust method of assessing the viability of technologies on specific vessels and trade routes that can be used to create a business case for financing. Rotors are relatively simple to retrofit and thus applicable to a wide variety of existing tonnage, which could provide an attractive solution to avoid the stranding of assets in a carbon-constrained future. The investment in Flettner rotors will prove increasingly beneficial through the favorable impact of installed WASP technologies on the vessel EEDI, raising the possibility of qualifying for incentives such as Green Port Fees. From a market-based perspective, WASP trade can be seen as a promising option for investment in the near term as the push for transparency in shipping broadens to include more types of supply chains.

As with all energy-efficiency investments, the payback period projection only holds when considering an owner-operator scenario. Other chartering models introduce the split-incentive barrier where there is a disconnect between the party that takes the risk of the investment and the party that benefits from it [60, 88, 91]. Thus, on the voyage- or time-charter market, the owner needs to recoup the costs through higher charter rates which make them less competitive, putting less efficient vessels at an advantage and creating a canonical market for lemons [3]. This opportunity is another potential application of independent energy metrics and standards that will increase transparency, empowering charterers to select vessels based on their performance and also owners to negotiate profit-sharing agreements with greater trust.

6

Conclusions and Recommendations

Figure 6.1.: E-Ship1, a 10500 DWT RoLo equipped with four 27 m Flettner rotors. In operation since 2010. (source: www.enercon.de).

The research work presented in these chapters can be sorted into two main themes: the RANS-CFD simulation effort for hulls of the DWA, and experimental results for low-aspect ratio appendages. Finally, at the initiative and organization of the author, a collaborative effort was undertaken to asses wind assist within present-day market and regulatory conditions.

RANS-CFD Simulation and DWA

The sailing performance for commercial ship types has been discussed as a special case for the well-known modeling of ship maneuvering: vessel response in the lateral plane at small drift (leeway) angles. The wind-assisted ship, operating with a steady-state leeway angle, is subject to a destabilizing Munk yawing moment. In fact, course stability for these ships is a key design constraint, with the CLR (the hydrodynamic centroid) as a principal performance metric. The separation behavior along the bilges, responsible for the non-linear sideforce, is acutely sensitive to the leeway angle and represents the chief simulation challenge. Variation in the vortex strength and separation location leads to changes in the distribution of the hydrodynamic sideforce along the ship hull, an undesirable effect. For appended hull cases in particular, the CLR was very well predicted. The impact of these appendage types on course-keeping for wind-assist vessels can be investigated with the RANS-CFD tool.

The meshing strategy for simulation validation and full-scale production runs is informed by a grid verification and parameter study, where numerical uncertainty is determined for several grid sets with differing meshing strategies, for a range of Courant numbers, and considering modeling choices such as wall treatment and turbulence models. It was observed that grids with a large refinement diffusion exhibited superior performance as measured by the calculated uncertainties. This difference is interpreted as a requirement on the refinement of the wake of the sailing vessel. The influence of cell size at the ship hull was most apparent for the sideforce uncertainty. Finally, improvement in geometric similarity for grid set Cnobl, defined without boundary layer cells, gave better-behaved convergence and resulted in lower uncertainty estimates, which implies that the uncertainty estimates for practical meshes (with boundary layer cells) may be overstated. A parameter study included modeling choices such as wall treatment and turbulence model selection, where an ensemble error, E_{Ens}, and simulation computation time was used to design the full-scale production runs.

A series of validation statements was made for the simulation of hulls from the Delft Wind-Assist Series. First, an explicit validation statement was made for the parent hull of the series operating at $Fn = 0.168$ and for leeway angles $\beta= 0°$, 6°, 9°. Next, a validation statement was made based on multiple validation points. Here, the knowledge of the numerical uncertainty was limited to three operating conditions for the Hull #1 only. Results for r/r_{ref} were presented for several subsets of the validation set, defined according to the assumptions made for the numerical uncertainty. The validation metric r/r_{ref} was less than one for all cases for the bare-hull validation set, and the simulation method is regarded as validated with

validation levels indicated in Table 3.12. Finally, the meshing strategy adopted for full-scale production runs was described, followed by a discussion of scale effects and validation level. Results for the sailing performance of hulls from the Delft Wind-Assist Series are presented here for simulations performed at model scale and full scale. The implications of simulation validation levels for the data reduction and derived quantities are also discussed. An effort was made to give physical explanations for the significant systematic differences.

New Experiments for Low Aspect Ratio Appendages

Bilge keels and centerline keels are categorized as boundary-layer appendages, where the working principle is the promotion of flow separation in the vessel boundary layer. The appendage typology is shown to mitigate the strong Munk yawing moment that is characteristic for wind-assisted commercial vessels, and to promote the non-linear sideforce component. Also, the sailing efficiency (resistance increase due to sideforce) of a hull fitted with bilge keels or centerline keels, presenting a sharp tip profile to the lateral flow, can be improved dramatically. An optimal arrangement of bilge keels will result in a pattern of separation that is beneficial to the course-keeping of the vessel and its sailing efficiency. Experimental results from towing tank experiments for the sailing performance of bilge keels, centerline keels, and other special typologies have been presented. The bilge keel, already commonplace in the naval architecture of ships, finds new purpose as an effective appendage for wind-assisted commercial ships.

The working principle for bilge keels is the promotion of flow separation. For sailing ships, placement of bilge keels raises the possibility of specifying the separation location and of inducing flow separation at leeway angles for which separation would not yet occur for the un-appended hull. Results for small keel heights affirm the dimensioning adopted for the test, where a simple geometric scaling would not be appropriate. The behaviour observed in the neighborhood of the nominal height, set such that the keel extends unambiguously through the entire height of the model-scale boundary layer, conforms to results reported by [33]. There is a linear relationship between bilge keel height and the coefficients for sideforce and sailing efficiency (indicating a constant behaviour if the appendage planform area is considered). In contrast with the bilge heel height, bilge keel position influences both the linear and non-linear coefficients for the yawing moment, rather than the sideforce strength. One exceptional result to highlight is the keel at position P2 (approximately midship), for which the variation in CLR with leeway angle is markedly reduced. The yaw response is nearly linear for appendages at positions P1 and P2 (linear behaviour for both sideforce and yaw would return a CLR with no variation for leeway angle). Response for bilge keel length is restricted to sideforce, whereas yaw moment is unaffected. As for the bilge keel height, the linear response for the linear coefficient implies a constant response if the appendage planform area is taken into account (see Section 6.1).

Techno-economic Assessment

Finally, whereas the physics of sailing is an endlessly absorbing topic, finding a suitable place for wind assist in present-day market conditions may be the more pressing task (as in Chapter 5). The performance of a WASP concept ship, a 19,500 DWT asphalt tanker with three Flettner rotors, has been assessed for operation on a North Sea route. The analysis was performed using a comprehensive vessel model, a fuel-optimized routing algorithm, and an economic assessment for payback period and net present value. The average fuel savings for the WASP concept vessel over two years of operation is 29.5%, corresponding to CO_2 savings of 3,330 tonnes annually and a payback period of 9.7 years under present fuel prices, excluding a CO_2 price and other environmental incentives.

Increased voyage time for minimum-fuel route optimization is presented in terms of equivalent transport work, and the implications for the economic assessment and environmental impact are discussed. The economic case for wind assist, presented as a net present value analysis, is placed within the present-day regulatory climate, including Green Port Fee incentives and prospective carbon pricing. The final chapter shows that wind propulsion can contribute to the mitigation agenda of international shipping in regions with strong wind speeds such as the North Sea. A compelling business case exists based on fuel savings and existing regulatory measures, a case that is further bolstered by protection against assets stranded due to environmental obsolescence.

6.1. Recommendations and Ongoing Work

- Refinement of DWA; hydro-mechanic modeling

    Implementation regression modeling based on neural network approach (forthcoming publication)

    Present work is focused on further exploiting the data sets of the bare-hull series using an artificial neural network (ANN) to reproduce vessel response. ANN models were trained using the DWA database of RANS-CFD solutions. Following the first presentation of results ([113]), the ANN model comparison error, validation accuracy and training accuracy are of the same order as the validation level for the underlying RAN-CFD data. The derived model is 'lite' enough to be implemented within the framework of a performance prediction program for batch simulation, where it is able to support design investigations or fleet-level scenario analysis. Other opportunities include reconstructing detailed flow fields at the propeller disc and other points of interest.

    Extension and refinement of the DWA

Further sub-series for the DWA are presently in development, beginning with a high-T/L series to accommodate deep-sea ships. At the outset of this research, the consensus in the Sail-Assist group was that small-to-medium coasters would be a likely first vessel type to adopt wind assist. The author has observed a considerable shift in perceptions regarding wind assist in the intervening years. With suitable subsidies, large-scale implementations are already sailing (see: Maersk Pelican and M.V. Afros). Also to be noted is the absence of the propeller gondola or other contribution to A_{Lat} aft in the present series. The bare-hull case is therefore rather unforgiving.

Further experimental validation of simulation flow fields using P.I.V. technique

The possibility to reconstruct flow velocity fields using an ANN tool must include the issue of simulation validation beyond the body force components treated in this thesis. As discussed, a chief simulation challenge was the modeling for flow separation over the curved surface of the vessel bilge, raising also the possibility to investigate the impact of turbulence simulators on flow separation behaviour.

- Further analysis of appended-hull data from Chapter 4

RANS-CFD simulation

Following the successful simulation validation result for deadwood/skeg cases on Hull #34, priority in the testing matrix during the 2018 experiment was given to bilge keel and centerline keels (which were not well-replicated with the adopted methodology). A series of appended cases is planned to isolate the effect of A_{Lat} aft for centerline specials and other aft-body shapes. This topic can be investigated using the RANS-CFD tool.

- Refinement of wind-assist vessel modeling

Integrate main propulsor modeling and more elaborate control laws such as minimum speed threshold, and battery/fuel cell regeneration.

Acknowledgements

Bibliography

[1]   M. Abdel-Maksoud, Müller, T. Xing, S. Toxopeus, F. Stern, Kim, K. Shawn Petterson, Tormalm, Gietz, Schiller, and T. Rung. "Experimental and Numerical Investigations on Flow Characteristics of the KVLCC2 at 30° Drift Angle". In: *SNAME Transactions* (Jan. 2016), p. 26.

[2]   M. Acciaro, P. N. Hoffman, and M. S. Eide. "The energy efficiency gap in maritime transport". In: *Journal of Shipping Ocean Eng* 3.10 (2013), pp. 1–10.

[3]   G. A. Akerlof. "The Market for "Lemons": Quality Uncertainty and the Market Mechanism". In: *The Quarterly Journal of Economics* 84.3 (1970), pp. 488–500.

[4]   ASME. *Standard for Verification and Validation in Computational Fluid Dynamics and Heat Transfer*. Tech. rep. American Society of Mechanical Engineers, 2009.

[5]   Z. Barai and T. Longva. *Estimated CO2 Emissions Reduction From Introduction of Mandatory Technical and Operational Energy Efficiency Measures for Ships*. Tech. rep. MEPC 63/INF 2. International Maritime Organization, 2011.

[6]   M. Bentin, D. Zastrau, M. Schlaak, D. Freye, R. Elsner, and S. Kotzur. "A New Routing Optimization Tool-influence of Wind and Waves on Fuel Consumption of Ships with and without Wind Assisted Ship Propulsion Systems". In: *Transportation Research Procedia*. Vol. 14. 2016, pp. 153–162. isbn: 4949192817. doi: `10.1016/j.trpro.2016.05.051`.

[7]   W. Beukelman. *Cross Fow Drag on a Segmented Model*. Tech. rep. TU Delft, 1989.

[8]   W. Beukelman. *Lift and Drag for a Low Aspect-Ratio Surface Piersing Wing-Model in Deep and Shallow Water*. Tech. rep. Delft University of Technology, 1993.

[9]   W. Beukelman. "Manoeuvring Coefficients for a Wing-Model in Deep and Shallow Water". In: *International Shipbuilding Progress* 45 (1998), p. 441.

[10]   W. Beukelman and J. M. J. Journée. "Hydrodynamic Transverse Loads on Ships in Deep and Shallow Water". In: *HADMAR'2001, 22nd Int Conf. Hydrodyn. Aerodyn. Mar* 22 (2001).

[11]   W. Bollay. "A New Theory for Wings of Small Aspect Ratio". PhD thesis. Pasadena, 1936.

[12] G. Bordogna, N. J. van der Kolk, J. C. Mason, J. Bonello, and A. Vrijdag. "Wind-assisted ship propulsion performance prediction, routing and economic analysis - a corrected case study". In: *Conference: RINA Wind Propulsion Conference*. London, UK: Royal Institute of Naval Architects, Oct. 2019.

[13] A. Bows-larkin, S. Mander, P. Gilbert, M. Traut, C. Walsh, and K. Anderson. *High Seas, High Stakes.* High Seas Final Report. Tyndall Centre for Climate Change Research, 2014.

[14] A. Braathen. "Application of a Vortex Tracking Method to the Prediction of Roll Damping". In: *Norwegean Inst. Technol. Univ TRONDHEIM* (Jan. 1987).

[15] W. M. S. Bradbury. "An Experimental Investigation of the Flow Past Hulls at Leeway". In: *Journal of Wind Engineering and Industrial Aerodynamics* 20.1-3 (1985), pp. 227–265.

[16] O. Buhaug, J. Corbett, O. Endresen, V. Eyring, J. Faber, S. Hanayama, D. Lee, D. Lee, H. Lindstad, A. Markowska, A. Mjelde, D. Nelissen, J. Nilsen, C. Palsson, J. Winebrake, W. Wu, and K. Yoshida. *Second IMO GHG Study*. Tech. rep. International Maritime Organisation, 2009.

[17] P. M. Carrica, A. Mofidi, K. Eloot, and G. Delefortrie. "Direct simulation and experimental study of zigzag maneuver of KCS in shallow waters". In: *Ocean Engineering* 112 (2016), pp. 117–133.

[18] CE Delft. "Regulated Slow Steaming in Maritime Transport: An Assessment of Options, Costs and Benefits". In: *The ICCT* 2012 (Mar. 2012).

[19] CE Delft and UMAS. *Study on methods and considerations for the determination of greenhouse gas emission reduction targets for international shipping*. Brussels, 2019.

[20] B. Celik and J. Li. "Assessment of Numerical Uncertainty for the Calculations of Turbulent Flow over a Backward-facing Step". In: *Internaional Journal for Numerical Methods in Fluids* 49 (2005), pp. 1015–1031.

[21] A. R. Claughton and J. C. Oliver. "Developments in Hydrodynamic Force Models for Velocity Prediction Programs". In: *Conference on The Modern Yacht*. Royal Institute of Naval Architects, Sept. 2003.

[22] H. W. Coleman and W. G. Steele. "Experimentation and Uncertainty Analysis for Engineers". In: *Sterling* 6.3 (June 1990), pp. 231–231. doi: `10.1002/qre.4680060315`.

[23] B. Comer, S. Chen, and R. D. "Rotors and bubbles: Route-based assessment of innovative technologies to reduce ship fuel consumption and emissions". In: *International Council on Clean Transportation* (2019).

[24] G. B. Deng, E. Guilmineau, P. Queutey, and M. Visonneau. "Ship Flow Simulations with the ISIS-CFD Code". In: CFD Workshop Tokyo. Tokyo: CFD Workshp Tokyo, 2005.

[25] G. B. Deng, P. Queutey, and M. Visonneau. "A Code Verificaion Exercise for the Unstructured Finite Volume CFD Solver ISIS-CFD". In: ECCOMAS-CFD. Delft, 2006.

[26] R. Duvigneau and M. Visonneau. "On the role played by turbulence closures in hull shape optimization at model and full scale". In: *Journal of Marine Science and Technology* 8 (2003), pp. 11–25.

[27] L. Eça, V. Guilherme, and M. Hoekstra. "Code Verification, Solution Verification, and Validation in RANS Solvers". In: *Proceedings ASME Conference ence on Ocean, Offshore, and Arctic Engineering* (2010).

[28] L. Eca and M. Hoekstra. "On the Accuracy of the Numerical Prediction of Scale Effects on Ship Viscous Resistance". In: Barcelona: International Conference on Computational Methods in Marine Engineering, 2005.

[29] L. Eça and M. Hoekstra. "The numerical friction line". In: *Journal of Marine Science and Technology* 13 (4 2008), pp. 328–345.

[30] L. Eça and M. Hoekstra. "A Proceedure for the Estimation of the Numerical Uncertainty of CFD Calculations Based on Grid Refinement Studies". In: *Journal of Computational Physics* 262 (2014), pp. 104–130.

[31] R. Eggers. "Operational Performance of Wind Assisted Ships". In: *10th Symposium on High- Performance Marine Vehicles (HIPER)*. Cortona, Italy, 2016.

[32] J. Faber, A. Markowska, D. Nelissen, M. Davidson, V. Eyring, and I. Cionni. *Technical support for European action to reducing Greenhouse Gas Emissions*. 2009.

[33] O. M. Faltinsen and B. Sortland. "Slow drift eddy making damping of a ship". In: *Applied Ocean Research* 9.1 (1987), pp. 37–46.

[34] J. V. Fenhann. "CO2 Emissions from International Maritime Shipping". 2017.

[35] A. Flettner. "The Flettner rotorship". In: *Engineering* 19 (1925), pp. 117–120.

[36] W. Froude. "On the Practical Limits of the Rolling of a Ship in a Seaway". In: *Trans. Inst. Nav. Archit.* 6 (1865), pp. 175–186.

[37] T. Fujiwara, G. Hearn, F. Kitamura, M. Ueno, and Y. Minami. "Steady sailing performance of a hybrid-sail assisted bulk carrier". In: *Journal of Marine Science and Technology* (2005), pp. 131–146.

[38] T. Fujiwara, K. Hirata, M. Ueno, and T. Nimura. "On Aerodynamic Characteristics of a Hybrid-Sail with Square Soft Sail". In: *Thirteenth International conference for Offshore polar engineering*. June 2003, pp. 326–333.

[39] T. Fujiwara, M. Ueno, and Y. Ikeda. "A new estimation method of wind forces and moments acting on ships on the basis of physical component models". In: *Journal of Japan Society of Naval Architects and Ocean Engineers* (2005).

[40] J. Gerritsma and J. A. Keuning. "Sailing yacht performance in calm water and in waves". In: *HISWA Symposiumon Yacht Design and Yacht Construction*. Amsterdam, 1992, pp. 233–245.

[41] J. Gerritsma, J. A. Keuning, and A. Versluis. *Sailing yacht performance in calm water and in waves*. 1993.

[42]   J. Gerritsma and R. Onnink. "Geometry, Resistance and Stability of the Delft Systematic Yacht Hull Series". In: *TU Delft Report* 520 (1981), pp. 46–106.

[43]   P. Gilbert, A. Bows-larkin, S. Mander, and C. Walsh. "Technologies for the high seas: meeting the climate challenge". In: *Carbon Management* 5.4 (2014), pp. 447–461.

[44]   R. G. Hills. "Model Validation: Model Parameter and Measurement Uncertainty". In: *Journal of Heat Transfer* 128 (April 2006), pp. 339–351.

[45]   S. F. Hoerner. *Fluid Dynamic Lift - Practical Information on Aerodynamic Drag and Hydrodynamic Resistance*. CA: Bakersfield, 1965.

[46]   S. F. Hoerner. *Fluid Dynamic Lift - Practical Information on Aerodynamic and Hydrodynamic Lift*. Vancouver: Mrs. Liselotte A. Hoerner, 1985.

[47]   J. P. Hooft. "Cross flow drag on a manoeuvring ship". In: *Ocean Engineering* (1994).

[48]   J. P. Hooft and F. Quadvlieg. "Non-linear hydrodynamic hull forces derived from segmented model tests". In: *in Marine simulation and ship manoeuvrability* 1996 (), pp. 399–409.

[49]   N. Ikeda, H. Y., and Tanaka. "Report no. 401: On roll Keels, damping force of ship - effect of friction of hull and normal force of bilge". In: *J. Kansai Soc. Nav. Archit.* 161 (1976).

[50]   IMO. *Guidance on treatment of innovative energy efficiency technologies for calculation and verification of the attained EEDI*. Tech. rep. International Maritime Organization, 2013.

[51]   IMO. *Initial IMO Strategy on Reduction of GHG Emissions from Ships*. Tech. rep. MEPC 304(72). Resolution. International Maritime Organization, 2018.

[52]   IMO. *The costs of GHG reduction in international shipping*. Tech. rep. ISWG-GHG 3/3. International Maritime Organization, 2018.

[53]   S. Inoue, H. Masayoshi, and K. Katsuro. "Hydrodynamic derivatives and ship manoeuvering". In: *International Shipbuilding Progress* (1981).

[54]   ITTC. *Force and Moment Uncertainty Analysis for Planar Motion Test*. Tech. rep. 2008.

[55]   ITTC. *Recommended Practices- Uncertainty Analysis in CFD Verification Proceedures*. Tech. rep. 2008.

[56]   ITTC. *Uncertainty Analysis in CFD: Verification and Validation, Methodology and Proceedures*. Tech. rep. 2008.

[57]   ITTC. *Recommended Procedures and Guidelines: Guide to the Expression of Uncertainty in Experimental Hydrodynamics*. Tech. rep. International Towing Tank Conference, 2014.

[58]   ITTC. *Validation and Verification of RANS Solutions*. Tech. rep. 2014.

[59]   W. Jacobs. "Estimation of stability derivatives and indices of various ship forms, and comparison with experimental results". In: *Journal of Ship Research* (1966), pp. 135–163.

[60] A. B. Jaffe and R. N. Stavins. "The energy-efficiency gap: What does it mean?" In: *Energy Policy* 22.10 (1994), pp. 804–810.

[61] R. T. Jones. *Properties of low-aspect ratio pointed wings at speeds below and above the speed of sound*. Tech. rep. 835. NACA, 1946.

[62] R. Karslen, G. Papachristos, and N. Rehmatulla. "An agent-based model of climate-energy policies to promote wind propulsion technology in shipping". In: *Environmental Innovation and Societal Transitions* 31 (June 2019), pp. 33–53.

[63] J. E. Kerwin. "A Velocity Prediction Program for Ocean Racing Yachts". In: *New England Sailing Yacht Symposium*. 1976.

[64] J. A. Keuning and B. J. Binkhorst. *Appendage Resistance of a Sailing Yacht Hull*. Chesapeak Sail Yacht Symposium. 1997.

[65] J. A. Keuning and U. B. Sonnenberg. "Approximation of the hydrodynamic forces on a sailing yacht based on the 'Delft Systematic Yacht Hull Series'". In: *HISWA Symposiumon Yacht Design and Yacht Construction*. 1998, pp. 99–152.

[66] J. A. Keuning and K. J. Vermeulen. "On the balance of large sailing yachts". In: *HISWA Symposiumon Yacht Design and Yacht Construction*. Amsterdam, 2002.

[67] J. A. Keuning and K. J. Vermeulen. "The yaw balance of sailing yachts upright and heeled". In: *16th Chesapeake Sailing Yacht Symposium*. 2003.

[68] K. Kijima and Y. Nakiri. *Prediction Method Of Ship Manoeuvrability In Deep And Shallow Waters*. 1990.

[69] J. A. Kramer, S. Steen, and L. Savio. "Experimental study of the effect of drift angle on a ship-like foil with varying aspect ratio and bottom edge shape". In: *Ocean Engineering* 121 (2016), pp. 530–545.

[70] H. E. Lindstad and S. E. Gunnar. "Low carbon maritime transport: How speed, size and slenderness amounts to substantial capital energy substitution". In: *Transportation Research Part D: Transport and Environment* 10.1016 (2015), pp. 244–256.

[71] U. Lloyd's Register. *Fuel production cost estimates and assumptions*. Zero-Emission Vessels: Transition Pathways. London, 2019. url: `http://info.lr.org/ZEV-transition-pathways`.

[72] J. Longo and F. Stern. "Effects of drift angle on model ship flow". In: *Experiments in Fluids* 32.5 (2002), pp. 558–569.

[73] S. Mander. "Slow steaming and a new dawn for wind propulsion: A multi-level analysis of two low carbon shipping transitions". In: *Maritime Policy* 75 (2017), pp. 210–216.

[74] Y. Minami, T. Nimura, T. Fujiwara, and M. Ueno. "Investigation into underwater fin arrangement effect on steady sailing characteristics of a sail assisted ship". In: *International Offshore and Polar Engineering Conference - Proceedings* (2003), pp. 318–325.

[75] M. M. Munk. *Remarks on the Pressure Distribution over the Surface of an Ellipsoid Moving Translationally Through a Perfect Fluid*. Tech. rep. NACA, 1924.

[76] D. NA. *Ecoliner*. Amsterdam, 2010.

[77] P. Naaijen, W. Shi, and J. Kherian. "Assessing the fuel savings by using auxiliary wind propulsion from traction kites". In: *RINA - Ship Design and Operation for Environmental Sustainability - Papers* (2010), pp. 27–37.

[78] D. Nelissen, M. Traut, J. Kohler, W. Mao, J. Faber, and S. Ahdour. "Study on the analysis of market potentials and market barriers for wind propulsion technologies for ships". In: *Shipping and Marine Technology* (2016). doi: `10.2834/68747`.

[79] J. N. Newman. *Marine Hydrodynamics*. Boston: MIT Press, 1977.

[80] K. Nomoto and H. Tatano. *Balance of Helm of Sailing Yachts*. 1979.

[81] Numeca Inc. *ISIS Theoretical Manual*. Tech. rep. Numeca International.

[82] W. L. Oberkampf. "A Proposed Framework for Computational Fluid Dynamics Code Calibration/Validation". In: *AIAA* (94-2540 1994).

[83] OECD. *Reducing Shipping Greenhouse Gas Emissions: lessons From Port-Based Incentives*. Tech. rep. OECD, 2018.

[84] K. Ouchi, K. Uzawa, A. Kanai, and M. Katori. *'Wind Challenger' the Next Generation Hybrid Sailing Vessel*. Tech. rep. University of Tokyo, 2013.

[85] Port of Rotterdam. *General Terms and Conditions including Port Tariffs*. Tech. rep. Port of Rotterdam, 2019.

[86] L. Prandtl. "Tragflügeltheorie". In: *Königliche Gesellschaft der Wissenschaften* (1918).

[87] P. Queutey and M. Visonneau. "An interface capturing method for free-surface hydrodynamic flows". In: *Computers and Fluids* 36 (November 2007), pp. 1481–1510.

[88] N. Rehmatulla, S. Parker, T. Smith, and V. Stulgis. "Wind technologies: Opportunities and barriers to a low carbon shipping industry". In: *Marine Policy* 75 (2017), pp. 217–226. doi: `10.1016/j.marpol.2015.12.021`.

[89] L. F. Richardson. "The Deferred Approach to the Limit". In: *Transactions of Royal Society London* 226 (1927), pp. 299–361.

[90] P. J. Roache. "Quantification of Uncertainty in Computational Fluid Dynamics". In: *Ann. Rev. of Fluid Mechanics* 29 (1997), pp. 123–160.

[91] I. Rojon and C. Dieperink. "'Blowin' in the wind? Drivers and barriers for the uptake of wind propulsion in international shipping". In: *Energy Policy* 67 (2014), pp. 394–402.

[92] M. Rosander and J. O. V. Bloch. *Modern Windships*. Ed. by K. E. Hansen. 2000.

[93]   T. Sarpkaya and J. L. O'Keefe. "Oscillating Flow about Two and Three-Dimensional Bilge Keels". In: *J. Offshore Mech Arct. Eng* 118 (Feb. 1996), pp. 1–6.

[94]   "Windship Technology". In: *Windship Technology*. Ed. by C. J. Satchwell. 1985.

[95]   J. Scott and et al. "The promise and limits of private standards in reducing greenhouse gas emissions from shipping". In: *Journal of Environmental Law* 29.2 (2017), pp. 231–262.

[96]   Secretariat. *EEDI Database – Review of Status of Technological Development*. Research rep. MEPC 68/INF.13. International Maritime Organization, 2015.

[97]   A. Skogman. "The practical Meaning of Lateral Balance for a Sail-Assisted Research Vessel". In: *Journal of Wind Engineering and Industrial Aerodynamics* 20.1 (1985), pp. 201–226.

[98]   T. Smith. *Reducing the Maritime Sector's Contribution to Climate Change and Air Pollution. Scenario Analysis: Take-up of Emissions Reduction Options and their Impacts on Emissions and Costs*. Tech. rep. Department for Transport. London, 2019.

[99]   T. Smith, J. Jalkanen, B. Anderson, J. Corbett, J. Faber, S. Hanayam, E. O'keefe, S. Parker, L. Johansson, L. Aldous, C. Raucci, M. Traut, S. Ettinger, D. Nelissen, D. Lee, S. Ng, A. Agarwal, J. Winebrake, M. Hoen, S. Chesworth, and A. Pandey. *Third IMO GHG Study*. London: International Maritime Organisation, 2014.

[100] T. Smith, P. Newton, G. Winn, G. L. A., and A. Rosa. "Analysis techniques for evaluating the fuel savings associated with wind assistance". In: *Low Carbon Shipping Conference*. 2013.

[101] F. Stern, R. Wilson, H. Coleman, and E. Paterson. "Comprehensive Approach to Verification and Validation of CFD Simulations–Part 1: Methodology and Procedures". In: *Journal of Fluids Engineering* (2001), pp. 793–810.

[102] F. Stern, R. Wilson, and J. Shao. "Quantitative V&V of CFD Simulations and Certification of CFD Codes". In: *International Journal for Numerical Methods in Fluids* 50 (2005), pp. 1335–1355.

[103] G. Struijk. "Hydrodynamics of Wind Assisted Ship Propulsion". In: *MSc Thesis* (2015).

[104] V. Stulgis and et. al. *Hidden treasure: financial models for retrofits*. Washington, 2014.

[105] S. L. Toxopeus. "Practical application of viscous-flow calculations for the simulation of manoeuvering ships". PhD thesis. 2011.

[106] M. Traut, A. Larkin, K. Anderson, C. McGlade, M. Sharmina, and T. Smith. "CO2 abatement goals for international shipping". In: *Climate Policy* 18.8 (2018), pp. 1066–1075.

[107] M. Traut, P. Gilbert, C. Walsh, A. Bows, A. Filippone, P. Stansby, and R. Wood. "Propulsive power contribution of a kite and a Flettner rotor on selected shipping routes". In: *Applied Energy* 113 (2014), pp. 362–372. doi: `10.1016/j.apenergy.2013.07.026`.

[108] Trondheim Port Authority. "Port Tariffs Trondheim". Accessed 05/08/2019. 2019. url: `https://trondheimhavn.no/tjeneste/havneregulativ`.

[109] S. Tsakonas. *Effect of Appendage and Hull Form on Hydrodynamic Coefficients of Surface Ships*. Tech. rep. Hoboken, NJ, 1959.

[110] United Nations. *The Paris Agreement*. Tech. rep. Accessed 9 Mar. 2017. United Nations, 2015. url: `http://unfccc.int/paris%5C_agreement/items/9485.php`.

[111] N. van der Kolk; G. Bordogna; J.C. Mason; J.M. Bonello; A. Vrijdag; J.F. Broderick; A. Larkin; T. Smith; I. Akkerman; J.A. Keuning; R.H.M. Huijsmans; "Wind-Assist for Commercial Ships: A Techno-Economic Assessment". In: *Ship and Offshore Structures* (2020). (manuscript under review).

[112] N. J. van der Kolk, J. A. Keuning, and R. H. M. Huijsmans. "Hydrodynamics of Wind-Assisted Ship Propulsion: Verification of RANS Simulations". In: *International Conference in Hydrodynamics*. International Conference for Ship Hydrodynamics. Egmond aan Zee, 2016.

[113] N. van der Kolk and B. S. Freeman. "Machine Learning Based Hydro-mechanic Modeling for Wind-assisted Ships". In: *InnovSAIL2020*. 2020.

[114] R. van 't Veer, X. Schut, and J. Pelerin. "Bilge Keel Loads and Hull Induced Pressures : Experimental Results". In: *Omae2015*. June 2015.

[115] van der Kolk N. J., A. I., J. A. Keuning, and R. H. M. Huijsmans. "Low aspect appendages for wind-assisted ships". In: *Journal of Marine Science and Technology* (2019). (manuscript under review).

[116] van der Kolk N. J., J. A. Keuning, and R. H. M. Huijsmans. "Part 1: Experimental Validation of a RANS-CFD Methodology for the Hydrodynamics of Wind-Assisted Ships Operating at Leeway Angles". In: *Ocean Engineering* 178 (2018), pp. 375–387. doi: `10.1016/j.oceaneng.2018.12.041`.

[117] N. J. van der Kolk. "Hydrodynamics of Wind-Assisted Ship Propulsion: Modelling of Hydrodynamic Sideforce". In: *HISWA Symposium on Yacht Design and Yacht Construction*. HISWA Technical Conference. Amsterdam, 2016.

[118] N. J. van der Kolk, I. Akkerman, J. A. Keuning, and R. H. M. Huijsmans. *Dataset: Bilge Keels for Course Stability and Sailing Efficiency of Wind-Assisted Ships*. en. 2019. doi: `10.4121/UUID:A9314E24-5D4C-4C46-9F99-391EE7CDC1EB`.

[119] N. J. van der Kolk, G. Bordogna, J. C. Mason, P. Desprairies, and A. Vrijdag. "Case study: Wind-assisted ship propulsion performance prediction, routing, and economic modelling". In: *Proceedings of the International Conference Power & Propulsion Alternatives for Ships*. London: The Royal Institution of Naval Architects, 2019.

[120] N. van der Kolk, I. Akkerman, J. A. Keuning, and R. HUuijsmans. "Part 2: Simulation Methodology and Numerical Uncertainty for RANS-CFD for the Hydrodynamics of Wind-Assisted Ships Operating at Leeway Angles". In: *Ocean Engineering* (2020). doi: `https://doi.org/10.1016/j.oceaneng.2020.107024`.

[121] I. M. Viola, P. Bot, and M. Riotte. "On the Uncertainty of CFD in Sail Aerodynamics". In: *International Journal for Numerical Methods in Fluids* 72 (2013), pp. 1146–1164.

[122] C. Walsh, S. Mander, and A. Larkin. "Charting a low carbon future for shipping: A UK perspective". In: *Maritime Policy* 82 (May 2017), pp. 32–40.

[123] R. Wilson, P. Carrica, and F. Stern. "Unsteady RANS method for ship motions with application to roll for a surface combatant". In: *Computers and Fluids* 35 (2006), pp. 501–524.

[124] T. Xing, S. Bhushan, and F. Stern. "Vortical and turbulent structures for KVLCC2 at drift angle 0, 12, and 30 degrees". In: *Ocean Engineering* 55 (2012), pp. 23–43.

[125] Y. Yoshimura. "A Prospect of Sail-Assisted Fishing Boats". In: *Fishing Science* 68.2 (2002), pp. 1815–1818.

[126] L. Yuankui, Z. Yingjun, and Z. Feixiang. "Minimal Time Route for Wind-Assisted Ships". In: *Marine Technology Society Journal* 48.3 (2014), pp. 115–124. issn: 00253324. doi: `10.4031/MTSJ.48.3.2`.

A

Delft Wind Assist Series

A.1. Series Definition

The Delft Wind Assist series is a set of 60 hull forms developed by researchers at Delft University of Technology. The parent hulls of the series are based on wind-assist concepts by Dykstra Naval Architects ([76]). The hull forms are varied in a systematic way so that the influence of particular form coefficients on the sailing behavior may be isolated an studied. The series is set up to span a design space that is presently meaningful for the application of wind-assist propulsion.

The main particulars for the Ecoliner parent hull are provided in Table A.1.

Table A.1.: Main particulars for the Ecoliner Parent hull.

	Full Scale
LOA [m]	138
Beam [m]	18
Draft [m]	6.5
Displacement [kg]	$11\,896 \times 10^3$
C_B	0.719
C_P	0.764
C_M	0.942
LCB [%]	50.13
Whetted Surface m^2	3.293

The hull forms are varied in a systematic way so that the influence of particular form coefficients on the sailing behavior may be isolated an studied. The series is set up to span a design space that is presently meaningful for the application of wind-assist propulsion.The DWA systematic hull series is composed of three sub-series's:

1st Series	General cargo ship
2nd Series	Deadrise variations; based on 19 and 20th century clipper ships
3rd Series	Low-C_P ships (ferry, cruise, and ro-pax types)

The sailing behavior of hull variants of the series has been analyzed with the RANS-CFD simulation tool described in Chapter 3. This database of full-scale simulation results is a representation of the sailing response for commercial ships. The sailing characteristics of a vessel that falls within the extents of the series is to be inferred from a meta-model for the response surface.
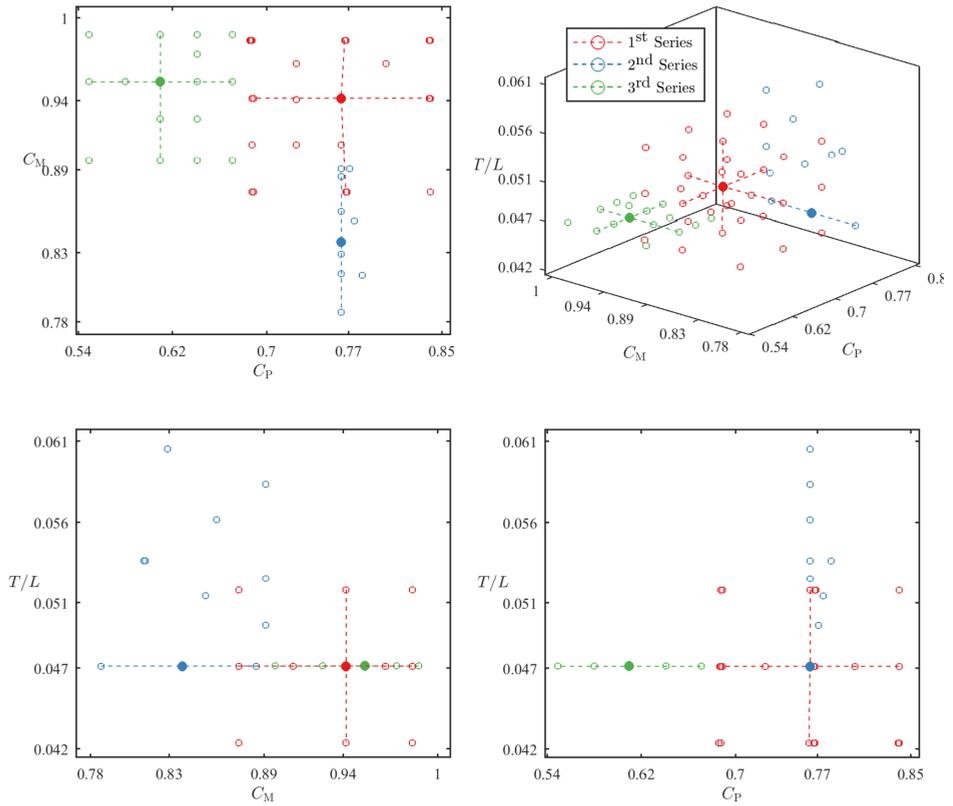
Figure A.1.: Composition of the Delft Wind Assist Series
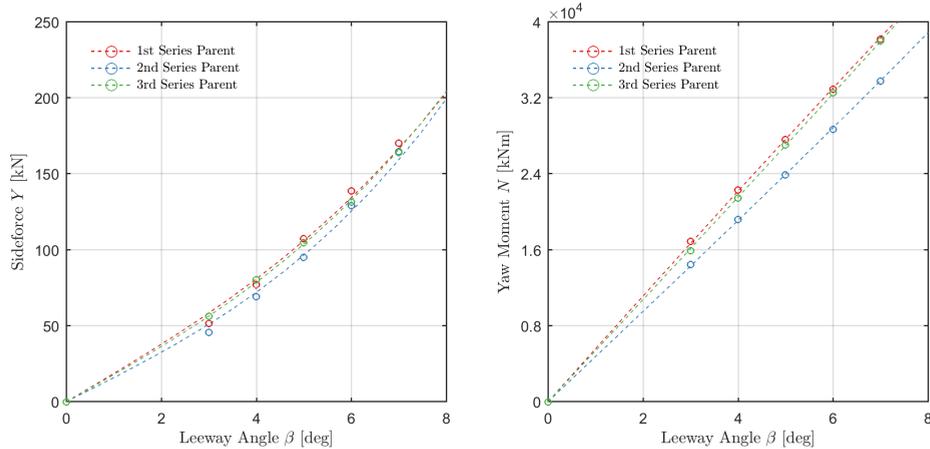
(a) Sideforce Y (b) Yaw moment N

Figure A.2.: Hydrodynamic response for Parent hulls of the Delft Wind Assist Series. Whereas Hull # 1 (1st Series parent) and #45 (3rd Series parent) share similar response, the deadrise parent (Hull #34) generates significantly less yawing moment. Simulation result.

1st Series: Ecoliner

The first series, developed by Struijk [103], and extended by the author, is a full factorial parameter variation for draft-to-length ratio T/L, Prismatic coefficient C_P, and Midship coefficint C_M. The Ecoliner concept [76] is the parent hull for this series and also the second series. The series comprises 42 hulls, for which the prismatic coefficient, the midship coefficient, the draft-to-length ratio, and the deadrise angle are systematically varied. The variation for prismatic coefficient is effected by lengthening or shortening the parallel mid-body. The midship coefficient is modified by increasing and decreasing the bilge radius. For variations in the draft-to-length ratio, the displacement is kept constant by reducing the beam accordingly.

The original series (hulls 1-27) was extended by the author following an analysis of the response surface (present work). Six new hulls (hulls 28-33) were added according to the Hessian of the response surface.

Figure A.3.: Hull #1 - Parent hull of the first series.

Table A.2.: Hydrostatics for hulls of the first series in the Delft Wind-Assist Series.

Hull ID # (Description)	C_B	C_P	C_M	C_{WP}	$L/\nabla^{\frac{1}{3}}$	L/B	B/T	T/L	R_b/T	Deadrise [deg]
1 (Parent)	0.719	0.764	0.942	0.883	6.10	7.67	2.77	0.047	0.615	0
series max	0.840	0.984	0.925	6.47	8.44	3.42	0.052	1.026	0	0
series min	0.686	0.874	0.832	5.82	6.90	2.29	0.042	0.280	0	0
2 (T+)	0.720	0.764	0.942	0.883	6.09	8.43	2.29	0.052	0.559	0
3 (T-)	0.719	0.763	0.942	0.882	6.10	6.90	3.42	0.042	0.684	0
4 (Cp+)	0.791	0.840	0.942	0.921	5.91	7.67	2.77	0.047	0.615	0
5 (Cp-)	0.649	0.689	0.942	0.861	6.31	7.67	2.77	0.047	0.615	0
6 (Cm+)	0.755	0.767	0.984	0.890	6.00	7.67	2.77	0.047	0.308	0
7 (Cm-)	0.671	0.768	0.874	0.874	6.24	7.67	2.77	0.047	0.923	0
8 (T+Cp+)	0.791	0.840	0.942	0.922	5.90	8.43	2.29	0.052	0.559	0
9 (T+Cp-)	0.649	0.689	0.942	0.862	6.31	8.43	2.29	0.052	0.559	0

Table A.2.: Hydrostatics for hulls of the first series in the Delft Wind-Assist Series.

Hull ID # (Description)	C_B	C_P	C_M	C_{WP}	$L/\nabla^{\frac{1}{3}}$	L/B	B/T	T/L	R_b/T	Deadrise [deg]
1 (Parent)	0.719	0.764	0.942	0.883	6.10	7.67	2.77	0.047	0.615	0
series max	0.840	0.984	0.925	6.47	8.44	3.42	0.052	1.026	0	0
series min	0.686	0.874	0.832	5.82	6.90	2.29	0.042	0.280	0	0
10 (T-Cp+)	0.790	0.839	0.942	0.921	5.91	6.90	3.42	0.042	0.684	0
11 (T-Cp-)	0.648	0.688	0.942	0.860	6.31	6.90	3.42	0.042	0.684	0
12 (T+Cm+)	0.756	0.768	0.984	0.891	6.00	8.43	2.29	0.052	0.280	0
13 (T+Cm-)	0.672	0.769	0.874	0.876	6.24	8.44	2.29	0.052	0.839	0
14 (T-Cm+)	0.755	0.767	0.984	0.889	6.00	6.90	3.42	0.042	0.342	0
15 (T-Cm-)	0.671	0.768	0.874	0.874	6.24	6.91	3.41	0.042	1.026	0
16 (Cp+Cm+)	0.826	0.840	0.984	0.925	5.82	7.67	2.77	0.047	0.308	0
17 (Cp+Cm-)	0.734	0.840	0.874	0.912	6.06	7.67	2.77	0.047	0.923	0
18 (Cp-Cm+)	0.676	0.687	0.984	0.868	6.22	7.67	2.77	0.047	0.308	0
19 (Cp-Cm-)	0.602	0.689	0.874	0.832	6.47	7.67	2.77	0.047	0.923	0
20 (T+Cp+Cm+)	0.827	0.840	0.984	0.925	5.82	8.43	2.29	0.052	0.280	0
21 (T+Cp+Cm-)	0.734	0.840	0.874	0.914	6.06	8.44	2.29	0.052	0.839	0
22 (T+Cp-Cm+)	0.677	0.688	0.984	0.868	6.22	8.43	2.29	0.052	0.280	0
23 (T+Cp-Cm-)	0.602	0.689	0.874	0.834	6.47	8.44	2.29	0.052	0.839	0
24 (T-Cp+Cm+)	0.826	0.839	0.984	0.924	5.82	6.90	3.42	0.042	0.342	0
25 (T-Cp+Cm-)	0.734	0.840	0.874	0.913	6.06	6.91	3.41	0.042	1.026	0
26 (T-Cp-Cm+)	0.675	0.686	0.984	0.866	6.22	6.90	3.42	0.042	0.342	0
27 (T-Cp-Cm-)	0.601	0.688	0.874	0.832	6.47	6.91	3.41	0.042	1.026	0
28 (Cp-1/2)	0.683	0.726	0.941	0.861	6.20	7.67	2.77	0.047	0.615	0
29 (Cm-1/2)	0.694	0.764	0.908	0.879	6.17	7.67	2.77	0.047	0.769	0
30 (Cp-1/2 Cm-1/2)	0.659	0.726	0.908	0.857	6.28	7.67	2.77	0.047	0.769	0

Continued on Next Page...

Table A.2.: Hydrostatics for hulls of the first series in the Delft Wind-Assist Series.

Hull ID # (Description)	C_B	C_P	C_M	C_{WP}	$L/\nabla^{\frac{1}{3}}$	L/B	B/T	T/L	R_b/T	Deadrise [deg]
1 (Parent)	0.719	0.764	0.942	0.883	6.10	7.67	2.77	0.047	0.615	0
series max	0.840	0.984	0.925	6.47	8.44	3.42	0.052	1.026	0	0
series min	0.686	0.874	0.832	5.82	6.90	2.29	0.042	0.280	0	0
31 (Cp- Cm-1/2)	0.625	0.688	0.908	0.835	6.39	7.67	2.77	0.047	0.769	0
32 (Cp-1/2 Cm+1/2)	0.702	0.726	0.967	0.865	6.14	7.67	2.77	0.047	0.462	0
33 (Cp+1/2 Cm+1/2)	0.776	0.802	0.967	0.907	5.94	7.67	2.77	0.047	0.462	0

2nd Series: Deadrise Series

For the initial series, deadrise is varied while maintaining a constant displacement. Alternatively, the lateral area might be held constant, as suggested by the typical non-dimensionalization of forces within the manoeuvring context. Finally, the global dimensions could be "relaxed" across the hulls of the initial series, in favour of maintaining similarity in other hull form parameters. The role of the hydrodynamic sideforce as a reactionary force to the transvers component of the sail force, with its linear proportionality with sail thrust, suggests scaling with the total resistance of the ship. This scaling is counter to existing approaches for sailing vessels, based in airfoil theory, but as the characterization of a commercial ship hull as a (low- aspect) wing is tenuous, it is felt that the more general approach where displacement is constant would allow for direct comparison between hulls.

The deadrise series is an extension of the first Ecoliner series. The series con-stitutes hulls purely with variations in deadrise (in so far as possible) for deadrise angles 6°, 10°, and 14°. Deadrise is introduced by drawing two lines, tangent to the bilge radii and at the requisite angle which meet along the centreline, forming the new keel. Care is taken to preserve the shape and second moment of the sec-tional area curve, and the distribution of lateral surface area along the length of the hull. The waterline entrance angle at the bow, and the sweep of the buttock lines along the aft-body are unchanged insofar as possible. The breadth of the waterline at the transom is held constant.

The lateral area is held constant for hulls 34-36, as suggested by the typical non-dimensionalization of forces within the manoeuvring context. This is achieved with affine stretching, with corresponding effect on the bilge immersion and the height of the vertical side-walls (seen as the 'span' of the wing). To study the influence of deadrise only, the bilge location is held constant for hulls 37-39, resulting in an increase for T/L. Further hulls are defined to investigate possible interactions between deadrise and bilge radius R_b/T, using hulls 6 (C_M +), and 7 (C_M-) of the first series. Finally, hulls with constant displacement are defined (hull numbers 42-44) using a Lackenby transformation.
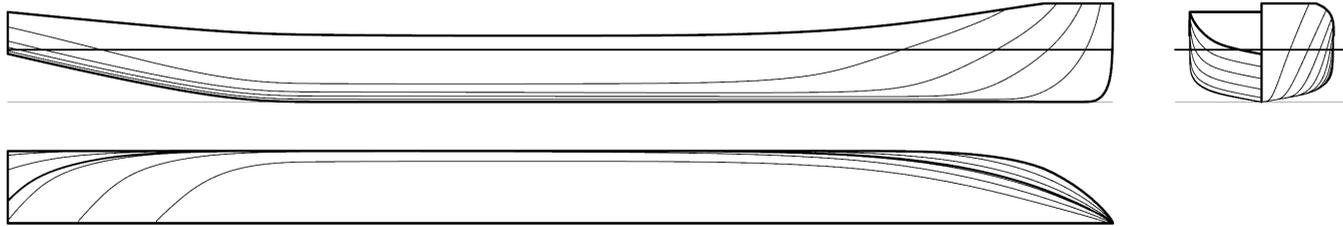
Figure A.4.: Hull #34 - Parent hull of the second series.

Table A.3.: Hydrostatics for hulls of the second series in the Delft Wind-Assist Series.

Hull ID # (Description)	C_B	C_P	C_M	C_{WP}	$L/\nabla^{\frac{1}{3}}$	L/B	B/T	T/L	R_b/T	Deadrise [deg]
34 (Parent)	0.641	0.764	0.838	0.883	6.33	7.67	2.77	0.047	0.691	10
series max	0.687	0.782	0.891	0.890	6.47	7.67	2.77	0.061	0.691	14
series min	0.602	0.764	0.787	0.874	5.78	7.67	2.16	0.047	0.598	6
35 (DR6 TL)	0.676	0.764	0.885	0.883	6.22	7.67	2.77	0.047	0.667	6
36 (DR14 TL)	0.602	0.764	0.787	0.883	6.47	7.67	2.77	0.047	0.679	14
37 (DR6)	0.681	0.764	0.891	0.883	5.98	7.67	2.48	0.053	0.629	6
38 (DR10)	0.657	0.764	0.860	0.883	5.92	7.67	2.32	0.056	0.623	10
39 (DR14)	0.634	0.764	0.829	0.883	5.85	7.67	2.16	0.061	0.614	14
40 (DR10 Cm+)	0.681	0.764	0.891	0.890	5.78	7.67	2.24	0.058	0.598	10
41 (DR10 Cm-)	0.623	0.764	0.815	0.874	6.13	7.67	2.43	0.054	0.649	10
42 (DR6 Disp)	0.687	0.771	0.891	0.883	6.08	7.67	2.63	0.050	0.655	6

Table A.3.: Hydrostatics for hulls of the second series in the Delft Wind-Assist Series.

Hull ID # (Description)	C_B	C_P	C_M	C_{WP}	$L/\nabla^{\frac{1}{3}}$	L/B	B/T	T/L	R_b/T	Deadrise [deg]
34 (Parent)	0.641	0.764	0.838	0.883	6.33	7.67	2.77	0.047	0.691	10
series max	0.687	0.782	0.891	0.890	6.47	7.67	2.77	0.061	0.691	14
series min	0.602	0.764	0.787	0.874	5.78	7.67	2.16	0.047	0.598	6
43 (DR10 Disp)	0.662	0.775	0.853	0.883	6.08	7.67	2.54	0.051	0.639	10
44 (DR14 Disp)	0.637	0.782	0.814	0.883	6.08	7.67	2.43	0.054	0.638	14

3rd Series: Low-C_{P} Ships

Ships with low-density cargo (Ro-pax or passenger ships), will have slender hull forms. These will generally be effective sailing hulls, with fine entry angle and low residuary resistance. This is accompanied by a shorter parallel mid-body / bilge.

Parameter variations for the Low-C_{P} series was arranged to investigate C_{P} and C_{M} (R_{b}/T). The hulls were defined using the same approach as for the 1st Series, where a finer subdivision was made (+1/2 corresponds to a +5% increase in the hull parameter.
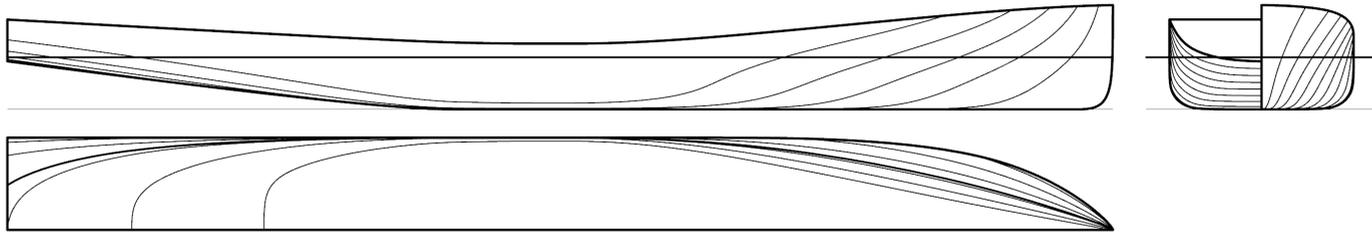
Figure A.5.: Hull #45 - Parent hull of the third series.

Table A.4.: Hydrostatics for hulls of the third series in the Delft Wind-Assist Series.

Hull ID # (Description)	C_B	C_P	C_M	C_{WP}	$L/\nabla^{\frac{1}{3}}$	L/B	B/T	T/L	R_b/T	Deadrise [deg]
45 (Parent)	0.582	0.610	0.954	0.805	6.03	6.00	3.54	0.047	0.615	0
series max	0.663	0.671	0.988	0.841	6.371	6.005	3.538	0.047	0.923	0
series min	0.493	0.549	0.897	0.747	5.769	5.998	3.534	0.047	0.308	0
46 Cp+	0.640	0.671	0.954	0.834	5.84	6.00	3.54	0.047	0.615	0
47 Cp-	0.524	0.549	0.954	0.769	6.24	6.00	3.54	0.047	0.615	0
48 Cm+	0.603	0.610	0.988	0.810	5.96	6.00	3.54	0.047	0.308	0
49 Cm-	0.547	0.610	0.897	0.782	6.15	6.01	3.53	0.047	0.923	0
50 Cm-$1/2$	0.566	0.610	0.927	0.792	6.08	6.00	3.54	0.047	0.769	0
51 Cp+$1/2$	0.611	0.641	0.954	0.818	5.93	6.00	3.54	0.047	0.615	0
52 Cp-$1/2$	0.553	0.580	0.954	0.784	6.13	6.00	3.54	0.047	0.615	0
53 Cp+Cm+	0.663	0.671	0.988	0.841	5.77	6.00	3.54	0.047	0.308	0

Continued on Next Page...

Table A.4.: Hydrostatics for hulls of the third series in the Delft Wind-Assist Series.

Hull ID # (Description)	C_B	C_P	C_M	C_{WP}	$L/\nabla^{\frac{1}{3}}$	L/B	B/T	T/L	R_b/T	Deadrise [deg]
45 (Parent)	0.582	0.610	0.954	0.805	6.03	6.00	3.54	0.047	0.615	0
series max	0.663	0.671	0.988	0.841	6.371	6.005	3.538	0.047	0.923	0
series min	0.493	0.549	0.897	0.747	5.769	5.998	3.534	0.047	0.308	0
54 Cp+Cm-	0.602	0.671	0.897	0.819	5.96	6.01	3.53	0.047	0.923	0
55 Cp-Cm+	0.543	0.549	0.988	0.781	6.17	6.00	3.54	0.047	0.308	0
56 Cp-Cm-	0.493	0.549	0.897	0.747	6.37	6.01	3.53	0.047	0.923	0
57 Cp+1/2Cm+	0.633	0.641	0.988	0.826	5.86	6.00	3.54	0.047	0.308	0
58 Cp+1/2Cm-	0.575	0.641	0.897	0.801	6.05	6.01	3.53	0.047	0.923	0
59 Cp+1/2Cm+1/2	0.625	0.641	0.974	0.823	5.88	6.00	3.54	0.047	0.461	0
60 Cp+1/2Cm-1/2	0.595	0.641	0.927	0.809	5.98	6.00	3.54	0.047	0.769	0

A.2. Data Reduction

All data is non-dimensionalised according to the maneuvering convention:

$$C_X = \frac{X}{\frac{1}{2}\rho V^2 LT} \tag{A.1}$$

$$C_Y = \frac{Y}{\frac{1}{2}\rho V^2 LT} \tag{A.2}$$

$$C_N = \frac{N}{\frac{1}{2}\rho V^2 L^2 T} \tag{A.3}$$

The non-dimensionalization of all results is based on (constant) hull geometry. This choice introduces and inconsistency when interpreting the behavior for coefficients such as the effective draft, where the varying planform area of the appendage is not included. An alternate data reduction approach would consider the behavior for each appendage relative to the bare hull value. The difference could then be scaled by the appropriate planform area. As will be seen in the discussion of results, the fidelity of the measurement system is already limiting for the absolute quantities presented.

Maneuvering Coefficients

The resistance, sideforce, and yaw moment are decomposed according to the maneuvering convention. A third-order model is assumed for the sideforce and yaw moment [10].

$$C_X = X_{\beta\beta}\beta^2 + C_{XO} \tag{A.4}$$

$$C_Y = Y_{\text{lin}}\beta + Y_{\text{non-lin}}\beta^3 \tag{A.5a}$$
$$C_Y = Y_\beta\beta + Y_{\beta\beta\beta}\beta^3 \tag{A.5b}$$

$$C_N = N_{\text{lin}}\beta + N_{\text{non-lin}}\beta^3 \tag{A.6a}$$
$$C_N = N_\beta\beta + N_{\beta\beta\beta}\beta^3 \tag{A.6b}$$

Sailing Efficiency

The resistance increase due to sideforce production is reported as an effective draft T_e, representing the efficiency for the sideforce production by the hull [64]. The

effective draft of a sailing ship is the span of a foil with equivalent behavior for the induced resistance, as determined from the slope of C_X vs. C_Y^2 [40].

$$X = \frac{1}{\pi \rho V^2 T_e^2} Y^2 + R_T \tag{A.7a}$$

$$C_X = \frac{1}{\pi AR_{\text{eff}}} C_Y^2 + C_{XO} \tag{A.7b}$$

$$T_e = \sqrt{\frac{TL \times AR_{\text{eff}}}{2}} \tag{A.7c}$$

The effective draft is presented in dimensionless form as T_e/T.

Center of Lateral Resistance

The center of lateral resistance (CLR) is determined as a proportion of the ship length L, measured with respect to the midship.

$$CLR = \frac{C_N}{C_Y} \tag{A.8}$$

Testing matrix

The nominal testing matrix for the hulls of the Delft Wind-Assist series was 25 simulations. Simulation time for a nominal drift sweep was 100 hours with the available computing resources. Whereas variation for the range of speeds and leeway angles is accomplished with the drift sweep, simulation for heeled conditions required a new mesh for each heel angle. These simulations are restricted to Froude number 0.168, as can be seen in the matrix provided in Table A.5. A complete sweep for heeled cases was performed for the parent hulls.

Table A.5.: Nominal testing matrix for hulls in the Delft Wind-Assist Series

Froude Number			
0.126	0.168	1.109	
Leeway [deg]			Heel [deg]
0			0
3			
4			
5			
6			
7			
9			
	0		
	3		0
	3		10
	4		
	5		0
	5		10
	5		20
	6		
	7		0
	7		20
	9		
		0	
		3	
		4	
		5	
		6	
		7	
		9	

Hull # 1   1st Series Parent

	--□--	--⊖--	--△--			●	✸		
Fn	**0.128**	**0.168**	**0.210**		**Heel**	**10°**	**20°**		
C_{Xo}	0.007	0.008	0.011	+/- 2%	Y_β	0.052	0.062	0.069	+/- 9%
$X_{\beta\beta}$	0.097	0.108	0.120	+/- 10%	$Y_{\beta\beta\beta}$	1.284	1.197	1.446	+/- 25%

C_{Xo}	0.007	0.008	0.011	+/- 1%	N_β	0.135	0.135	0.137	+/- 1%
T_e/T	0.393	0.441	0.588	+/- 15%	$N_{\beta\beta\beta}$	-0.158	-0.143	-0.196	+/- 50%
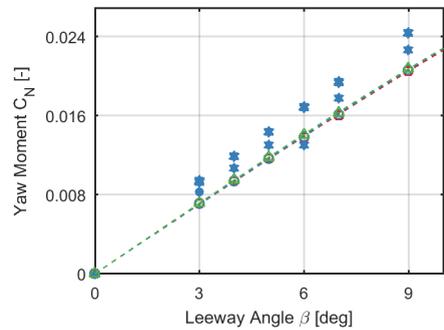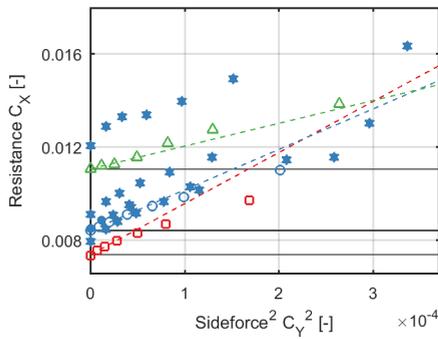
Figure A.6.: Data reduction for hull #1 (Parent hull of the 1st Series).

Hull # 2   1st Series T+

	-- □ --	-- ○ --	-- △ --			●	✱		
Fn	**0.128**	**0.168**	**0.210**		**Heel**	**10°**	**20°**		
C_{Xo}	0.007	0.007	0.010	+/- 2%	Y_β	0.054	0.061	0.068	+/- 6%
$X_{\beta\beta}$	0.103	0.110	0.114	+/- 11%	$Y_{\beta\beta\beta}$	1.751	1.845	2.075	+/- 11%
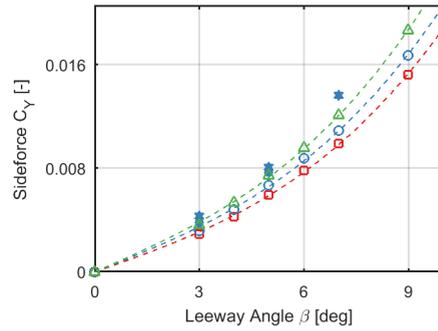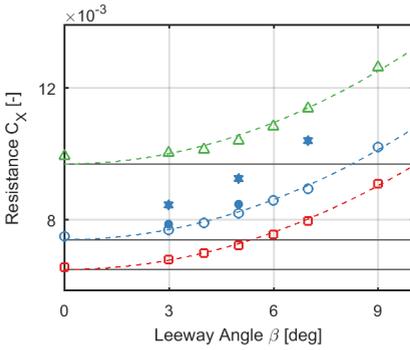
C_{Xo}	0.007	0.008	0.010	+/- 2%	N_β	0.146	0.147	0.149	+/- 1%
T_e/T	0.410	0.445	0.594	+/- 17%	$N_{\beta\beta\beta}$	-0.180	-0.205	-0.241	+/- 54%
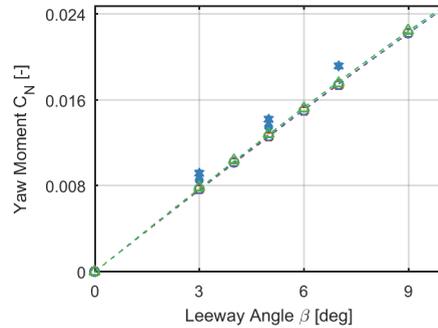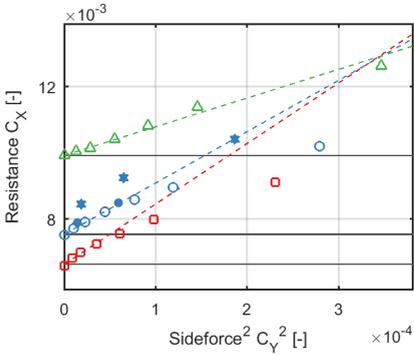
Figure A.7.: Data reduction for hull #2.

Hull # 3   1st Series T-

	--☐--	--⊙--	--△--			●	✸		
Fn	**0.128**	**0.168**	**0.210**		**Heel**	**10°**	**20°**		
C_{Xo}	0.008	0.010	0.012	+/- 1%	Y_β	0.044	0.059	0.064	+/- 9%
$X_{\beta\beta}$	0.095	0.104	0.117	+/- 9%	$Y_{\beta\beta\beta}$	1.190	0.847	1.099	+/- 28%

C_{Xo}	0.008	0.010	0.013	+/- 2%	N_β	0.123	0.123	0.125	+/- 1%
T_e/T	0.360	0.427	0.497	+/- 28%	$N_{\beta\beta\beta}$	-0.163	-0.114	-0.166	+/- 51%
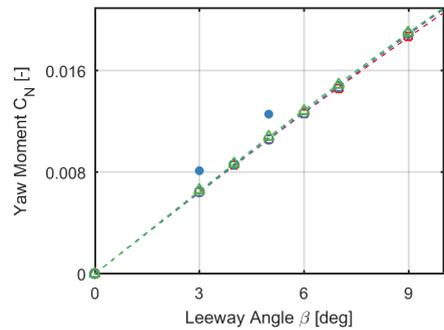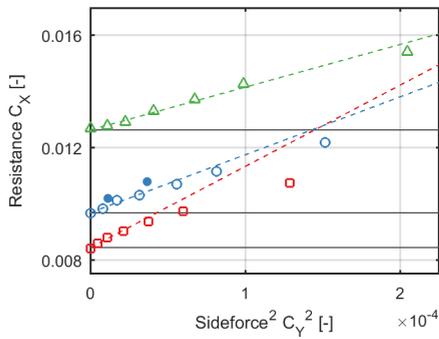
Figure A.8.: Data reduction for hull #3.

Hull # 4   1st Series Cp+

Fn	0.128	0.168	0.210		Heel	10°	20°		
C_{Xo}	0.008	0.010	0.015	+/- 1%	Y_β	0.027	0.041	0.046	+/- 15%
$X_{\beta\beta}$	0.075	0.081	0.102	+/- 13%	$Y_{\beta\beta\beta}$	1.675	1.521	1.779	+/- 19%

C_{Xo}	0.008	0.010	0.015	+/- 1%	N_β	0.143	0.143	0.141	+/- 2%
T_e/T	0.364	0.401	0.370	+/- 19%	$N_{\beta\beta\beta}$	-0.475	-0.530	-0.583	+/- 24%
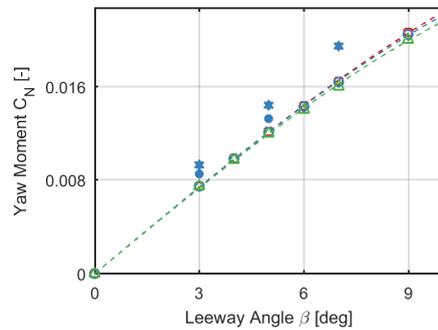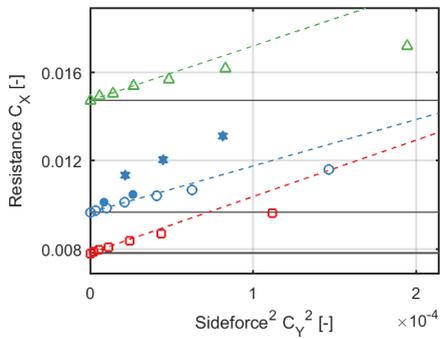
Figure A.9.: Data reduction for hull #4.

187

Hull # 5   1st Series Cp-

	--□--	--⊙--	--△--			●	✹		
Fn	**0.128**	**0.168**	**0.210**		**Heel**	**10°**	**20°**		
C_{Xo}	0.007	0.008	0.010	+/- 1%	Y_β	0.044	0.052	0.062	+/- 7%
$X_{\beta\beta}$	0.089	0.097	0.099	+/- 7%	$Y_{\beta\beta\beta}$	1.425	1.320	1.478	+/- 15%

C_{Xo}	0.007	0.008	0.010	+/- 1%	N_β	0.124	0.125	0.129	+/- 1%
T_e/T	0.378	0.403	0.465	+/- 18%	$N_{\beta\beta\beta}$	-0.007	0.001	-0.090	+/- 315%
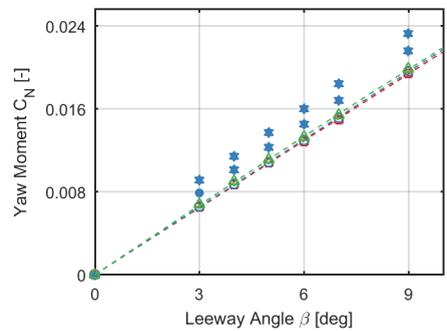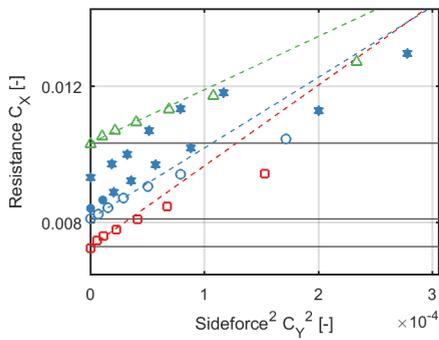
Figure A.10.: Data reduction for hull #5.

Hull # 6   1st Series Cm+

Fn	0.128	0.168	0.210		Heel	10°	20°		
C_{Xo}	0.008	0.009	0.011	+/- 2%	Y_β	0.059	0.069	0.077	+/- 17%
$X_{\beta\beta}$	0.116	0.130	0.133	+/- 13%	$Y_{\beta\beta\beta}$	2.014	1.991	2.099	+/- 33%

C_{Xo}	0.008	0.009	0.011	+/- 1%	N_β	0.144	0.144	0.147	+/- 2%
T_e/T	0.457	0.494	0.668	+/- 22%	$N_{\beta\beta\beta}$	-0.336	-0.313	-0.396	+/- 49%
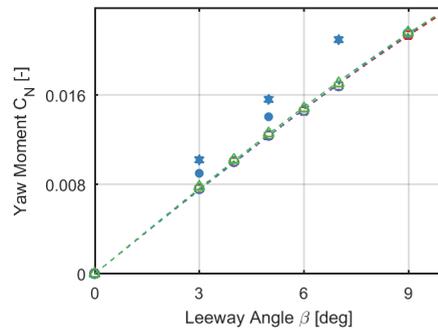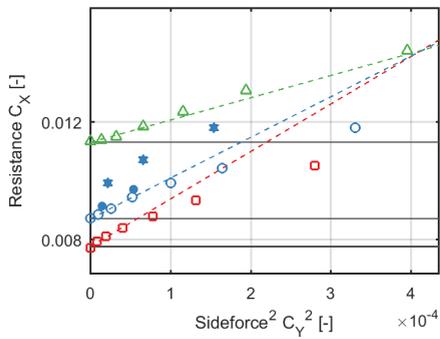
Figure A.11.: Data reduction for hull #6.

189

Hull # 7   1st Series Cm-

	--□--	--⊙--	--△--			●	✱		
Fn	**0.128**	**0.168**	**0.210**		**Heel**	**10°**	**20°**		
C_{Xo}	0.007	0.008	0.011	+/- 1%	Y_β	0.048	0.056	0.063	+/- 8%
$X_{\beta\beta}$	0.092	0.102	0.107	+/- 10%	$Y_{\beta\beta\beta}$	1.303	1.223	1.414	+/- 18%

C_{Xo}	0.007	0.008	0.011	+/- 2%	N_β	0.123	0.124	0.126	+/- 1%
T_e/T	0.381	0.415	0.507	+/- 27%	$N_{\beta\beta\beta}$	0.073	0.100	0.032	+/- 111%
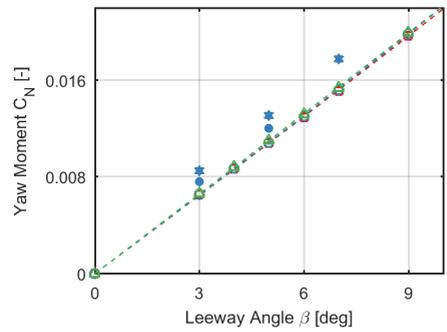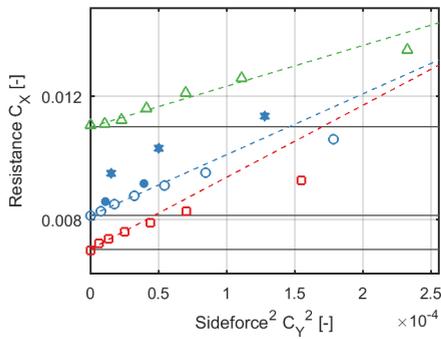
Figure A.12.: Data reduction for hull #7.

Hull # 34   2nd Series Parent

	-- □ --	-- ○ --	-- △ --			●	✳		
Fn	**0.128**	**0.168**	**0.210**		**Heel**	**10°**	**20°**		
C_{Xo}	0.007	0.008	0.011	+/- 2%	Y_β	0.044	0.053	0.059	+/- 11%
$X_{\beta\beta}$	0.108	0.113	0.113	+/- 10%	$Y_{\beta\beta\beta}$	1.729	1.585	1.774	+/- 19%
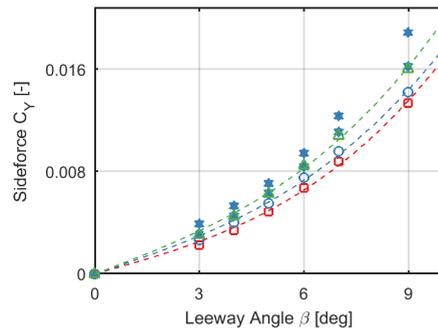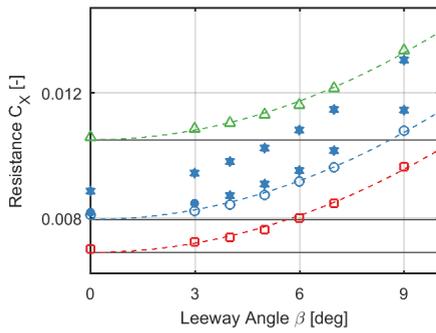
C_{Xo}	0.007	0.008	0.011	+/- 2%	N_β	0.114	0.115	0.117	+/- 1%
T_e/T	0.365	0.405	0.436	+/- 19%	$N_{\beta\beta\beta}$	0.128	0.142	0.074	+/- 66%
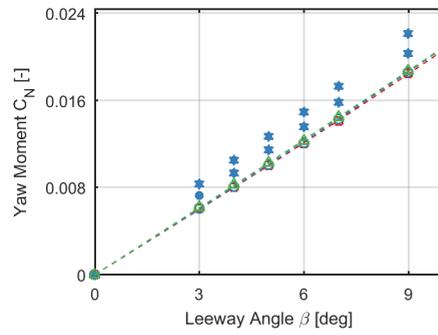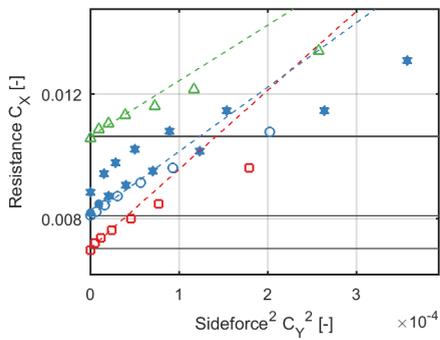
Figure A.13.: Data reduction for hull #34, parent of 2nd Series.

Hull # 45 3rd Series Parent

	--□--	--⊙--	--△--			●	✳		
Fn	**0.128**	**0.168**	**0.210**		**Heel**	**10°**	**20°**		
C_{Xo}	0.008	0.009	0.011	+/- 1%	Y_β	0.053	0.059	0.078	+/- 2%
$X_{\beta\beta}$	0.122	0.124	0.126	+/- 8%	$Y_{\beta\beta\beta}$	1.490	1.356	1.216	+/- 6%
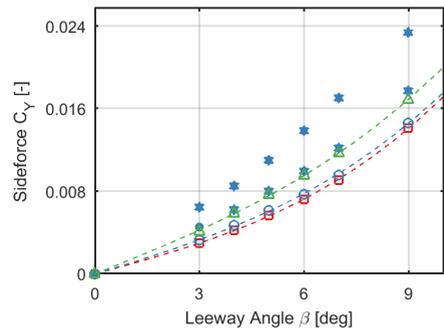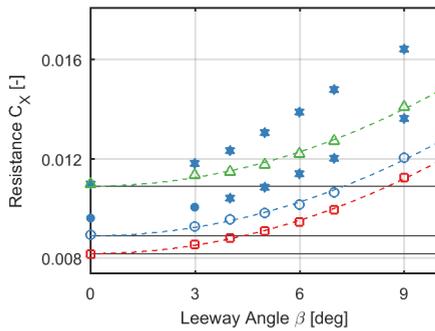
C_{Xo}	0.008	0.009	0.011	+/- 3%	N_β	0.128	0.130	0.135	+/- 1%
T_e/T	0.344	0.380	0.515	+/- 27%	$N_{\beta\beta\beta}$	0.119	0.090	-0.007	+/- 83%
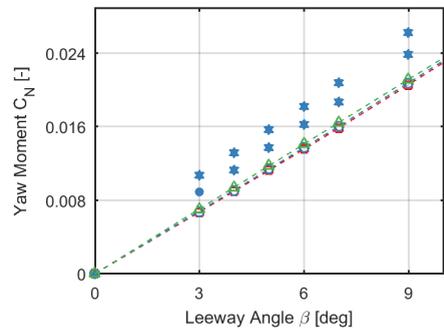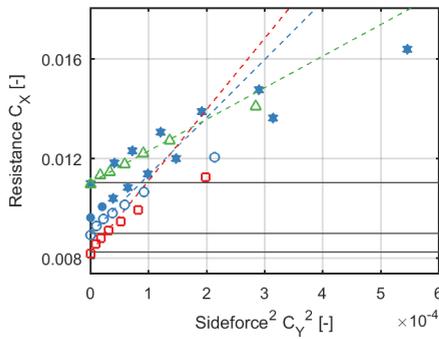
Figure A.14.: Data reduction for hull #45, parent of 3rd Series.

A.3. Appended Hull Series

Several hulls of the Delft Wind Assist series are fitted with diverse appendages during towing tank experiments (see: Chapter 4 and Appendix B). Simulation validation for high-aspect ratio appendages (rudders and skegs) was successful, and the validation level for vessel course stability in particular was very good. The flow mechanism for center-line barkeels and bilge keels, the promotion of separation in the boundary layer, was not reproducible with the RANS-CFD method adopted. Experimental results for variations in appendage height, length, and position for these appendage types is presented in Chapter 4 [118].

The following nomenclature is adopted for the appendage variants: Each appendage keel variant is labeled with a letter and four numbers, specifying keel type, the longitudinal position, keel length and keel height, and finally, the hull number. Special cases are designated with a single number as CS1, CS2. The special geometries for centerline keels are variations on deadwood-centerline keel combinations. Results are presented showing the data reduction as described in Appendix A.2.
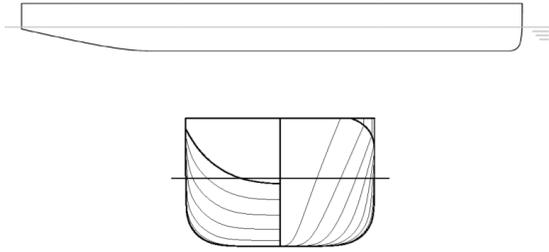
ID: Bare Hull (1)

$C_{X0} = 0.020 +/-0.001$
$X_{\beta\beta} = 0.17 +/-0.07$

$Y_{\beta} = 0.09 +/-0.01$
$Y_{\beta\beta\beta} = 1.37 +/-0.26$
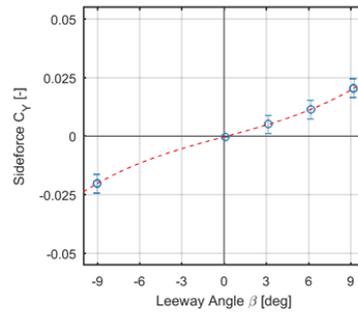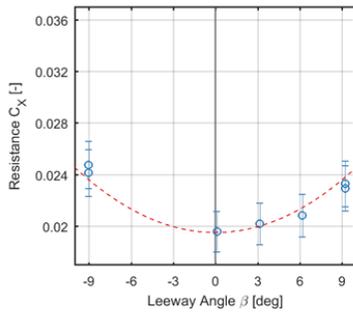
$C_{X0} = 0.020 +/-0.000$
$T_e/T = 0.59 +/-0.05$

$N_{\beta} = 0.13 +/-0.01$
$N_{\beta\beta\beta} = -0.25 +/-0.25$
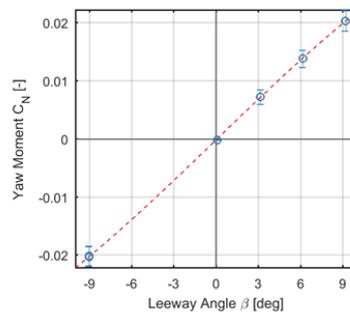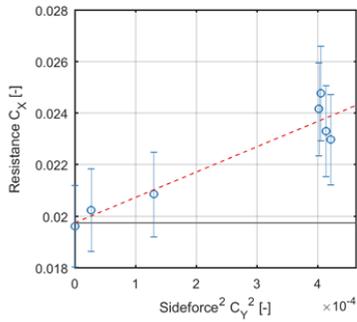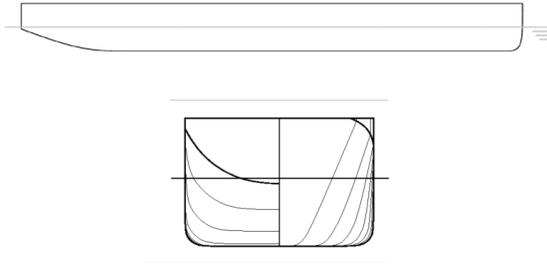
ID: Bare Hull (16)

C_{X0} = 0.024 +/-0.001
$X_{\beta\beta}$ = 0.23 +/-0.05

Y_{β} = 0.11 +/-0.01
$Y_{\beta\beta\beta}$ = 1.67 +/-0.48
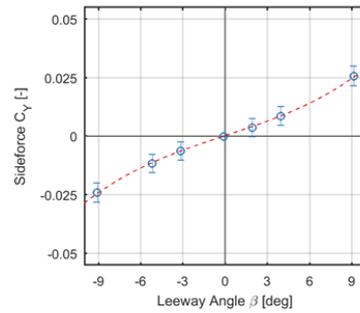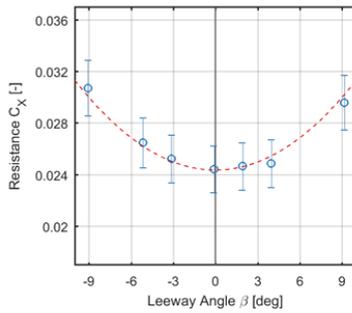
C_{X0} = 0.025 +/-0.000
T_e/T = 0.62 +/-0.03

N_{β} = 0.14 +/-0.01
$N_{\beta\beta\beta}$ = -0.68 +/-0.31
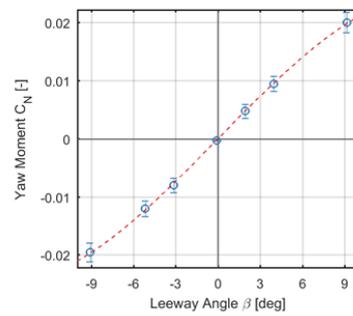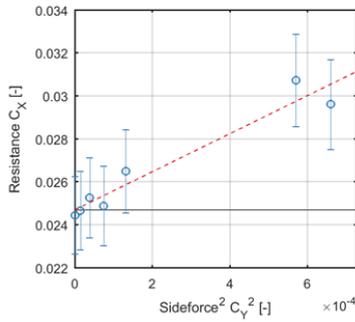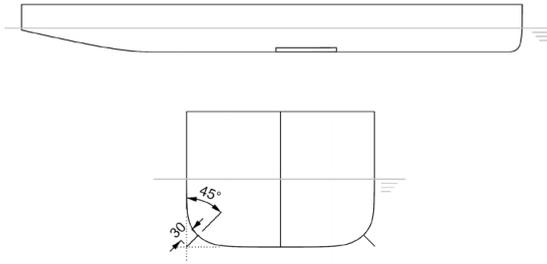
ID: B-P2-L1-H3 (1)

C_{X0} = 0.021 +/-0.001
$X_{\beta\beta}$ = 0.27 +/-0.07

Y_{β} = 0.18 +/-0.01
$Y_{\beta\beta\beta}$ = 2.77 +/-0.23
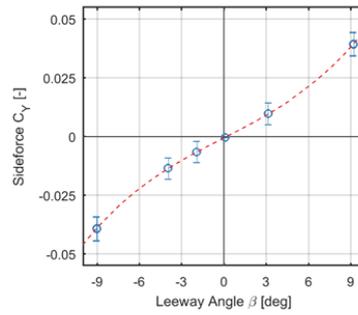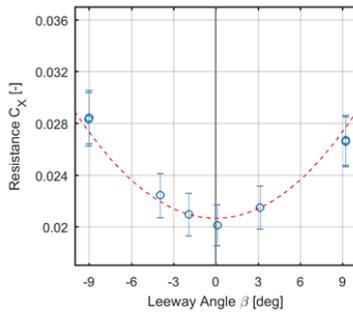
C_{X0} = 0.021 +/-0.002
T_e/T = 0.88 +/-0.15

N_{β} = 0.13 +/-0.00
$N_{\beta\beta\beta}$ = -0.12 +/-0.14
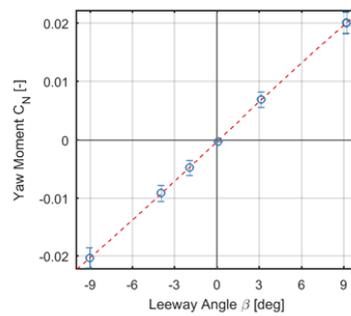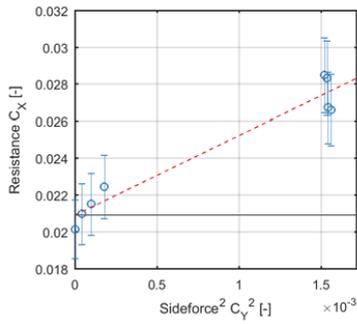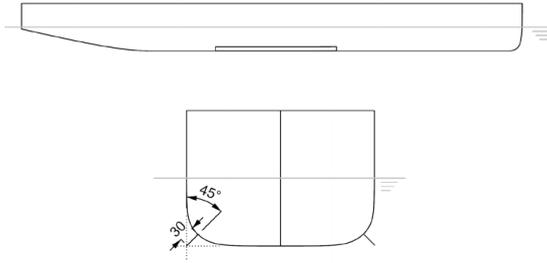
ID: B-P2-L2-H3 (1)

$C_{X0} = 0.020$ +/-0.001
$X_{\beta\beta} = 0.34$ +/-0.06

$Y_{\beta} = 0.20$ +/-0.02
$Y_{\beta\beta\beta} = 2.76$ +/-0.76
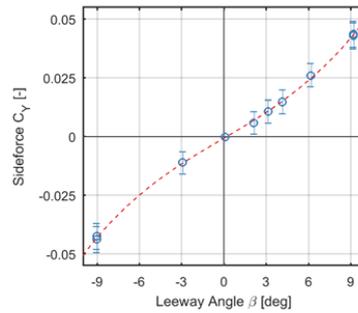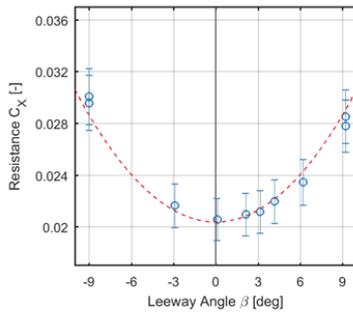
$C_{X0} = 0.021$ +/-0.000
$T_e/T = 0.88$ +/-0.03

$N_{\beta} = 0.12$ +/-0.01
$N_{\beta\beta\beta} = 0.11$ +/-0.25
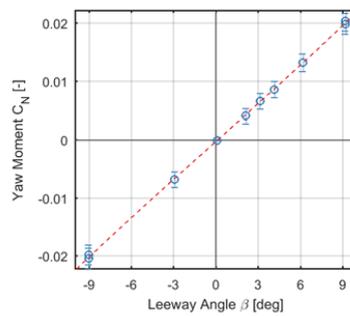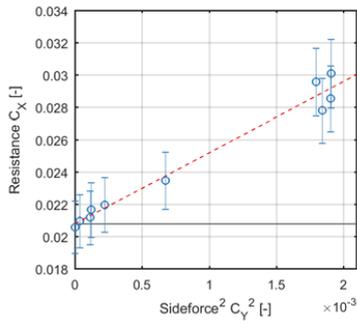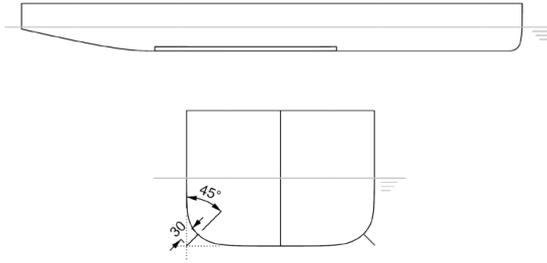
ID: B-P2-L3-H3 (1)

C_{X0} = 0.021 +/-0.000
$X_{\beta\beta}$ = 0.32 +/-0.01

Y_{β} = 0.24 +/-0.02
$Y_{\beta\beta\beta}$ = 2.37 +/-0.89
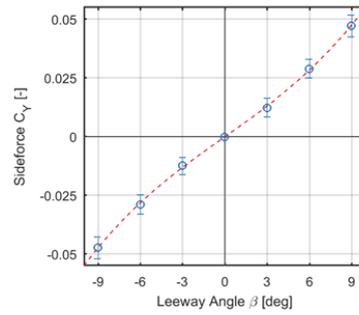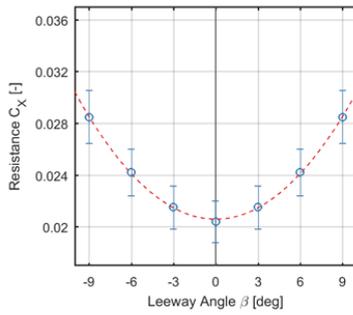
C_{X0} = 0.021 +/-0.001
T_e/T = 0.99 +/-0.17

N_{β} = 0.13 +/-0.01
$N_{\beta\beta\beta}$ = 0.04 +/-0.27
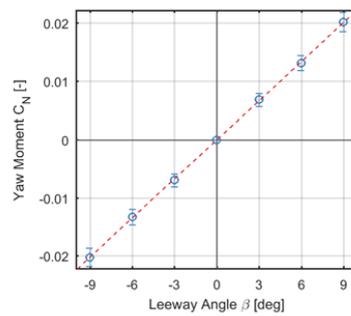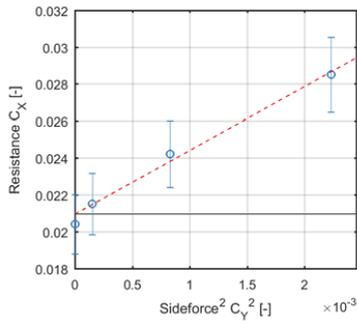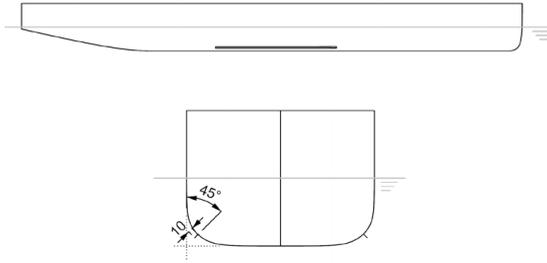
ID: B-P2-L2-H1 (1)

C_{X0} = 0.020 +/-0.001
$X_{\beta\beta}$ = 0.21 +/-0.06

Y_{β} = 0.13 +/-0.01
$Y_{\beta\beta\beta}$ = 1.49 +/-0.32
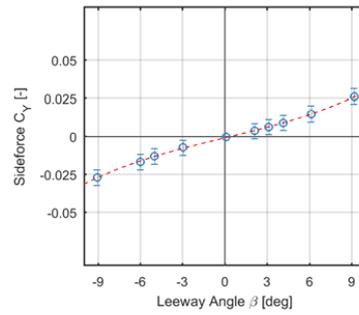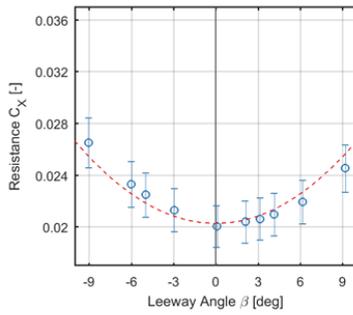
C_{X0} = 0.021 +/-0.000
T_e/T = 0.68 +/-0.04

N_{β} = 0.13 +/-0.00
$N_{\beta\beta\beta}$ = -0.18 +/-0.12
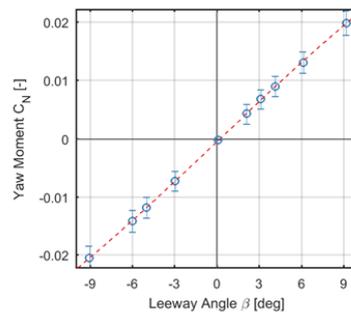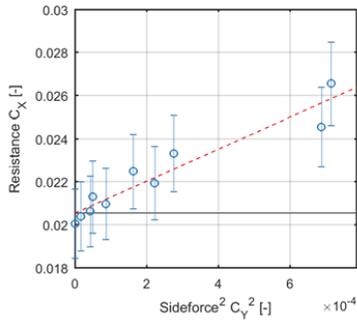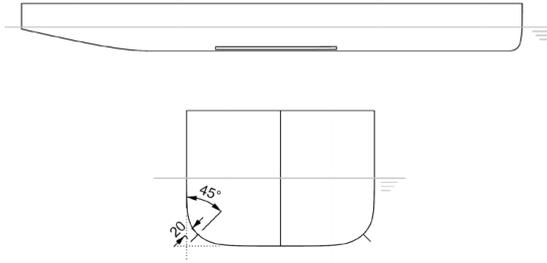
ID: B-P2-L2-H2 (1)

C_{X0} = 0.021 +/-0.001
$X_{\beta\beta}$ = 0.27 +/-0.07

Y_β = 0.17 +/-0.01
$Y_{\beta\beta\beta}$ = 1.84 +/-0.49
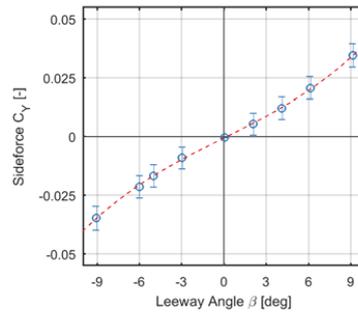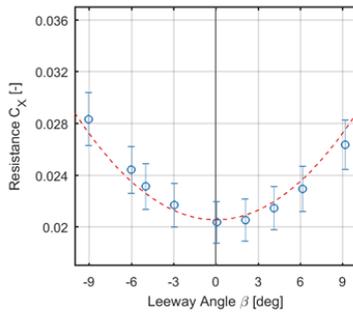
C_{X0} = 0.021 +/-0.000
T_e/T = 0.78 +/-0.06

N_β = 0.13 +/-0.00
$N_{\beta\beta\beta}$ = -0.05 +/-0.06
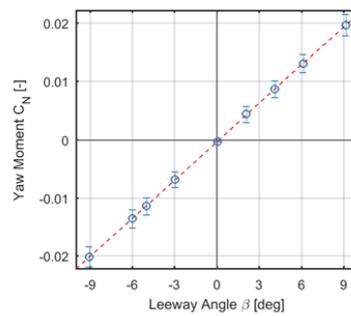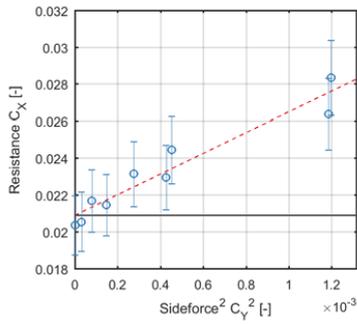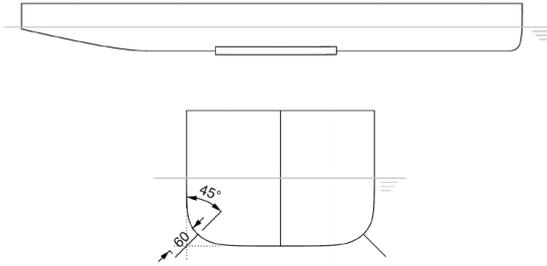
ID: B-P2-L2-H4 (1)

C_{X0} = 0.021 +/-0.001
$X_{\beta\beta}$ = 0.55 +/-0.09

Y_{β} = 0.32 +/-0.01
$Y_{\beta\beta\beta}$ = 5.54 +/-0.72
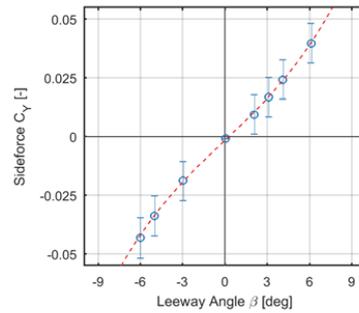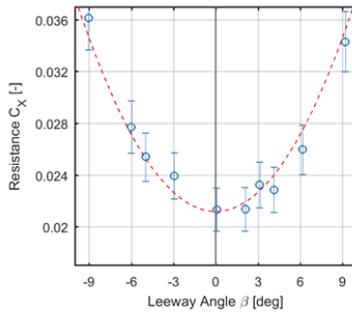
C_{X0} = 0.022 +/-0.001
T_e/T = 1.18 +/-0.09

N_{β} = 0.13 +/-0.00
$N_{\beta\beta\beta}$ = 0.07 +/-0.21
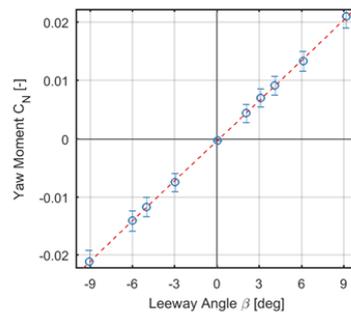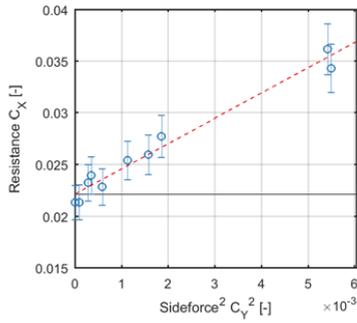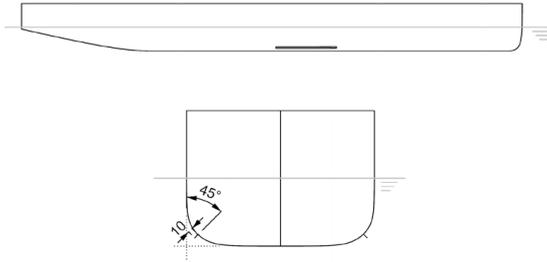
ID: B-P2-L1-H1 (1)

C_{X0} = 0.020 +/-0.001
$X_{\beta\beta}$ = 0.20 +/-0.06

Y_{β} = 0.12 +/-0.00
$Y_{\beta\beta\beta}$ = 1.75 +/-0.19
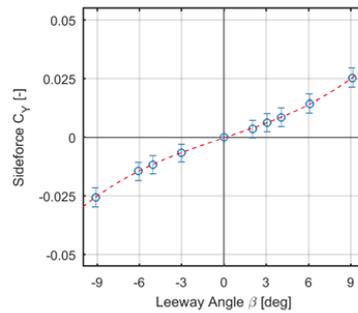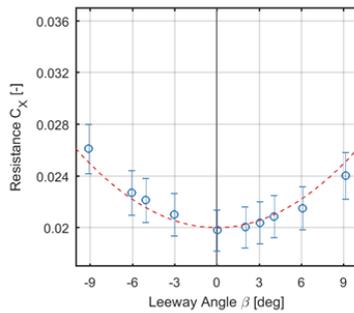
C_{X0} = 0.020 +/-0.000
T_e/T = 0.67 +/-0.05

N_{β} = 0.13 +/-0.00
$N_{\beta\beta\beta}$ = -0.16 +/-0.18
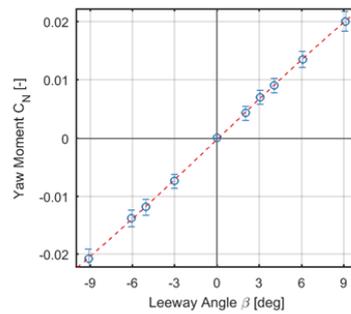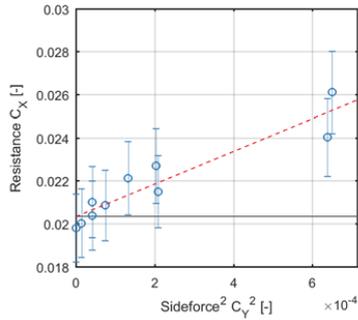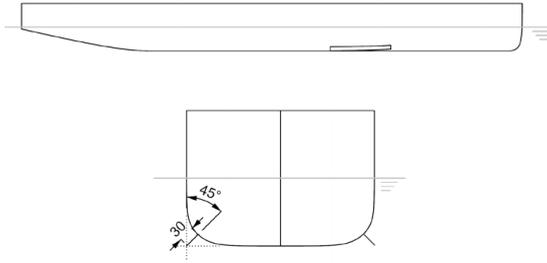
ID: B-P1-L1-H3 (1)

$C_{X0} = 0.020$ +/-0.001
$X_{\beta\beta} = 0.32$ +/-0.06

$Y_{\beta} = 0.17$ +/-0.01
$Y_{\beta\beta\beta} = 2.91$ +/-0.25
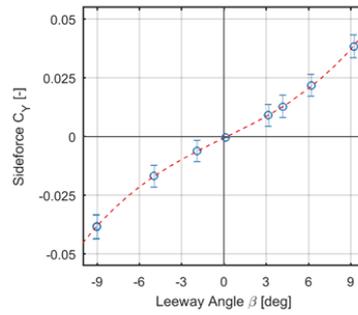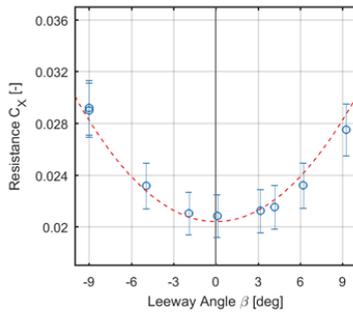
$C_{X0} = 0.021$ +/-0.000
$T_e/T = 0.80$ +/-0.03

$N_{\beta} = 0.13$ +/-0.00
$N_{\beta\beta\beta} = 0.10$ +/-0.07
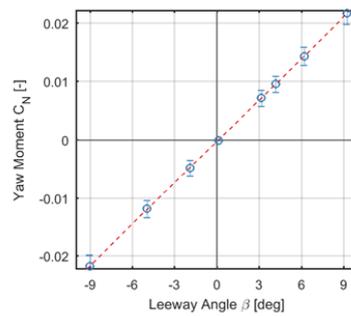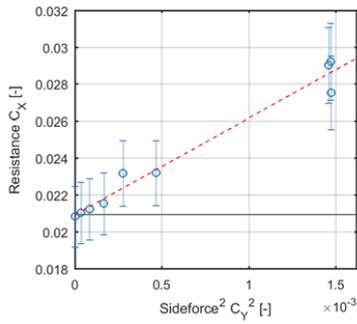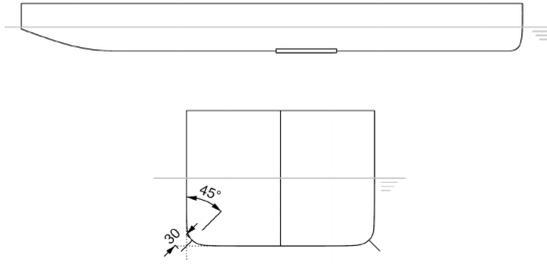
ID: B-P2-L1-H3 (16)

$C_{X0} = 0.025$ +/-0.001
$X_{\beta\beta} = 0.39$ +/-0.07

$Y_\beta = 0.22$ +/-0.01
$Y_{\beta\beta\beta} = 2.77$ +/-0.66
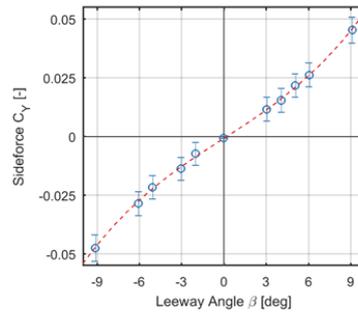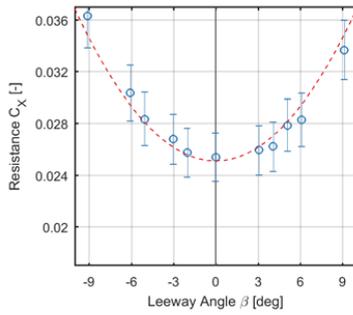
$C_{X0} = 0.026$ +/-0.000
$T_e/T = 0.87$ +/-0.05

$N_\beta = 0.14$ +/-0.01
$N_{\beta\beta\beta} = -0.12$ +/-0.30
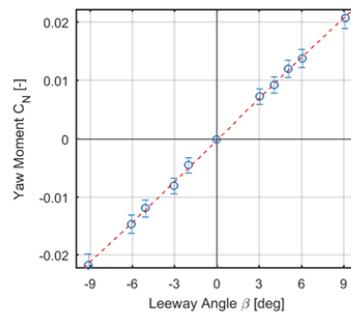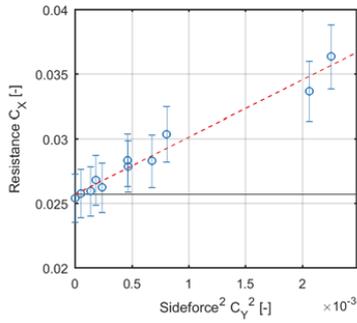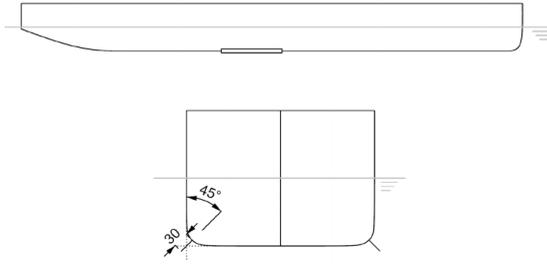
ID: B-P3-L1-H3 (16)

C_{X0} = 0.025 +/-0.001
$X_{\beta\beta}$ = 0.33 +/-0.06

Y_{β} = 0.20 +/-0.02
$Y_{\beta\beta\beta}$ = 2.60 +/-0.95
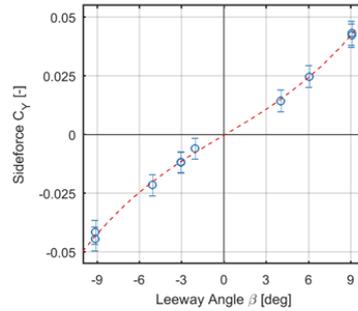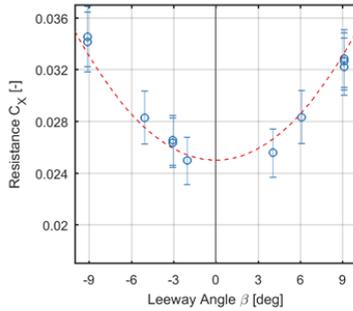
C_{X0} = 0.026 +/-0.001
T_e/T = 0.89 +/-0.10

N_{β} = 0.13 +/-0.01
$N_{\beta\beta\beta}$ = -0.51 +/-0.31
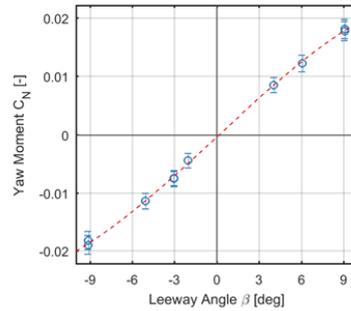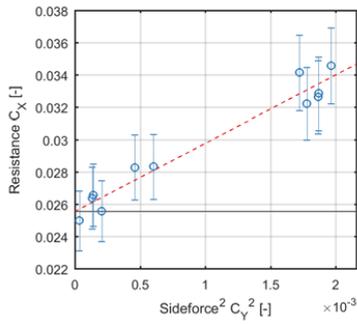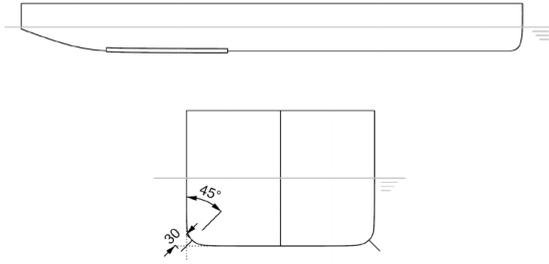
ID: B-P4-L2-H3 (16)

C_{X0} = 0.025 +/-0.001
$X_{\beta\beta}$ = 0.41 +/-0.05

Y_{β} = 0.24 +/-0.01
$Y_{\beta\beta\beta}$ = 3.28 +/-0.66
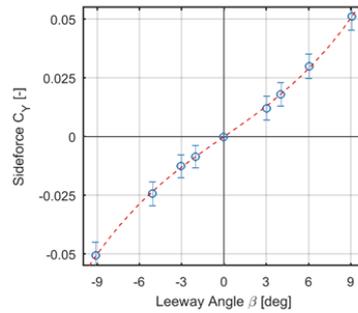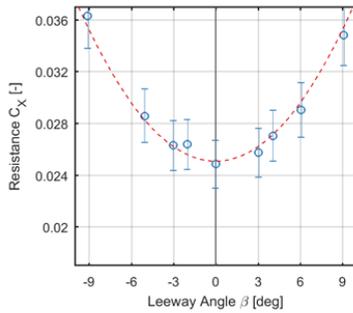
C_{X0} = 0.026 +/-0.001
T_e/T = 0.94 +/-0.09

N_{β} = 0.10 +/-0.01
$N_{\beta\beta\beta}$ = -0.50 +/-0.31
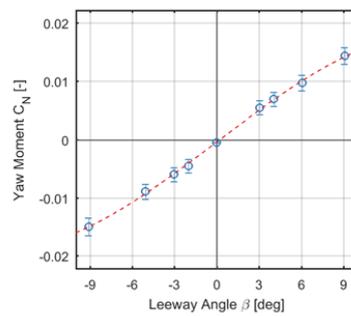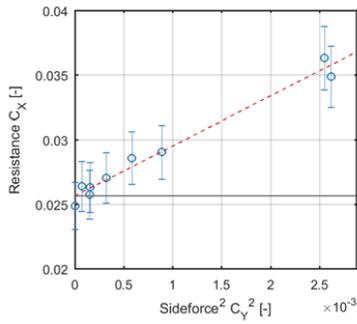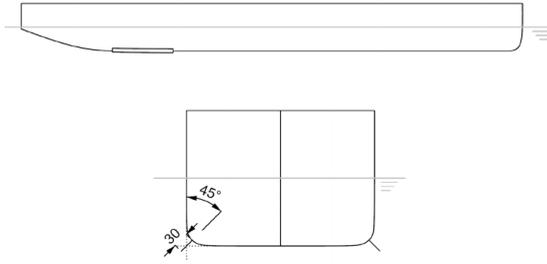
ID: B-P5-L1-H3 (16)

C_{X0} = 0.025 +/-0.001
$X_{\beta\beta}$ = 0.35 +/-0.05

Y_{β} = 0.22 +/-0.01
$Y_{\beta\beta\beta}$ = 2.24 +/-0.65
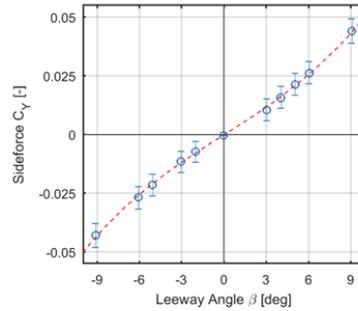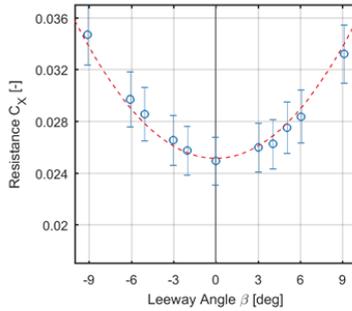
C_{X0} = 0.026 +/-0.000
T_e/T = 0.87 +/-0.05

N_{β} = 0.11 +/-0.00
$N_{\beta\beta\beta}$ = -0.40 +/-0.22
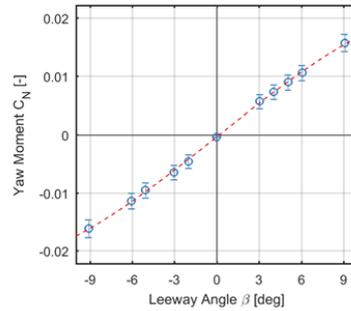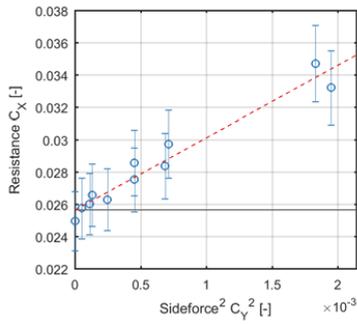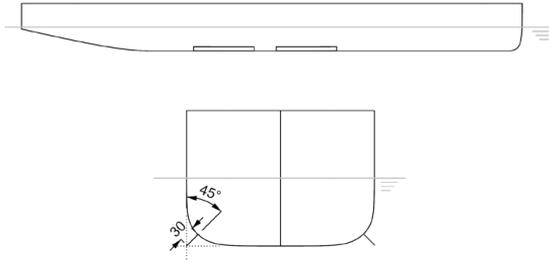
ID: Bilge Special 1 (1)

C_{X0} = 0.021 +/-0.001
$X_{\beta\beta}$ = 0.35 +/-0.04

Y_{β} = 0.22 +/-0.02
$Y_{\beta\beta\beta}$ = 2.31 +/-0.82
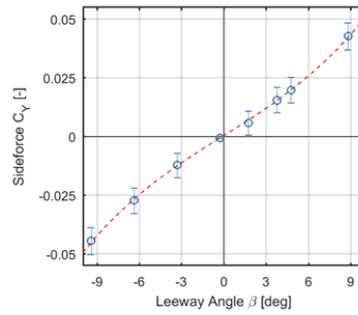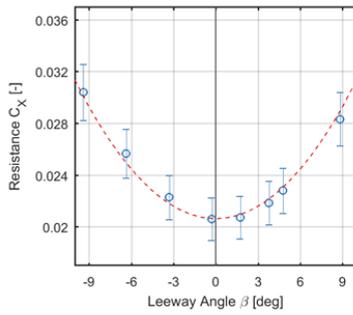
C_{X0} = 0.021 +/-0.001
T_e/T = 0.86 +/-0.06

N_{β} = 0.12 +/-0.00
$N_{\beta\beta\beta}$ = 0.12 +/-0.17
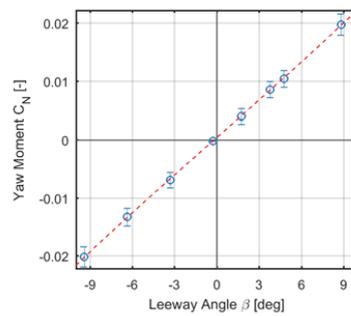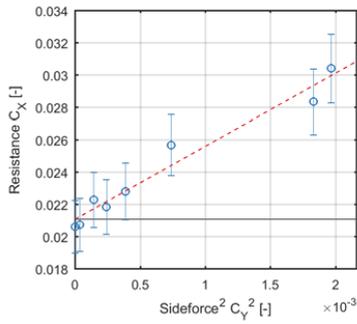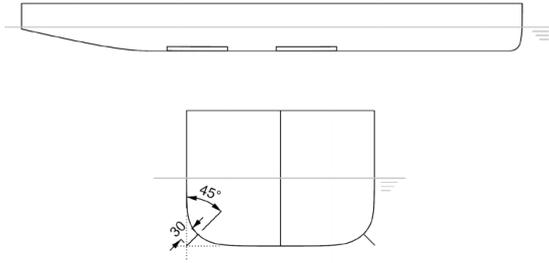
ID: Bilge Special 2 (1)

C_{X0} = 0.021 +/-0.001
$X_{\beta\beta}$ = 0.34 +/-0.06

Y_{β} = 0.23 +/-0.02
$Y_{\beta\beta\beta}$ = 2.26 +/-0.98
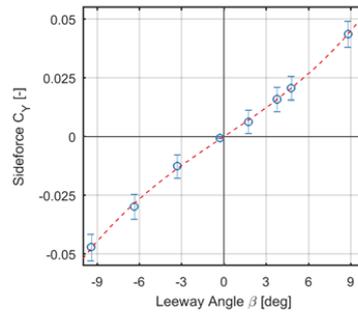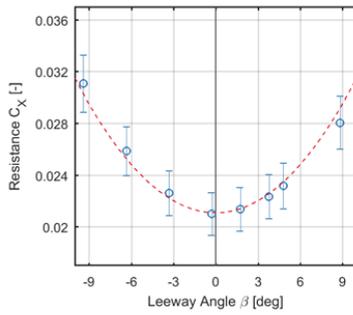
C_{X0} = 0.021 +/-0.001
T_e/T = 0.91 +/-0.07

N_{β} = 0.12 +/-0.00
$N_{\beta\beta\beta}$ = -0.14 +/-0.16
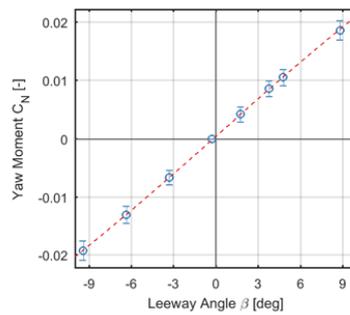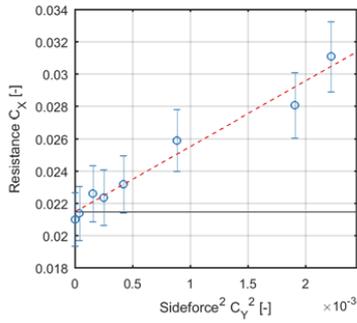
Table A.6.: Complete array of testing matrix for bilge keel geometries

Bilge Keel Set	Identifier	Position [mm]	Length [mm]	Height [mm]	Hull
f(length)	B-P2-L1-H3 (1)	1735	333	30	1
	B-P2-L2-H3 (1)	1735	667	30	1
	B-P2-L3-H3 (1)	1735	1000	30	1
f(position)	B-P1-L1-H3 (1)	2035	333	30	1
	B-P2-L1-H3 (1)	1735	333	30	1
	B-P2-L1-H3 (16)	1735	333	30	16
	B-P3-L1-H3 (16)	1435	333	30	16
	B-P5-L1-H3 (16)	835	333	30	16
	B-P2-L2-H3 (1)	1735	667	30	1
	B-P4-L2-H3 (16)	1135	667	30	16
f(height)	B-P2-L2-H1 (1)	1735	667	10	1
	B-P2-L2-H2 (1)	1735	667	20	1
	B-P2-L2-H3 (1)	1735	667	30	1
	B-P2-L2-H4 (1)	1735	667	60	1
f(AR=0.06)	B-P2-L1-H1 (1)	1735	333	10	1
	B-P2-L2-H2 (1)	1735	667	20	1
	B-P2-L3-H3 (1)	1735	1000	30	1
f(AR=0.18)	B-P2-L1-H3 (1)	1735	333	30	1
	B-P2-L2-H4 (1)	1735	667	60	1
$f\left(h/h_b\right)$	B-P2-L1-H3 (1)	1735	333	30	1
	B-P2-L1-H3 (16)	1735	333	30	16

Figure A.15.: Bilge keel variants
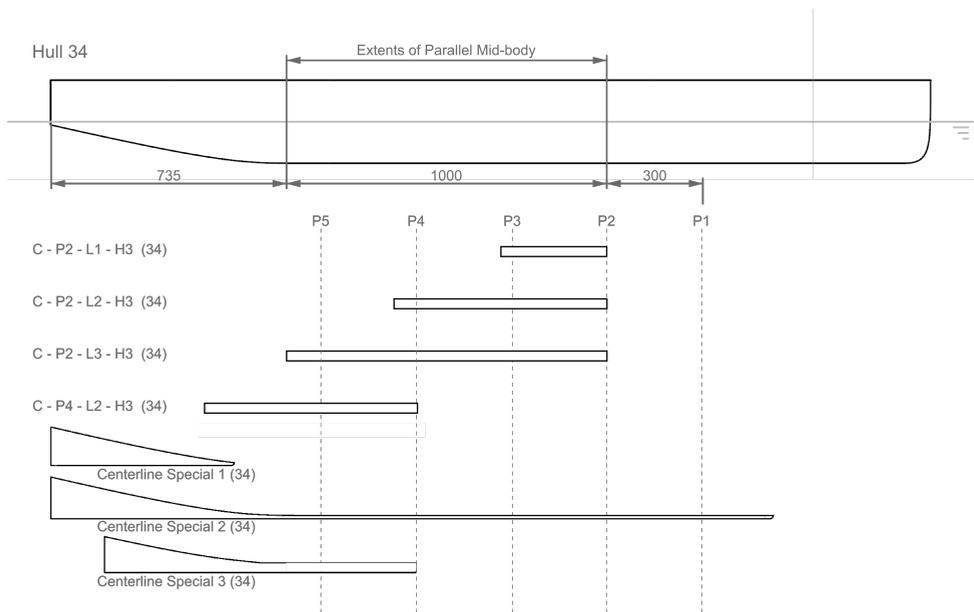
Figure A.16.: Centreline-keel appendages

Table A.7.: Complete array of testing matrix for centerline keel geometries

Keel Set	Identifier	Position [mm]	Length [mm]	Height [mm]	Hull
f(length)	C-P2-L1-H3 (34)	1735	333	30	34
	C-P2-L2-H3 (34)	1735	667	30	34
	C-P2-L3-H3 (34)	1735	1000	30	34
f(CL keel)	C-P2-L1-H3 (34)	1735	333	30	34
	B-P2-L1-H3 (1)	1735	333	30	1
	B-P2-L1-H3 (16)	1735	333	30	16
	C-P4-L2-H3 (34)	1135	667	30	34
	B-P4-L2-H3 (16)	1135	667	30	16

Centerline Special 1 (34)
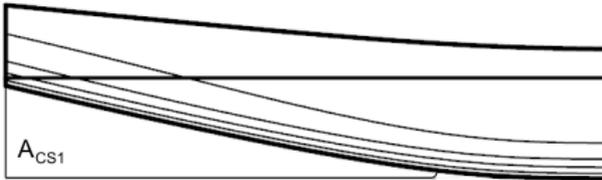
Centerline Special 2 (34)

10 mm
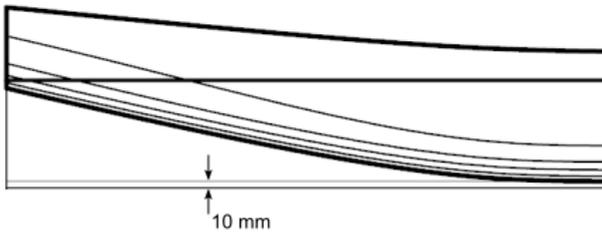
Centerline Special 3 (34)

$\frac{A_{CS1}}{2}$ $\frac{A_{CS1}}{2}$

30 mm
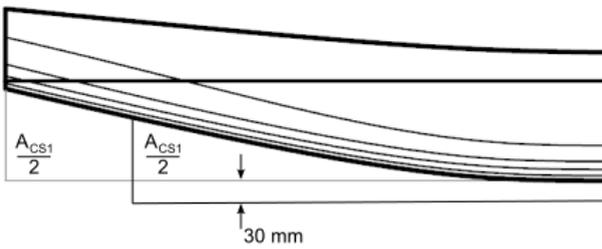
Figure A.17.: Deadwood varations tested on Hull #34, parent hull of the 2nd Series of the DWA series.

B

Uncertainty Analysis

No one believes the CFD results
except the one who performed the
calculation, and everyone believes
the experimental results except the
one who performed the experiment.

P.J. Roache, 1998

This appendix is a compilation of uncertainty analyses associated with this thesis work, meant to support the material in Chapters 3 and 4. The appendix is divided into three parts:

1. RANS-CFD Verification

2. Validation Experiment (2016)

3. Bilge keel and centerline keel Experiment (2018)

B.1. RANS-CFD Verification

The maturity of Reynolds Averaged Navier-Stokes computational fluid dynamics (RANS-CFD) solvers offers ready, inexpensive analysis for a large number of hull variations. However, simulations that remain computationally affordable may be unable to model the flow patterns occurring around a sailing commercial ship. Fluid flow around the ship will experience separation effects and will become entrained in large vortices in the wake of the ship, both phenomena that are likely to challenge the physical modelling for RANS-CFD simulations. Compromises made for the modelling of separation behaviour and for the evolution of separated flow structures around the hull of the sailing ship point to a concerted simulation verification study in support of experimental validation. The predominance of large-scale separated flow structures in the wake of the sailing ship, an artifact of sideforce production necessary for sailing, points to a careful estimate for the numerical uncertainty. It is otherwise impossible to discern between perhaps substantial modelling errors and the numerical uncertainty. In this section, a detailed report of the determination of the numerical uncertainty is given. The results of this study are used to inform the meshing strategy for simulation and to select the requisite grid spacing and time step for a desired numerical uncertainty.

A numerical simulation will have some error associated with discretization and an error associated with the iterative solution approach for the non-linear flow equations. Several governing bodies publish standards for CFD simulation verification, including the International Towing Tank Committee (ITTC) [55, 56, 58] and the American Society of Mechanical Engineers (ASME) [4]. The Grid Convergence Index (GCI) of Roache [90] is commonly accepted, thanks in part to his strong advocacy for standardization of journal policies regarding uncertainty reporting for computational fluid dynamics. His influence is seen throughout subsequent work on this topic. The ITTC recommendations include the correction factor method of Stern and Wilson [101], the GCI of Roache, and an approach for oscillatory convergence. Several methods are investigated in [112]: the GCI of Roache [90], its elaboration by Eça and Hoekstra [30], the Correction Factor of Stern [101], and the Approximate Error Spline of Celik [20]. The method of Eça and Hoekstra was most robust for its ability to cope with nonconforming observed-order-of-convergence and otherwise anomalous convergence behaviour, and this method is followed for the discretization uncertainty for the remainder of this study. When not possible, the Correction factor mathod of Stern [101] was adopted.

The numeric error is written as the root-sum-squared sum of discretization errors and iterative errors, with corresponding uncertainty, while disregarding round-off errors [123]:

$$\delta^2_{\mathrm{Num}} = \delta^2_{\mathrm{D}} + \delta^2_{\mathrm{I}} \rightarrow U^2_{\mathrm{Num}} = U^2_{\mathrm{D}} + U^2_{\mathrm{I}} \tag{B.1}$$

Most CFD verification procedures for discretization errors originate in the work of Richardson [89], who identified the asymptotic approach to a continuum solution for finite difference calculations with increasing grid refinement. The so-called Richardson extrapolation was adopted by Roache [90] to estimate the uncertainty due to discretization errors in CFD. Beginning with the generalized Richardson extrapolation:

$$\phi_{\mathrm{RE}} = \phi_0 \cong \phi_1 + \frac{\phi_1 - \phi_2}{r^p - 1} \tag{B.2}$$

$r = h_2/h_1$ is the grid refinement ratio for a characteristic grid height h. This is an expression for the function value at zero-grid spacing, based on the function value at a series of geometrically similar grids, h_i. For unsteady simulations, the time step has been scaled together with the grid spacing to achieve a constant Courant number for all grids. The exponent p is either the theoretical (second-order for space and time) or observed order of convergence. The observed order of convergence is calculated from a grid triplet as:

$$p_{\mathrm{Obs}} = \frac{\ln(\frac{\phi_3 - \phi_2}{\phi_2 - \phi_1})}{ln(r)} \tag{B.3}$$

The difference $\delta_{\mathrm{RE}} = \phi_0 - \phi_1$ is an estimate of the error for grid one, corresponding to a 50 % uncertainty band when this value is interpreted as a single realization of that error. Thus:

$$U_{50\%} = \delta_{\mathrm{RE}} = \frac{\phi_1 - \phi_2}{r^p - 1} \tag{B.4}$$

One might argue that δ_{RE} is derived from multiple realizations of the function: ϕ_1, ϕ_2, ϕ_3.

Finally, to extend the confidence interval to 95 % Roache defines the Grid Convergence Index (GCI) as:

$$GCI = F_{\mathrm{S}} * |\delta_{\mathrm{RE}}| \tag{B.5}$$

F_{S} is interpreted as the coverage factor or, in engineering parlance, as the factor of safety. Roache suggests $F_{\mathrm{S}} = 3$ for rudimentary grid convergence studies involving two grids, and $F_{\mathrm{S}} = 1.25$ for more rigorous studies. The method is predicated on monotonic convergence behaviour for simulations with increasing mesh refinement or decreasing time step. The convergence ratio, R, must satisfy the following condition:

$$0 < R < 1$$

$$R = \frac{\phi_3 - \phi^2}{\phi_2 - \phi_1} \tag{B.6}$$

This requirement leads to essential practical issues that complicate the application of Richardson extrapolation theory to RANS-CFD, chief among which is the definition of a family of systematically refined grids that lies within the asymptotic range and yet remains computationally feasible. Also problematic are limiters used in the discretization of the flow equations, modelling requirements for the 1st cell height at the ship hull, and non-conforming convergence rate where higher order terms in the power series expansion play a role.

The efforts of Roache have been carried further by Eça and Hoekstra [27, 30], who applied a least-squared approach to the determination of p_{Obs} to accommodate data scatter for the grid solution $< h_i, \phi_{i>}$. This method therefore requires at least four solutions on systematically refined grids. Eça and Hoekstra also incorporate the error estimates with prescribed orders [82], when data scatter is such that a reliable estimate for the order of convergence, p, is not feasible. In these cases, convergence is assumed to proceed with either first or second order, or with mixed order:

$$\delta_1 = c_1 h$$
$$\delta_2 = c_2 h^2 \tag{B.7}$$
$$\delta_{12} = c_1 h + c_2 h^2$$

Also, recognizing that CFD for practical ship flows precludes the true approach to the asymptotic range while using systematically refined grids, Eça and Hoekstra propose a weighting within the least-squared minimization that favors the fine-grid solutions.

$$\Delta_\phi = \frac{max(\phi) - min(\phi)}{n - 1} \tag{B.8}$$

A selection is made among the available error estimates based on the observed order of convergence and the standard deviation for each fit for the solution on n grids. The extents of what is considered to be an expected value for p may be discussed, as the safety factor more than doubles at the boundary of this set. Eça and Hoekstra state that values of p_{Obs} that fall between 0.6 and 2.1 may be treated with confidence, so that F_S =1.25. For cases where p_{Obs} is greater or less than the expected order of convergence, the power-series estimates with prescribed orders that best fits the data is selected, with an increased F_S =3. Other researchers have questioned this substantial penalty for the uncertainty, especially for datasets that exhibit monotonic convergence with an order that is near to two [102, 121].

$$U_{Eca} = \begin{cases} F_S \delta_i + \sigma_{fit} + |\phi_i - \phi_{fit}| & \sigma_{fit} < \Delta \\ 3^{\sigma_{fit}}/\Delta_\phi (F_S \delta_i + \sigma_{fit} + |\phi_i - \phi_{fit}|) & \sigma_{fit} \geq \Delta \end{cases} \tag{B.9}$$

When the error estimator has been selected, the uncertainty is determined by comparing the data range parameter, Δ_ϕ, with the standard deviation of the fit σ_{fit}.

The correction method of Stern is also based on the GCI, but includes a further refinement for the F_S. C,F_S is determined by comparing the observed rate of convergence with the theoretical order for the simulation, and as a measure of the proximity of the grids used to the asymptotic range:

$$U_C = \frac{r^p - 1}{r^{p_{\mathrm{Est}}} - 1}$$ (B.10)

If the observed order, p, is equal to the estimated order then C is unity. For solutions outside the asymptotic range ($C \neq 1$), the sign and magnitude of C is used to determine the uncertainty according to:

$$C = \begin{cases} [9.6(1 - C)^2 + 1.1]|\delta_{\mathrm{RE}}| & |1 - C| < 0.125 \\ [2|1 - C| + 1]|\delta_{\mathrm{RE}}| & |1 - C| >= 0.125 \end{cases}$$ (B.11)

The final form of Equation (B.11) has developed from communications between Stern et al. [101, 102] and Roach [90], the product of which being that these approaches exhibit comparable behavior. For example, for the limit as $C \to 1$, $U = 1.1|\delta_{\mathrm{RE}}|$. This approach gives a smooth behaviour for the F_S, in contrast with the method of Roach or Eça.

Grid Set Construction Using Hexpress

The construction of a systematically refined set of unstructured grids using the Numeca meshing tool, Hexpress, is achieved by varying initial cell subdivision, which defines the cell size, and refinement diffusion, which defines the thickness of each refinement level, such that refinement diffusion doubles with each grid subdivision ($dx/2$). In Figure B.1, cells adjacent to a surface are given to illustrate these concepts. In Figure B.1(a), the wall has a refinement level equal to two and a refinement diffusion equal to one. The size of the largest cell on the right is defined by the initial subdivision of the computational domain. That cell is refined twice in the vicinity of the wall, and each refinement level is one cell thick. Figure B.1(b) is a detail of the cells adjacent to the wall. The refinement diffusion, or the thickness of each refinement level, is one. In Figure B.1(c), these cells have been divided once, so that $r=2$. Here, the thickness of each refinement level is two, which is to say that the refinement diffusion has doubled.

Courant Number Study

The target Courant number for validation and production runs is selected based on systematic variations in the Courant number performed on three grids, A2, B1, and B3. Simulations for variations in Courant number were performed at 6° leeway. Details for the Courant number study are presented in Table B.2.
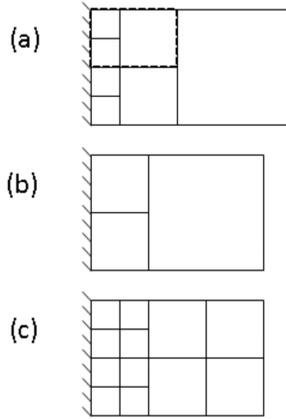
Figure B.1.: Illustration of the relationship between refinement level and refinement diffusion for mesh refinement.

Table B.1.: Details of mesh construction.

Grid ID	N	h_{Vol}	h/h_1	BL Cells	Y^+		Courant	
	10×10^6	m			Mean	Max	Max	FS
A4	2.0	0.067	1.83	5	56.5	84	3.9	2.6
A3	3.0	0.060	1.61	4	47.9	75	7.4	4.2
A2	4.7	0.051	1.38	3	47.9	73	6.0	2.8
A1	12	0.037	1.00	3	52.5	80	6.7	3.3
B4	2.0	0.072	1.51	4	54.4	78	7.5	5.0
B3	3.2	0.061	1.29	3	55.1	79	6.1	4.3
B2	5.3	0.052	1.09	3	53.8	80	5.3	4.2
B1	6.8	0.048	1.00	3	49.0	87	5.7	3.8
C4	0.88	0.095	2.30	5	51	122	4.0	1.8
C3	1.4	0.083	2.01	5	53	128	3.8	2.1
C2	2.6	0.068	1.63	3	53.1	114	4.7	1.9
C1nobl	8.8	0.041	1.00	0	40.8	89	2.9	1.5
C4nobl	0.73	0.089	2.15		60.4	93	5.5	3.4
C3nobl	1.1	0.077	1.86		52.2	86	5.9	2.8
C2nobl	2.0	0.062	1.50		42.5	81	5.4	1.8
C1nobl	8.8	0.041	1.00		40.8	89	2.9	1.5

Table B.2.: Details of Courant number study.

Courant (target)	Courant (realized)		
	Grid A2	Grid B1	Grid B3
0.25	0.24	-	-
0.5	0.49	-	0.36
1	0.98	1.17	1.09
4	2.97	4.64	4.30
16	-	18.41	16.99
50	-	54.06	-

Numerical uncertainty

The numerical uncertainty is calculated according to the method of Eça and Hoek-stra for the discretization uncertainty, which includes the influence of errors due to spatial and temporal discretization,. The time step is scaled together with the grid spacing to maintain a constant Courant number and a consistent numerical method. Simulation for grid set A were performed at 0° and 6° leeway. Simulations for grid set B was performed at 6° leeway. Simulations for grid set C and Cnobl were performed at 0° and 9°. All simulations for discretization uncertainty were performed for (target) Courant number equal to four.

The simulation verification exercise is performed for the forces integrated over the ship hull: resistance X, sideforce Y, and yaw moment N. In the following, a complete documentation of the calculation of the simulation discretization uncertainty U_D is detailed. be discussed for each component. Some results are repeated from Chapter 3. Also, the results for the Courant number study are presented. Finally, the meshing strategy, grid spacing, and target Courant number are defined for validation simulations.

For each component: X, Y, and N, the following calculation details are reported: the convergence ratio R, p_{Obs}, the fit selected by the uncertainty procedure, the ratio σ_{fit}/Δ_ϕ, the factor of safety applied, the Richardson extrapolated value ϕ_0, and the uncertainty $U_{h_{Vol}\approx0.07}$ for each grid set, where all four grid sets overlap (see Table B.1). This corresponds to a cell count of approximately 2 000 000, or grids A4, B4, and C2. Finally, uncertainties computed for each component, on all grids are provided in Table B.4.

The procedure for the grid uncertainty of the yaw moment is very well behaved for grid set A. For other grid sets the convergence behaviour is such that the safety factor is increased to three and a second-order fit is applied. Results from grids C and Cnobl are poorly fit, as indicated by σ_{fit}/Δ_ϕ. In particular, C2nobl, which exhibits oscillatory convergence, and where the large difference for the term $(\phi_i - \phi_{fit})$ from Equation (3.7) results in large uncertainties (see Figure B.3). The Richardson extrapolation value for zero-grid spacing differs by 8 % for grid C and Cnobl. The values for zero-grid spacing of grid sets A and B lie within 3 % of each-other.

The results presented above can be better interpreted by recalling the grid set
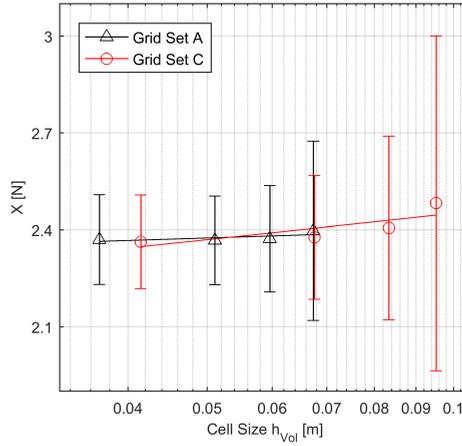
Figure B.2.: Resistance convergence for grid discretization ($\beta = 0°$). U_D indicated with error bars.
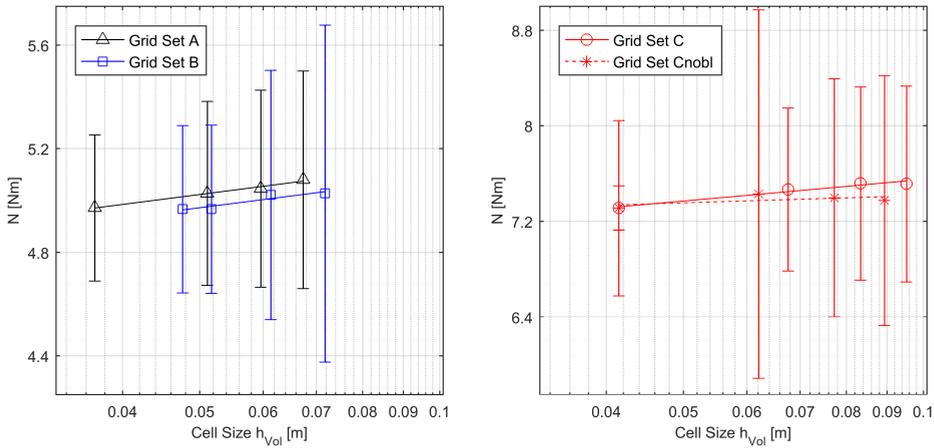
Figure B.3.: Yaw moment convergence (left: $\beta = 6°$, right: $\beta = 9°$). U_D indicated with error bars.

Table B.3.: Calculation details for grid uncertainty estimate for yaw moment.

Grid Set	R	p_Obs	Fit	σ_{fit}/Δ_ϕ	F_S	ϕ_0	$U_{h_\mathrm{Vol}\approx0.07}$ [%]
A ($\beta = 6°$)	3.06	0.65	δ_RE	0.21	1.25	4.75	8.3
B ($\beta = 6°$)	0.00	3.22	δ_2	0.34	3	4.83	13
C ($\beta = 9°$)	3.14	3.10	δ_2	0.99	3	7.21	9.1
Cnobl ($\beta = 9°$)	−3.59	2.78	δ_2	2.04	3	7.32	22

Table B.4.: Complete results for numerical uncertainty.

Grid ID	h_{Vol}	$U_{\mathrm{Num}} : X$		$U_{\mathrm{Num}} : Y$		$U_{\mathrm{Num}} : N$	
	m	N	%	N	%	N m	%
$\beta = 0°$							
A4	0.067	0.28	12				
A3	0.060	0.16	6.9				
A2	0.051	0.14	5.8				
A1	0.037	0.14	5.9				
C4	0.095	0.52	21				
C3	0.083	0.28	12				
C2	0.068	0.19	8.1				
C1nobl	0.041	0.14	6.1				
$\beta = 6°$							
A4	0.071	0.24	9.3	0.46	32	0.42	8.3
A3	0.063	0.14	5.3	0.27	20	0.38	7.5
A2	0.054	0.11	4.4	0.17	13	0.36	7.1
A1	0.039	0.09	3.4	0.04	3.0	0.28	5.7
B4	0.072	0.48	18	0.30	21	0.65	13
B3	0.061	0.47	18	0.22	17	0.48	10
B2	0.052	0.34	13	0.18	14	0.32	6.5
B1	0.048	0.36	14	0.14	11	0.32	6.5
$\beta = 9°$							
C4	0.095	0.75	25	1.00	39	0.82	11
C3	0.083	0.40	14	0.65	27	0.81	11
C2	0.068	0.31	11	0.33	14	0.68	9.1
C1nobl	0.041	0.19	6.6	0.04	1.9	0.19	2.5
C4nobl	0.089			0.39	17	1.04	22
C3nobl	0.077			0.26	11	1.00	20
C2nobl	0.062			0.13	6.0	1.54	22
C1nobl	0.041			0.02	1.0	0.73	9.3

definition in terms of the cell size dx and the refinement diffusion (see Figure 3.9). First, the large uncertainty values reported for grid set B are interesting as the cell size dx for grids B1-B3 is smaller than the cell size dx for Grid A2. On the other hand, the two largest grids, A1 and C1nobl, where quite small uncertainties are computed for all force components, have the largest refinement diffusion. This is interpreted as a consequence of proper resolution of the wake of shed vorticity associated with sideforce production. For the grid definition for validation simulations, the refinement diffusion parameter should be prioritised over cell size dx. The general trend for the poor performance of grid set B does not hold for the uncertainty for sideforce U_{Num}: Y. For grids A2-A4 and B2-B4, where the refinement diffusion varies uniformly, one can observe the influence of the cell size dx on the sideforce uncertainty, which increases quickly for grid set A after grid A2 (cell size $dx = 0.006$ ($\approx L/500$).

Courant Number Study

Time-discretization uncertainties are determined for three grids, A2, B1, and B3, following the same procedure as above. The temporal uncertainty corresponding to a target Courant number of four is reported. This is the same target Courant number used for the discretization uncertainty calculations presented above.

Courant number variation on grid B1 returns an observed order of convergence equal to 1.55 and σ_{fit}/Δ_ϕ less than one, yet the uncertainty $U_{\mathrm{Co}\approx4}$ is the largest calculated. By contrast, grids A2 and B3 returned an observed order of convergence outside the range prescribed by Eça and Hoekstra and switch to the mixed order fit δ_{12} with safety factor equal to three. The ϕ_0 value for grids A2 and B3 differ from ϕ_0 value of grid B1 by 5.9 % and 3.1 % respectively, which is in accordance with the presence of considerable discretization uncertainty calculated for sideforce on these grids (for A2: U_{D} =13%, B1: U_{D} =14%, B3: U_{D} =17%). Finally, the ϕ_0 value for zero-time step for grid A2 differs from the ϕ_0 value for zero grid spacing for grid set A by 6.3 %, while the extrapolated values for zero time step for grid B1 and zero grid spacing for grid set B differ by 10 %.

The value for yaw moment varies very little with Courant number, and the time discretization uncertainty is insignificant. Extrapolations for zero-time step lie within 1 % of each other and within 6 % of the extrapolated zero-grid size value. The fitting for the observed order of convergence does not succeed. The method of Eça and Hoekstra returns the safety factor of three with very small values for σ_{fit}/Δ_ϕ, except for grid B3, where oscillatory convergence is observed.

Table B.5.: Calculation details for Courant number parameter study for sideforce.

Grid	R	p_{Obs}	Fit	σ_{fit}/Δ_ϕ	F_{S}	ϕ_0	$U_{\mathrm{Co}\approx4}$ [%]
A2	2.44	19.97	δ_{12}	0.22	3	1.35	3.7
B1	−0.48	1.55	δ_{RE}	0.90	1.25	1.27	5.8
B3	0.33	0.29	δ_{12}	0.05	3	1.31	3.3
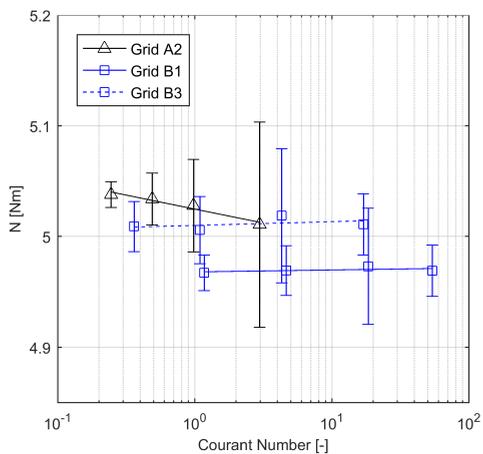
Figure B.4.: Yaw moment convergence behaviour for Courant number variation ($\beta = 6°$) U_T indicated with error bars.

Table B.6.: Calculation details for Courant number parameter study for yaw moment.

Grid	R	p_Obs	Fit	σ_{fit}/Δ_ϕ	F_S	ϕ_0	$U_{\mathrm{Co}\approx4}$ [%]
A2	0.64		δ_{12}	0.13	3	5.04	1.8
B1	0.53		δ_{12}	0.15	3	4.97	0.4
B3	−0.25		δ_{12}	1.03	3	5.01	1.2

Table B.7.: Complete results for Courant number study.

Courant	Mean		Grid A2		Grid B1		Grid B3	
	$U_T{:}X$		$(U_D = 4.4\%)$		$(U_D = 14\%)$		$(U_D = 18\%)$	
	N	%	N	%	N	%	N	%
50	0.25	9.4			0.25	9.4		
16	0.19	7.0			0.24	9.0	0.13	5.0
4	0.07	2.8	0.05	2.1	0.14	5.3	0.03	1.0
1	0.03	1.2	0.02	0.7	0.03	1.1	0.05	1.9
0.5	0.02	0.6	0.01	0.3			0.02	0.9
0.25	0.00	0.2	0.00	0.2				
	$U_T{:}Y$		$(U_D = 13\%)$		$(U_D = 11\%)$		$(U_D = 17\%)$	
	N	%	N	%	N	%	N	%
50	0.13	9.8			0.13	9.8		
16	0.07	5.7			0.04	7.3	0.06	4.2
4	0.06	4.3	0.05	3.7	0.07	5.8	0.04	3.3
1	0.04	2.9	0.06	4.7	0.03	2.1	0.03	2.0
0.5	0.04	2.7	0.05	3.9			0.02	1.5
0.25	0.02	1.8	0.02	1.8				
	$U_T{:}N$		$(U_D = 7.1\%)$		$(U_D = 6.5\%)$		$(U_D = 10\%)$	
	Nm	%	Nm	%	Nm	%	Nm	%
50	0.02	0.5			0.02	0.5		
16	0.04	0.8			0.05	1.1	0.03	0.5
4	0.06	1.2	0.09	1.8	0.02	0.4	0.06	1.2
1	0.03	0.6	0.04	0.8	0.02	0.3	0.03	0.6
0.5	0.02	0.5	0.02	0.5			0.02	0.5
0.25	0.01	0.2	0.01	0.2				

B.2. Validation Experiment (2016)

Experiments were designed to obtain validation data with minimal uncertainty. As detailed in Chapter 3, the validation data was collected during two experimental campaigns, in 2015 and 2016. The setup for the experiment was altered for the 2016 campaign. The fully constrained setup, with the six-component measurement frame, rather than the sailing yacht set-up, gave better control over the position of the model, and provides extra flexibility when designing the arrangement of sensors; again with the aim to minimize experimental uncertainty. The 2016 experiments are described in the remainder of this section. The yacht setup of the Delft Ship Hydro-mechanics laboratory is documented in [65]. Test setup, post-processing, and uncertainty assessment follows ITTC guidelines [54, 57].
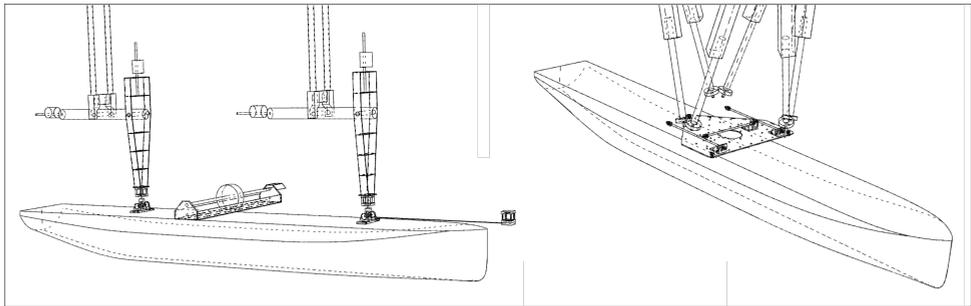
Figure B.5.: Sailing yacht (left) and hexapod (right) experimental setup.
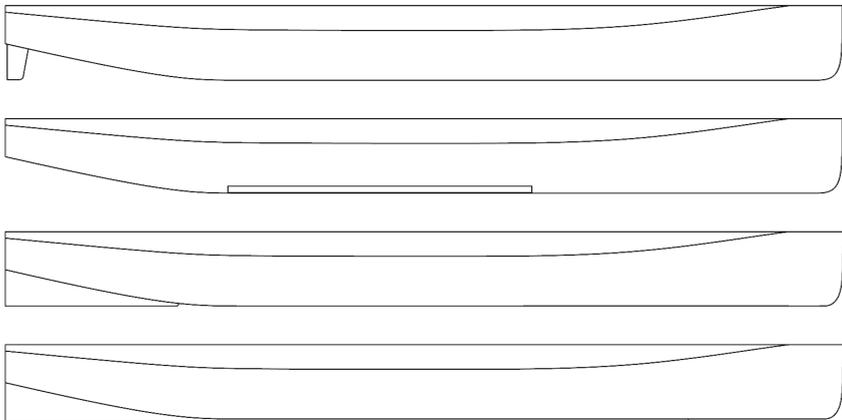
Figure B.6.: Appended validation hulls (2016) (top to bottom): Hull #1 with Rudder, Hull #1 with Bilge keels, Hull #34 with Skeg, Hull #34 with Skeg and Bar keel

Test Set-up

The model is mounted below the hexapod actuator. Extra load cells will be calibrated before testing begins in case a load cell is ruined. The target weight for each model is ½ of its displacement. Peak forces under acceleration are reduced by reducing the inertial contribution. The uncertainty for strip correction was a leading contributor for experimental uncertainty in the tests of G. Struijk. Repeats at the speeds of interest (indicated with an astrix below) are included to increase the sample size and hopefully to reduce the uncertainty for this quantity. The force sensors and connecting pins for the z-direction are dimensioned according to half the displacement, so the model can be pressed into the water up to the design waterline and lifted out of the water. For the nominal VPP sweep, the model is towed at three speeds corresponding to Fn = 0.128, 0.168, 0.21, and four leeway angles, giving 12 runs total.

During the 2016 test campaign, the models were tested in fully captive setup. The models were connected to the hexapod with the six-component measurement frame. The measurement frame is designed to resolve any applied force or moment into orthogonal forces and moments. The hexapod setup is illustrated in Figure B.5 (right), with the top plate of the six-component frame removed for clarity. The arrangement of the sensors on the measurement frame was made to obtain the best possible fidelity for the sideforce. The model is hereby restrained in all degrees of freedom, as in the simulation set-up. The hexapod set-up will allow for precise setting of the leeway angle; will remove uncertainties associated with ballasting, trim, and roll; and will simplify the experimental procedure. The rudder is added to the Hull #1 in the tank. The rudder angle should be set to zero and six degrees with a high degree of precision. The rudder has turbulence stimulators at one-quarter-chord from the leading edge. The rudder is expected to lie within the turbulent wake of the hull, but the possibility exists for laminar flow over some part of the rudder. The position of the model is recorded using a Certus optical tracking system. All signals are filtered with a low-pass filter set to 100 Hz before sampling to prevent aliasing. The signal is sampled at a frequency of 1000 Hz and written to disc.

The measurement campaign was three weeks long. To assure that a consistent procedure was followed, the following protocol was adopted:

1. Model set to zero leeway position for nul measurement.

2. Model set to leeway angle for second nul measurement.

3. Carriage accelerated to test speed. 10 seconds is allowed for the flow to reach a steady condition.

4. Measurements recorded for 60 seconds.

The nominal rest period between runs was 20 minutes. The test program is arranged so that high-speed runs and repeat runs were interspersed regularly, and so that a low-speed run did not immediately follow a high-speed run. The first run of each day, and the first run after a weekend, was marked in the measurement log.

Turbulence Stimulators

The models were fitted with turbulence stimulators to ensure a turbulent boundary layer along the hull. The correction for an added resistance due to turbulence stimulation was determined according to the standard practice of the Delft Ship Hydromechanics Laboratory by comparing resistance curves obtained for single- and double strip configurations. The turbulence stimulation strip resistance coefficient was determined for Hull #34 - Bare. This value is adopted for all other data, including results from the 2015 experiment. The resistance is corrected for the change in resistance due to the presence of turbulence stimulators:

$$\Delta R_{\mathrm{TS}} = \frac{1}{2}\rho V^2 C_{\mathrm{TW}} A_{\mathrm{TW}} \tag{B.12}$$

A_{TW} is the area of the turbulence stimulator.

Bow Wave Measurements

As a further qualitative check for the simulations, the interface capturing for the asymmetric bow wave was compared to measurements from experiments. The profile of the bow wave was measured using cameras and grid markings on the ship. The images were de-warped to correct for lens effect and perspective and scaled so that one is pixel was equal to 0.5 mm. It was then possible to measure the position of the maximum and minimum wave elevation. This exercise was performed for Hull #34 – Bare.

Experimental Uncertainty

The experimental uncertainty is determined according to the ITTC guideline for planar motion tests [54]. The following error components were found to be significant: bias errors arising from the measurement of forces and moments with the six-component frame, bias errors arising from model misalignment in the tank, bias errors due to geometric faults in the model construction, and an end-to-end estimate of the precision error for the complete experimental setup. The calculation of U_{X} is detailed for Hull #34 - Bare at $Fn = 0.17$ and β=9° in Table 3.4. An accounting of the precision limit in the 2016 validation experiment is plotted in Figure B.7.
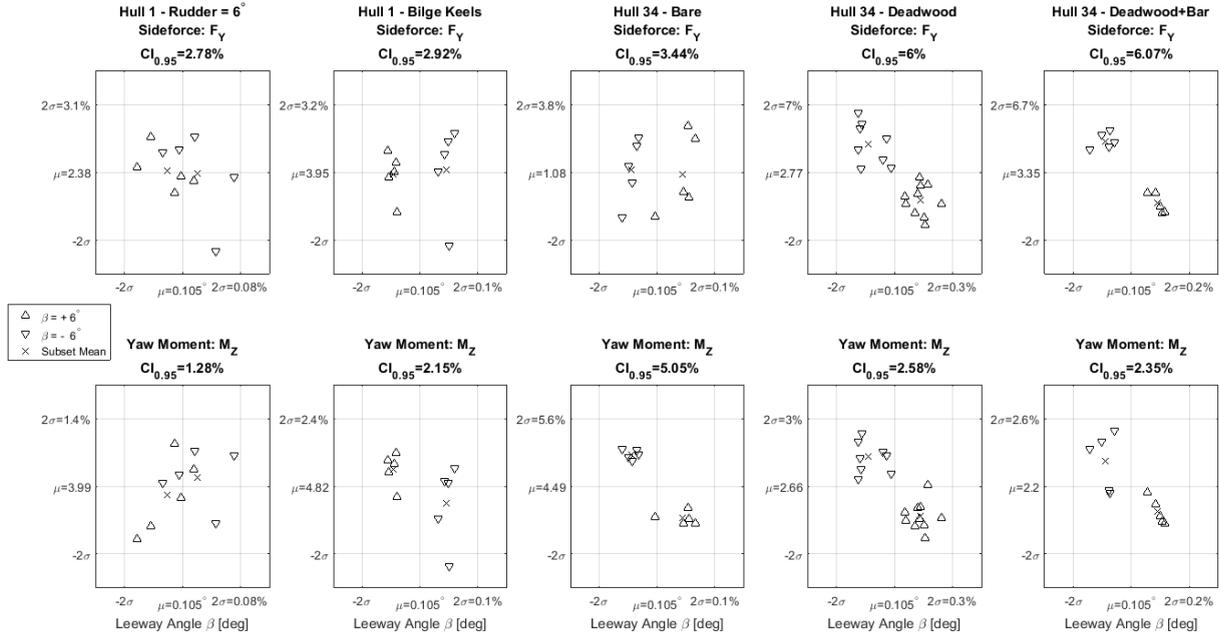
Figure B.7.: Precision bias estimate for 2016 Experiment. A vector sum of the offset determined using the zero-crossing for sideforce and yaw is used to estimate the alignment fault.

Test Set-up

The model is mounted below the hexapod actuator. The model is hereby restrained in all degrees of freedom, as in the simulation set-up. The hexapod set-up will allow for precise setting of the leeway angle; will remove uncertainties associated with ballasting, trim, and roll; and will simplify the experimental procedure. The 6-dof measurement frame is arranged with the highest possible sensitivity for forces in the horizontal plane. The measurement of horizontal forces is performed using 30-Newton load cells. Extra load cells will be calibrated before testing begins in case a load cell is ruined. The target weight for each model is ½ of its displacement. Peak forces under acceleration are reduced by reducing the inertial contribution. The uncertainty for strip correction was a leading contributor for experimental uncertainty in the tests of G. Struijk. Repeats at the speeds of interest (indicated with an astrix below) are included to increase the sample size and hopefully to reduce the uncertainty for this quantity. The force sensors and connecting pins for the z-direction are dimensioned according to half the displacement, so the model can be pressed into the water up to the design waterline and lifted out of the water. For the nominal VPP sweep, the model is towed at three speeds corresponding to Fn = 0.128, 0.168, 0.21, and four leeway angles, giving 12 runs total.

Validation Results

Further results for the validation exercise are presented, following the material already given in Chapter 3. The direct validation for Hull #1 – Bare at Fn=0.168 and leeway angles β = 0°, 6°, 9° is given, and the multivariate validation statement is made for appended hulls in the Wind-Assist Series.

Appended-hull validation case

The results for X_i for appended r/r_{ref} is subject to the same qualifications outlined above for the bare-hull result. For the appended cases, shown in Figure B.9, the resistance increase due to sideforce is generally over-predicted, a trend that also present for the bare hull cases (excepting Hull #16). As with any lifting profile, the production of sideforce for wind-assist vessels is characterised by a wake of vortices. The presence of numerical dissipation may be introducing a non-physical energy loss to the accounting for energy lost in shed vorticity. Though an apparently systematic error is observed, the validation level for this quantity is much too large to consider making a correction.

Simulation and experimental values for sideforce and yaw angle are presented in Figure B.10 and Figure B.11. An excellent agreement is observed (when rudder stall angles are removed), indicating that the simulation methodology may be used to study the sailing balance of wind-assist vessels for these appendage types.

Test Definition Repeats Repeat runs are necessary whenever the experimental set-up is changed. The ITTC guideline specifies 10 repeat runs to determine the reliability of the measurement system. The measurement of transverse forces is of interest, therefore repeats are carried out with a leeway angle of +/- 6 degrees. For

Hull #1

Hull #16

Hull #19

Hull #34
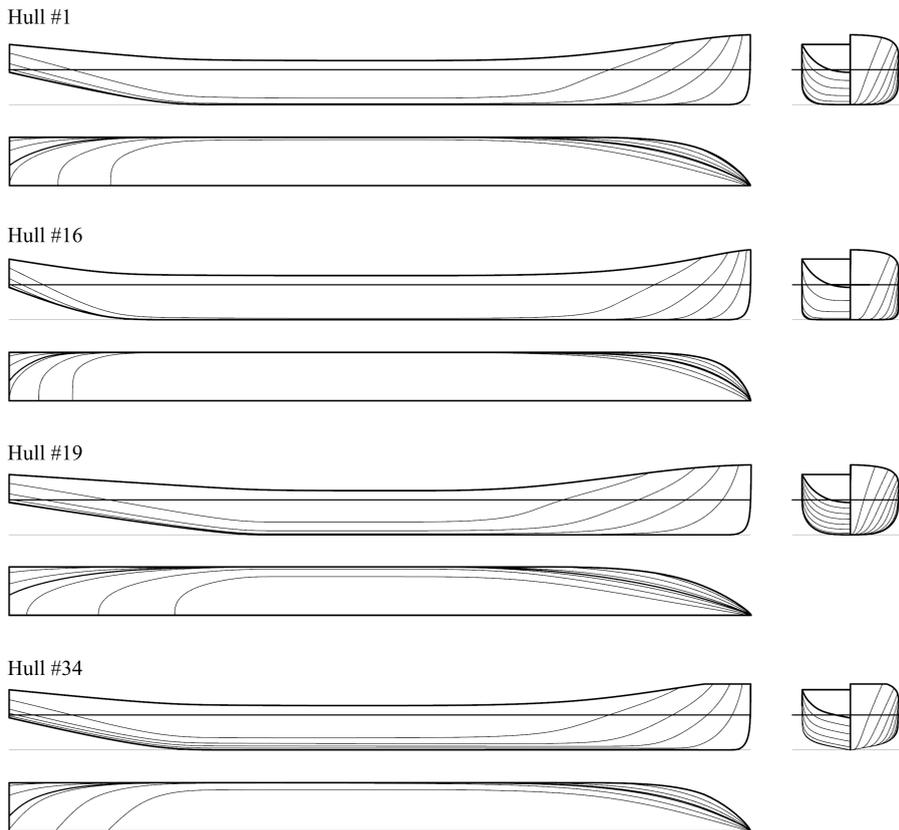
Figure B.8.: Linesplans for hulls of the validation set.
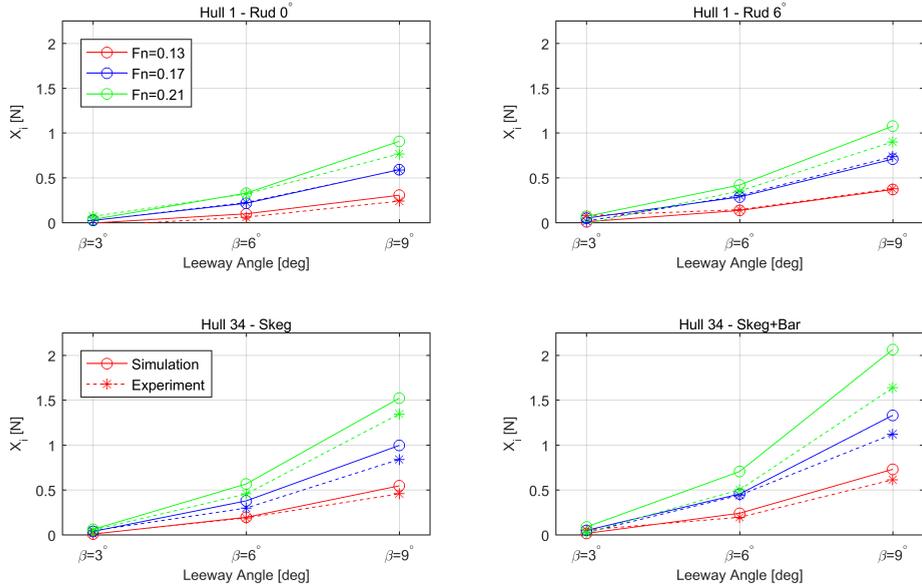
Figure B.9.: Simulation and experimental results for appended cases for resistance due to leeway.
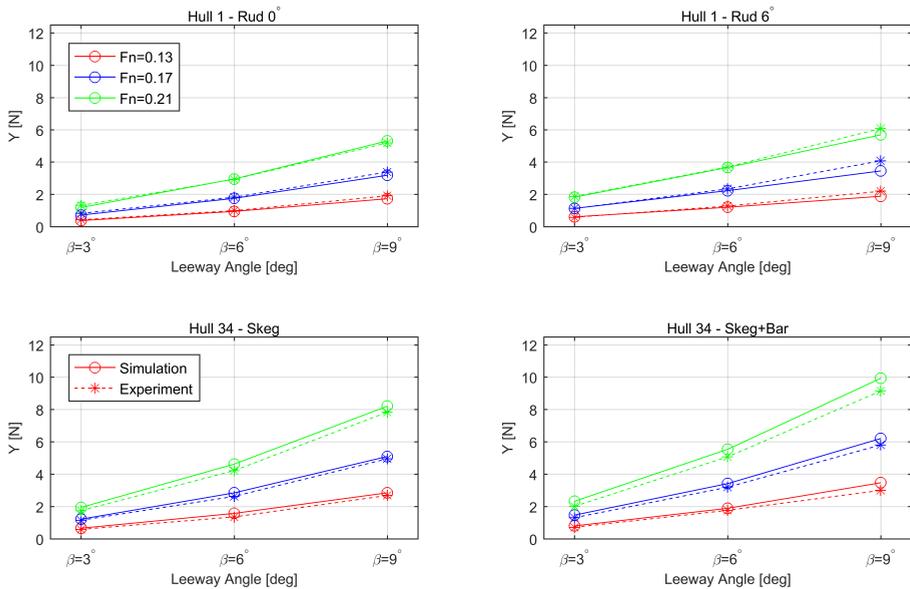
Figure B.10.: Simulation and experimental results for appended cases for sideforce.
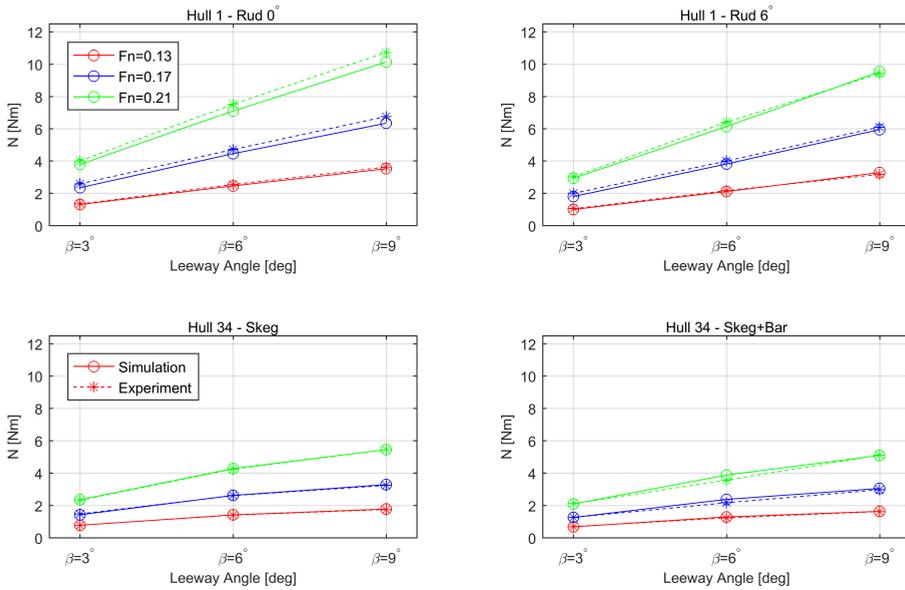
Figure B.11.: Simulation and experimental results for appended cases for yaw moment.

this leeway angle, expected forces for longitudinal and transvers load cells are approximately equal. The repeat runs are interspersed throughout the measurements of each model variation.

B.3. Bilge Keel Campaign (2017)

The analysis for measured quantities follows a straightforward application of the towing tank standard procedure [54]. For derived quantities such as effective draft, T_e/T, a more deliberate assessment of the experimental uncertainty is required. The objective in this experiment was to reveal the sailing characteristics of bilge keels, rather than to generate data suitable for validation. The uncertainty assessment is presented to attest that the measurement fidelity was sufficient for the small quantities of interest, and that the measurement setup could accommodate high sensitivity to model alignment and geometric errors whilst carrying out an experimental campaign during which the model was repeatedly removed to rebuild the bilge keel geometry.

The discussion of the uncertainty for measured quantities is devoted to resistance and the induced resistance in particular, which has been identified as the most demanding for the fidelity of the measurement system.

The following bias errors are found to be significant: calibration for the measurement frame, alignment of the model, and construction of the model geometry. Three components of the experimental system will be discussed: the design and
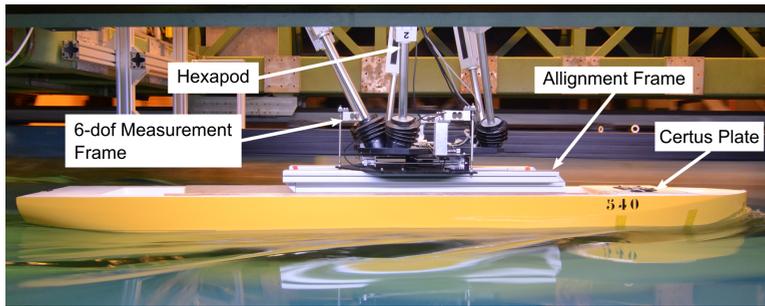
Figure B.12.: Overview of experimental setup with key components labeled

calibration of the six degree-of-freedom measurement frame, the alignment frame, and the reproducibility of appendage geometries. A complete reporting of the uncertainty assessment is included in the data archive [118].

Measurement frame

The design of the six degree-of-freedom (6-dof) measurement frame is informed foremost by the relatively small induced resistance, compared to the other measured quantities and especially compared to the displacement of the ship model. See Figure B.12 for experimental setup. Whereas the weight of displaced water is approximately 90 kg, the induced resistance is typically less than one Newton. The strain gauges had to accommodate the rather large inertial loading while accelerating the model, yet be able to measure variations in the induced resistance. Zemic L6J load cells with 3 kg capacity were used for forces measured in the lateral plane. The sensors are fitted to a 6-dof measurement frame that uses an arrangement of necked pins to decompose a loading state into orthogonal forces and moments. This arrangement of gauges and pins will introduce a further stiffness to the calibra-

Table B.8.: Estimates for the precision limit (B-P3-L1-H3 (16), Fn=0.21, leeway angle β= 9°)

Set	Resistance		Sideforce		Yaw Moment	
	μ [N]	U_{95} [%]	μ [N]	U_{95} [%]	μ [Nm]	U_{95} [%]
Complete Set (Figure 4.6)	7.03	2.5	9.26	3.9	10.9	5.4
First Realisation (15/12/2017)	6.97	2.1	9.17	4.0	10.7	2.8
Second Realisation (7/1/2018)	7.08	1.9	9.36	2.9	11.2	2.0
Alignment Frame (Figure B.13)	7.02	1.9	9.26	2.9	10.9	4.8

tion factor of the individual gauges. Also, the mechanical complexity of the frame compounds the hysteresis effect of individual gauges. A calibration is performed after frame assembly to verify alignment of the components and to control for the effect of frame stiffness and hysteresis. The bias error, determined from the frame calibration by the SEE method [22], is reported in Table B.9 for the resistance.

Alignment Frame

An alignment frame was designed to enable repeated, precise mounting of the model beneath the measurement frame. The level of precision attained was measured with a series of 10 repeat measurements, for which the model was disconnected from the measurement frame before each run. The result for this test for the resistance is plotted in Figure B.13. This result is taken as the precision limit for the experimental setup.

The model was disconnected repeatedly from the measurement system to allow construction of each bilge keel variant. Each reassembly of the measurement setup raises the possibility of model misalignment in the tank. The precision achieved with the alignment frame was sufficient to allow for a single alignment for each hull, accomplished with a set of positive and negative repeat measurements. The nominal test matrix for each appendage variant included an equal number of positive and negative leeway angels. The fitting for maneuvering coefficients and effective draft is therefore insensitive to (small) misalignment for the model, which would be manifest as a constant y-intercept in the regression fits. The bias for alignment was determined as the root-sum-squared combination of leeway angles for zero sideforce and moment - a conservative estimate.

Table B.9.: Details for calculation of experimental uncertainty for resistance for keel variant B-P3-L1-H2 (16) at Fn=0.21 and leeway angle $\beta = 9^o$. The uncertainty u' is given as a percentage of the measured value. The geometric error is the dominant term.

Θ	$\frac{\partial X}{\partial \Theta}$	δ_Θ	u_Θ [N]	u'_Θ [%]
X	0.0094	0.0423N	0.084	1.2
β	0.0011	0.0029rad	3.19×10^{-6}	0.0
T	0.0024	0.002m	0.185	2.6
P			0.135	1.9

B. Uncertainty Analysis
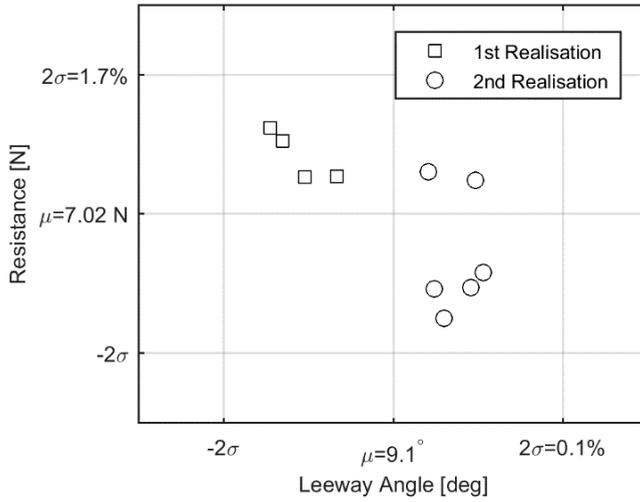
Figure B.13.: Precision limit of the alignment frame for resistance
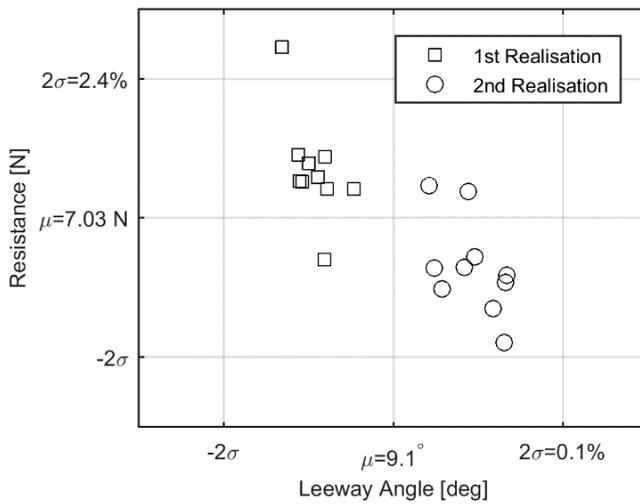
Figure B.14.: Complete set of repeat runs for precision limit for resistance $n = 20$.

Appendage Geometry

The reproducibility of the appendage variations was tested by rebuilding and retesting case B-L3-P3-H3 (16) at the end of the campaign. The result for the resistance is plotted in Figure B.13. The mean value and the two-sigma value is indicated. Results for the 95% confidence interval, based on the complete set of 20 repeat measurements are provided in Figure B.14 and Table B.8. Whereas the close grouping for these measurements lends assurance to the reproducibility of the model geometry, it would be inappropriate to derive a geometric bias contribution from this test because the difference in the measurements for the first and second realization of the bilge keel geometry may be the result of other error sources besides a geometric fault. Therefore, a geometric error is assumed based on the tolerance achieved during the preparation of the slits in the bilges of the hull models and the experience of the bilge keel assembly.

Derived Quantities

The 95% confidence intervals for maneuvering coefficients, the CLR, and the effective draft are included in all figures in the discussion of Chapter 4. The uncertainty associated with some derived quantities is rather large. For example, the number of available data points for fitting a third-order polynomial is limiting for the higher-order terms in the maneuvering equations. For the CLR, for which the uncertainty follows a direct application of uncertainty propagation rules, the relatively small sideforce in the denominator in the equation for CLR results in large sensitivity coefficient in the uncertainty propagation. The symmetry of the testing matrix, with a distribution of positive and negative leeway angles, means the bias contribution for model orientation may be disregarded for the maneuvering coefficients and the effective draft. In light of the relative magnitude of the uncertainties of the remaining bias contributions outlined above, the uncertainty reported for maneuvering coefficients and the effective draft is simply the uncertainty associated with fitting the associated models, without considering the uncertainty for the measured quantities as derived in the previous section.

List of Figures

List of Tables

Nico van der Kolk

EU and US citizenship   5-5-1985

m   +31 681457981
e   n.j.vanderkolk@tudelft.nl
    nicovanderkolk@gmail.com
s   nicov.d.kolk

Summary

I am a well-trained engineer with a specialization in fluid mechanics, with broad experience in towing tank experimentation and numerical simulation; and I am soon completing my Ph.D. research at the ship hydromechanics laboratory of Delft University of Technology, in the Netherlands. I am actively looking for a new opportunity to carry on with my research in ship hydro-mechanics. I am a well-rounded candidate: I have the necessary technical background, work and research experience, and a passion for the topic that will motivate me to excel. I can provide several academic and professional references.

Related Employment

2016-2017   Teaching Assistant: Ship Motions and Maneuvering III – TU Delft NL
- Supervised and assessed 50 master-level students. Led software tutorials.

Summer 2012   Research engineer at Damen Shipyards – Gorinchem NL
- Created numerical simulation and design tool for complex system.
- Worked independently with SIMULINK software package.

2009-2011   Naval architect with Marine Innovation & Technology – Berkeley CA
- Preliminary sizing and design including interaction with clients, extensive drafting responsibilities, project documentation, field work.
- Designing experimental system for towing tank experiments.

2007   Design Engineer for Lagrangian Drifter Network – UC Berkeley
- Designed and prototyped a small drifting sensor.
- Developed buoyancy control and propulsion system.

2000, 2001, 2004   Apprentice at Karl's Boat Shop – Cape Cod MA
- Carpentry, fiberglass work, prep for paint, and any number of other odd jobs.

Education

2015 –2019   **Technical University Delft**
Ph.D. Candidate: Marine Technology: Ship Hydromechanics specialization.
"Sailing Efficiency and Course Stability of Wind-assisted Ships"

2011 –2014   **Technical University Delft**
M.Sc. Marine Technology: Ship Hydromechanics specialization.

2006 – 2009   **University of California, Berkeley**
B.S. Mechanical Engineering: Ocean Engineering specialization.

2003 – 2006   **University of California, Santa Cruz**
B.A. History: European History specialization.

Languages, skills

English (fluent), Dutch (fluent), Czech, French.
International collaboration, experimentation, numerical simulation.

List of Publications

10. N. J. van der Kolk. "Hydrodynamics of Wind-Assisted Ship Propulsion: Modelling of Hydrodynamic Sideforce". In: *HISWA Symposium on Yacht Design and Yacht Construction*. HISWA Technical Conference. Amsterdam, 2016

9. N. J. van der Kolk, J. A. Keuning, and R. H. M. Huijsmans. "Hydrodynamics of Wind-Assisted Ship Propulsion: Verification of RANS Simulations". In: *International Conference in Hydrodynamics*. International Conference for Ship Hydrodynamics. Egmond aan Zee, 2016

8. N. J. van der Kolk et al. *Dataset: Bilge Keels for Course Stability and Sailing Efficiency of Wind-Assisted Ships*. en. 2019. doi: `10.4121/UUID:A9314E24-5D4C-4C46-9F99-391EE7CDC1EB` (Appendix A)

7. N. J. van der Kolk et al. "Case study: Wind-assisted ship propulsion performance prediction, routing, and economic modelling". In: *Proceedings of the International Conference Power & Propulsion Alternatives for Ships*. London: The Royal Institution of Naval Architects, 2019

6. van der Kolk N. J. et al. "Low aspect appendages for wind-assisted ships". In: *Journal of Marine Science and Technology* (2019). (manuscript under review) (Chapter 4)

5. van der Kolk N. J., J. A. Keuning, and R. H. M. Huijsmans. "Part 1: Experimental Validation of a RANS-CFD Methodology for the Hydrodynamics of Wind-Assisted Ships Operating at Leeway Angles". In: *Ocean Engineering* 178 (2018), pp. 375–387. doi: `10.1016/j.oceaneng.2018.12.041`

4. N. van der Kolk et al. "Part 2: Simulation Methodology and Numerical Uncertainty for RANS-CFD for the Hydrodynamics of Wind-Assisted Ships Operating at Leeway Angles". In: *Ocean Engineering* (2020). doi: `https://doi.org/10.1016/j.oceaneng.2020.107024` (Chapter 3)

3. G. Bordogna et al. "Wind-assisted ship propulsion performance prediction, routing and economic analysis - a corrected case study". In: *Conference: RINA Wind Propulsion Conference*. London, UK: Royal Institute of Naval Architects, Oct. 2019

2. N. van der Kolk; G. Bordogna; J.C. Mason; J.M. Bonello; A. Vrijdag; J.F. Broderick; A. Larkin; T. Smith; I. Akkerman; J.A. Keuning; R.H.M. Huijsmans; "Wind-Assist for Commercial Ships: A Techno-Economic Assessment". In: *Ship and Offshore Structures* (2020). (manuscript under review) (Chapter 5)

1. N. van der Kolk and B. S. Freeman. "Machine Learning Based Hydro-mechanic Modeling for Wind-assisted Ships". In: *InnovSAIL2020*. 2020 (Chapter 2)